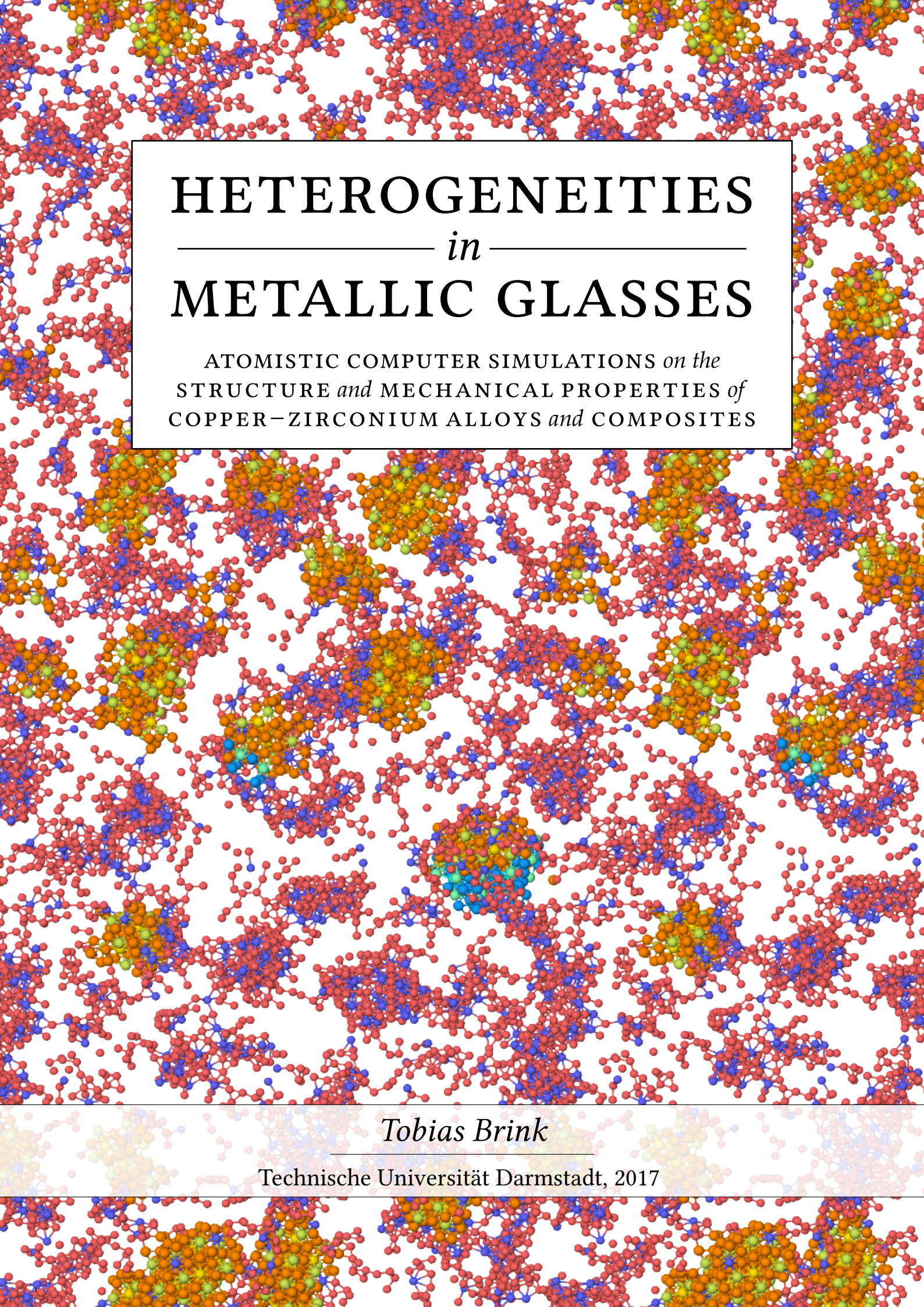

HETEROGENEITIES *in* METALLIC GLASSES

ATOMISTIC COMPUTER SIMULATIONS *on the* STRUCTURE *and* MECHANICAL PROPERTIES *of* COPPER–ZIRCONIUM ALLOYS *and* COMPOSITES

Tobias Brink

Technische Universität Darmstadt, 2017

HETEROGENEITIES IN METALLIC GLASSES: ATOMISTIC COMPUTER SIMULATIONS ON THE STRUCTURE AND MECHANICAL PROPERTIES OF COPPER–ZIRCONIUM ALLOYS AND COMPOSITES

Zur Erlangung des akademischen Grades Doktor-Ingenieur (Dr.-Ing.)
genehmigte Dissertation von Dipl.-Ing. Tobias Brink, geboren in Koblenz

Fachgebiet Materialmodellierung
Fachbereich Material- und Geowissenschaften
Technische Universität Darmstadt

Referent: Prof. Dr. rer. nat. Karsten Albe
Korreferent: Prof. Dr.-Ing. Jürgen Eckert
1. Prüfer: Prof. Dr.-Ing. Karsten Durst
2. Prüfer: Prof. Dr. rer. nat. Michael Vogel

Tag der Einreichung: 17. Oktober 2016
Tag der Prüfung: 7. Dezember 2016

Darmstadt 2017
D17

On the cover: Visualisation of precipitates grown in a $Cu_{64}Zr_{36}$ glass after an annealing procedure. The picture shows the crystalline phases C14 and C15 in orange and light blue, as well as networks of favourable copper and zirconium polyhedra in red and blue, while all other atoms were deleted.

Please cite this document as:
URN: urn:nbn:de:tuda-tuprints-58586
URL: http://tuprints.ulb.tu-darmstadt.de/5858/

Dieses Dokument wird bereitgestellt von tuprints,
E-Publishing-Service der TU Darmstadt
http://tuprints.ulb.tu-darmstadt.de
tuprints@ulb.tu-darmstadt.de

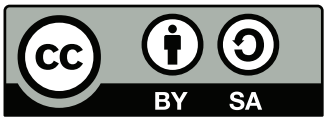

ERKLÄRUNG ZUR DISSERTATION

Hiermit versichere ich, die vorliegende Dissertation selbständig mit Hilfe der angegebenen Quellen und Hilfsmittel angefertigt zu haben. Alle Stellen, die aus Quellen entnommen wurden, sowie alle Daten, die aus Kollaborationen stammen, sind als solche kenntlich gemacht. Diese Arbeit hat in gleicher oder ähnlicher Form noch keiner Prüfungsbehörde vorgelegen, ein Promotionsversuch wurde von mir bisher nicht unternommen.

Darmstadt, den 17. Oktober 2016

(Tobias Brink)

CONTENTS

LIST OF FIGURES

LIST OF TABLES

LIST OF ABBREVIATIONS

BMG	bulk metallic glass
CNA	common neighbour analysis
DFT	density-functional theory
EAM	embedded-atom method
GUM	geometrically unfavoured motif
HEA	high-entropy alloy
MD	molecular dynamics
ML	monolayer
MRO	medium-range order
PEL	potential energy landscape
RDF	radial distribution function
SRO	short-range order
SSA	solid-state amorphisation
STZ	shear transformation zone
TEM	transmission electron microscopy
VDOS	vibrational density of states

NOMENCLATURE

a	lattice constant
A	area
c	lattice constant
c_{ij}, c_{ijkl}	components of the stiffness tensor
C, C_p, C_V	heat capacity (general, at constant pressure, at constant volume)
d	diameter, thickness
E	energy
E_{coh}	cohesive energy
E_{kin}	kinetic energy
E_{pot}	potential energy
E_{tot}	total energy, sum of potential and kinetic energy
$\mathcal{E}$	Young's modulus
f	crystalline volume fraction
F	Helmholtz free energy
$\mathbf{F}$	force vector
g	vibrational density of states, usually $g(\omega)$, $g(\nu)$
g_{RDF}	radial distribution function

$\mathcal{G}$	shear modulus
$\mathcal{G}_1,\ldots,\mathcal{G}_5$	Kelvin shear moduli, see Sec. 2.5.3
h, $\hbar$	Planck constant, reduced Planck constant $\hbar = h/2\pi$, $h = 6.626\,070\,040(81) \cdot 10^{-34}$ Js [CODATA 2014]
k_B	Boltzmann constant, $k_\mathrm{B} = 1.380\,648\,52(79) \cdot 10^{-23}\,\mathrm{JK}^{-1}$ [CODATA 2014]
$\mathcal{K}$	bulk modulus
l	a length
m	mass
N	number of particles/atoms
p	pressure
r	radius, (interatomic) distance
s_{ij}, s_{ijkl}	components of the compliance tensor
S	entropy
t	time
δt	integration timestep (MD)
T	temperature
T_g	glass transition temperature
T_m	melting point
U	internal energy
v_g	group velocity
$\mathbf{v}$	velocity
V	volume
$\mathbf{x}$	position vector
x, y, z	cartesian coordinates
Z	atomic number
α, β	species of atoms, often atom i has species α and atom j has species β
γ	shear strain
$\check{\gamma}$	engineering shear strain
ε	strain
$\check{\varepsilon}$	engineering strain
ζ	interface energy
η_i	Green–Lagrangian strain tensor of atom i, "atomic strain tensor" for short
η_i^Mises	von Mises local shear invariant of atom i, "atomic shear strain" for short
Θ	Debye temperature
Λ	geometry factor depending on crystalline volume fraction f and precipitate geometry, see Chap. 8
ν	frequency
ν_D	Debye frequency
ν_Poisson	Poisson's ratio
ξ	partial velocity auto-correlation function
Ξ	velocity auto-correlation function
ρ	density
ρ_n	number density, i.e., atoms per unit volume
σ	stress
$\check{\sigma}$	engineering stress
σ_y	yield stress

τ	shear stress
$\check{\tau}$	engineering shear stress
τ_y	yield shear stress
ϕ	pair potential
ψ	shear localisation parameter
ω	angular frequency, $\omega = 2\pi\nu$
ω_D	angular Debye frequency, $\omega_D = 2\pi\nu_D$
Ω	atomic volume

ABSTRACT

The present thesis deals with molecular dynamics computer simulations of heterogeneities in copper–zirconium metallic glasses, ranging from intrinsic structural fluctuations to crystalline secondary phases. These heterogeneities define, on a microscopic scale, the properties of the glass, and an understanding of their nature and behaviour is required for deriving the proper structure–property relations. In terms of composite systems, we start with the amorphisation of copper nanolayers embedded in a metallic glass matrix. While copper is an fcc metal with a high propensity for crystallisation, amorphisation can in fact occur in such systems for thermodynamic reasons. This is due to interface effects, which are also known from heterogeneous interfaces in crystals or from grain boundary complexions, although in absence of lattice mismatch. In single-phase glasses, intrinsic heterogeneities are often discussed in terms of soft spots or geometrically unfavourable motifs (GUMs), which can be considered to be mechanically weaker, defective regions of the glass. We investigate the relation between these motifs and the boson peak, an anomaly in the vibrational spectrum of all glasses. We demonstrate a relation between the boson peak and soft spots by analysing various amorphous and partially amorphous samples as well as high-entropy alloys. Finally, we treat the plastic deformation of glasses, with and without crystalline secondary phases. We propose an explanation for the experimentally observed variations of propagation direction, composition, and density along a shear band. These variations of propagation direction are small in the case of single-phase glasses. A considerably greater influence on shear band propagation can be exerted by precipitates. We systematically investigate composites ranging from low crystalline volume fraction up to systems which resemble a nanocrystalline metal. In this context, we derive a mechanism map for composite systems and observe the breakdown of these mechanisms with increasing crystalline volume fraction during the transition towards the nanocrystalline state.

ZUSAMMENFASSUNG

Die vorliegende Dissertation beschäftigt sich mit molekulardynamischen Computersimulationen von Heterogenitäten in Kupfer-Zirkonium-Gläsern, die von intrinsischen Fluktuationen bis hin zu kristallinen Sekundärphasen reichen. Auf einer mikroskopischen Skala definieren diese Heterogenitäten die Eigenschaften des Glases. Es ist daher notwendig ihre Natur und ihr Verhalten zu verstehen, um die korrekten Struktur-Eigenschaft-Beziehungen zu bestimmen. Für Komposite wird als Erstes die Amorphisierung von Kupfernanoschichten in einer metallischen Glasmatrix behandelt. Kupfer ist ein kubisch flächenzentriertes Metall, welches eine starke Neigung zur Kristallisation aufweist. Trotzdem können diese Nanoschichten aus thermodynamischen Gründen amorphisieren. Dies geschieht durch Grenzflächeneffekte, wie sie auch von heterogenen Kristallgrenzflächen oder von Korngrenzzwischenphasen bekannt sind. Die Gitterfehlanpassung dieser Systeme ist im vorliegenden Fall bezeichnenderweise nicht vorhanden. In einphasigen Gläsern werden intrinsische Heterogenitäten oft im Kontext von „Soft-Spots“ oder geometrisch ungünstigen Motiven (GUMs) diskutiert. Diese können als mechanisch geschwächte, defekte Regionen im Glas verstanden werden. Hier wird der Bezug zwischen diesen Regionen und dem Boson-Peak, einer Anomalie, die im Vibrationsspektrum aller Gläser auftritt, untersucht. Es wird durch Untersuchungen an verschiedenen amorphen und teilamorphen Proben, sowie an Hochentropielegierungen gezeigt, dass ein Zusammenhang zwischen Boson-Peak und Soft-Spots existiert. Abschließend wird die plastische Deformation von Gläsern mit und ohne kristalline Zweitphasen behandelt. Eine Erklärung der experimentell beobachteten Variation von Ausbreitungsrichtung, Zusammensetzung und Dichte entlang eines Scherbandes wird vorgeschlagen. Die Variationen der Ausbreitungsrichtung sind klein im Falle von einphasigen Gläsern. Einen erheblich größeren Einfluss auf die Scherbandausbreitung wird von Ausscheidungen ausgeübt. Eine systematische Untersuchung von Kompositsystemen von geringem Kristallanteil bis hin zu nanokristallinen Systemen erlaubt die Erstellung einer Mechanismenkarte. Ein Zusammenbruch dieser Mechanismen kann beim Übergang in den nanokristallinen Zustand beobachtet werden.

Part I

INTRODUCTION AND METHODOLOGY

During the last decades, our knowledge of the structure and the mechanisms of mechanical deformation of metallic glasses was enriched by a combination of experimental investigation and modelling. The first part of this thesis is therefore devoted to a review of the state of the art of experiment and simulation, some open questions in the field that this thesis tries to answer, and available computational techniques to model and analyse metallic glasses. The final chapter of this introduction is devoted to a detailed evaluation of some widely-used interatomic potentials for modelling amorphous Cu–Zr systems.

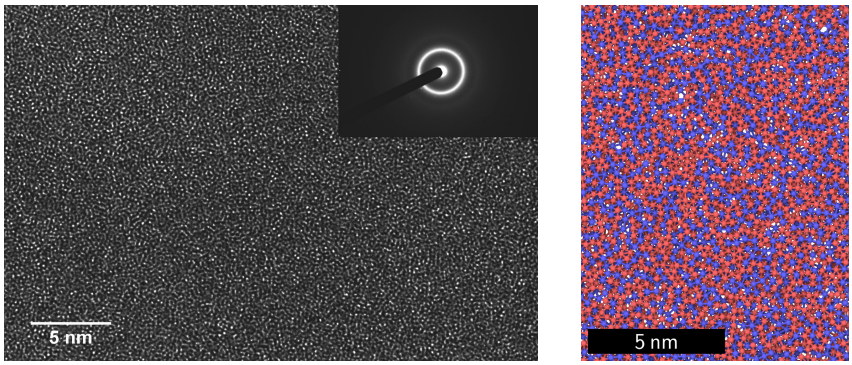

The structure of a solid critically influences its properties. The pictures exemplify the amorphous structures in metallic glasses: The left picture is a TEM image of a Cu–Zr-based metallic glass,† while a computer simulation of a $Cu_{64}Zr_{36}$ glass structure is shown on the right. At first glance, no regular structure emerges. We will see later that amorphous solids still exhibit some degree of order and how to find it.

† from Krämer, Kormout, Setman, Champion, and Pippan, *Production of Bulk Metallic Glasses by Severe Plastic Deformation*, Metals **5**, 720 (2015), DOI: 10.3390/met5020720.

1

METALLIC GLASSES

Glasses are most commonly known in the form of oxide glasses, such as transparent silicate glasses, which were already in use in the ancient world. Following a more rigorous definition, glasses encompass all amorphous solids that were prepared by passing a glass transition while cooling from the melt.[1,2] This definition also includes the more recent material class of metallic glasses. Metals have a strong tendency towards crystallisation, which means that very high cooling rates are required to freeze them in the metastable glassy state.[1] This was accomplished for the first time by Klement, Willens, and Duwetz in 1960 for a droplet of Au_3Si.[3] The resulting flake was amorphous but quickly decomposed into complex crystalline phases. The interest in metallic glasses increased with the discovery of alloys whose critical cooling rates were low enough to obtain bulk samples.[4–8] These glasses are highly alloyed and are called bulk metallic glasses (BMGs) if the casting thickness in the smallest dimension exceeds some arbitrary threshold between 1 mm[9,10] and 1 cm.[11,12] They are characterised by a high yield strength, a large elastic limit, and high corrosion resistance.[1,9,10,12–14] Additionally, some BMGs are attractive for medical applications,[15] others are used as catalysts,[16] and others again exhibit interesting magnetic properties.[10] The main obstacles to their widespread use as structural materials are the macroscopically brittle failure at room temperature[12,13,17] and the economical production of bulk samples.[12] The latter problem is solved to the point that patents for mobile phone cases made of metallic glasses have been filed,[18] but the former problem is still a matter of ongoing research.[19]

In this thesis, we are concerned mainly with $Cu_{64}Zr_{36}$ glasses. Zirconium-based glasses are widely used, although usually at least ternary or quaternary alloys are preferred for their higher glass-forming ability.[8,20–23] In the binary Cu–Zr system, the three compositions $Cu_{64}Zr_{36}$,[24,25] $Cu_{50}Zr_{50}$,[26,27] and $Cu_{46}Zr_{54}$[28] are known for their comparatively large casting thicknesses, which exceed 2 mm. The $Cu_{64}Zr_{36}$ alloy has been the subject of a wide range of simulation studies, not least because of the availability of reliable interatomic potentials.[29] The atomic-level structure of the material is well investigated[30] and it is therefore a solid starting point for further studies.

While many fundamental questions of the glassy state remain unsolved (some of which will be laid out in the following sections), the focus of this thesis is not on the glass as a homogeneous solid, but rather on the heterogeneities in the material, which have been capturing increasing interest in recent years. Heterogeneities range from inherent structural fluctuations[31] to crystalline secondary phases,[13,32,33] all of which influence the mechanical properties of the macroscopic sample. In the last decade,

advances in tailoring mechanical properties by embedding crystalline phases in the glass matrix were made. Consequently, this thesis places an emphasis on glasses with crystalline secondary phases. Apart from that, we will also discuss heterogeneities in shear bands and the connection between disorder and the vibrational density of states of glasses.

1.1 GLASS FORMATION

Just as in the laboratory, metallic glasses in computer simulations must be "synthesised". In contrast to crystals, where the regular arrangement on a lattice allows procedural construction of whole samples with a minimum of parameters, the complex structure of metallic glasses is not accessible to such generation and requires that the samples are quenched from the melt. Consequently, an understanding of glasses starts at the glass transition. Phenomenologically, the glass transition is well described.[34] We will discuss some theoretical models in Sec. 1.1.1 on the free volume model and in Sec. 1.1.2 on the potential energy landscape model.

Generally, a glass always forms from an under-cooled liquid. Under-cooling or super-cooling occurs when a liquid is cooled below the melting point without crystallisation. This can be achieved only if the crystallisation kinetics are sufficiently slow, for example by avoiding heterogeneities—such as impurities or contact with container walls—which accelerate crystal growth rates.[35] With decreasing temperature, the viscosity of the super-cooled liquid increases until a glass transition occurs.[34] This glass transition is, somewhat arbitrarily, defined as the temperature where viscosity surpasses 10^{12} Pa s, corresponding to relaxation times on the order of minutes to hours.[34,36] At this point, diffusion is sufficiently sluggish on experimental timescales that the liquid is "frozen" and transitions to a solid state, the glass. This means

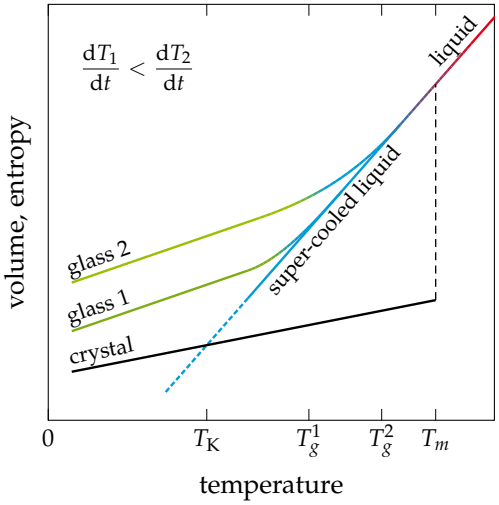

FIGURE 1.1: The glass transition. A liquid cooled below the melting point is called a super-cooled liquid. At the cooling-rate-dependent glass transition temperature T_g, the kinetics of the super-cooled system freeze and it becomes solid. The curves for volume and entropy look similar in many materials, especially for metals. An exception would be water, where the volume of the crystal is higher than that of the liquid. The cross-over point where the entropy of the liquid becomes smaller than the entropy of the crystal is assumed to be the theoretical limit for a glass transition and is called the Kauzmann temperature T_K.

that a glass can be obtained from any liquid as long as the cooling rate is sufficiently fast to undergo a glass transition before crystallisation sets in. As shown in Fig. 1.1, the glass transition temperature T_g depends on the cooling rate, and is therefore a kinetic phenomenon and not a true phase transition. Nevertheless, the glass transition possesses several similarities to a second order phase transition: Enthalpy, entropy, and volume are continuous at T_g, while the heat capacity exhibits something akin to a smeared-out discontinuity.[34] If the liquid and the glass are the same phase, one could ask why the glass is defined as a solid at all. This is because it exhibits all the traits we require from a solid, at least on experimental timescales: (i) A glass has a positive shear modulus, i.e., it resists shear deformation and (ii) the atomic configurations in a glass are stable, although it lacks long-range order.[2]

Very successful empirical descriptions of the liquid and glassy states exist. The Vogel–Fulcher–Tammann law describes the viscosity μ well over several orders of magnitude as[34]

$$\mu = \mu_0 \exp\left(\frac{k}{T - T_\infty}\right), \tag{1.1}$$

where μ_0 and k are adjustable parameters and T_∞ gives the deviation from Arrhenius behaviour; the viscosity becomes infinite at T_∞. Different glass-forming systems are characterised by their deviation from Arrhenius behaviour. Those that follow it closely (such as SiO_2) are called *strong* liquids and those that deviate significantly (e.g., *ortho*-terphenyl) are called *fragile* liquids.[37,38] Metallic glasses are situated in the middle between strong and fragile, although the better glass formers appear to be stronger.[39–42] $Cu_{64}Zr_{36}$ was found to be more fragile than ternary Cu–Zr-based alloys, but still stronger than typical fragile glass formers, which are often organic.[43,44]

An interesting phenomenon, called the "entropy crisis", appears in the deeply super-cooled region (Fig. 1.1). At the Kauzmann temperature T_K the entropy of the super-cooled liquid becomes lower than that of the crystalline solid.[45] An extrapolation would suggest that super-cooled liquids can obtain negative entropy in violation of the third law of thermodynamics. This is resolved in one of two ways: Either the extrapolation of entropy is invalid[46] or an "ideal" glass state exists which will always intervene before the low-entropy state in the liquid is attained.[47]

A figure of merit for the glass-forming ability of a material is the critical cooling rate to avoid crystallisation and undergo a glass transition. The oxide glasses can be cooled rather slowly. SiO_2, for example, has critical cooling rates on the order of $10^{-3}\,\mathrm{K/s}$ to $10^{-4}\,\mathrm{K/s}$.[48] BMGs, on the other hand, have rates ranging from $10^{3}\,\mathrm{K/s}$ down to $0.1\,\mathrm{K/s}$.[9–11] The large differences between metallic systems have been explained by empirical rules which define good glass formers. Multi-component alloys have more complex unit cells which crystallise less easily; large size differences between the constituent elements increase the packing density of the liquid and suppress diffusion; liquids near eutectics are stable at low temperatures and require less under-cooling to reach T_g; and negative heat of mixing increases the solid–liquid in-

terface energy and therefore the critical nucleus size for crystallisation.[9–11] Examples of good glass-forming alloys are Zr–Ti–Cu–Ni–Be and Pd–Cu–Ni–P.[11]

Variation of the cooling rate not only controls the crystallisation kinetics and T_g, it also affects the final glass state as indicated in Fig. 1.1. This is especially important in computer simulations where cooling rates are high and care needs to be taken to obtain glasses that are comparable to experiment. It was shown that the structure and properties of $Cu_{64}Zr_{36}$ in atomistic computer simulations depend critically on the cooling rate.[49–52] The strain localisation is higher for more slowly cooled samples,[52] which corresponds more closely to the result expected from experiment. Cooling rates of around $10^{10}\,s^{-1}$ are often used and seem to reproduce realistic plasticity mechanisms under deformation while still being realisable with currently available computing resources.[50–53]

1.1.1 *The free volume model*

A description of the mechanisms behind the glass transition is sought after since the early last century. One of the first widely recognised models to explain the glass transition uses the concept of free volume. The original model by Cohen and Turnbull[54–56] uses a few simple assumptions to derive a consistent picture of the glass transition. While this concept is widely used and intuitive, it does not accurately describe the mechanisms in metallic systems as we will discuss at the end of this section.

The free volume model assumes that there is no phase transition between the liquid and the glass. This is reasonable, as the glass transition temperature is dependent on the kinetics of cooling in contrast to—for example—the melting point. Free volume itself is defined as the total volume minus the sum of atomic or molecular volumes and can be redistributed without energy change. The atoms or molecules diffuse by moving into the free volume, but can only do so if the free volume surpasses a critical threshold. Below that threshold the diffusivity is effectively zero. Above, the diffusion coefficient D follows the relation[54]

$$D = D_0 \exp\left(-\frac{k\,\Omega^*}{\Omega_f}\right), \tag{1.2}$$

where D_0 and k are constants, Ω_f is the free volume per atom or molecule, and Ω^* is the minimum free volume required for a jump. The temperature dependence of the free volume was derived for a Lennard–Jones potential, which adequately describes the free volume in solids and liquids with van der Waals interactions.[54] The thermal expansion at low temperature is in the harmonic regime and is assumed to result in very little free volume. When the anharmonic regime in the potential is reached, free volume is produced. When a critical amount of free volume is reached, the diffusivity jumps up and the glass "melts". The entropy due to the redistributable free volume finally makes the liquid state the thermodynamically stable phase since the crystalline solid has very little free volume. A consequence of this model is that all

liquids—even simple structures like hard spheres or metals—can undergo a glass transition. This is suppressed only because the glass transition stands in competition with crystallisation kinetics, which is fast for metals and other simple atomic systems. A good glass-forming BMG has little free volume in the melt, thereby slowing down diffusion and therefore crystallisation.[11] A reduction in free volume can be achieved by size mismatches between the constituent atoms which allow for denser packing.

The free volume model seems very convincing, but as already pointed out in the original publication,[54] and more recently by Egami,[57] the experimental data for metals do not support the assumptions of the model. Self-diffusion in liquid metals can be fitted, but the critical free volume turns out to be around 10% of the atomic volume. This suggests that metal atoms can easily squeeze into voids of the size of an ion core. Consequently, the pressure dependence of the diffusivity is much lower than predicted by the free volume theory, which should be very pressure sensitive. It was found that irradiation leads to defects and reduced short-range order, but not to void formation.[58–60] If the disorder in metallic glasses was nothing but increased free volume, this free volume could rearrange into clusters of voids for which no experimental evidence was found. Indeed, easy redistribution of free volume over the sample seems unlikely; the model does not explain the different glass states obtained by different cooling rates or why shear bands persist for years after deformation. If the diffusivity depended only on the redistributable free volume, an unrelaxed glass should be able to get rid of its excess free volume and relax towards an ideal glass state.

Despite these shortcomings, the concept of free volume as a phenomenological measure of disorder in glasses remains popular. It is useful in such a capacity, but the underlying picture of diffusion in liquid and glassy metals should not be accepted as correct. Nowadays, the term "free volume" is instead often used to describe any excess volume and is indicative of disorder and reduced density. As stated above, a decreased density *does* lead to higher diffusivity in line with Cohen and Turnbull's ideas, although not quantitatively.

1.1.2 *Potential energy landscape*

The concept of the potential energy landscape (PEL) was developed a few years later, and provides an intuitive, qualitative picture of the glass transition and the glass state. The idea, first formulated by Goldstein in 1969, is that the system samples a constant PEL, which is a function of the positions of all atoms and the shape of which defines the properties of the system.[61] In the liquid, the PEL is freely sampled. When passing the glass transition temperature, though, some large barriers can no longer be surmounted, trapping the system in the metastable glass state. This means that the height of the barriers defines the glass transition temperature. It also means that a distribution of different barriers exists and that these should lead to different

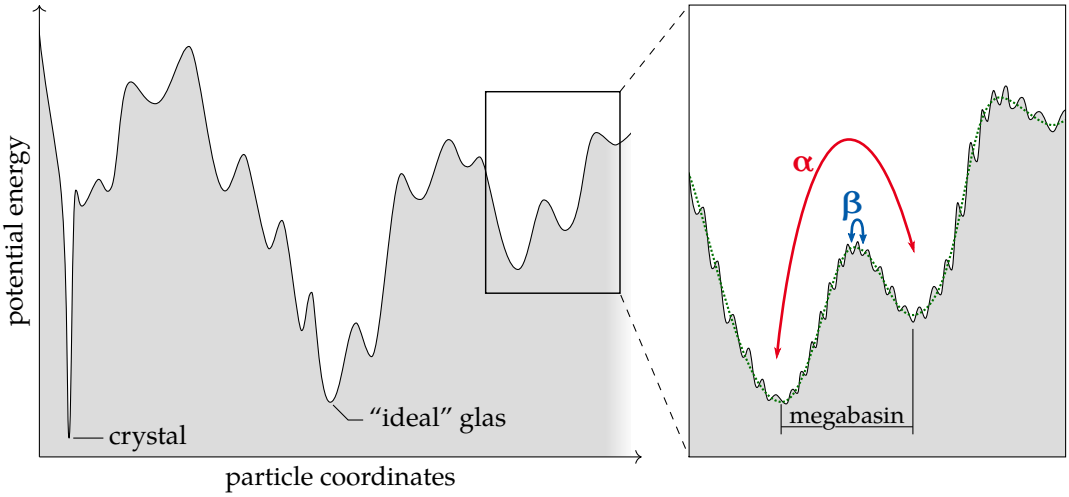

FIGURE 1.2: Schematic representation of a potential energy landscape. From afar, the energy landscape consists of a multitude of basins representing amorphous states with a high barrier towards the crystalline state. The amorphous basins are broad and those configurations corresponding to very stable glasses are deep. Zooming into a basin shows that the basin itself consists of smaller local minima. Traversing these corresponds to the fast β processes, while changing basins corresponds to an α process, composed of a range of β processes.

measurable relaxation times. Johari and Goldstein could show that this is the case by measuring an additional β relaxation with low activation energy.[62] Until then, only the primary α relaxation was known. Additionally, they found a range of activation times, indicating a distribution of activation barriers and justifying the picture of the PEL consisting of a range of high and low barriers as sketched in Fig. 1.2.

A fully developed argument of the PEL can now be used to explain the phenomena in glasses and around the glass transition.[36,63] Above T_g, only α relaxations were measured, while below T_g a split into α and β relaxations is observed as well as a disappearance of the α relaxations. This is consistent with the PEL picture: The liquid has enough thermal energy to pass the α barriers, whereas the glass is trapped in a megabasin. Inside the basin only the smaller β transitions take place. It is assumed that the β relaxations correspond to localised events, while the α relaxations are complex cooperative rearrangements which are made up of individual β events.[34,36] The vibrational entropies of the different basins are most likely approximately equal, which means that the entropy crisis at the Kauzmann temperature is due to configurational entropy.[63] This would result in negative entropy, indicating that there is an "ideal" glass state which has the lowest potential energy of all amorphous configurations and which prevents the existence of a liquid with negative entropy. We saw in Fig. 1.1 that the ideal glass state is never reached, but that the glass state is instead dependent on parameters like the cooling rate. The PEL picture also provides an explanation of this cooling rate dependence: With faster cooling rates, the system

has not enough time to sample different megabasins before being frozen inside one. For fast cooling rates, the basin in which the glass most likely ends up is far from the ideal glass. With slow cooling rates, the system can still escape from an unfavourable basin on experimental timescales before a further reduction of temperature slows down the kinetics too much.

Angell's concept of strong and fragile glass formers[37] can also be described using the PEL.[63] In strong glass formers, the α/β bifurcation is weak or absent and the glass only exhibits β transitions. This means that the strong glass exists in a deep megabasin with no chance of an escape via α transition. The fragile glass, on the other hand, can still access certain α transitions and switch between megabasins because the barriers are lower. The coexistence of both time scales leads to the non-Arrhenius behaviour of the viscosity that is typical for fragile glass formers.

The PEL is an attractive model because it can not only explain phenoma related to the glass transition, but it was also used in the context of mechanical deformation and plasticity, as we will see later. The downside is that the exact shape of the PEL is unknown and still subject of ongoing research. Because of its complexity, the complete PEL can never be known or be intelligible, but only treated statistically. As an alternative, Iwashita and Egami proposed the exploration of local energy landscapes to obtain a more quantitative picture.[64]

1.1.3 *Amorphous phases at interfaces*

The left side of Fig. 1.3 shows various routes for preparing bulk amorphous metals. This includes the glass formation as discussed before, but also other non-equilibrium methods. Ion irradiation of a crystal leads to local melt–quench processes due to the high-energy impacts, disturbing the lattice structure and implanting impurities.[65] Just as in the case of the glass transition, the disorder is kinetically trapped in the system. Similarly, amorphous thin films can be produced using high deposition rates.[66] This is once again a non-equilibrium process and equilibrium deposition of metal films regularly results in crystalline phases on a variety of substrates. Examples include, but are not limited to, iron on amorphous carbon substrates;[67] Cu, Ag, Al, Au, and Ni on sapphire substrates;[68–70] and Ni on tungsten substrates.[71] In fact, it seems that all amorphous metals result from quickly-frozen kinetics which suppress crystallisation.

While this is true for bulk samples, it is quite possible to observe energetically-driven amorphisation at the nanoscale. Figure 1.3 lists the most prominent examples on the right side. High-angle, high-energy grain boundaries in some polycrystalline metal systems reduce their energy by amorphisation, driven by the large misorientation of the neighbouring crystal lattices.[72] While the thermodynamically stable state of the system is the single crystal, the amorphisation is nevertheless driven by a reduction in free energy. When going to ever smaller grain sizes, a nanocrystalline in-

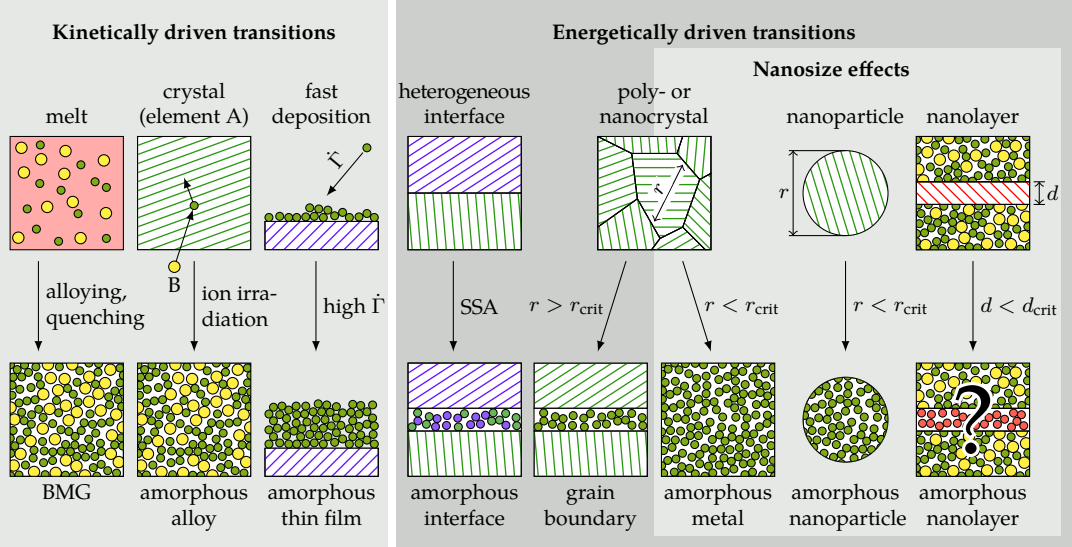

FIGURE 1.3: Different routes to amorphous metals. The left part of the schematic shows kinetically-driven transitions, which lead to metastable bulk amorphous metals. The most prominent is the bulk metallic glass, which is produced by rapid quenching from the melt. At the nanoscale, amorphous metals can become energetically favourable either because of lattice mismatch at grain boundaries or interfaces or because of nanosize effects. Recent experiments[83] suggest that amorphisation may also occur in metallic nanolayers embedded in metallic glasses even in absence of lattice mismatch and at sizes where thin films were found to be crystalline.

stability occurs: As evidenced by molecular dynamics simulations of Lennard-Jones systems, polycrystals with a grain size smaller than some critical value collapse completely and only leave an amorphous grain boundary phase behind.[73,74] A similar effect occurs for metallic nanoparticles: To reduce the surface energy the particles form low-symmetry phases.[75] These low-symmetry phases consist of structural motifs that are not space filling and are therefore sometimes called "amorphous" in the literature.[75] Thermodynamically stable amorphous phases were also found in heterogeneous interfaces between crystalline materials. These amorphous interphases result again from the misorientation and lattice mismatch between the adjacent crystallites.[76–78] In contrast to the grain boundary, there exists no stable single-phase, single-crystal state for these systems. This effect is called solid-state amorphisation (SSA) and has recently also been discussed in the framework of complexion formation,[79] as well as for thin metallic films embedded in a different crystal phase.[80–82] In the latter case, the amorphisation is suppressed for films thicker than a critical value.

While this energetically-driven SSA is immediately plausible because of size and lattice mismatches, an SSA for a thin metallic layer embedded in a metallic glass matrix appears unlikely because of the lack of the former effects. This conventional wisdom was recently called into question by experimental evidence:[83] Iron nanolayers

embedded in a $Co_{75}Fe_{12}B_{13}$ glass were found to be amorphous up to a certain thickness. As iron is known to be very resistant against amorphisation, this is a surprising result. The energy of an interface between the amorphous metal and the metallic glass would have to be much lower than the usual interface or surface energies of the metal: Amorphisation in equilibrium conditions was not observed on other substrates (see e.g. Ref. 67). The thermodynamics of this phenomenon, however, could not be resolved yet, as the layer was deposited by magnetron sputtering. The sputtering process itself is a non-equilibrium process, opening up the results to the discussion if the amorphisation is not due to the kinetics of the preparation process.

1.2 STRUCTURE OF METALLIC GLASSES: SHORT-RANGE AND MEDIUM-RANGE ORDER

In the previous section we already established that the defining feature of glasses is their disorder. While this seems obvious, disorder is not binary and order within disorder or vice-versa are common features of materials. The epitome of ordered atomic structures is of course the single-crystal, which has periodic long-range order. What this means is that structural units are repeated by translation and are space-filling, i.e., the units can be repeated infinitely often without gaps between them.[84] Among these are of course the dense packings (fcc and hcp) often present in metals. Ignoring defects in crystalline matter, the next step down on the continuum of order are quasi-crystals.[85–87] These materials cannot support long-range order by translation, as they exhibit rotational symmetries that are not periodic, but are ordered, defect-free phases, some even thermodynamically stable, with macroscopic scale. They differ from amorphous materials by their regular diffraction patterns due to which they are nowadays categorised as crystals.[84] Amorphous materials instead show diffuse diffraction patterns that at first glance suggest complete disorder.[21,22] Investing some thought into the matter or simply taking a look at experimental pair distribution functions makes evident that there is more to these materials: Of course, atoms cannot overlap because of core–core repulsion, prefer certain bonds and coordination numbers over others, and—in the case of metals—want to be packed densely.[84] The arrangements of next neighbours is therefore not random, but follows certain ordering statistics: We call this the short-range order (SRO). The SRO in metallic glasses has been the subject of extensive research and the reader is referred to Ref. 30 for an exhaustive review. Here, we will only touch on the pertinent points for Cu–Zr-based glasses as applicable to this thesis.

It has been known for some time that metallic glasses, especially the good glass formers, are densely packed since they are only about 0.3%–1.0% less dense than the competing crystalline phases.[10] Indications for significant SRO were found early on in experiments,[88] although the exact nature of this order is mostly known from computer simulations. SRO is often defined by the shape of the polyhedra spanned

by the neighbouring atoms (a more rigorous definition and a method to find these polyhedra in simulations is presented in Sec. 2.6.2). In isolation, much denser packings than fcc or hcp exist, but they exhibit packing frustration: It is impossible to combine them into a single, void-free solid. The locally most dense packing depends on the size differences between atomic species. For the different resulting coordination numbers, specific favourable polyhedra, sometimes called *Z clusters*, were identified.[30,89,90] These are characterised by a high number of five-folded bonds. These are bonds between a central atom and a neighbouring atom that share five other neighbours. In $Cu_{64}Zr_{36}$, copper prefers the Z12 cluster—often denoted as $\langle 0, 0, 12, 0\rangle$ according to its Voronoi polyhedron, or simply as a full icosahedron (see Sec. 2.6.2)—which consists of five-folded bonds only. These clusters are energetically preferable, densely packed, and stiff.[50,52,91–93] Zirconium preferably appears in a range of Z15 and Z16 clusters but seems to be relatively featureless in contrast to copper.[30,31,94] As in all metallic glasses, there are no large voids but the space between favourable polyhedra is filled by geometrically unfavoured motifs (GUMs)—defective Z clusters or completely disordered arrangements.[31,95] The GUMs relieve the packing frustration and are necessary ingredients of the amorphous configuration. While this "glue" enables the formation of void-free solids, they are always less dense than the simple crystal structures. Both types of ordered and disordered motifs, sometimes called "liquid-like" and "solid-like" regions, play fundamental roles, for example, in the elastic and plastic response of the glass.[96–98]

A question of theoretical interest is the continuing reduction of disorder in the amorphous state. Nelson pointed out early on that the favoured polyhedra of glasses also occur in Frank–Kasper phases (such as the Laves phases) and that the ideal glass, if it exists, may resemble a Frank–Kasper phase with infinite unit cell.[90] In practice, the question is if there is an upper limit of favourable polyhedra that can be accommodated by a glass, which is exacerbated by the fact that the relative occurrence of these structural features could not yet be quantified.[31] Evidence for the existence of different polyhedra comes mostly from computer simulations[52,92,94,99,100] and from reverse Monte-Carlo modelling of x-ray data.[99,101–103] It is only recently that the clusters predicted by atomistic simulations could be observed directly in thin films via nano- and Ångstrøm-beam electron diffraction measurements by Hirata and colleagues.[104,105] Their experiments also confirmed that even the favoured polyhedra always occur in a slightly distorted way,[105] indicating some intrinsic residual stress in glasses on the atomic level.

Depending on the specific glass, the spatial extent of order may go even further: The arrangement of the next-neighbour polyhedra themselves is also subject to preferential configurations, the medium-range order (MRO). MRO was also measured,[88] but the details of atomistic models are still under discussion. In cases where the glass can be treated as a host of one species with a low solute concentration of another element, Miracle's efficient cluster packing model can accurately describe the MRO.[106–108] In this theory, the Z clusters defined by a central solute atom are treated

as units and their preferential arrangement is described as fcc- or hcp-like. In reality, the composition of the glass is such that the "solute" atoms bond with each other, leading to an MRO that is more network-like.[93,94,99,100,109,110] In simulations on $Cu_{64}Zr_{36}$, a "backbone" of interlocking icosahedra can be identified.[93,94,109,110] This finding is supported by a recent publication from Liu *et al.*, which reports experimental measurements consistent with face-sharing or interpenetrating icosahedral networks.[111] In the picture of geometrically favourable and unfavourable motifs, the GUMs are located in-between these networks[93,95] and the consequences of their presence in the glass are discussed in Sec. 1.8.1.

1.3 EQUILIBRIUM PHASES IN THE COPPER–ZIRCONIUM SYSTEM

As discussed earlier, a so-called "homogeneous" glass is in itself already a very heterogeneous material at the sub-nanometre to nanometre scale. In this thesis, we will go somewhat further and introduce crystalline secondary phases into the amorphous matrix. Thus, it is necessary to shortly survey the equilibrium phases in the Cu–Zr system. The complete phase diagram is still under discussion, but certain important features are universally agreed upon.[112–115] Figure 1.4 is a reproduction from Wang

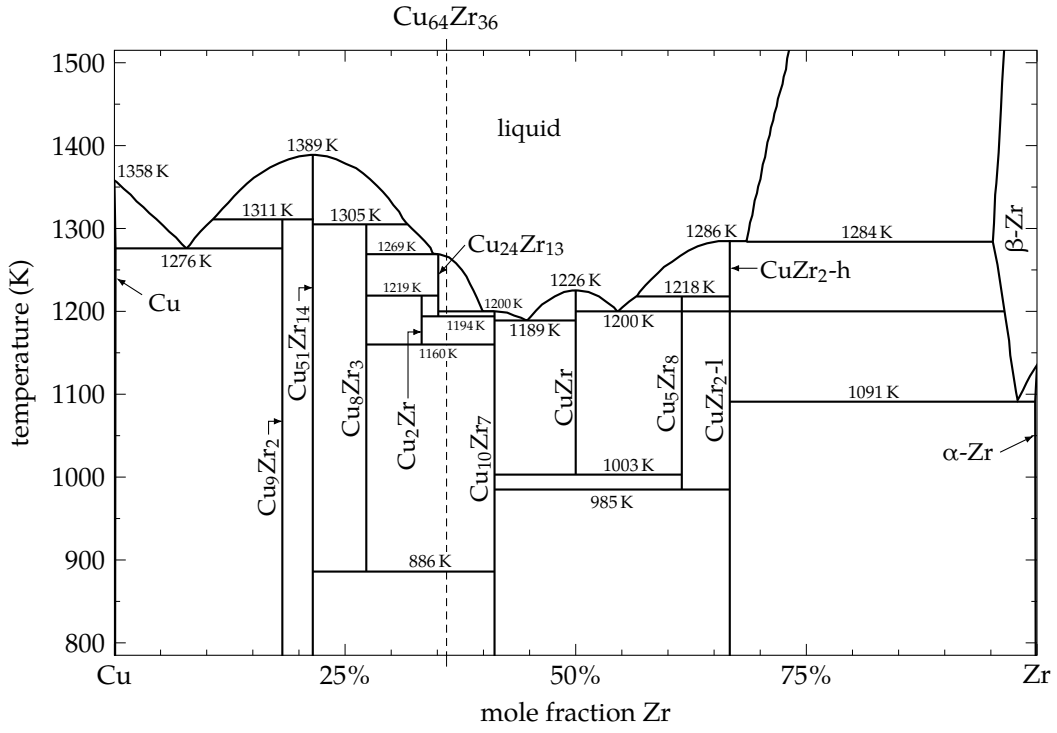

FIGURE 1.4: Cu–Zr phase diagram reproduced from Ref. 115. The composition of the bulk metallic glass former $Cu_{64}Zr_{36}$ used in this thesis is indicated by a dashed line.

et al. which includes the controversially discussed Cu_2Zr phase.[115] In the relevant range for glass-forming Cu–Zr alloys, the intermetallic phases $Cu_{51}Zr_{14}$, $Cu_{10}Zr_7$, and $CuZr_2$ are generally accepted as stable at room temperature.[112–115] The Cu_8Zr_3 phase was proposed to be stable under ambient conditions,[114] but most authors agree that it decomposes into $Cu_{51}Zr_{14}$ and $Cu_{10}Zr_7$ at low temperatures.[112,113,115]

Technologically, the high-temperature CuZr phase is relevant as it can be synthesised in metastable form in Cu–Zr-based BMGs, where it appears in the B2 or B19′ crystal structure.[116–120] In the as-cast sample, most crystallites appear in the B2 structure[119] and undergo a martensitic transition to B19′ during deformation.[120] The CuZr phase is easy to obtain by annealing and is used often to influence the mechanical properties of the resulting composite as discussed in detail in Sec. 1.6. Decomposition into $Cu_{10}Zr_7$ and $CuZr_2$ is suppressed kinetically.

1.3.1 *Laves phases*

Another phase that has recently become of interest in atomistic computer simulations is the Cu_2Zr phase. This phase was first proposed tentatively as a high-temperature stable phase by Kneller and colleagues,[112] although its inclusion in the phase diagram is controversial.[114] The crystal structure of the Cu_2Zr phase is still not conclusively determined, but Laves phases were sometimes found in computer simulations.[121–123] The relevance of this is that the most common Laves phases, C14 and C15, are made up of $\langle 0, 0, 12, 0\rangle$ copper icosahedra and Frank–Kasper Z16 zirconium polyhedra on a diamond superlattice.[84] In C14, the diamond superlattice is hexagonal, in C15 it is cubic. The $\langle 0, 0, 12, 0\rangle$ copper icosahedra are a defining feature of Cu–Zr glasses (see Sec. 1.2), which means that the interface energy and therefore the critical nucleus size should be low, leading to high nucleation rates.

In equilibrium phase diagrams, the phase is found only far above the glass transition temperature.[112,115] Computer simulations by Tang and Harrowell[122] using a potential by Mendelev and colleagues[124] show that this potential incorrectly predicts Cu_2Zr as a stable low-temperature phase. While this phase does not precipitate in actual Cu–Zr glasses, the possibility of growing crystallites in a metallic glass in simulational timescales is opened up. This was shown recently by Zemp *et al.*, who obtained small Laves-like crystallites in a $Cu_{64}Zr_{36}$ glass.[110,123] The early stages of crystal growth resemble the relaxation of these glasses, which is characterised by an increasing icosahedra fraction[93,100,125] until the icosahedra assemble in a Laves phase. Because of this similarity to relaxation processes, it is likely that the interface energy of Laves crystallites is low, that the critical nucleus is therefore small, and that the crystallisation kinetics is thus fast. In contrast to pure Cu–Zr systems, where these Laves phases do not seem to play a role, they are important crystalline phases in some Cu–Zr–Ti glasses[126] and Vitreloy 1,[127] giving these results additional technological relevance.

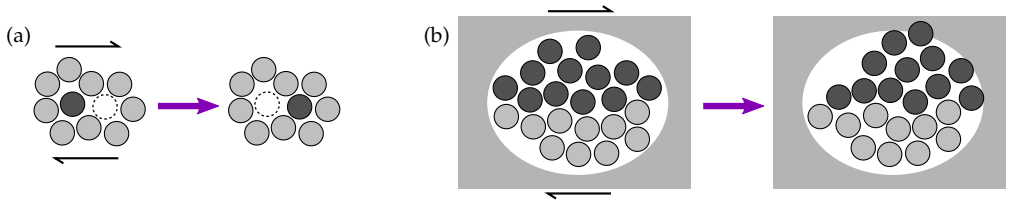

FIGURE 1.5: Shear transformation zones. (a) The model according to Spaepen in which deformation is carried by single-atom jumps.[128] (b) The shear transformation zone concept according to Argon, which treats a sheared cluster of atoms as an Eshelby inclusion.[132]

1.4 SHEAR TRANSFORMATION ZONES

Because of the lack of a lattice, the concept of extended line defects like dislocations does not make sense in amorphous solids. Both homogeneous and heterogeneous plastic flow have been observed in metallic glasses (discussed in detail in Sec. 1.5). The first step in understanding their plasticity is therefore a formulation of the microscopic mechanism of deformation. The earliest concept, illustrated in Fig. 1.5 (a), is due to Spaepen and is based on the free volume theory.[128] Deformation is carried by diffusive next-neighbour jumps as described in Sec. 1.1.1; an applied shear stress reduces the diffusion barrier. Inhomogeneous, i.e., localised, deformation takes place in shear bands that are softened by the deformation. In these regions, a steady state of creation of weakening disorder and annihilation of free volume by diffusion takes place. The weakness of Spaepen's model lies in its use of the free volume theory for metallic systems, where it was shown to be deficient. Indeed, cooperative atomic motion rather than single-atom jumps was observed in computer simulations.[125,129–131]

A more successful model was proposed by Argon.[132,133] Here, the units of plastic deformation are shear transformation zones (STZs), groups of atoms that undergo a small shear transformation under applied stress [Fig. 1.5 (b)]. This shear transformation is imagined to take place in an elastic matrix, resulting in a geometry comparable with Eshelby's inclusion. The model assumes that there are regions of high free volume which correspond to weaker bonding and which are therefore susceptible to shear transformation. In fact, a system should contain a whole range of activation barriers on a rough PEL (cf. Sec. 1.1.2). Argon assumed that at small stresses only a few sites can be activated and that the system is effectively elastic. The original model was therefore mainly formulated for high temperatures and high stresses, where the STZs are activated all over the system and are not percolated. In this regime, the STZs are uncorrelated and the picture of an Eshelby inclusion is applicable. Argon formulated a flow equation based on the transition state theory in which the shear rate $\dot{\gamma}$ amounts to

$$\dot{\gamma} = \alpha_0 \gamma_0 \nu_0 \exp\left(-\frac{\Delta F}{k_B T}\right) \sinh\left(\frac{\tau \gamma_0 \Omega_0}{k_B T}\right). \tag{1.3}$$

TABLE 1.1: Parameters of the Argon model for homogeneous flow in metallic glasses. The parameters α_0, γ_0, and ν_0 seem to be universal, while Ω_0 and ΔF are material parameters. Often, instead of the STZ volume Ω_0, the number of participating atoms N_0 is given which is why this value is listed here. Numbers were reported in many publications and the references listed here are not exhaustive.

α_0	γ_0	ν_0	N_0	ΔF
1 [132,133]	0.1 [132,133]	1 THz [132,133]	3–150 [53,129,131, 133,150]	0.5 eV–5 eV [14,53,131,132]

Here, α_0 is the fraction of atoms susceptible to deformation and is assumed to be on the order of unity for homogeneous deformation, γ_0 is the shear strain of the STZ, ν_0 the attempt frequency of STZ activation, ΔF the activation barrier, τ the applied shear stress, and Ω_0 the volume of the STZ. Values for the parameters of the model are listed in Tab. 1.1. The picture of the STZ is also applicable to the low-temperature regime, although the shape of the STZ changes to a disk. This slightly modifies the barrier ΔF due to Eshelby stresses, a detail which can often be ignored in practice. Argon also derived a condition for shear localisation which he formulated in terms of a flow instability due to shear rate fluctuations.[132] The shear rate equation itself was developed for homogeneous deformation, but Spaepen pointed out that a shear localisation could be included by adjusting the fraction of available jump sites, here in form of the parameter α_0, to correspond to the shear band volume.[128] While the model is generally accepted for unpercolated STZs, it contains no description of cooperative STZ activity.

The STZ model was developed further into an effective temperature theory with the help of computer simulations by Falk, Langer, Bouchbinder, and others.[130,134–140] The disorder in the system is characterised by an effective temperature that replaces the equilibrium temperature of the Argon model. It is assumed that the population of activated STZs can be described by the structural state of the system, i.e., the effective temperature. Additionally, the STZs are more complex and include an orientational dependence of stress response.

The idea of STZs is in line with the PEL picture, although it is still not entirely clear if STZ activation should represent an α or β transition. STZs are often postulated as reversible[140] and it seems reasonable that certain low-barrier STZs can be activated thermally. Indeed, simulations find a whole range of low-barrier events,[141–143] supporting the idea that STZ activation is a β transition. On the other hand, the barrier ΔF in the Argon model is much higher than many of these local structural excitations, indicating that these excitations may combine in unknown ways to an α event that would be called an STZ from a macroscopic viewpoint.[131,142,143] In terms of structure–property relations, a clear correlation between the structure and fertile sites for STZ activation was recently found and will be discussed in Sec. 1.8.1

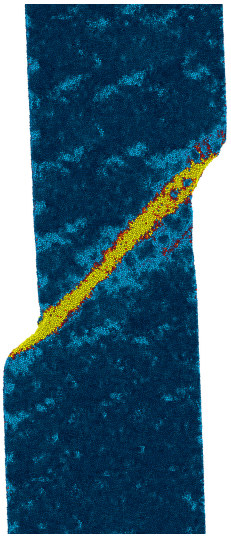

FIGURE 1.6: A shear band in a simulated $Cu_{64}Zr_{36}$ metallic glass. The atoms are coloured according to a measure of local shear strain, revealing the completely localised deformation and absence of necking. While the failure appears brittle from a macroscopic viewpoint, the material locally flows by rearranging atomic configurations instead of breaking stiff bonds, reminiscent of a ductile material. Data from an unpublished simulation by the author.

1.5 PLASTIC DEFORMATION

As already indicated in the previous section, the macroscopic deformation of metallic glasses can either be homogeneous or heterogeneous.[14] In the former case, the deformation is distributed all over the sample as in Argon's high-temperature STZ model. Heterogeneous deformation, on the other hand, means shear localisation in one or more shear bands, an example from a simulation is shown in Fig. 1.6. These shear bands undergo shear softening and therefore localise the deformation after they form. Because the deformation is localised in a small region, a sample under tension fails immediately after the elastic limit. While this behaviour is often called "brittle", it differs from classical brittle materials, such as ceramics, by a reproducible yield stress and microscopic mechanisms that more closely resemble ductile deformation mechanisms.

Experimentally, the transition from heterogeneous to homogeneous flow was found to depend on the applied strain rate as well as the temperature. A map partially based on the work of Schuh *et al.* in Ref. 14 is reproduced in Fig. 1.7. In the experimental regime of strain rates below $10^4\,\mathrm{s}^{-1}$, an increase of temperature leads to an increased shear band nucleation rate which is measurable as flow serrations.[14] Every flow serration is thought to be a new shear band propagating through the sample. Increasing the strain rate puts the flow along an existing shear band in competition with the nucleation of new shear bands, which means that flow serrations reduce with increasing strain rate. The area of no flow serration was first introduced as "homogeneous" deformation, as no pop-ins were observed during nanoindentation.[144] Computer simulations, on the other hand, always observe shear banding in this region,[52,145] so that the lack of flow serrations is probably related to the low number of shear bands.

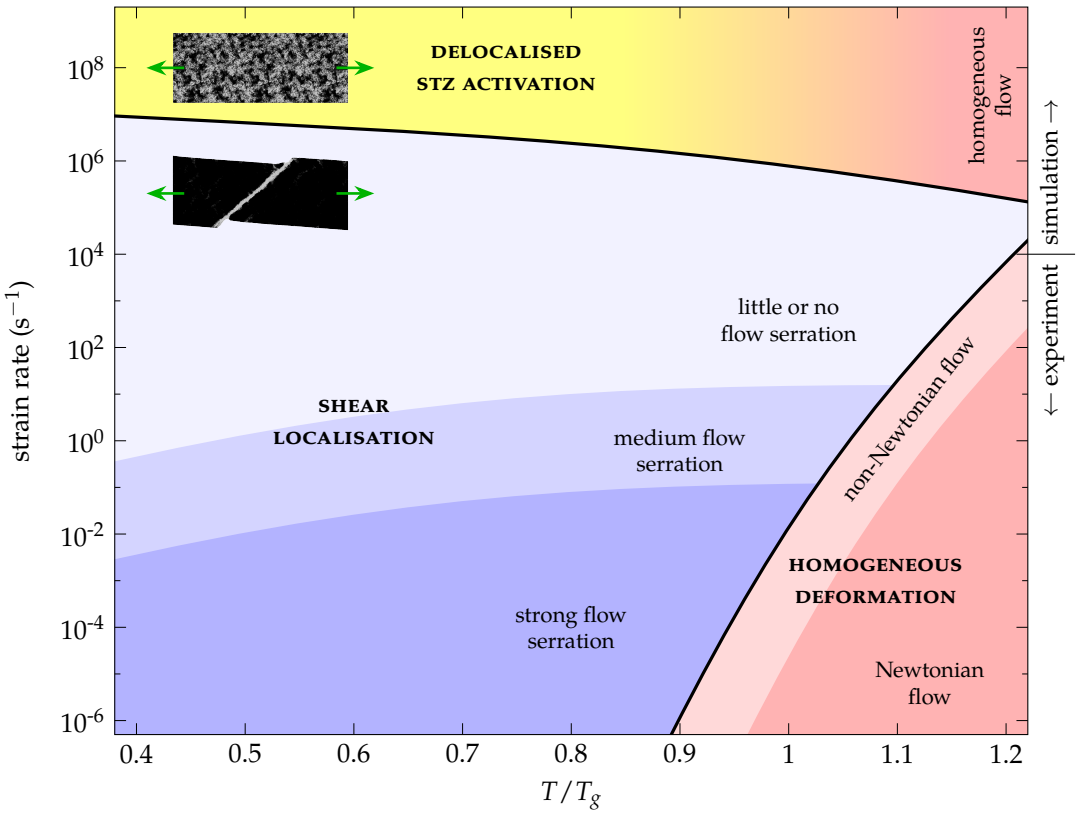

FIGURE 1.7: Deformation map for metallic glasses. For experimentally accessible strain rates, shear localisation in form of shear bands occurs up to temperatures close to T_g, at which point the deformation becomes homogeneous. Below, shear banding is a nucleation phenomenon, meaning that higher temperatures lead to multiplication of shear bands and therefore more flow serrations. In simulations, strain rates may surpass the shear band nucleation rates, instead favouring the competing mechanism of delocalised STZ activation. With increasing temperature, the rates for isolated STZ activation go down, meaning that shear band nucleation is kinetically suppressed at even lower strain rates. At some temperature the delocalised STZ activation should merge with the high-temperature homogeneous flow regime. The experimental regime (strain rates below 10^4) is reproduced from Ref. 14 and extended by a schematic of high strain rate simulation phenomena.

At higher temperatures, true homogeneous flow is observed.[14] This is due to the thermal activation of STZs all over the sample, which activate on timescales faster than the imposed strain. Increasing the strain rate therefore suppresses this homogeneous deformation as the shear band nucleation rate can overcome the activation of a sufficient number of delocalised STZs. With sufficiently high strain rates, this occurs even above T_g. In simulations, a second regime of homogeneous flow is observed.[145] In contrast to the aforementioned effects, increasing the strain rate above a certain limit suppresses shear banding in favour of homogeneous, delocalised STZ activation. Also in contrast to the low strain rate regime, Albe *et al.* report that an increase

in temperature *decreases* the critical strain rate for this homogeneous deformation.[145] On one hand, Cheng and Ma pointed out that experiments are often carried out on bulk samples which contain stress concentrators that are not included in atomistic simulations.[146] These stress concentrators reduce the yield stress but also lead to a localised deformation. While the same authors demonstrate that the glasses in computer simulations have higher fictive temperatures and lower barriers in the PEL,[146] this cannot explain the inverse temperature dependence of the transition between shear banding and delocalised STZ activation for high strain rates as depicted in Fig. 1.7. The solution can be found when treating both isolated STZ activation and shear banding as nucleation phenomena, where shear bands have higher and STZs lower activation barriers. At low temperatures in the experimental strain rate regime, shear bands always have time to form. When going to very high strain rates, the strain rate overcomes the time scale for shear band nucleation and stress is instead relieved by delocalised STZs.[145] Increasing the temperature in this regime increases the low-barrier rates much more than the high-barrier rates, thereby favouring the delocalised STZ activation. It was proposed that shear localisation is increased by heterogeneities[146] and simulations prove that this is the case even for high temperatures and strain rates.[53,145] A consequence for the setup of simulations is that the strain rates should be sufficiently low to end up in the regime of shear banding so that the results are at least comparable to the experiments with little flow serration. We would assume that the behaviour of a single shear band is independent of further rate changes, as the flow serrations are thought to be connected to the nucleation of shear bands and an increase of serrations only indicates a multiplication of shear banding events.

Simulational and experimental studies also report differences in yield stress. The PEL was employed to explain these differences:[146] Because of the higher cooling rate in simulations, less-relaxed glasses with lower barriers result, which consequently have a lower yield stress when properly scaled and compared with experiments. Simulations also revealed a connection between yield stress and structure, where a more pronounced MRO (in earlier publications only evidenced by increased SRO, which was shown to form networks later) leads to higher yield stresses.[50,91,94] This of course agrees with the PEL picture, where slowly cooled glasses are more ordered and therefore reside in deeper potential energy basins.

The exact mechanism of shear band nucleation itself is not conclusively solved. The theory underlying the experimental regime of Fig. 1.7 assumes that shear band formation starts with the activation of a single STZ.[144] STZs in the neighbourhood of this event are easier to activate because of the local stress field of the activated STZ. Agglomerated STZs then form a shear band nucleus that grows into a mature shear band under further load. Other models assume a percolation of STZs along a plane of highest resolved shear stress, resulting in a homogeneous shear band nucleation which is often observed in simulations.[17,147] It seems clear that heterogeneous shear band nucleation at, and propagation from, stress concentrators is the relevant mech-

anism in real-world samples,[17] comparable to heterogeneous dislocation nucleation. More recent publications by Klaumünzer, Maaß, and Löffler propose a two-stage model.[148,149] In the first stage, a shear band front propagates from one end of the sample to the other. In the second stage, slip along this shear band occurs, resulting in macroscopically observable deformation.

Johnson and Samwer proposed a yield criterion for metallic glasses based on a cooperative shear model, an ingredient missing from Argon's description.[150] Yield occurs when a critical fraction of STZs in the system are activated. This is related to an average elastic shear limit criterion, $\tau_y = \gamma_{\mathrm{STZ}} \cdot \mathcal{G}$, where yield is a fold catastrophe. Here, γ_{STZ} is the critical shear of an STZ and $\mathcal{G}$ the shear modulus of the glass. This results in a yield shear stress τ_y of

$$\tau_y = \tau_y^0 - \tau_y^0 \left[\frac{k_{\mathrm{B}} T}{\Delta E_{\mathrm{pot}}} \frac{\mathcal{G}(T)}{\mathcal{G}(T_g)} \ln \frac{\omega_0}{c\dot{\gamma}} \right]^{\frac{2}{3}}, \tag{1.4}$$

where τ_y^0 is the yield stress at absolute zero, ΔE_{pot} is the activation barrier for an STZ, ω_0 an attempt frequency, c a constant, and $\dot{\gamma}$ the applied shear rate. This idea only proposes a critical STZ fraction and should therefore be independent of the degree of shear localisation. Indeed, in simulations only small deviations of yield stress were found between scenarios in which shear banding occurred and scenarios in which STZs were activated in a delocalised fashion.[145]

Shear band widths of around 10 nm are consistently observed in experiments[151] and in computer simulations.[94,125,152] On the other hand, it was shown in simulations that shear bands widen under continued deformation, although this widening only becomes significant at very large strains.[153] Therefore, it most likely only appears in those mature shear bands that underwent large deformation and consequently lead to failure. The widths of these shear bands cannot be measured *ex-situ*.

Finally, the flow serrations during deformation have garnered recent interest again. Maaß and colleagues discussed serrations in terms of stick–slip behaviour, showing that a single serration corresponds to a single shear band activation.[154] They describe the stick–slip behaviour by three stages:[149] The stage of shear band initiation occurs before or at the beginning of a stress drop.[155,156] After that, the sample simultaneously slips along a plane on a single shear band.[157,158] Finally, the shear band arrests, the stress drop in the serration stops, and the elastic stress in the system starts rising again.[149] In contrast to Schuh *et al.*,[144] Maaß and colleagues explain the number of serrations in the deformation map (Fig. 1.7) not in terms of shear band nucleation, but as a competition between the applied deformation rate and the speed of shear band slip:[149,155] If the temperature-dependent shear band speed falls below the speed of the applied deformation, serrated flow occurs because the shear band cannot keep up with the externally imposed strain.

Usually, serrations and stick–slip behaviour are thus connected either with the nucleation of a new shear band or with the arrest and restart of a mature shear

band. Transmission electron microscopy (TEM) investigations[151,159] and sub-micron strain measurements[160] in the group of Wilde have recently revealed that stick–slip-like behaviour may even occur on a single shear band during the propagation of its front: Shear strain, structure, and density are heterogeneous along a single shear band with length scales between 100 nm and 400 nm. Nanoindentation experiments by Maaß *et al.* indicate that large, inhomogeneous residual stress fields may remain in micrometre-sized areas around the shear band.[161] These observations are unforeseen and a complete explanation is still outstanding, as they imply that some sort of stick–slip may occur even during the initial propagation of the shear band front.

1.5.1 *Improving the plasticity*

For practical structural applications, glasses with a pronounced plasticity are sought after. Many ideas to overcome the limited plasticity of metallic glasses are derived from established concepts in the field of crystalline plasticity. Before transferring these concepts to glasses, though, one should take note that the microscopic deformation mechanisms obviously differ between metallic glasses and crystals [see Figs. 1.8 (a)–(b)]. Dislocations in crystalline lattices are line defects, carry a finite shear slip, and are initially distributed more or less homogeneously over the sample. Dislocations can also block each other, which leads to strain hardening. Plastic deformation is homogeneous at first, until necking occurs and the material fails. Shear bands in metallic glasses, on the other hand, are two-dimensional defects and can slip indefinitely. They exhibit shear softening that leads to immediate shear localisation and failure.

Nevertheless, we can transfer some ideas from the established field of microstructure engineering in crystals to metallic glasses. Figure 1.8 (c) introduces the idea of nanocrystals: Dislocations are more and more confined by the grain boundaries, leading to pile-up and hardening (discussed in more detail in Sec. 1.6.1 in a different context). A transfer of this microstructure to the glass is a relatively new idea. "Grain boundaries" in the form of glass–glass interfaces are introduced[162,163] and stay stable at ambient conditions.[164,165] In some cases, they may be chemically different from the bulk glass due to segregation.[166,167] In contrast to nanocrystalline metals, the deformation in nanoglasses is defined by the interfaces, which partake simultaneously in the plastic deformation. This deformation is more homogeneous and therefore more ductile, but the resulting yield stress is lower and the synthesis of these materials is still in its infancy.[145,163]

A more promising alternative is the introduction of crystalline secondary phases in the form of precipitates, illustrated in Fig. 1.8 (d). The advantage is that crystallites can be grown *in situ* by a thermal annealing treatment.[13] An exact annealing program can be used to control the volume fraction and the shape of the crystallites. In crystalline materials, precipitates act as obstacles to dislocation movement, thereby

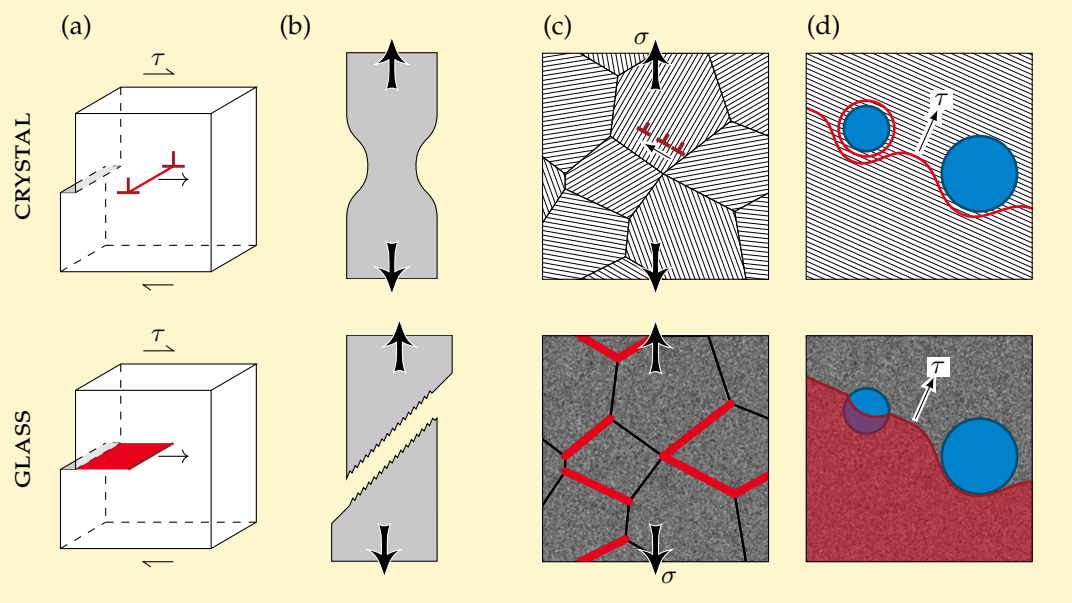

FIGURE 1.8: Tailoring mechanical properties in metallic glasses by microstructure engineering. Crystals and glasses have different microscopic mechanisms of plastic deformation. (a) While crystals deform by the nucleation and propagation of dislocations, which are line defects, metallic glasses form two-dimensional shear bands. (b) Dislocations can block each other, leading to strain hardening, (initially) homogeneous deformation, and ductility; while metallic glasses soften in deformed regions leading to strain localisation. Despite the differences in the mechanisms of plasticity between glasses and crystals, we can transfer some ideas from the established field of microstructure engineering in crystalline matter. (c) One idea is to introduce glass–glass interfaces and to thereby obtain a nanoglass, an analogue of nanocrystalline matter. (d) Another possibility is the introduction of secondary crystalline phases to influence the propagation of shear bands similar to precipitation hardening mechanisms in crystals.

hardening the material. In metallic glasses, one could imagine that precipitates fill the same role for shear bands. Indeed, improved ductility is found for a range of different composites,[32,33,168–181] but the underlying mechanisms are poorly understood.

1.6 MECHANICAL PROPERTIES OF COMPOSITES

For composites with a metallic glass matrix and crystalline secondary phases, improved compressive ductility was found in Cu–Zr-based,[168–172,182] Cu–Ti-based,[173] and Zr–Ti-based glasses.[32,33,174] A small tensile ductility with 1% to 2% strain was observed for Cu–Zr composites containing nanocrystals,[175–177] while a higher volume fraction of the crystalline phase can lead to significant tensile ductility as reported for Zr–Ti-based,[174,178] Ti-based,[179] and Cu–Zr-based glasses[180,181] (see Fig. 1.9). The enhancement of macroscopic ductility of glasses with a high crystalline volume fraction

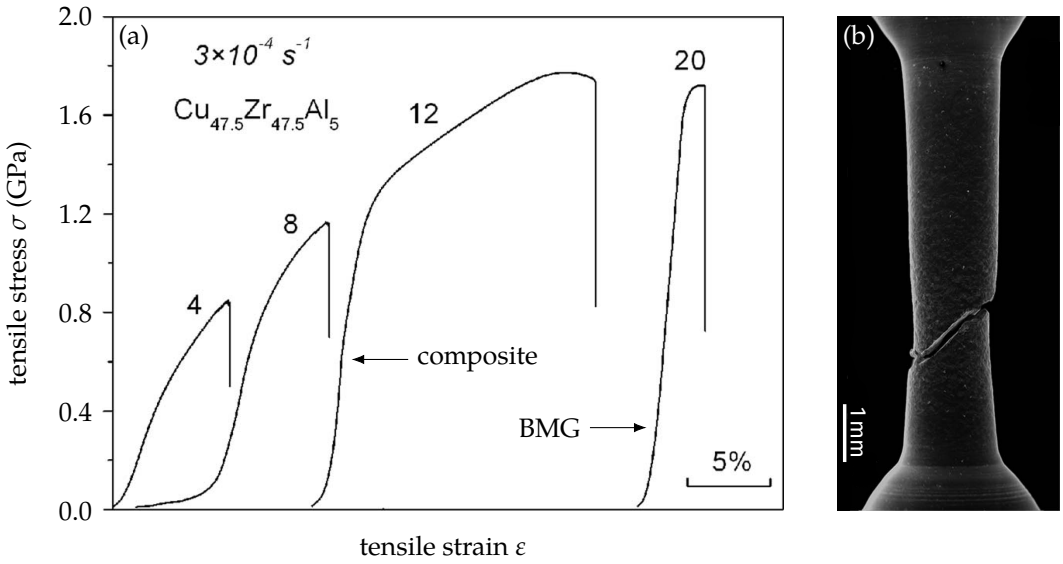

FIGURE 1.9: Experimental tensile stress–strain curves of $Cu_{47.5}Zr_{47.5}Al_5$ crystal–glass composites after different annealing treatments. (a) The numbers above the curves indicate how often the initially crystalline alloy was re-melted to increase the fraction of the amorphous phase. After twelve cycles, an optimal composite with high yield strength and ductility is achieved. After twenty cycles, the sample was mostly amorphous and shows the typical behaviour of a metallic glass: High yield strength accompanied by low ductility. (b) The optimal composite shows clear necking before fracture. Images adapted from Ref. 180, DOI: 10.1063/1.4754853.

is relatively well understood. There is a correlation between the location of dendrites and the occurrence of shear-band patterns.[32,33] Shear bands are constrained by the crystalline phase, and the number of shear bands is increased.[174] The co-deformation of matrix and crystallites can be explained by simple composite models and indeed, high volume fractions of ductile phases improve the ductility of the composite, while brittle phases do not.[183] Optimal volume fractions between 40% and 80% have been proposed for Cu–Zr-based glasses.[184]

The influence of nanoprecipitates on the mechanical properties, on the other hand, is still not clear. Shear-band patterns were also observed in glasses with spherical precipitates of diameter 2 nm[170] and there is evidence from experiment and simulational that the crystal–glass interfaces serve as shear band nucleation sites.[145,185,186] Conversely, these interfaces also act as sources and sinks for dislocations in the crystalline phase and STZs are activated by interaction with dislocations at the interface.[187–189] The precipitates themselves may grow during deformation and enhance the plasticity of the material.[169,171,175–177,190] An increased growth rate of crystallites was observed in shear bands[191] and related to enhanced diffusion inside the shear bands[125,192,193] but crystallisation can also be purely homogeneous and stress-

driven.[194] The deformation-grown crystallites contain twins which occur only in larger precipitates[175,177,190] and were proposed as the origin of strain hardening during nanoindentation,[171] as well as increased plastic strain during compression.[169] It was demonstrated that reducing the stacking-fault energy of B2 CuZr by alloying enhances twinning and leads to a higher tensile ductility.[195] The volume change during a martensitic transformation from the B2 to the B19′ phase in Cu–Zr-based glasses was proposed as the origin of toughening[175,196] but Corteen *et al.* argued that the volume change is too small to significantly toughen the composite and instead favour the multiplication of shear bands as the reason.[197]

The influence of the precipitates on shear bands is unclear, although atomistic computer simulations have shed some light on the matter. In quasi-2D molecular statics simulations of a binary Lennard–Jones system with a nanocrystal inclusion, Lund and Schuh identified three deformation mechanisms of the precipitate:[198] For small crystallites, the deformation is accommodated either by rotation or mechanical dissolution of the particle. For larger precipitates dislocations are nucleated; heterogeneously for precipitates smaller than the shear band and homogeneously for larger ones. However, it is somewhat unclear how the observed homogeneous dislocation nucleation depends on the artificially induced shear band and the resulting stress state in the system. Simulations by Shi and Falk show nucleation of shear bands at interfaces, as well as bending and blocking of shear bands at crystallites.[199] Because of the high volume fraction, though, these simulations rather resemble a nanocrystalline system, although the initiation of plastic deformation at interfaces is in agreement with the simulations by Albe and colleagues on low volume fractions of crystalline phase.[145] Similar observations were also made by Zhou *et al.* but the crystallites were arranged to simulate a highly confined geometry of dendritic precipitates.[200]

1.6.1 *Relation to nanocrystalline materials*

Research on nanocrystalline metals in recent years also approached the plasticity of crystal–glass composites from the other end: Nanocrystalline metals consist mainly of crystalline grains, but certain features of the deformation of metallic glasses were observed for very small grain sizes.[201–203] An explanation is sought mainly in the properties of the grain boundary phase which is thought to behave glass-like. The motivation behind ever-decreasing grain sizes down to the nanometre scale is of course the "smaller is stronger" principle. The semi-empirical Hall–Petch relation,[204]

$$\sigma_y = \sigma_0 + \frac{k}{\sqrt{d}}, \tag{1.5}$$

describes the yield stress σ_y as a function of grain size d. The theoretical single crystalline strength σ_0 is enhanced by dislocation pile-up inside the grains.[204] The constant k is called the Hall–Petch constant and is material dependent.

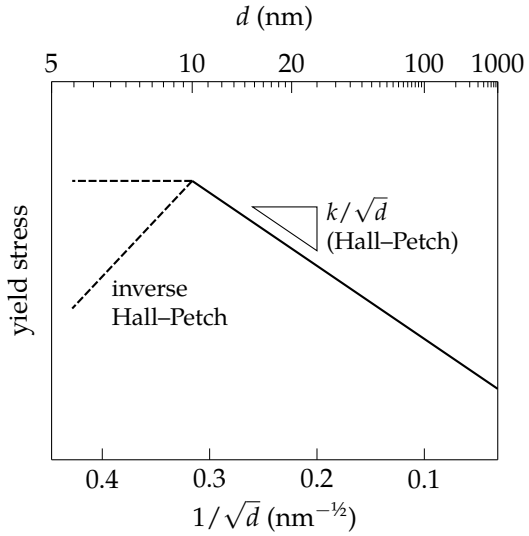

FIGURE 1.10: Hall–Petch relation and its breakdown at low crystallite sizes. Below 10 nm, either a plateau or a reduction of the yield stress is expected. The reduction was dubbed inverse Hall–Petch effect.

This relation starts to break down in the nanocrystalline regime, where additional mechanisms start to play a role, such as grain rotation, grain sliding, and grain growth;[205] grain-boundary migration;[206] and emission, pinning, and absorption of dislocations at the grain boundaries.[207] With grain sizes on the order of 10 nm, the strengthening either reaches a plateau, or the material is weakened again[201,208] (cf. Fig. 1.10). In this regime, the volume fraction of grain boundaries is very high and intra-granular plasticity is increasingly replaced by inter-granular plasticity, which was found to have certain similarities to the deformation of metallic glasses. Trelewicz and Schuh performed nanoindentation experiments on very small-grained Ni–W alloys and found that they exhibited pop-in events similar to those observed in indentation on metallic glasses.[201] The impression exhibited shear offsets in the surrounding pile-up, indicative of shear banding. The grain boundary phase was shown to have a lower shear modulus which starts affecting the effective macroscopic shear modulus in the Hall–Petch breakdown regime,[202] making the structure reminiscent of the liquid-like/solid-like division in metallic glasses. Under deformation, the grain boundary phase starts yielding the earliest, followed by dislocation glide and much later grain growth.[209] This hints to the fact that a glass-like deformation in the grain boundary is preferred but suppressed because of the compatibility requirement for macroscopic slip.[204] A $T^{2/3}$ scaling, just as the one found by Johnson and Samwer for metallic glasses,[150] was found by Grewer and Birringer for the grain-boundary shear and slip mechanisms, suggesting STZ-like deformation mechanisms.[203] These intriguing early results hint to the importance of the deformation mechanisms in metallic glasses also in the realm of nanocrystalline matter. This regime is highly suggestive of a switch from pure compatibility-defined plasticity (the strongest phase dictates macroscopic yield) to a plasticity that is controlled by a multitude of effects, many of them defined by the weakest phase.

1.7 THERMAL RELAXATION OF SHEAR BANDS

If we assume that plastic deformation of a metallic glass is equivalent to a stress-mediated α transition in the PEL, it seems unlikely that the system can return to its original megabasin without crossing large activation barriers. Instead, the system should sample new megabasins if it stays below the glass transition temperature. Several studies show that shear bands retain either structural disorder, chemical disorder, or free volume when annealed below T_g.[210,211] Others report a complete restoration of ductility or hardness,[212,213] although that may not indicate a complete structural recovery. Computer simulations show that complete structural recovery is only possible by thermal annealing above the glass transition,[125] consistent with the view that the shear band is trapped in a deep megabasin. There is also evidence that the shear band state exhibits increased diffusion due to higher free volume[125,193] which is conducive to crystallisation.[191,192,214–216] The three known possibilities for thermal relaxation in shear bands are therefore

(i) partial healing, with recovery of some properties,

(ii) complete healing, which needs sufficient thermal activation, and

(iii) crystallisation.

All of those mechanisms are thought to be closely related to the diffusivity in the shear band.

1.8 VIBRATIONAL ANOMALIES

Amorphous materials exhibit some anomalies in their vibrational density of states (VDOS) that are unknown in crystals and that are related (or thought to be related) to their disordered structure. In 1971, a linear temperature dependence of the heat capacity of glasses below 1 K was discovered by Zeller and Pohl[217] instead of the expected T^3 dependence according to the Debye model. This phenomenon was explained quickly thereafter by two-state tunnelling systems in the glass.[218,219] Because of the disorder, local double-well potentials exist through which the atoms of the glass can tunnel, thereby modifying the vibrational spectrum and the heat capacity.

Much less well understood is a phenomenon at higher frequencies and temperatures. In the frequency range around 1 THz, an excess of vibrational modes over the crystalline state and the predictions of the Debye model appear. These excess modes appear as a peak when the VDOS is plotted as g/ν^2 over ν (Fig. 1.11). This peak is called the "boson peak" for historical reasons since its temperature dependence in scattering experiments is that of bosons,[220] and was first found in vitreous silica in 1959 by Flubacher *et al.*[221] Although the boson peak has been known for decades and has been found in almost all amorphous solids, its origin is still controversially discussed.

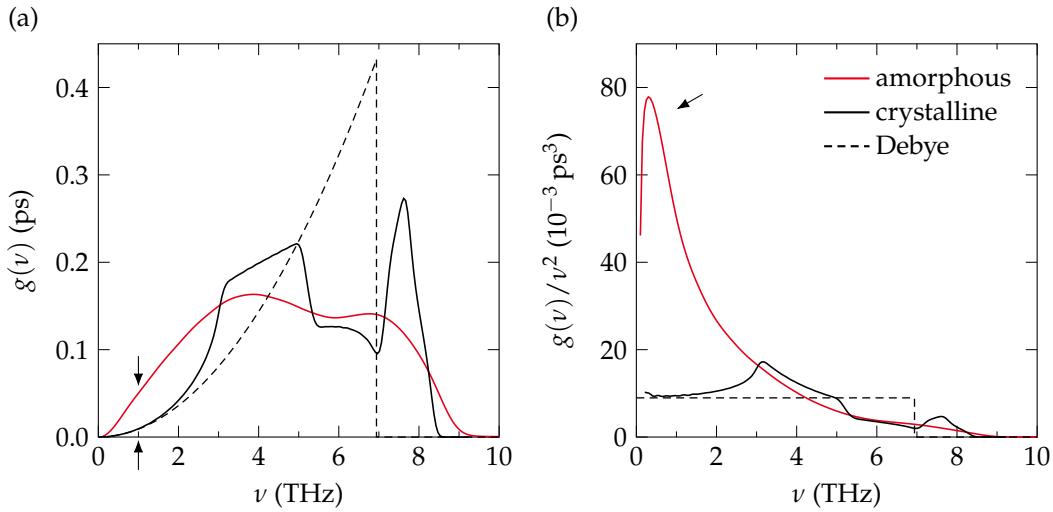

FIGURE 1.11: Example of a boson peak. (a) At low frequencies the Debye model is a good approximation for the crystalline phonon density of states, whereas the amorphous solid exhibits an excess of states around 1 THz. (b) This excess is most easily visualised in a g/ν^2 over ν plot, where these modes appear as a peak, the so-called boson peak. Data from Sec. 6.3.

The first models trying to explain the boson peak were based on a scattering of phonons at density fluctuations.[222] Around the same time, the soft potential model was developed,[223–227] which assumes an interaction of acoustic phonons with quasi-localised modes arising from "defects" in the disordered structure.[228–230] The nature of these defects was subject to a range of studies, and loosely packed atoms[227,231–234] as well as interstitialcy-like defects[235,236] were proposed. Grigera *et al.* interpreted the boson peak as a precursor of a dynamical instability.[237] Schirmacher and colleagues developed a theory in which fluctuating force or elastic constants give rise to the additional modes that make up the boson peak.[220,238–241] In agreement with this picture, regions of reduced short-range order, stiffness, and mechanical strength were connected to the boson peak.[95,234,242,243] This regions are called "soft spots" and are discussed further down in detail. For silicon-based glasses, similar findings exist[244,245] and a relation between the bending rigidity of the silicon tetrahedra, the shear modulus, and the boson peak was proposed.[246]

It was also suggested that the boson peak is predictive of the fragility of the glass, where fragile glass formers show a weak boson peak that disappears at T_g, while strong glass formers exhibit a strong boson peak that persists in the liquid state.[34] If we go back to the PEL picture, this suggests that structural features responsible for the boson peak persist in the liquid because the basin in which strong glasses reside is so deep that it is not left completely even in the melt slightly above T_g (cf. Sec. 1.1.2).

In contrast to these theories, which describe the boson peak as additional modes present only in glasses, Taraskin *et al.* proposed that the boson peak is related to the first van Hove singularity of the crystal, which is shifted to lower frequencies by

fluctuating force constants.[247] More recently, work by Chumakov and colleagues received attention:[248–252] Measurements on oxide glasses suggest that the boson peak is simply a van Hove singularity that is shifted because of the lower volume density of the glass compared to the crystal. These authors criticise alternative models like Schirmacher's as they do not explicitly treat the (pseudo-)Brillouin zone and therefore do not include the necessary van Hove singularities.[251] Furthermore, the argument is that disordered systems are always less dense than ordered ones. That leads to a lower transversal sound velocity, to a smaller size of the (pseudo-)Brillouin zone, and in consequence to a shift to lower frequencies, the result of which was interpreted as a boson peak.[251]

1.8.1 *Soft spots and mechanical properties*

Argon already argued that STZ activation barriers should follow a distribution instead of a single value, assuming that there are regions more susceptible to deformation than others.[132] Early on in the development of STZ mean-field theories, fits of the model to simulation data already revealed that regions with decreased shear moduli must exist.[130] In experiments, heterogeneous elastic response was measured and soft sites were found to make up a significant fraction of the sample[96] and are on the length scales of STZs.[253] Investigations of the vibrational spectrum of amorphous solids connected soft modes—which are often associated with the boson peak—to atomic rearrangements.[242,254,255] Later on, structural indicators—such as low packing density or GUMs—were connected to these soft modes.[234,243] Structural "defects" in glasses were found to be sites for atomic rearrangements and STZs[93,234] and they were shown to persist on the timescales of the relaxation times of the glass.[256] Bringing the picture together, a correlation between atomic packing, the low-frequency modes of the boson peak, and sites susceptible to STZ activation was discovered recently by Ma, Ding, and others.[31,95] These authors suggest that the ductility of a glass can be affected by tuning the amount of soft spots retained after the glass transition, for example by increasing the cooling rate.[257]

While it is surprising at first that the vibrations in an amorphous solid—indicators of the *elastic* response—should be predictive of plasticity, the soft spot picture seems to pull structure, vibrations, and plasticity together. A detraction from this view—and the view that the boson peak may have significant relevance to the behaviour of amorphous metals—are recent experiments which assign the vibrational response solely to the decreased density of glasses.[248] In fact, soft spots in metallic glasses are reported to be less densely packed[234] and could therefore assert a purely elastic influence on the phonon density of states. While a correlation between soft spots and the boson peak seems assured at least in the case of metallic glasses, an outstanding question is if this is due to the decreased density or due to the structure and/or softening.

1.9 OPEN QUESTIONS

The research presented in this thesis is driven by some of the open questions described before. These questions are:

- **Can single-element amorphous metals be stabilised in an amorphous matrix and in absence of lattice mismatch?** Typically, amorphous metals are synthesised by fast quenching or mechanical deformation. Energetic driving forces for amorphisation are only known in cases of lattice mismatch at interfaces or grain boundaries, where energetically favourable ordered phases do not exist. In the case of thin films of fcc metals embedded in a glass matrix, a driving force to amorphisation seems unlikely as the surface energy of thin films does not destabilise the crystalline phase. Recent experimental evidence, though, points towards an amorphisation of just such a system,[83] although it is still unclear if this is simply a kinetic effect due to the deposition conditions.
- **What is the relation between the boson peak and heterogeneities in metallic glasses?** The origin of the boson peak is still subject to controversy. Either this vibrational anomaly is connected to glass-specific heterogeneities which are suspected to play a role in the plasticity of the material, or the boson peak is simply a smeared-out feature of the crystalline vibrational spectrum. Many theories exist, but this phenomenon has been mostly discussed in terms of single-phase or model glasses, not in terms of defective glasses or composites.
- **How is the shear band path influenced by heterogeneities?** The mechanical properties of glasses can be tuned by introducing crystalline secondary phases, a field that has grown tremendously over the last decade. It is clear that heterogeneities must influence the path of the shear band, but knowledge of the underlying mechanisms is still incomplete. In addition to this, it was recently shown that even shear bands in macroscopically homogeneous glasses deviate from a straight propagation path. It is unclear if inherent variations of the glass structure are active on this scale, or if this is a property of shear bands independent of the medium.
- **Does the deformation of a glass matrix with a high density of crystallites follow the same physical description as the deformation of a nanocrystal with small grain sizes?** A connection between the strength of nanocrystals below the Hall–Petch breakdown regime and metallic glasses has already been proposed. Indeed, a certain similarity between crystal–glass composites with high crystalline volume fraction and nanocrystalline matter seems probable. Instead of starting from the nanocrystalline state and reducing the grain sizes ever further, one could instead imagine to start from a glass and subsequently increase the crystalline volume fraction, trying to find the transition from typical glass to typical nanocrystal behaviour.

2

METHODS AND MODELS

The macroscopic behaviour of metallic glasses is governed by processes on the nanoscale. To further improve our understanding of these materials, insights with atomic resolution are needed. While experiments, especially high-resolution imaging techniques, can provide very good data, necessary *in-situ* observations are often impossible due to limited time resolution. Atomistic simulations were very successful in the past to uncover deformation processes, their governing laws, and structure–property relations. By inherently containing information about position and trajectory of all simulated atoms, atomistic computer simulations provide easy access to a whole range of data with high spatial and temporal resolution. In this thesis, our tool of choice is molecular dynamics (MD). The principles behind this method as well as methods to analyse these simulations are described in this chapter.

2.1 MOLECULAR DYNAMICS

Describing the dynamic behaviour and interaction of an ensemble of particles, such as atoms in a solid, is an N-body (many-body) problem. Many-body problems lack analytic solutions and numerical solutions are computationally demanding. MD is the method of choice for the efficient simulation of liquids and condensed matter. MD makes use of the Born–Oppenheimer approximation,[258] which states that the electrons are so fast compared to the nuclei that they can react instantaneously to the nucleus' motion. We can therefore treat electrons separately from the nuclei. Furthermore—because of the great mass and low velocity of the nuclei—we can treat them classically using Newton's equations of motion. It is sufficient to treat the nuclei as mass points, as they are small compared to the interatomic distances and the electronic shell. In the so-called "classical" MD the interaction between atoms is modelled by an empirical potential which supplies the forces on the atoms, treating the electrons only implicitly. "Classical" is somewhat of a misnomer as empirical potentials are often derived from quantum-mechanical considerations. To study the time evolution of a system, we need to perform a time integration of the many-body equation of motion

$$m_i \ddot{\mathbf{x}}_i = \mathbf{F}_i(\mathbf{x}_1, \ldots, \mathbf{x}_N) + \mathbf{F}_{\text{ext}}(\ldots), \tag{2.1}$$

where m_i is the atomic mass of atom i, $\mathbf{x}_i$ is its position, and $\mathbf{F}_i$ is the force on atom i due to all other atoms. The force $\mathbf{F}_{\text{ext}}$ represents possible external forces, some of which are discussed below.

MD simulations are computationally efficient. The interatomic forces $\mathbf{F}_i$ are usually due to short-ranged interactions, which means that the force overwhelmingly depends on atoms inside a cutoff distance from atom i. Firstly, this means that the computation time scales $\mathcal{O}(N)$ with the number of particles N. Secondly, the simulation box can be divided into smaller cells in real-space for which the forces can be calculated independently. The advantage of this is that the force calculation—the computationally most expensive part of the simulation—can be performed independently on different CPUs or nodes. In fact, this problem is "embarrassingly parallel",[259] meaning that the individual parts of the calculation are independent of each other and therefore the computation time is halved when the number of CPUs is doubled. As the system sizes studied in this thesis are rather big (up to 40 million atoms), we needed a simulation package capable of massively parallel simulation. This is provided by the free software package LAMMPS.[260]

2.1.1 *The Velocity Verlet algorithm*

Performance and long-term stability are the qualities demanded of the time integrator. The LAMMPS package uses a variant of the Verlet integration,[261] the Velocity Verlet integrator.[262] This algorithm uses the velocities $\mathbf{v}_i$ in addition to forces and positions. As all similar numerical integration schemes, the Velocity Verlet divides time into discrete steps of length δt. Every timestep, positions and velocities are updated:

1. update the position $\mathbf{x}_i(t+\delta t) = \mathbf{x}_i(t) + \mathbf{v}_i(t)\delta t + \frac{1}{2}\frac{\mathbf{F}_i}{m_i}\delta t^2$
2. get the forces $\mathbf{F}_i(t+\delta t)$ from the potential
3. update the velocities $\mathbf{v}_i(t+\delta t) = \mathbf{v}_i(t) + \frac{1}{2}\frac{\mathbf{F}_i(t) + \mathbf{F}_i(t+\delta t)}{m_i}\delta t.$

At the end of each timestep, time is increased by δt and the next timestep is started until the requested simulated time-span has passed. In the beginning, the velocities are either initialised to zero, to user-defined velocities, or according to a Maxwell–Boltzmann distribution appropriate for the desired temperature. The choice of timestep controls the accuracy (smaller is better) and the performance (larger is faster). Usually, a good choice for δt is one hundredth of the period of the fastest vibration in the system. The error is of order $\mathcal{O}(\delta t^2)$.

2.1.2 *Boundary conditions*

Simulated particles are contained in a spatial domain, the so-called simulation box or simulation cell. Most often, this box is a parallelepiped, although more exotic variants exist. When using MD simulations as-is, surfaces naturally appear since the simulated domain is not infinite. The number of atoms that can reasonably be accommod-

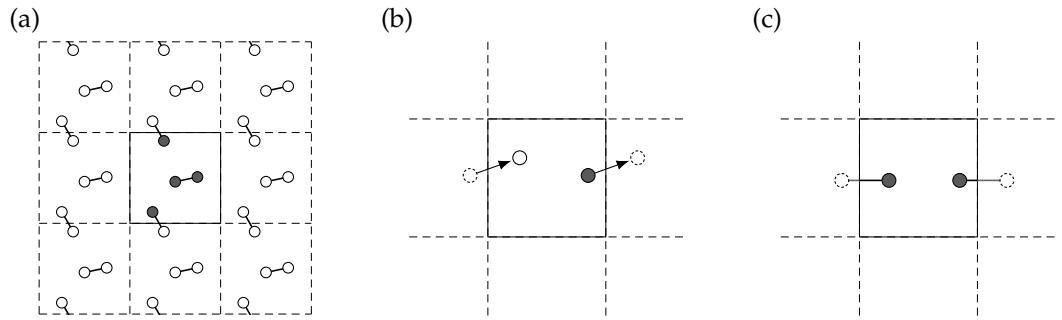

FIGURE 2.1: Periodic boundary conditions. Schematic of a simulation of dimers. (a) Virtually, an infinite number of images of the central simulation cell is defined. In the actual implementation, atoms that move out of the central box move back in on the other side (b) and bonds are between an atom and the closest image of its neighbour (c).

ated in a simulation box with today's computing resources lies somewhere between ten to hundred million atoms. Even one billion atoms of copper make up a material block with a weight of just 100 fg. With such a high surface to volume ratio it is hard to talk about "bulk" materials. To keep the simulation demands low, a trick is used. Instead of simple open boundaries, periodic boundary conditions can optionally be used. Formally, an infinite amount of images of the simulation box are introduced for every periodic direction, see Fig. 2.1 (a). In practice, two tricks are used to implement this. First, any atom that leaves the simulation domain on one side enters it again from the other side [Fig. 2.1 (b)]. Second, the distance between atoms i and j—used for the force calculation described below—is defined as the distance between atom i and the closest *image* of atom j [Fig. 2.1 (c)]. Although a fully periodic system is surface free, one still needs to make the simulation box big enough, otherwise finite-size effects can occur.[263] In the case of open boundaries, LAMMPS uses "shrink-wrap" boundaries which make the simulation box as small as possible while still containing all atoms. This has the advantage that the box volume still approximately corresponds to the solid volume in some cases.

2.1.3 *Thermostat and barostat*

By default an MD simulation treats an isolated system, i.e., a microcanonical ensemble. The number of atoms, the volume, and the energy are conserved. Often, we want to control the temperature of the system and require a canonical ensemble instead. This requires a modification of the equations of motion. We use a Nosé–Hoover thermostat,[264,265] in which the system couples to a virtual heat bath. This is achieved by adding an additional "frictional" force to the equations of motion that depends on the difference to the desired target temperature. In contrast to a real friction, this force can also accelerate atoms in case the current temperature is lower than the tar-

get temperature. A parameter that represents the strength of the coupling to the heat bath must be provided by the user; it determines how fast the target temperature should be reached and must be tuned to avoid unphysical behaviour of the thermostat. The Nosé–Hoover thermostat preserves the physically correct fluctuations of the canonical ensemble.

Sometimes, one not only wants to control the temperature of the system but also the pressure—or more generally the stress tensor. Therefore, the simulation of an isothermal–isobaric ensemble is needed. A pressure control due to a barostat can be implemented in a similar way to the Nosé–Hoover thermostat. A formulation using a full stress tensor was developed by Parinello and Rahman.[266]

LAMMPS implements the equations of motion by Shinoda, Shiga, and Mikami[267] for the full isothermal–isobaric ensemble. Both the barostat and the thermostat can be enabled and disabled independently, allowing simulations in the microcanonical, canonical, isothermal–isobaric, and isoenthalpic–isobaric ensembles.

2.1.4 *Molecular statics*

MD simulations are always performed at finite temperatures. Sometimes, ground-state calculations with empirical potentials are useful. So-called molecular statics calculations provide a reliable way to obtain a 0 K state by using a local optimisation algorithm. Such an algorithm is used to minimise the potential energy, often by also using its gradient, the forces.

LAMMPS implements a range of optimisation algorithms which not only vary the atomic positions, but can also optimise the box shape to reach a desired stress state (which may be zero). This can be used, for example, to calculate lattice constants and densities. In this thesis, we use the Polak–Ribière version of the conjugate gradient algorithm.[268,269] This algorithm uses only the gradient, i.e., the forces, and works well for functions that are approximately quadratic near the minimum, which is the case for the potential wells in solids. It should be noted that this algorithm only finds the closest minimum in the parameter space.

2.2 INTERATOMIC POTENTIALS

In Eq. 2.1, the only material-dependent quantity was the atomic mass m_i. The physics of the bonding and therefore of the whole system is contained in the forces $\mathbf{F}_i$. Often, a (semi-)empirical formulation for the potential energy per atom, E^i_{pot}, is derived and the forces are calculated from it:

$$\mathbf{F}_i = -\vec{\nabla}_i E_{\text{pot}}, \quad \text{with} \quad E_{\text{pot}} = \sum_i E^i_{\text{pot}}. \tag{2.2}$$

Therefore, we speak of *interatomic potentials*. If a formulation uses the forces directly we speak of *force-fields*.

Depending on the type of interatomic interaction, different mathematical frameworks have been used. The simplest option is a pair potential which simply depends on interatomic distances, i.e., $E_i = \sum_{j(\neq i)} \phi(r_{ij})$. These potentials can only describe densely-packed structures and are usually used when their high performance matters more than the accurate quantitative description of specific materials. More sophisticated potentials include Tersoff-type potentials in various variants[270,271] which have been widely used for covalently-bonded materials, especially for semiconductors. An alternative is provided by the so-called MEAM potentials[272] and many other types of potentials of varying complexity. Embedded-atom method (EAM) potentials are used successfully for a wide range of metallic systems and are popular because of their computational efficiency. Several parametrisations for Cu–Zr exist and EAM potentials are therefore the potential class of choice for the work presented in this thesis.

2.2.1 *Embedded-atom method*

The idea of the embedded-atom method, or EAM for short, was first proposed by Daw and Baskes[273] and is based on the quasi-atom theory.[274,275] In this theory, an impurity placed on a position $\mathbf{x}$ in a lattice is assumed to experience a locally uniform environment. Stott and Zaremba showed, related to the Hohenberg–Kohn theorem,[276] that the energy of the impurity is a functional of the electron density ρ at point $\mathbf{x}$ of the defect-free lattice.[274] That is, $E = F_Z[\rho(\mathbf{x})]$, where the functional F_Z depends on the atomic number Z of the impurity. Daw and Baskes extended that formalism by treating each atom as an impurity in the host of all other atoms.[273,277] The embedding energy F_i of atom i, defined as the difference in energy between an atom in a uniform electron gas and the isolated atom, depends only on the local electron density at $\mathbf{x}_i$ in the EAM formalism. This derivation neglects the core–core repulsion which is added back in by a simple pair potential ϕ. This leads to

$$E^i_{\text{pot}} = F_\alpha\left[\rho(\mathbf{x}_i)\right] + \sum_{j(\neq i)} \phi_{\alpha\beta}(r_{ij}). \tag{2.3}$$

By the above derivation we can see that this energy is the cohesive energy in the ground state. The functional for the embedding term is defined differently for each species α of the embedded atom. A physically meaningful analytical form is unknown, so usually splines are fitted to physical properties to obtain F_α for different species. The electron density ρ is approximated by a sum over the atomic densities of the constituents of the host by $\rho(\mathbf{x}_i) = \sum_{j(\neq i)} \rho_\beta(r_{ij})$. The function ρ_β—different for every species β of the host atom j—is also not analytically defined but empirically fitted. This gives the basic formulation of the EAM potential:

$$E^i_{\text{pot}} = F_\alpha\left[\sum_{j(\neq i)} \rho_\beta(r_{ij})\right] + \frac{1}{2}\sum_{j(\neq i)} \phi_{\alpha\beta}(r_{ij}). \tag{2.4}$$

The pair potential $\phi_{\alpha\beta}$ was originally defined by a mixing rule of effective charges of α and β,[277] but in the potentials used in this thesis the pair terms are splines fitted for all combinations α, β of species. The idea of the electron gas and the lack of angular terms in the EAM are a good fit for systems with metallic bonding as treated in this thesis.

A slight modification of the EAM potential is the Finnis–Sinclair-type potential:[278]

$$E^i_{\text{pot}} = F_\alpha \left[\sum_{j(\neq i)} \rho_{\alpha\beta}(r_{ij}) \right] + \frac{1}{2} \sum_{j(\neq i)} \phi_{\alpha\beta}(r_{ij}). \tag{2.5}$$

The only difference to the classic Daw and Baskes formulation is that the electron density $\rho_{\alpha\beta}$ is now dependent on the species of atom i *and* atom j.

We use both types of potentials and refer the reader to Chap. 3 for a discussion of the specific parametrisations for amorphous Cu–Zr systems.

2.3 SAMPLE PREPARATION AND MECHANICAL TESTING

Depending on the system or property being investigated, we use different simulation setups that are described in detail in the corresponding chapters. For now we only give a general introduction to mechanical testing by MD simulations.

Most of our simulations use a glass matrix, with and without crystalline secondary phases. In contrast to crystalline matter, where the exact atomic arrangement on the lattice is known from experiments, the glass state lacks such long-range order. Therefore our glasses are produced by cooling down from the melt with a cooling rate of 10^{10} K/s. It has been shown that this rate is sufficiently slow to obtain Cu–Zr-based glasses that exhibit the experimentally observed shear banding instead of flowing homogeneously.[50–53] Still, this cooling rate is orders of magnitude faster than any experiment and is a compromise between accurate reproduction of a relaxed glass structure and computational feasibility. After obtaining the glass, secondary phases, surfaces, and other heterogeneities can be inserted. The resulting systems are always equilibrated at the desired target temperature and target volume or pressure.

Mechanical deformation can be performed using a constant stress (controlled via the barostat) or with a constant strain rate (controlled by scaling the simulation box in a periodic direction). We use the latter method, in which the atomic positions are scaled together with the simulation box with a constant engineering strain rate. We used either uniaxial tension or shear simulations. In order to accommodate the lateral contraction under tension, we used either open boundaries or a barostat set to a pressure of zero in the lateral directions. This is not necessary in shear, where we

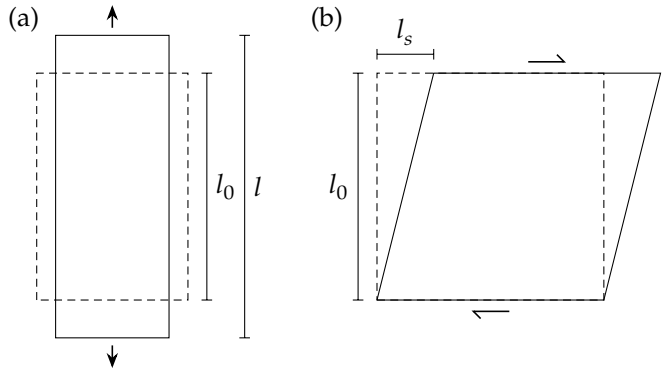

FIGURE 2.2: Engineering strain definitions. (a) Tensile loading. (b) Volume-conserving shear. The dashed lines indicate the initial shape of the sample.

used a volume conserving shear (see note in Sec. 2.5). For simplicity, we always use the engineering (shear) strain definitions

$$\check{\varepsilon} = \frac{l - l_0}{l_0} \qquad \text{and} \qquad \check{\gamma} = \arctan \frac{l_s}{l_0} \approx \frac{l_s}{l_0}, \tag{2.6}$$

with lengths as sketched in Fig. 2.2. The stress reported by LAMMPS is a true stress as long as the volume of the solid is the same as the volume of the simulation box. For periodic boundaries as we use them, this is always the case. For flat surfaces with shrink-wrap open boundaries, this is also correct, although the value starts to deviate from the actual stress as soon as a shear offset appears on the surface, introducing vacuum inside the simulation cell. We will ignore this effect and treat these stresses as true stresses, especially as this is effectively the case until yield. The only setups in which we need to resort to the engineering stress definition are those were the volume of the simulation box is not filled completely by the solid, such as a nanowire. Here, we use the initial volume of the sample to scale the stress output of LAMMPS.

The setup of the simulated tensile tests is similar to the standard experiment, although our strain rates are again much higher than obtainable in the laboratory. As laid out in Sec. 1.5, high strain rates lead to delocalised STZ activation which is not observed experimentally. To remain in a regime that is comparable to the experiment, it was found that strain rates between $10^7\,\mathrm{s}^{-1}$ and $10^8\,\mathrm{s}^{-1}$ are sufficiently slow to observe the appropriate shear banding behaviour in $Cu_{64}Zr_{36}$ glasses.[53,145] These rates are also close to the maximum that can be obtained with the currently available computational power. If we move in a regime where shear banding is observed, no further change of mechanism due to strain rate is expected and the results should be comparable to experiment. The only difference is the amount of serrations which have been attributed either to shear band nucleation[144] or propagation kinetics.[149] These represent later stages during plastic deformation that are not observable in simulations anyway. As the suppression of shear banding at very high rates is due to the nucleation kinetics, no influence of the rate on the shear band front propagation is expected: Once nucleated, a shear band moves with the velocity of a transverse

sound wave.[17] A quick estimation with a shear modulus of $\mathcal{G} \approx 35\,\mathrm{GPa}$ and a density of $\rho \approx 7.5\,\mathrm{g/cm^3}$ gives a sound velocity of $\sqrt{\mathcal{G}/\rho} \approx 2200\,\mathrm{m/s}$, which is very fast compared to the deformation. We therefore expect that the propagation of shear bands is independent of the strain rate in the regime used in our simulations.

2.4 ATOMIC-LEVEL MEASURES OF DEFORMATION

In order to detect activated STZs and shear bands, a simple displacement analysis that calculates the vector difference between the current atomic position and a reference position is not sufficient. After shear banding, two halves of the sample are displaced against each other and no atom remains at its place even if subtracting a change in simulation box shape. A more local definition that can also be calculated per atom is needed. The free software package OVITO[279] implements an algorithm[280] that starts by considering the nearest neighbours of an atom i. It then calculates a local deformation gradient tensor J_i based on the relative displacements of the neighbouring atoms compared to a reference state. A Green–Lagrangian strain tensor η_i is derived from the deformation gradient as

$$\eta_i = \frac{1}{2}\left(J_i J_i^{\mathrm{T}} - I\right), \tag{2.7}$$

where I is the identity matrix. The calculation of the deformation gradient can optionally be performed by scaling the simulation box of the reference state to the current dimensions, thereby excluding the macroscopic deformation of the sample. This is appropriate to capture localised plastic deformation, such as shear bands, but must not be done when probing the elastic deformation on an atomic scale. From η_i, a von Mises local shear invariant can be calculated:[280]

$$\eta_i^{\mathrm{Mises}} = \sqrt{\eta_{yz}^2 + \eta_{xz}^2 + \eta_{xy}^2 + \frac{(\eta_{yy} - \eta_{zz})^2 + (\eta_{xx} - \eta_{zz})^2 + (\eta_{xx} - \eta_{yy})^2}{6}}. \tag{2.8}$$

The index i was omitted on the right-hand side of the equation for notational simplicity. The tensor η_i can be used as a strain tensor and is from here on out simply called the "atomic strain tensor", while η_i^{Mises} will be called "atomic shear strain" in accord with popular usage. A shear band usually exhibits atomic shear strains in excess of 0.2–0.3.[52,125]

A strain localisation parameter ψ was proposed by Cheng *et al.*[52] It is defined as

$$\psi = \sqrt{\frac{1}{N}\sum_{i=1}^{N}\left(\eta_i^{\mathrm{Mises}} - \overline{\eta}^{\mathrm{Mises}}\right)^2} \qquad \text{with} \qquad \overline{\eta}^{\mathrm{Mises}} = \frac{1}{N}\sum_{i=1}^{N}\eta_i^{\mathrm{Mises}}. \tag{2.9}$$

A ψ of zero corresponds to a completely homogeneous deformation.

2.5 ELASTICITY AND RELATED TENSORS

The elastic response of a system to externally applied stress is an important quantity in engineering applications and on a theoretical level. The elastic response of a solid is directly connected to the stiffness of the interatomic bonds and its symmetry is connected to the symmetry of the atomic structure of the solid itself.

The stress response σ_{ij} to an applied strain ε_{kl} in the linear elastic regime is given by the general formulation of Hooke's law,

$$\sigma_{ij} = c_{ijkl}\varepsilon_{kl} \quad \text{with } i,j,k,l = 1,2,3, \tag{2.10}$$

where c_{ijkl} are the components of a fourth-rank tensor: the stiffness tensor. Because of symmetry, this tensor can be reduced to a symmetric 6×6 matrix. We follow the Voigt notation as used in Ref. 281, where

$$\begin{pmatrix} \sigma_{11} & \sigma_{12} & \sigma_{31} \\ \sigma_{12} & \sigma_{22} & \sigma_{23} \\ \sigma_{31} & \sigma_{23} & \sigma_{33} \end{pmatrix} = \begin{pmatrix} \sigma_1 & \sigma_6 & \sigma_5 \\ \sigma_6 & \sigma_2 & \sigma_4 \\ \sigma_5 & \sigma_4 & \sigma_3 \end{pmatrix} \quad \text{and} \tag{2.11}$$

$$\begin{pmatrix} \varepsilon_{11} & \varepsilon_{12} & \varepsilon_{31} \\ \varepsilon_{12} & \varepsilon_{22} & \varepsilon_{23} \\ \varepsilon_{31} & \varepsilon_{23} & \varepsilon_{33} \end{pmatrix} = \begin{pmatrix} \varepsilon_1 & \tfrac{1}{2}\varepsilon_6 & \tfrac{1}{2}\varepsilon_5 \\ \tfrac{1}{2}\varepsilon_6 & \varepsilon_2 & \tfrac{1}{2}\varepsilon_4 \\ \tfrac{1}{2}\varepsilon_5 & \tfrac{1}{2}\varepsilon_4 & \varepsilon_3 \end{pmatrix}, \tag{2.12}$$

giving a simplified Hooke's law of

$$\sigma_i = c_{ij}\varepsilon_j \quad \text{with } i,j = 1,2,\ldots,6. \tag{2.13}$$

In the literature, the factor ½ is sometimes omitted, leading to inconsistent definitions for c_{ij} with i or $j \geq 4$.

The inverse of the stiffness tensor, called the compliance tensor s_{ij}, is also used and gives a measure of the strain resulting from an externally applied stress state. The use of symbols opposite to the first letters of the names of the tensors is unfortunate but standard.

A NOTE ON LAMMPS. Instead of the conventional pure shear strain, LAMMPS by default uses a volume conserving shear. For the example of xz shear, the traditional shear is shown on the left, LAMMPS' shear definition on the right:

$$\begin{pmatrix} 0 & 0 & \varepsilon_{31} \\ 0 & 0 & 0 \\ \varepsilon_{31} & 0 & 0 \end{pmatrix} \qquad \begin{pmatrix} 0 & 0 & 0 \\ 0 & 0 & 0 \\ \varepsilon_5 & 0 & 0 \end{pmatrix}. \tag{2.14}$$

For small strains those are equivalent (excepting a small rotation about the y axis) and it is

$$\varepsilon_5 \approx 2\varepsilon_{31}. \tag{2.15}$$

In the conventional definition, the volume of a sheared simulation box can be expressed in terms of the vectors **a**, **b**, and **c**—which span the undeformed cell—and the strain ε_{31} via

$$V_{\text{sheared}}(\varepsilon_{31}) = \left(1 - \varepsilon_{31}^2\right) \cdot \Big(\mathbf{a} \cdot (\mathbf{b} \times \mathbf{c})\Big), \tag{2.16}$$

which makes the two definitions incompatible for larger strains. In practice and for the purposes of this thesis this difference is only critical for the calculation of elastic constants. As these are calculated at very small strains anyway, we can from now on ignore this distinction.

2.5.1 *Calculation*

The elastic constants can be calculated in two ways. Both start from a fully relaxed sample at zero stress. In the first method, we apply only one strain component, keeping all others zero. We do this once for each strain component, relax, obtain the stress state and calculate the elastic constant via

$$c_{ij} = \frac{\sigma_i}{\varepsilon_j}. \tag{2.17}$$

In the second method, all stress components except one are set to zero. We do this once for each stress component, relax, obtain the strain, and calculate

$$s_{ij} = \frac{\varepsilon_i}{\sigma_j}. \tag{2.18}$$

This method can also be used to extract a per-atom compliance tensor. By applying an external stress, all atoms will be subjected to the same stress. We can extract an atomic strain tensor with OVITO as discussed in Sec. 2.4 and apply Eq. 2.18 to each atom. Equation 2.17 is not useful on a per-atom level, as we cannot impose a uniform strain on all atoms.

2.5.2 *Average moduli*

Often, we are interested in more practically applicable values, such as the shear modulus $\mathcal{G}$, or the bulk modulus $\mathcal{K}$. For isotropic materials, only one value exists for both and is given by[281]

$$\mathcal{G} = \frac{c_{11} - c_{12}}{2} \qquad \text{and} \qquad \mathcal{K} = \frac{c_{11} + 2c_{12}}{3}. \tag{2.19}$$

For crystals, these values are anisotropic. In the polycrystalline case, effective moduli can be defined by averaging. A lower bound is given by the Reuss approximation[282]

$$\mathcal{G}_\mathrm{R} = \frac{15}{4(s_{11}+s_{22}+s_{33}) - 4(s_{12}+s_{13}+s_{23}) + 3(s_{44}+s_{55}+s_{66})} \tag{2.20}$$

$$\mathcal{K}_\mathrm{R} = \frac{1}{(s_{11}+s_{22}+s_{33}) + 2(s_{12}+s_{13}+s_{23})}, \tag{2.21}$$

an upper bound by the Voigt approximation[283]

$$\mathcal{G}_\mathrm{V} = \frac{1}{15}(c_{11}+c_{22}+c_{33}-c_{12}-c_{13}-c_{23}) + \frac{1}{5}(c_{44}+c_{55}+c_{66}) \tag{2.22}$$

$$\mathcal{K}_\mathrm{V} = \frac{1}{9}(c_{11}+c_{22}+c_{33}) + \frac{2}{9}(c_{12}+c_{13}+c_{23}). \tag{2.23}$$

The Voigt–Reuss–Hill moduli were proposed to estimate a practical average value:[284]

$$\mathcal{G}_\mathrm{VRH} = \frac{1}{2}(\mathcal{G}_\mathrm{V}+\mathcal{G}_\mathrm{R}) \qquad \mathcal{K}_\mathrm{VRH} = \frac{1}{2}(\mathcal{K}_\mathrm{V}+\mathcal{G}_\mathrm{K}) \tag{2.24}$$

$$\mathcal{E}_\mathrm{VRH} = \frac{9\mathcal{K}_\mathrm{VRH}\cdot\mathcal{G}_\mathrm{VRH}}{3\mathcal{K}_\mathrm{VRH}+\mathcal{G}_\mathrm{VRH}} \qquad \nu^\mathrm{VRH}_\mathrm{Poisson} = \frac{3\mathcal{K}_\mathrm{VRH}-2\mathcal{G}_\mathrm{VRH}}{6\mathcal{K}_\mathrm{VRH}+3\mathcal{G}_\mathrm{VRH}}. \tag{2.25}$$

2.5.3 *Kelvin notation*

An alternative to the Voigt notation was proposed by Kelvin.[285] One advantage of this notation is that we always obtain one bulk modulus and five shear moduli from this matrix, which are all clearly defined. In an isotropic system, the Kelvin shear moduli $\mathcal{G}_1$ to $\mathcal{G}_5$ are equal and correspond to two times the classic shear modulus definition: $\mathcal{G}_{1,\dots,5} = 2\mathcal{G}$. We define the different shear moduli in such a way, that they increase in stiffness from $\mathcal{G}_1$ (lowest) to $\mathcal{G}_5$ (highest). This is especially useful when looking at per-atom moduli, where the averages developed for polycrystals are ill-defined. Instead, one can, e.g., observe partial softening on an atomic level by considering only $\mathcal{G}_1$. This method has already been used to connect the boson peak to fluctuating moduli in a model glass.[243]

The Kelvin notation can easily be obtained from the Voigt notation of the stiffness tensor by the element-wise multiplication

$$c_{ij}^\mathrm{Kelvin} = B_{ij}c_{ij}^\mathrm{Voigt}, \qquad \text{with} \qquad B = \begin{pmatrix} 1 & 1 & 1 & \sqrt{2} & \sqrt{2} & \sqrt{2} \\ 1 & 1 & 1 & \sqrt{2} & \sqrt{2} & \sqrt{2} \\ 1 & 1 & 1 & \sqrt{2} & \sqrt{2} & \sqrt{2} \\ \sqrt{2} & \sqrt{2} & \sqrt{2} & 2 & 2 & 2 \\ \sqrt{2} & \sqrt{2} & \sqrt{2} & 2 & 2 & 2 \\ \sqrt{2} & \sqrt{2} & \sqrt{2} & 2 & 2 & 2 \end{pmatrix}. \tag{2.26}$$

We follow Derlet *et al.* in calculating the shear moduli by first projecting out the volume changes[243]

$$c' = P^{\mathrm{T}} \cdot c^{\mathrm{Kelvin}} \cdot P, \qquad \text{with} \qquad P = \begin{pmatrix} +\frac{2}{3} & -\frac{1}{3} & -\frac{1}{3} & 0 & 0 & 0 \\ -\frac{1}{3} & +\frac{2}{3} & -\frac{1}{3} & 0 & 0 & 0 \\ -\frac{1}{3} & -\frac{1}{3} & +\frac{2}{3} & 0 & 0 & 0 \\ 0 & 0 & 0 & 1 & 0 & 0 \\ 0 & 0 & 0 & 0 & 1 & 0 \\ 0 & 0 & 0 & 0 & 0 & 1 \end{pmatrix}, \tag{2.27}$$

and then calculating the eigenvalues of c'. These eigenvalues now correspond to the five Kelvin shear moduli.

2.6 STRUCTURE ANALYSIS

While there is still discussion about the exact short- and mid-range order in metallic glasses, the identification of structural motifs in computer simulations of metallic glasses and crystalline metals is well established. In this thesis, we employ standard methods, such as the radial distribution function (RDF), which is also accessible to the experiment, the Voronoi tessellation, and the common neighbour analysis (CNA). All of these methods are available in the software package OVITO.[279]

2.6.1 *Radial distribution function*

The RDF, also called pair distribution function or pair correlation function, is a measure for the probability to find an atom at a distance r from another atom. It is accessible to experimental measurement by Fourier transform of the structure factor.[286] The RDF contains information about the order in the system and various values, such as the density, can be extracted from it. For randomly distributed points in space, its value is 1. Generally, it is defined as

$$g_{\mathrm{RDF}}(r) = \frac{1}{4\pi r^2 \rho_n N} \sum_{i=1}^{N} \sum_{j(\neq i)} \delta(r - r_{ij}), \tag{2.28}$$

where r_{ij} is the distance between atoms i and j, the δ is the Dirac delta function. The formula is normalised by the density of randomly distributed points ρ_n. The sum over $\delta(r - r_{ij})/(4\pi r^2)$ is the number density of atoms in the shell at radius r; the thickness of the shell is the width of the Dirac delta, it is infinitesimally small. Take note that the dimension of the Dirac delta is the inverse of the dimension of its argument, resulting in g_{RDF} being dimensionless. In practice, and as available in LAMMPS and OVITO, a

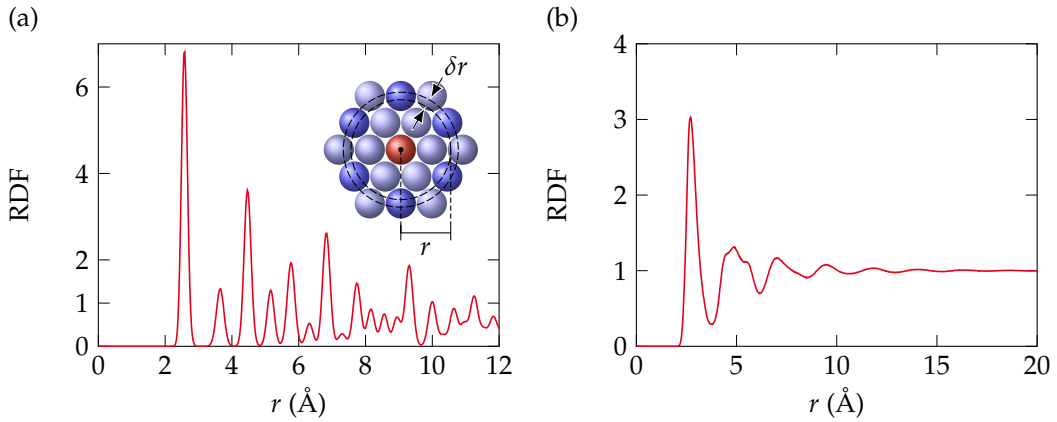

FIGURE 2.3: Radial distribution function for an fcc metal (a) and a $Cu_{64}Zr_{36}$ glass (b). The inset in (a) shows how the RDF is calculated: The value at r is the number density of atoms in the shell between r and $r + \delta r$ which are marked in dark blue.

discrete formulation is used. Here, the shell has a width of δr and the RDF is defined as

$$g_{\mathrm{RDF}}(r) = \frac{1}{\rho_n N \frac{4}{3}\pi\left[(r^3 + \delta r^3) - r^3\right]} \sum_{i=1}^{N} \sum_{j(\neq i)} \begin{cases} 1 & r \leq r_{ij} < r + \delta r \\ 0 & \text{otherwise} \end{cases}, \tag{2.29}$$

where the rightmost summand is a Kronecker delta function. An example of this calculation can be seen in Fig. 2.3.

For multi-component systems, partial RDFs between atoms of type α and type β can be defined as

$$g^{\alpha\beta}_{\mathrm{RDF}}(r) = \frac{N}{4\pi r^2 \rho_n N_\alpha N_\beta} \sum_{i\in\alpha} \sum_{\substack{j\in\beta \\ j(\neq i)}} \delta(r - r_{ij}) \tag{2.30}$$

or, in the discretised case,

$$g^{\alpha\beta}_{\mathrm{RDF}}(r) = \frac{N}{\rho_n N_\alpha N_\beta \frac{4}{3}\pi\left[(r^3 + \delta r^3) - r^3\right]} \sum_{i\in\alpha} \sum_{\substack{j\in\beta \\ j(\neq i)}} \begin{cases} 1 & r \leq r_{ij} < r + \delta r \\ 0 & \text{otherwise} \end{cases}. \tag{2.31}$$

In crystalline materials, one would imagine that the RDF consists of delta functions at radii corresponding to the lattice positions. In reality, these functions are smeared out because of thermal and zero-point vibrations [cf. Fig. 2.3 (a)]. For glasses, the RDF contains limited information about the short-range order (first peak), and mid-range order (r up to 1 nm to 2 nm). After that, the RDF approaches unity, as there is obviously no long-range order in amorphous systems and the distribution becomes completely random [cf. Fig 2.3 (b)]. As the data is averaged radially, information about

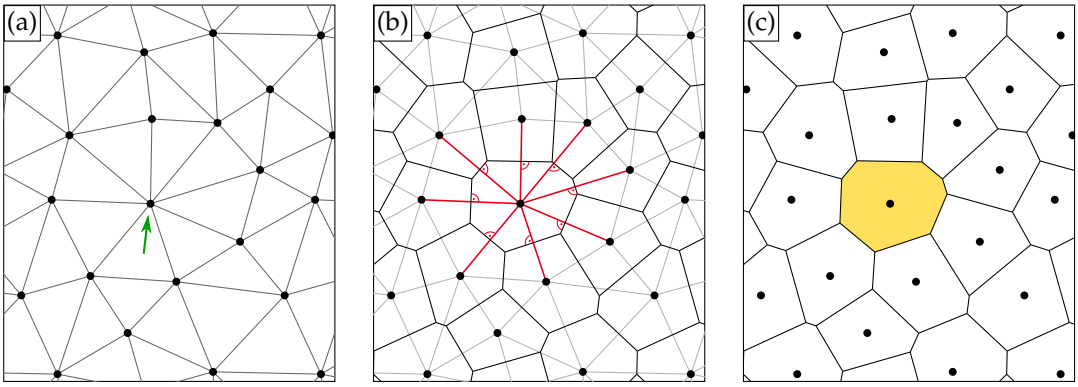

FIGURE 2.4: 2D Voronoi tessellation. (a) As a first step, apply the Delaunay triangulation, which connects every point with its neighbours. The number of connecting lines radiating from a point is its coordination number (for the marked point it is 8). (b) Draw a line perpendicular to these connecting lines at the middle of every connecting line. This gives the Voronoi polygons. (c) The volume enclosed by a Voronoi polygon contains only a single point and can be used to assign an area to the point.

the exact nature of the short-range order is lost. To characterise the glass in more detail, a local geometry analysis—such as the Voronoi analysis presented in the next section—is needed.

2.6.2 *Voronoi analysis*

The Voronoi tessellation is a method to partition n-dimensional space into volumes around points in that space.[287–290] The Voronoi tessellation is dual to the corresponding Delaunay triangulation.[291] The concept is most easily demonstrated in two dimensions, as illustrated in Fig. 2.4. The Delaunay triangulation connects all points such that no point is inside the circumcircle of the triangle defined by three connected points [Fig. 2.4 (a)]. In a solid, the connecting lines can be thought of as bonds and their number is the coordination number of the atom. In a next step, Fig. 2.4 (b), planes are constructed in the middle of all connecting lines, such that the plane is perpendicular to connecting line on which it is placed. The smallest area around a point delimited by these planes is a Voronoi polygon [Fig. 2.4 (c)]. In 2D, this method is useful to assign a number of neighbours and an area to points.

In 3D, the Voronoi tessellation is similar to the construction of a Wigner–Seitz cell.[84] It is also much more useful than in 2D, because in addition to the neighbours and the volume, we obtain differently shaped faces on the Voronoi polyhedron. Figure 2.5 demonstrates this for an atom in an fcc lattice and an icosahedral unit in a metallic glass. By counting the number of i-edged faces, we can construct a Voronoi index. Most commonly, the notation $\langle n_3, n_4, n_5, n_6 \rangle$ is used, where n_i denotes the number of i-edged faces. The sum of the Voronoi indices is the coordination number,

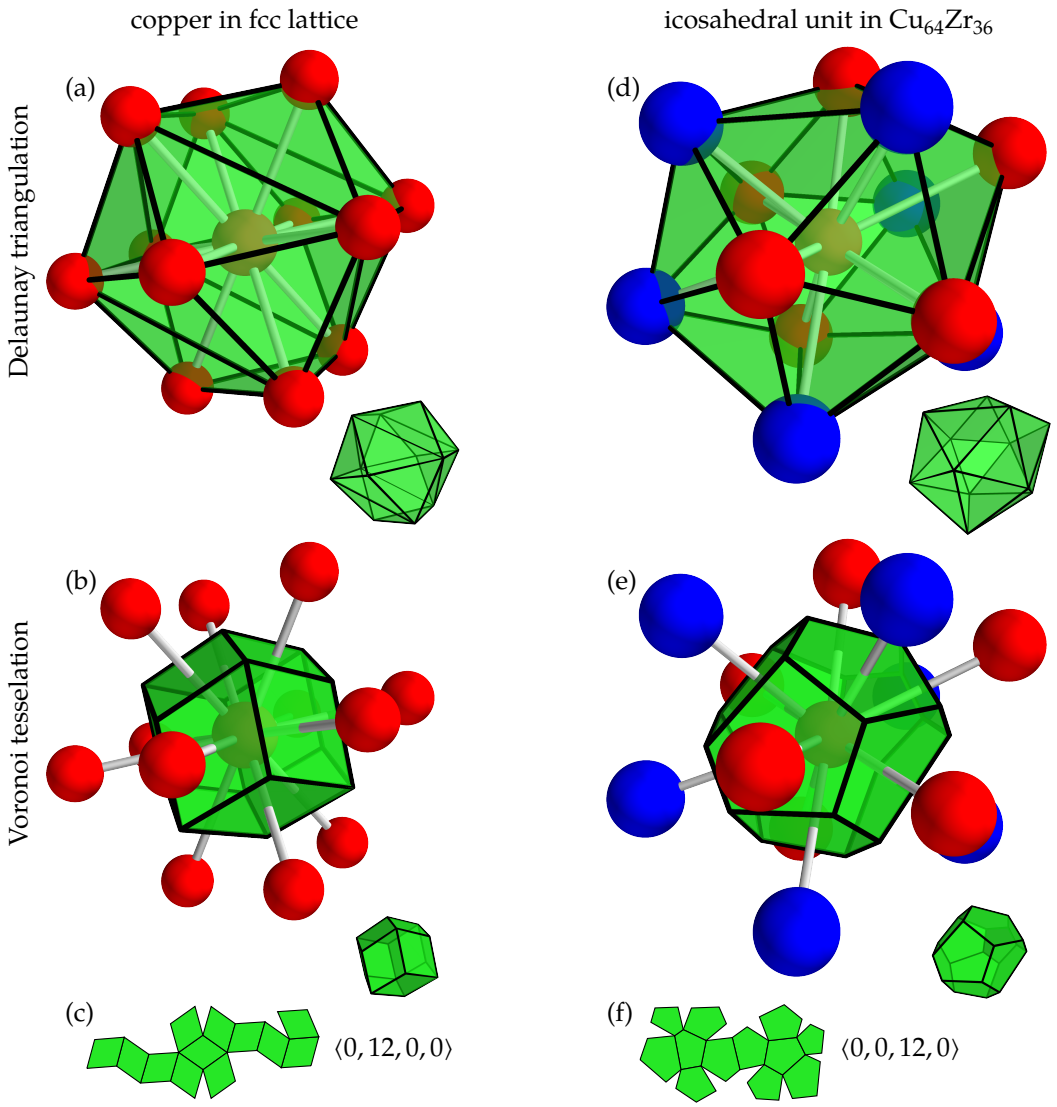

FIGURE 2.5: Voronoi polyhedra in condensed matter. (a) Polyhedron around an atom in a face-centred cubic lattice. The Voronoi polyhedron (b) is a rhombic dodecahedron. Looking at the unfolded polyhedron (c), we see 12 rhombi giving a Voronoi index of $\langle 0, 12, 0, 0 \rangle$. (d) A copper-centred icosahedral unit in a $Cu_{64}Zr_{36}$ glass. The icosahedral units in metallic glasses take their name from the polygon spanned by the neighbours of the central atom. (e) The Voronoi polyhedron itself is a dodecahedron which has 12 five-sided faces (f).

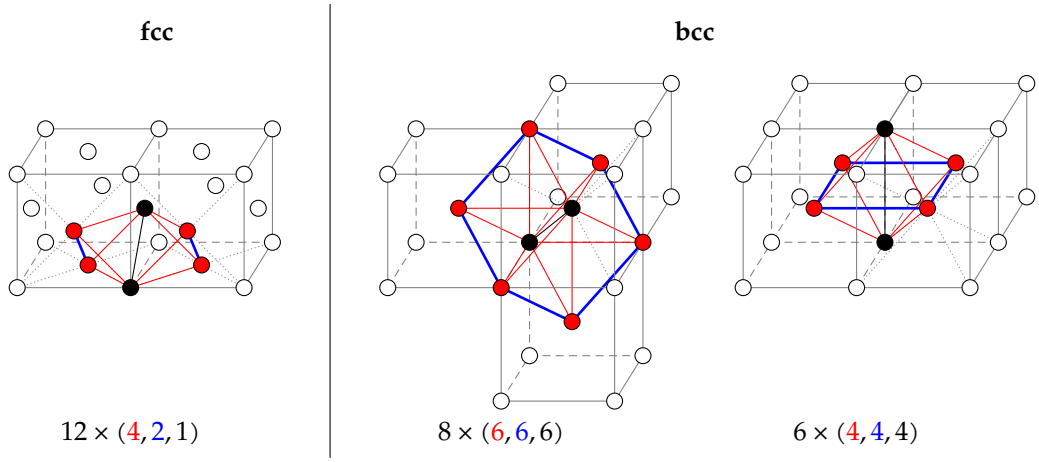

FIGURE 2.6: CNA indices for fcc and bcc crystal structures. The CNA index is defined for every bond as a triplet of the number of common neighbours (red), the number of bonds between common neighbours (blue), and the longest chain of bonds between common neighbours. For bcc, the second neighbour shell needs to be taken into account, otherwise there would be no common neighbours.

as the number of faces is equal to the number of Delaunay lines or bonds. A histogram of the occurrence of the different Voronoi polyhedra gives information about the short-range order of a metallic glass. The $\langle 0, 0, 12, 0 \rangle$ polyhedron, or "icosahedral unit", is a common feature in metallic glasses.[50,52,91–93] The name icosahedral unit comes from the shape of the polyhedron spanned by the neighbouring atoms, not from the shape of the Voronoi polyhedron which is a dodecahedron. As discussed in Sec. 1.2, atoms in amorphous solids prefer five-fold bonds. These bonds can easily be identified with the Voronoi analysis, they correspond to the n_5 faces. Figure 2.5 illustrates this nicely: The crystalline structure has the same coordination number but the bonds are four-fold, while the icosahedron only has five-fold bonds.

2.6.3 *Identifying crystal structures*

A commonly used method to identify crystal structures is the common neighbour analysis (CNA).[292–294] The concept is illustrated in Fig. 2.6. The neighbours of an atom are identified, either using a cutoff or with an adaptive method,[294] and three numbers are calculated for every bond. The first number is the number of common neighbours of the two bonded atoms. The second number is the number of bonds between those common neighbours. The third number is the number of bonds in the longest chain formed by these shared neighbours. Different crystal structures have a defined number of bonds with specific triplets and can be identified thereby with atomic resolution. In some structures, such as bcc, there are no common neighbours and therefore the second neighbour shell is taken into account.

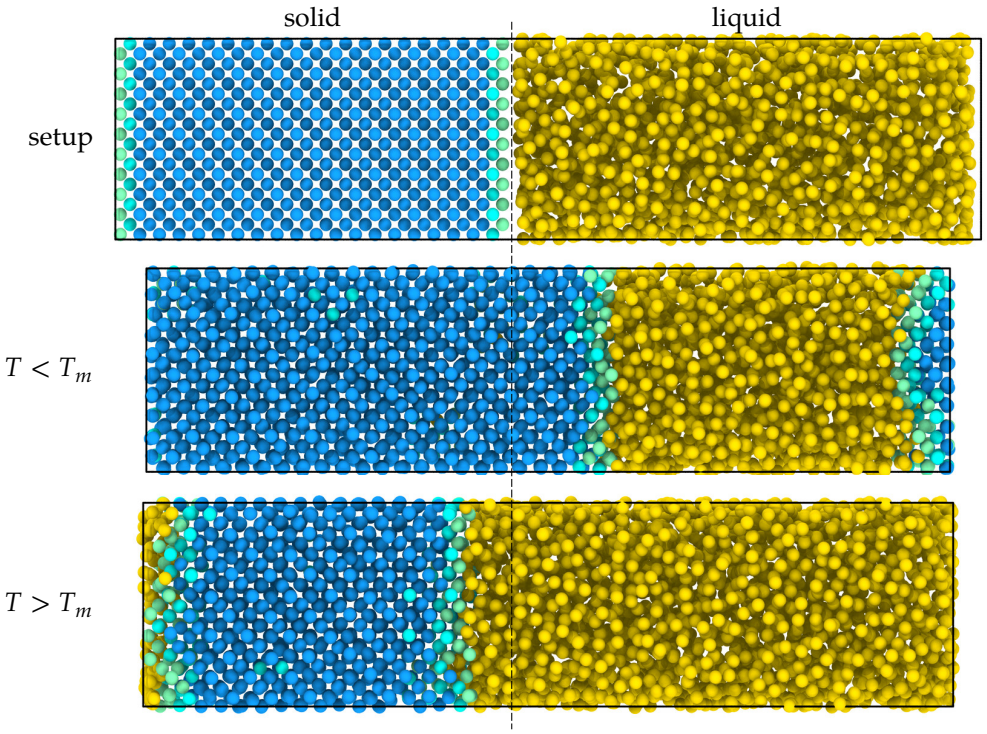

FIGURE 2.7: Simulation setup to determine the melting point of a material. A crystalline solid is inserted into a simulation box together with the melt and the position of the interface is recorded. When equilibrating this system at different temperatures, the interface will move. If the temperature is below the melting point, the crystal will grow; a temperature above T_m will lead to melting.

For diamond lattices, there are no common neighbours and the second and third neighbour shell is not well separated. Small thermal excitations or elastic strains can disturb the CNA in a way to make it completely unreliable. An extension of the CNA method was developed to solve this problem and to make it possible to differentiate between cubic and hexagonal diamond. Details can be found in Ref. 295. Both the CNA and the diamond identification are implemented in OVITO.

Additionally, we applied an atomic structure identification algorithm that uses pattern matching on the medium-range order to differentiate complex structures like twins and stacking faults in Chap. 8.[296]

2.7 MELTING POINT

The determination of a melting point with MD simulations is not straightforward. A naive method would be to cool a melt and record the temperature at which crystallites start to appear. This method fails because deep undercooling is a common

phenomenon in simulations. This is for two reasons: First, the cooling rate is relatively high and second, solidification is a nucleation phenomenon which depends on the probability of a random crystallite growing above a critical size.[35] In comparison to a real sample, the simulation box is small, making it statistically less likely for such a rare event to occur. Additionally, solidification often starts at heterogeneous interfaces[35] which are usually not included in the simulations. The problem is the same when starting from the solid. A defect-free solid can be heated far above the melting temperature without actually melting.

The solution is to include both phases into a single simulation box as shown in Fig. 2.7. The system is equilibrated at a given temperature and the thermodynamically stable phase will grow quickly, solving the problem of kinetics. The melting point can now be found, e.g., by using the bisection method starting with two temperatures below and above the suspected melting point. We use this method in Sec. 5.4 in order to determine the melting points of the Laves phases C14 and C15.

2.8 VIBRATIONAL AND THERMODYNAMIC PROPERTIES

In crystal lattices, vibrations are quantised in quasi-particles, the phonons.[286] The phonon density of states can be used to calculate the (vibrational) heat capacity of a system[286] and has therefore been of interest for a long time. Phonons can also be found in amorphous materials despite the missing lattice.[297] In addition to phonons, more localised modes were also found in amorphous systems (see Sec. 1.8) and we will therefore use the more general term vibrational density of states (VDOS) from now on. A simple shape of the VDOS was first proposed by Debye to explain the low-temperature heat capacity[298] but the actual VDOS can also be measured accurately in experiment. This section will introduce the Debye model, methods to determine the VDOS from simulation, and formulas to derive quantities like free energy and heat capacity from the VDOS.

2.8.1 *The Debye model*

The Debye model is an approximation of the heat capacity for isotropic solids with a mono-atomic basis.[298] This relatively simple model assumes a phonon density of states $g(\omega) \propto \omega^2$ up to a cutoff frequency ω_D, the Debye frequency. Despite its simplicity, this model can be applied to a wide range of materials. We will discuss the model and its shortcomings for describing amorphous materials below.

The density of states is assumed to be

$$g(\omega)\mathrm{d}\omega = \begin{cases} \dfrac{V}{2\pi^2}\dfrac{\omega^2}{v_g^3}\mathrm{d}\omega & \omega < \omega_\mathrm{D} \\ 0 & \omega \geq \omega_\mathrm{D}, \end{cases} \tag{2.32}$$

where V is the unit cell volume and v_g the group velocity of the phonons. For amorphous systems, an effective volume has to be assumed if one wants to calculate the heat capacity directly from this model. This is troublesome and we will avoid it here. Using Eq. 2.32, the internal energy due to vibrations can be derived to[298]

$$U_{\mathrm{vib}}(T) = \frac{9N}{\omega_{\mathrm{D}}^3} \int_0^{\omega_{\mathrm{D}}} \frac{\hbar\omega^3}{\exp\left(\frac{\hbar\omega}{k_{\mathrm{B}}T}\right) - 1} \mathrm{d}\omega, \tag{2.33}$$

where N is the number of particles. The Debye frequency can also be expressed in terms of a Debye temperature Θ:

$$k_{\mathrm{B}}\Theta = \hbar\omega_{\mathrm{D}}. \tag{2.34}$$

This parameter is used in the formula for the heat capacity c_V, which is given by[298]

$$C_V(T) = \left(\frac{\partial U}{\partial T}\right)_V = 9Nk_{\mathrm{B}}\frac{T^3}{\Theta^3} \int_0^{\Theta/T} \frac{x^4 \mathrm{e}^x}{(\mathrm{e}^x - 1)^2} \mathrm{d}x. \tag{2.35}$$

If heat capacity data is available, the Debye temperature can be obtained by fitting Eq. 2.35. The only free parameter is Θ. Numerically, the problem with Eq. 2.35 is that the exponential functions are prone to floating point overflows. Using $\operatorname{csch} x = \sinh^{-1} x = 2\mathrm{e}^x/(\mathrm{e}^{2x} - 1)$, we can replace the exponentials by

$$\frac{\mathrm{e}^x}{(\mathrm{e}^x - 1)^2} = \frac{1}{4}\operatorname{csch}^2\left(\frac{x}{2}\right). \tag{2.36}$$

This leads to the numerically preferable formula

$$C_V(T) = 9Nk_{\mathrm{B}}\frac{T^3}{\Theta^3} \int_0^{\Theta/T} \frac{x^4}{4} \operatorname{csch}^2\left(\frac{x}{2}\right) \mathrm{d}x. \tag{2.37}$$

There are two important approximations of Eq. 2.35 for low and high temperatures.[298] For low temperatures, it is $\Theta/T \to \infty$ and therefore

$$C_V = \frac{12\pi^4}{5} Nk_{\mathrm{B}}\frac{T^3}{\Theta^3}. \tag{2.38}$$

This is Debye's famous T^3-law for the low temperature heat capacity.

For high temperatures, it is $\Theta/T \to 0$ and the integral can be simplified to

$$\int_0^{\Theta/T} \frac{x^4 \mathrm{e}^x}{(\mathrm{e}^x - 1)^2} \mathrm{d}x \approx \int_0^{\Theta/T} \frac{x^4 \cdot 1}{(1 + x - 1)^2} \mathrm{d}x = \int_0^{\Theta/T} x^2 \mathrm{d}x = \frac{1}{3}\frac{\Theta^3}{T^3}, \tag{2.39}$$

which gives a heat capacity of

$$C_V(T) = 3Nk_\mathrm{B}, \tag{2.40}$$

the Dulong–Petit law for classical systems.[299]

Given that the zero point vibrations have half the energy of thermally excited phonons at the same frequency,[297] we obtain

$$U_0 = \int_0^{\omega_D} \frac{\hbar\omega}{2} g(\omega)\mathrm{d}\omega = \frac{9}{8}Nk_\mathrm{B}\Theta \tag{2.41}$$

for the zero point energy. As U_0 depends only on Θ, it is very useful to extract the Debye temperature from internal energy data.

This model is quite successful in capturing the overall shape of the heat capacity, but the VDOS is overly simplified. Crystals exhibit anomalies like the van Hove singularities and the boson peak in amorphous systems is notable because it is a large excess over the Debye model.[297] This means that the VDOS of a given material should be calculated directly.

2.8.2 *Calculation of the vibrational density of states*

The VDOS for a given structure can be calculated by obtaining the dynamical matrix[297] or via the velocity auto-correlation function.[300] The dynamical matrix is defined only for crystal lattices. Because of the periodic boundaries in a computer simulation, this may be circumvented by treating the whole simulation box as a unit cell, but the dynamical matrix becomes unwieldy for larger boxes. For several thousand atoms, calculations become much too slow and the velocity auto-correlation function is the preferred quantity. Both approaches are detailed below.

Velocity auto-correlation method

The calculation of the VDOS via the velocity auto-correlation function is applicable to all materials but loses information about the dispersion relation and the band structure. The idea behind this method is that the VDOS is the Fourier transform of the velocity auto-correlation function.[300]

The velocity auto-correlation function Ξ is defined as[228]

$$\Xi(t) = \frac{\left\langle \sum_{i=1}^{N} m_i \mathbf{v}_i(t)\cdot\mathbf{v}_i(0) \right\rangle}{\left\langle \sum_{i=1}^{N} m_i \mathbf{v}_i^2(0) \right\rangle} = \left\langle \sum_{i=1}^{N} m_i \mathbf{v}_i(t)\cdot\mathbf{v}_i(0) \right\rangle \Big/ Nk_\mathrm{B}T, \tag{2.42}$$

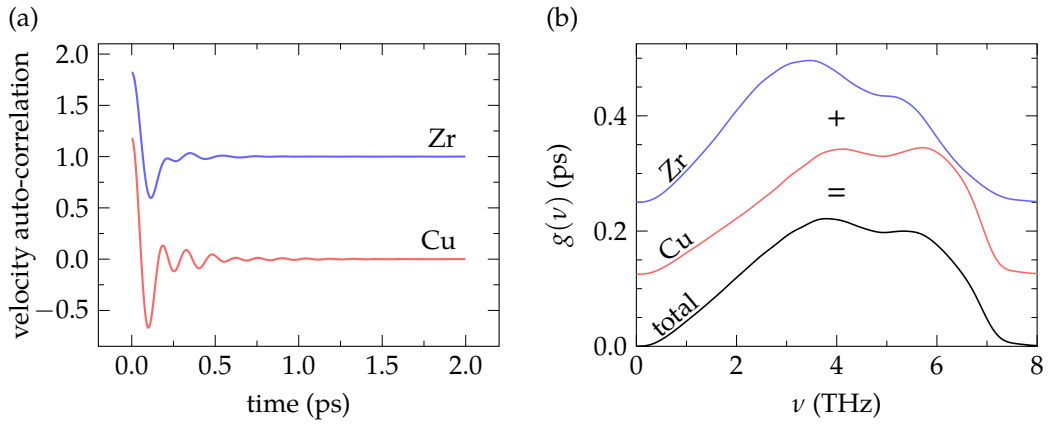

FIGURE 2.8: Calculation of the VDOS from velocity auto-correlation data. (a) Example velocity auto-correlation functions for a $Cu_{64}Zr_{36}$ glass. The auto-correlation functions are divided by the number of atoms and the curve for zirconium is shifted by 1 in the y axis. (b) The partial and total VDOS resulting from a Fourier transform. The partial densities of states where also normalised.

with $v_i(t)$ being the velocity of particle i at time t, where the choice of $t = 0$ is arbitrary for a system in equilibrium. For multi-element systems, this can also be written as

$$\Xi(t) = \frac{\overset{\text{number of elements}}{\sum_{i=1}} m_i \left\langle \sum_{j=1}^{N_i} \mathbf{v}_j(t) \cdot \mathbf{v}_j(0) \right\rangle}{N k_\mathrm{B} T} = \frac{\overset{\text{number of elements}}{\sum_{i=1}} m_i \xi_i(t)}{N k_\mathrm{B} T}, \tag{2.43}$$

where ξ_i is a partial auto-correlation function without normalisation for element i. This is useful, as it allows the calculation of partial densities of states while still allowing the later summation to the complete VDOS. This works by rewriting the Fourier transform as follows:

$$\begin{aligned} g(\omega) &= \int_{-\infty}^{+\infty} \Xi(t) \mathrm{e}^{-\mathrm{i}\omega t} \mathrm{d}t = \int_{-\infty}^{+\infty} \frac{\sum_i m_i \xi_i(t)}{N k_\mathrm{B} T} \mathrm{e}^{-\mathrm{i}\omega t} \mathrm{d}t \\ &= \sum_i \frac{m_i}{N k_\mathrm{B} T} \int_{-\infty}^{+\infty} \xi_i(t) \mathrm{e}^{-\mathrm{i}\omega t} \mathrm{d}t = \sum_i \frac{N_i m_i}{N k_\mathrm{B} T} g_i(\omega), \end{aligned} \tag{2.44}$$

where g_i are partial densities of states. Those are normalised to $\int g_i(\omega) \mathrm{d}\omega = 1$, wherefore the number of atoms N_i contributing to g_i re-appears in the last term. An example of a total VDOS calculated from partial densities of states is shown in Fig. 2.8. The partial VDOS can not only be calculated for different atomic species but also simply for a subset of atoms of interest, for example for atoms in a shear band.

In practice, a discrete Fourier transform—usually FFT—is used. The noise in the data can be reduced by averaging several, independently-calculated velocity auto-

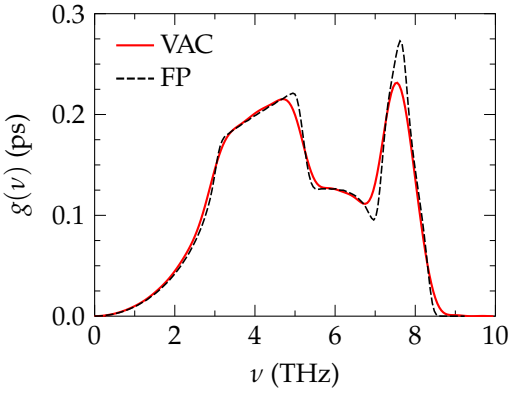

FIGURE 2.9: VDOS of fcc copper calculated with the frozen-phonon method (FP) and the Fourier transform of the velocity auto-correlation function (VAC). The results from the frozen-phonon calculations are much sharper and the method should be preferred if it is applicable.

correlation functions first. The long "tail" of Ξ should be cut to avoid spurious oscillations after the Fourier transform and zero-padding should be used to increase the resolution of the Fourier transformed data. In general, the normalisation $\int g(\omega)\mathrm{d}\omega = 1$ is assured by the formulas given above, but in practice it is easier to drop the factor $1/Nk_\mathrm{B}T$ and normalise afterwards.

Frozen-phonon method

The frozen-phonon method is based on the idea that the displacement of a single atom in a supercell introduces forces acting on all other atoms in the cell, which depend on the harmonic force constant matrix.[301–304] By choosing appropriate displacements based on the crystal symmetry, the dynamical matrix can be derived from the force constant matrix with a small amount of force calculations. This method is implemented in the free software package PHONOPY.[305] PHONOPY produces the supercells with displaced atoms, the forces on the atoms are then calculated using LAMMPS with the appropriate potential, and the VDOS is finally calculated again by PHONOPY.

If the frozen-phonon method can be used, it yields better results than the Fourier transform of the velocity auto-correlation function. The reason is that the Fourier transform smears out sharp features like van Hove singularities (cf. Fig. 2.9). In the few cases were a crystalline VDOS is needed, we therefore prefer the frozen-phonon method.

2.8.3 *Thermodynamic properties and the harmonic approximation*

Properties such as the free energy or the heat capacity can be derived from the VDOS using the harmonic or the quasi-harmonic approximation. The harmonic approximation assumes a system of harmonic oscillators and derives relations between the frequency of these oscillators and various thermodynamic properties.[306] This approximation is only valid for low temperatures, because all solids have anharmonic potentials. This can be adjusted by using the quasi-harmonic approximation, which

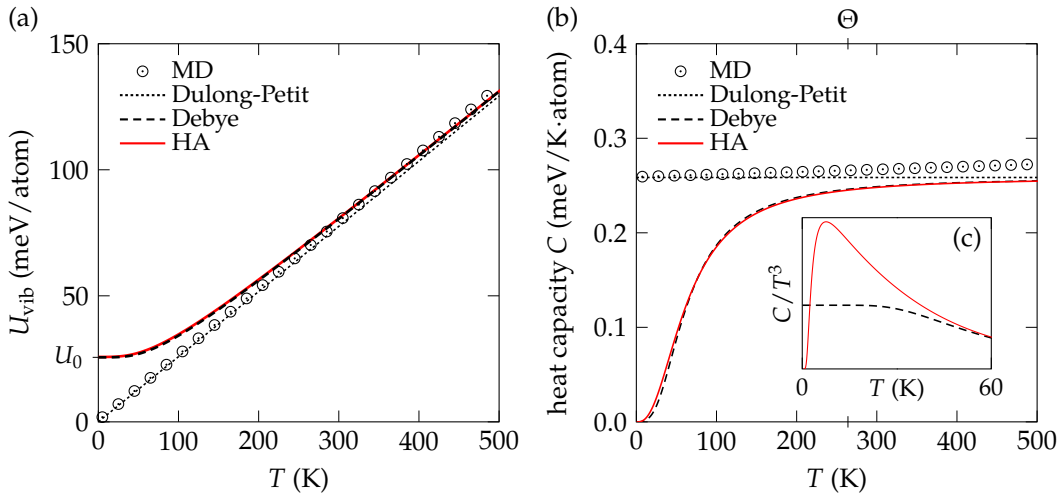

FIGURE 2.10: Comparison of different models for internal energy (a) and heat capacity (b) of a $Cu_{64}Zr_{36}$ glass. The Debye temperature Θ was extracted from U_0 of the harmonic approximation (HA). The MD simulation is a classical system and therefore follows the Dulong–Petit $C = 3Nk_B T$ law. The excess at higher temperatures is an effect of the anharmonic contributions that are included in none of the three other models. The Debye model correctly includes quantum-mechanical effects, but fails to capture the boson peak because of its simplistic model for the phonon density of states. A reasonable method to obtain this peak is the harmonic approximation using a density of states obtained from MD. This can be seen in (c), where the heat capacity divided by T^3 is plotted, so that the low temperature Debye model is constant, while the harmonic approximation reveals the boson peak.

assumes that the anharmonic effects are limited to a thermal expansion.[307] The effect of this expansion can be included by measuring the VDOS for different volumes close to the ground-state value, calculating free energies as functions of temperature for all volumes, and finding a minimum path of the free energy in V, T space. We are mostly interested in low-temperature heat capacities and therefore stay with the simpler harmonic approximation.

In the harmonic approximation, the internal energy U, the free energy F, and the heat capacity C are given by:[306]

$$F = 3Nk_B T \int_0^\infty \ln\left[2\sinh\left(\frac{1}{2}\frac{h\nu}{k_B T}\right)\right] g(\nu)\mathrm{d}\nu \tag{2.45}$$

$$U = \frac{3}{2}N \int_0^\infty h\nu \coth\left(\frac{1}{2}\frac{h\nu}{k_B T}\right) g(\nu)\mathrm{d}\nu \tag{2.46}$$

$$C = 3Nk_B \int_0^\infty \left(\frac{1}{2}\frac{h\nu}{k_B T}\right)^2 \sinh^{-2}\left(\frac{1}{2}\frac{h\nu}{k_B T}\right) g(\nu)\mathrm{d}\nu. \tag{2.47}$$

The factor 3 is due to the dimensionality of the physical system: There are 3 oscillators per atom. It should be noted that, due to the assumption of harmonic oscillators, it is $C = C_V = C_p$. This is again a reasonable approximation at low temperatures only.

One could ask why the heat capacity is not simply calculated from MD. It is $U = \langle E_{\text{tot}} \rangle$, and the total energy is available from simulation. The heat capacity would then simply be

$$C_V = \left(\frac{\partial U}{\partial T} \right)_V . \tag{2.48}$$

The reason is illustrated in Fig. 2.10, which compares different models of the heat capacity for a $Cu_{64}Zr_{36}$ glass. MD simulations implement a classical Newtonian system and do not include quantum effects; all vibrational modes are active at all temperatures. The internal energy and heat capacity extracted from MD resemble therefore the results predicted by Dulong and Petit.[299] The only difference is that anharmonic effects can be observed at high temperatures. The harmonic approximation using a VDOS calculated for the glass, as well as the Debye model with a Debye temperature extracted from the zero-point energy, predict the typical shape due to quantum effects. The shortcomings of the Debye model are apparent in Fig. 2.10 (c), which shows the boson peak in the heat capacity calculated by the harmonic approximation compared with the Debye model. The latter assumes a simplified shape of the VDOS and cannot capture the anomalies present in the low-temperature heat capacity of many materials. In cases where a low-temperature heat capacity is needed, we therefore use the harmonic approximation.

3 EVALUATION OF INTERATOMIC POTENTIALS

As described in Sec. 2.2, the interatomic potential is the crucial component in MD simulations. If the model for the interatomic forces is incorrect, the results obtained in the simulation are unreliable. While perfect accuracy is impossible—mainly because computationally efficient schemes need to make approximations—it is important to know where a given potential succeeds and where it fails. Thus, we first introduce the available EAM-type potentials for Cu–Zr alloys below, and compare some important materials properties as predicted by these potentials afterwards.

3.1 PARAMETRISATION BY MENDELEV ET AL.

Primarily, we use a Finnis–Sinclair-type potential by Mendelev and colleagues[124] which is an improved version of their earlier potential.[308] This potential was first fitted to the lattice parameters and formation energies of several Cu, Zr, and Cu–Zr structures. Afterwards, the cross-terms were improved by fitting to liquid density, mixing enthalpy, and the RDF of $Cu_{64.5}Zr_{35.5}$. The updated potential exhibits a reasonable glass transition temperature of around 800 K and features a better reproduction of the experimental RDF. Our testing showed that this potential can be used with a timestep of $\delta t = 2\,\text{fs}$ which we employ throughout this thesis. From here on, this potential will simply be called the "Mendelev potential".

3.2 PARAMETRISATION BY WARD ET AL.

The potential by Ward *et al.* is also a Finnis–Sinclair-type potential, for which the elemental terms were taken from Ref. 309. The cross-terms were automatically fitted to several Cu–Zr compounds.[310] This leads to a lower quality for the cross-terms, but we expect a more reasonable description of the pure elements. For this reason, we additionally employ this potential in cases where copper phases play a role. This potential is also used with $\delta t = 2\,\text{fs}$ in this thesis. From here on, this potential will simply be called the "Ward potential".

3.3 PARAMETRISATION BY CHENG ET AL.

The potential by Cheng, Ma, and Sheng[311] is an EAM potential that was fitted to ab-intio MD simulations of several compounds. Our testing showed that the timestep needs to be reduced to 1 fs for this potential, otherwise problems will occur particu-

larly in the interface between different phases. As implemented in LAMMPS and due to a lower cutoff value, this potential uses less computing time than the other two potentials depending on the specific supercomputer architecture.

3.4 COMPARISON

3.4.1 *Copper–zirconium glass*

As a first step, we prepared metallic glass samples for all three potentials. The samples consist of 504 864 atoms, leading to a final size of around $20 \times 20 \times 20\,\mathrm{nm}^3$ at 50 K. For this, we quenched the material from the melt with 10^{10} K/s, a cooling rate that has been shown to be sufficiently slow to produce realistic glass structures.[50–53] Figure 3.1 shows the atomic volume plotted over the temperature. The glass transition has been identified by analysis of the RDF: A split of the second peak is a signature of the glass and is not observed in the liquid.[53,312] This does not give a clear transition temperature, but all potentials exhibit a T_g between 800 K and 900 K. The literature value of 787 K is slightly below that,[25,313] which can be attributed to the very fast cooling rate in the simulation. Instead of a bend, the glass transition looks more like a smeared-out step, independent of the potential. This was observed before[51,53] and has been connected to the formation of icosahedral units.[314] It seems reasonable to assume that the high cooling rate keeps the system out of equilibrium around T_g, whereas the icosahedra have more time to form in the experiment, leading to a smoother curve.

As a next step, we calculated 0 K properties of the material with molecular statics simulations. The cohesive energy and density—directly obtainable from simulation output—are listed in Tab. 3.1. The density is higher when using the Ward potential, but seems to agree better with the literature value.[315] Although this value was measured at 300 K, the thermal expansion in this range is not so high that it invalidates a

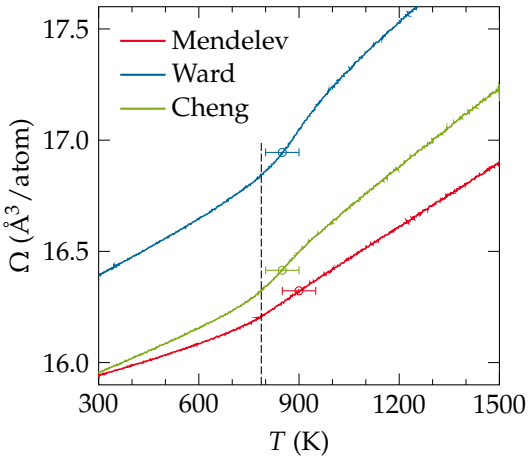

FIGURE 3.1: Quenching curves for $Cu_{64}Zr_{36}$. The dashed line indicates a typical experimental glass transition temperature of 787 K.[25,313] The error bars indicate an estimation of the glass transition temperature in simulation obtained by observing a split of the second peak in the RDF.[53,312]

TABLE 3.1: Properties of a $Cu_{64}Zr_{36}$ glass calculated with the three different potentials at 0 K. Listed are the cohesive energy E_{coh}, the number density ρ_n, the density ρ, the bulk ($\mathcal{K}$), Young's ($\mathcal{E}$), and shear ($\mathcal{G}$) moduli, Poisson's ratio $\nu_{Poisson}$, and the components of the stiffness tensor c_{ij}. Literature data was obtained at room temperature.

	Mendelev	Ward	Cheng	Literature		References
E_{coh}	−4.483	−4.563	−4.609		eV/atom	
ρ_n	63.17	61.87	63.39		nm^{-3}	
ρ	7.710	7.553	7.738	7.53	g/cm^3	[315]
$\mathcal{K}$	131	123	121	104	GPa	[313]
$\mathcal{E}$	76	140	74	86–97, 116	GPa	[25, 313, 317, 318]
$\mathcal{G}$	27	53	26	34–36	GPa	[313, 318]
$\nu_{Poisson}$	0.40	0.31	0.40	0.33–0.35		[313, 318]
c_{11}	167	194	156		GPa	
c_{12}	113	87	103		GPa	
c_{44}	27	53	27		GPa	

rough comparison. We further calculated the elastic constants of the glasses. We started by obtaining the stiffness tensor of the systems using a script distributed with LAMMPS.[260] This script simply exploits Hooke's law by performing small deformations of the initial structure and calculating the resulting stresses in a molecular statics run. The resulting stiffness tensor consists of two independent components, c_{11} and c_{12}, and $c_{44} = \frac{1}{2}(c_{11} - c_{12})$, which is typical for isotropic materials.[281] From these, we can obtain more commonly used values, such as the bulk modulus $\mathcal{K}$, the Young's modulus $\mathcal{E}$, the shear modulus $\mathcal{G}$, and Poisson's ratio $\nu_{Poisson}$. The relations are:[281]

$$\mathcal{K} = \frac{1}{3}\left(c_{11} + 2c_{12}\right), \tag{3.1}$$

$$\mathcal{E} = \frac{c_{11}^2 + c_{11}c_{12} - 2c_{12}^2}{c_{11} + c_{12}}, \tag{3.2}$$

$$\mathcal{G} = \frac{3\mathcal{K}\mathcal{E}}{9\mathcal{K} - \mathcal{E}}, \text{ and} \tag{3.3}$$

$$\nu_{Poisson} = \frac{3\mathcal{K} - \mathcal{E}}{6\mathcal{K}}. \tag{3.4}$$

The comparison with the literature values in Tab. 3.1 reveals that all three glasses are slightly too stiff in hydrostatic compression, although the Young's and shear modulus are roughly in the right order of magnitude. The glass obtained with the Ward potential is much too stiff.

Finally, the simulation provides data beyond what is accessible in experiment, and local structure can be assessed by Voronoi tessellation. The results of this analysis are plotted in Fig. 3.2. All potentials correctly reproduce the high fraction of copper-

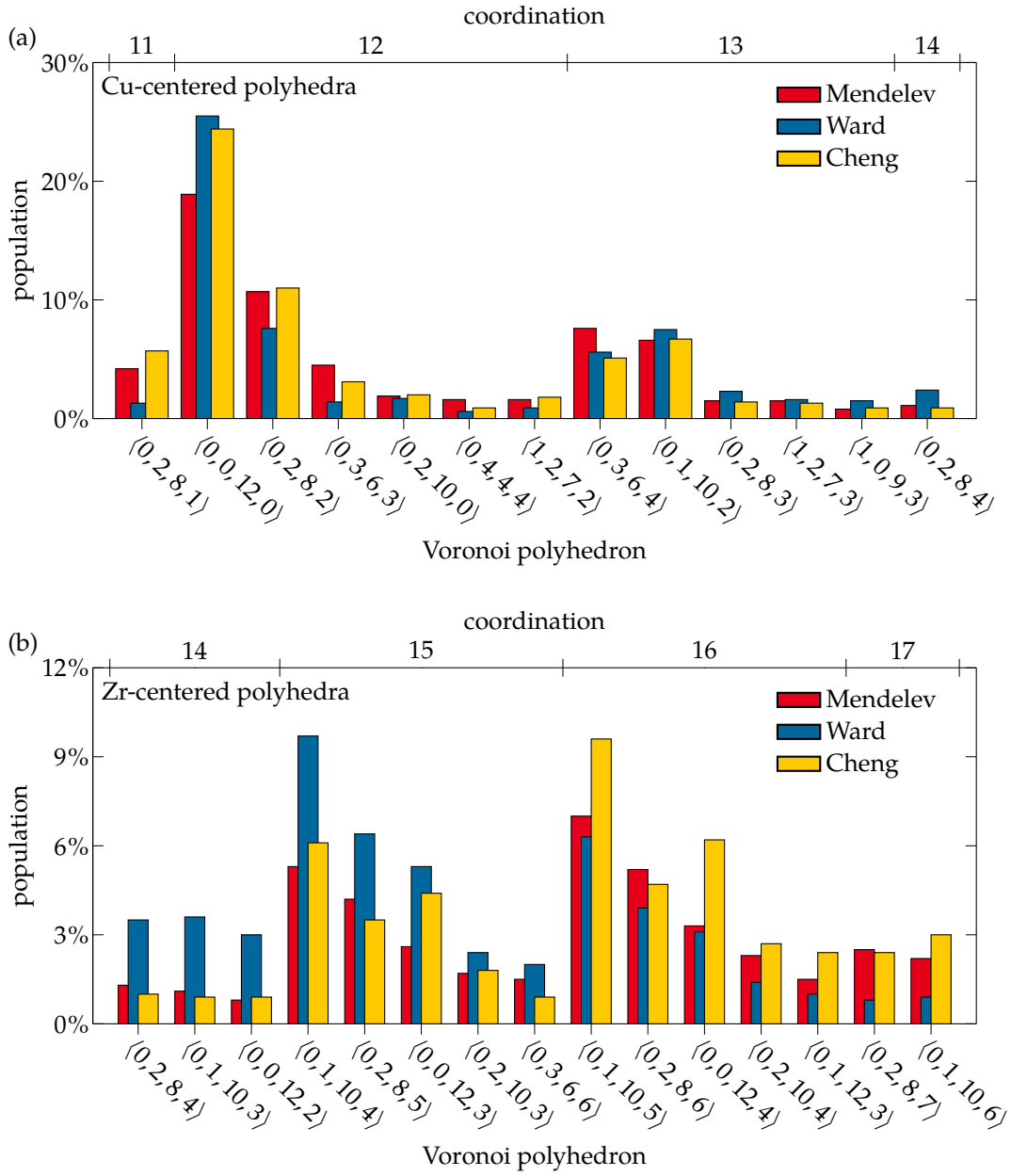

FIGURE 3.2: Voronoi statistics for the different EAM potentials. (a) The copper-centred polyhedra show the typical dominance of the $\langle 0,0,12,0\rangle$ polyhedra. (b) The potentials differ more significantly in the statistics of zirconium-centred polyhedra, although as dominance of $\langle 0,1,10,4\rangle$ and $\langle 0,1,10,5\rangle$ polyhedra is a common feature. In all cases, five-folded bonds (the third number in the Voronoi index notation) prevail in the glass structure.

TABLE 3.2: Properties of Cu in the fcc structure for the different potentials at 0 K. Listed are the lattice constant a, the cohesive energy E_{coh}, the bulk modulus $\mathcal{K}$, the Young's moduli ($\mathcal{E}$) along the $\langle 100 \rangle$ and $\langle 111 \rangle$ directions, and the components of the stiffness tensor c_{ij}. For all cubic metals except molybdenum, the Young's modulus should be maximal for $\langle 111 \rangle$,[281] which is not the case with the Ward potential. Literature values for the elastic constants are also 0 K values.

	Mendelev	Ward	Cheng	Literature		References
a	3.639	3.614	3.597	3.61	Å	[286]
E_{coh}	−3.283	−3.540	−3.541	−3.49	eV/atom	[286]
$\mathcal{K}$	145	245	151	142	GPa	[319]
$\mathcal{E}_{\langle 100 \rangle}$	70	354	91		GPa	
$\mathcal{E}_{\langle 111 \rangle}$	213	273	189		GPa	
c_{11}	178	432	194	176	GPa	[319]
c_{12}	129	151	129	125	GPa	[319]
c_{44}	85	104	73	82	GPa	[319]

centred icosahedral $\langle 0, 0, 12, 0 \rangle$ units (cf. Sec. 1.2). In terms of zirconium-centred polyhedra the potentials show more variation, with a tendency of the Ward potential to favour lower coordination numbers. Experimentally, the statistics of the different polyhedra are unknown and we therefore cannot judge the relative merit of the structures produced using the different potentials and simply provide the data here. As an aside: We noted in Sec. 1.2 that atoms in amorphous solids tend towards five-fold bonds, indicated by the third entry in the Voronoi notation. We can see in Fig. 3.2 that these five-fold bonds form the majority of all bonds.

3.4.2 *Copper*

In addition to the heterogeneous glass, we are also interested in the mechanical properties of crystal–glass composites. So, an evaluation of the crystalline phases is in order. We start with pure fcc copper. The lattice constant, cohesive energy, and elastic constants are listed in Tab. 3.2. The experimental lattice constant is reproduced well by all three potentials but the Mendelev potential underestimates the cohesive energy. Continuing to the elastic properties, we note that the relations of the elastic constant in cubic crystals are, of course, different than in isotropic materials. The bulk modulus is straightforward and the same as Eq. 3.1:

$$\mathcal{K} = \frac{1}{3}\left(c_{11} + 2c_{12}\right). \tag{3.1}$$

The Young's modulus of a single-crystal obviously depends on the loading axis,[281] in contrast to the isotropic case. We give the minimum and maximum values, which

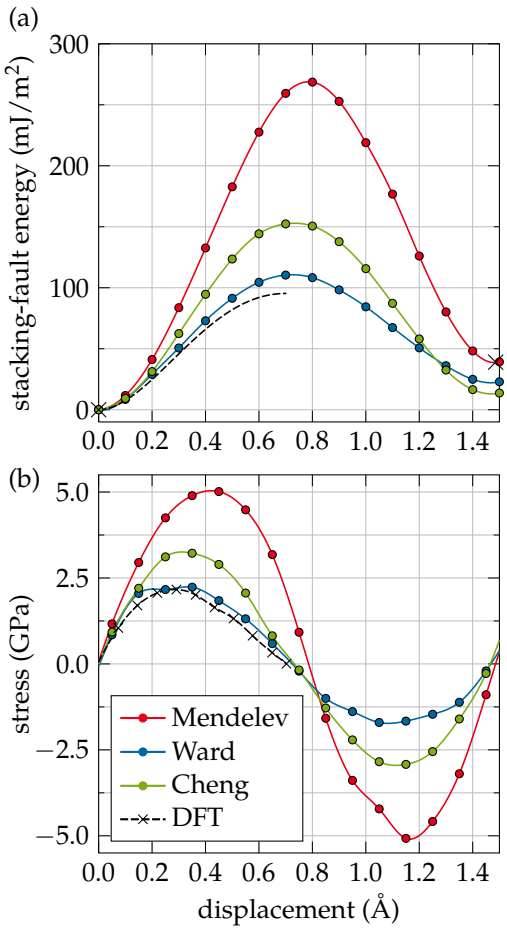

FIGURE 3.3: Generalised stacking-fault energy curves for copper. (a) A plot of the stacking-fault energy over the displacement shows that the Mendelev potential has a huge barrier to homogeneous dislocation nucleation. While the Cheng potential fares better, only the Ward potential is able to reproduce realistic values. (b) The stresses calculated via $\sigma = -\nabla E_{\text{pot}}/A$ exhibit the same trend. DFT data for the stress curve are from Ref. 316 and the corresponding stacking-fault energies are approximated by numerical integration of the stress data. The MD data for the Ward and Mendelev potentials was first published in Ref. 338.

occur in directions $\langle 100 \rangle$ and $\langle 111 \rangle$. For convenience, we use the components of the compliance tensor,[281]

$$s_{11} = \frac{c_{11} + c_{12}}{c_{11}^2 + c_{11}c_{12} - 2c_{12}^2}, \quad s_{12} = \frac{-c_{12}}{c_{11}^2 + c_{11}c_{12} - 2c_{12}^2}, \quad \text{and} \quad s_{44} = \frac{1}{c_{44}}. \tag{3.5}$$

With this, we can calculate[281]

$$\mathcal{E}_{\langle 100 \rangle} = \frac{1}{s_{11}} \qquad \text{and} \qquad \mathcal{E}_{\langle 111 \rangle} = \frac{1}{s_{11} - \frac{2}{3}\left(s_{11} - s_{12} - \frac{1}{2}s_{44}\right)}. \tag{3.6}$$

A subsequent comparison with literature shows that the Ward potential has an extremely high stiffness for copper, while the other two potentials are reasonable. Additionally, it is $\mathcal{E}_{\langle 100 \rangle} > \mathcal{E}_{\langle 111 \rangle}$ in the Ward potential, which—for the cubic metals—should only be the case in molybdenum.[281]

Still, the property of interest is mostly the plastic deformation. A figure of merit for homogeneous dislocation nucleation is the unstable stacking fault energy and the resulting critical stress. One can obtain a generalised stacking-fault energy curve from

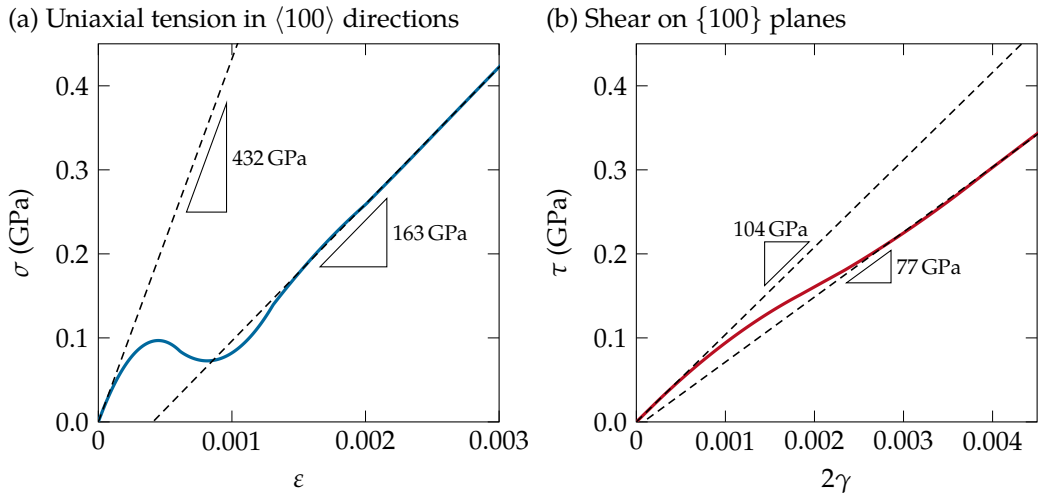

FIGURE 3.4: Elasticity of copper simulated with the Ward potential. The two subfigures show an anomaly in the potential at small strains: The elasticity is not linear and the system is very stiff.

simulation and Ogata *et al.* calculated this for copper using density-functional theory (DFT).[316] Using MD, we employed the same methodology in which two halves of a single crystal are displaced relative to each other on a {111} plane in the corresponding ⟨112⟩ direction. The atoms were allowed to relax only perpendicular to the displacement plane. The results are shown in Fig. 3.3. Clearly, the best fit is obtained by the Ward potential, while the critical stresses in the other potentials are much too high.

This seems to contradict the finding that the Ward potential is much stiffer than the other two potentials. A look at the elastic response of a copper crystal over a range of strains (Fig. 3.4) resolves this contradiction: The elasticity at low strains is not linear, but varies in stiffness. The script used to obtain the stiffness tensor employs very low strains, sampling the very stiff initial regions of the curves. Relevant for the dislocation nucleation are the values at higher strains, though. While the mechanical behaviour of the potential is unphysical in the limit of low strains, we still evaluate it for the limited use case of plastically deformable copper precipitates.

In a real composite system, the dislocation nucleation will not be homogeneous, but will most likely be initiated at the interface. A measure for heterogeneous dislocation nucleation would thus be useful. We attempted a rough estimate by shearing a copper cylinder of diameter 10 nm. For this, we fixed the atoms on both ends of the cylinder and moved the upper fixed atoms with a constant velocity. We kept the system at a constant temperature of 50 K, which is also the temperature range in which we conduct most deformation tests of the glasses. The geometry, also depicted in Fig. 3.5 (b), leads to a shear deformation on the (111) plane of the fcc crystal in [110] direction. This is the "softest" direction and gives the lower bound for dislocation

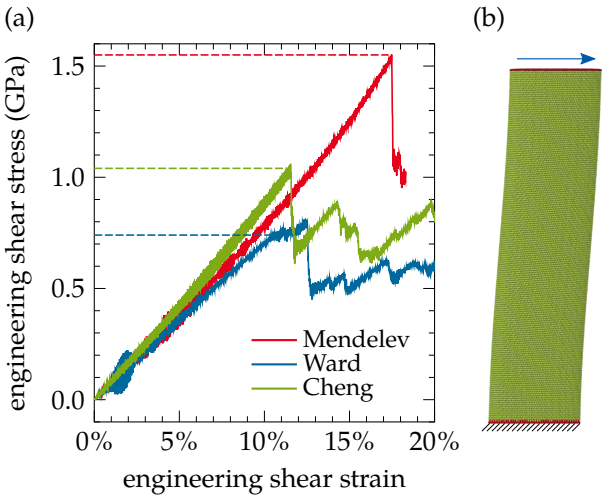

FIGURE 3.5: Shear tests on copper nanowire with a diameter of 10 nm with different potentials. (a) Shear stress–strain curves, with dashed lines indicating the yield shear stress. (b) Simulation setup: The wire is sheared in [110] direction of the fcc crystal structure on the (111) plane. The red atoms are fixed and the atoms on the top are shifted with a constant velocity to shear the nanowire. Data for the Ward and Mendelev potentials was first published in Ref. 338.

nucleation. The resulting stress–strain curves are shown in Fig. 3.5 (a). The fluctuations at low shear strains when using the Ward potential are most likely due to the aforementioned anomalies of the potential. The yield shear stresses are

1.55 GPa	for Mendelev,	(3.7)
0.74 GPa	for Ward, and	(3.8)
1.04 GPa	for Cheng.	(3.9)

Typical yield stresses for metallic glasses are in the range of gigapascals. If we assume that the shear band propagates on a plane tilted 45° towards the tensile axis it seems likely that the resolved shear stress available at yield to deform a copper precipitate is only sufficient when using the Ward potential.

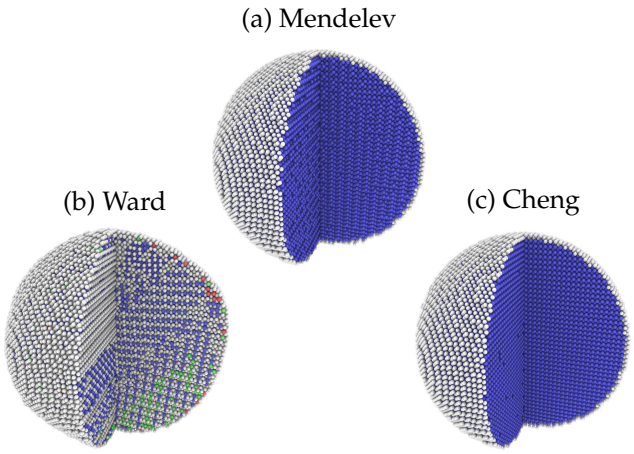

FIGURE 3.6: Nanoparticle with a diameter of 15 nm relaxed at 50 K for 100 ps with different potentials. Colour coding shows CNA, blue is bcc (= B2), green is fcc, white is unidentified. The B2 crystal collapses when simulated with the Ward potential.

TABLE 3.3: Properties of CuZr in the B2 structure for the different potentials at 0 K. Listed are the lattice constant a, the cohesive energy E_{coh}, the bulk modulus $\mathcal{K}$, the Young's moduli ($\mathcal{E}$) along the $\langle 100 \rangle$ and $\langle 111 \rangle$ directions, and the components of the stiffness tensor c_{ij}. In the Mendelev potential the B2 structure is unstable in favour of a slightly tetragonal form, for which we also list the lattice constant c and additional elastic constants. In the Ward potential the B2 structure is unstable, therefore these results are not listed here. Literature values for elasticity and cohesive energy are from ground-state calculations and are therefore also 0 K values. The references for the lattice constant include room temperature measurements as well as ground-state calculations.

	Mendelev	Cheng	Literature		References
a	3.158	3.256	3.26–3.28	Å	[320–322]
c	3.380			Å	
c/a	1.07				
E_{coh}	−5.030	−5.076	−4.975	eV/atom	[321]
$\mathcal{K}$	133	108	120	GPa	[321]
$\mathcal{E}_{(100)}$	37	32		GPa	
$\mathcal{E}_{(001)}$	140			GPa	
$\mathcal{E}_{\langle 111 \rangle}$	279	128		GPa	
c_{11}	146	123	138	GPa	[322]
c_{33}	243			GPa	
c_{12}	125	101	113	GPa	[322]
c_{13}	118			GPa	
c_{44}	71	49	44	GPa	[322]
c_{66}	80			GPa	

3.4.3 *Copper–zirconium crystal phase*

In Cu–Zr-based metallic glasses, precipitates appear commonly in B2 or B19′ phases during quenching or after an annealing procedure.[119,120] We will use the B2 structure, which commonly appears after annealing, while the B19′ phase is often the result of a stress-induced martensitic transformation. A first test, detailed in Fig. 3.6, already reveals that the B2 phase is not stable when simulated with the Ward potential. All further investigations are therefore only performed for the other two potentials. We again calculated lattice constants, cohesive energy, as well as elastic constants. Here, we found that the B2 structure is also unstable in the Mendelev potential in favour of a slightly tetragonal version of the structure. In the end, this is no impediment for simulations with composites, as the difference in plastic response should be minimal. For tetragonal crystals, the calculation of elastic constants is more involved than for cubic crystals. We start by using the compliance tensor for notational convenience:[281]

$$s_{11} = \frac{c_{13}^2 - c_{11}c_{33}}{2(c_{11} - c_{12})c_{13}^2 - (c_{11}^2 - c_{12}^2)c_{33}} \qquad s_{33} = \frac{-(c_{11} + c_{12})}{2c_{13}^2 - (c_{11} + c_{12})c_{33}} \tag{3.10}$$

$$s_{12} = \frac{c_{13}^2 - c_{12}c_{33}}{2(c_{11} - c_{12})c_{13}^2 - (c_{11}^2 - c_{12}^2)c_{33}} \qquad s_{13} = \frac{c_{13}}{2c_{13}^2 - (c_{11} + c_{12})c_{33}} \tag{3.11}$$

$$s_{44} = \frac{1}{c_{44}} \qquad s_{66} = \frac{1}{c_{66}}. \tag{3.12}$$

From this, we obtain

$$\mathcal{K} = \frac{1}{2s_{11} + s_{33} + 2(s_{12} + 2s_{13})}, \text{ and} \tag{3.13}$$

$$\mathcal{E}_{(100)} = \frac{1}{s_{11}}, \quad \mathcal{E}_{(001)} = \frac{1}{s_{33}}, \quad \mathcal{E}_{\langle 111\rangle} = \frac{9}{2s_{11} + s_{33} + 2s_{44} + s_{66} + 2(s_{12} + 2s_{13})}. \tag{3.14}$$

A comparison to the literature in Tab. 3.3 shows a relatively good agreement, although the description of the structure by the Mendelev potential obviously suffers from the transition to the tetragonal phase.

3.4.4 *Conclusions*

We can conclude that the Mendelev and Cheng potentials are both viable candidates to simulate metallic glasses. We estimate that the properties of the metallic glass are reproduced slightly better by the Mendelev potential. While the B2 structure is only stable in the Cheng potential, we conclude that the slight tetragonal distortion in the Mendelev potential is no hindrance to simulate composites. Both potentials have a much too high critical stress for dislocation nucleation in copper. Here, the Ward potential produces sufficiently "soft" copper precipitates, although it has other deficiencies as pointed out above. Given that, we will mainly use the Mendelev potential and resort to the Ward potential in cases where a plastically deformable copper phase is needed. In one case (Chap. 7) we resorted to using the Cheng potential because of its better performance.

Part II

STRUCTURE, THERMODYNAMICS, AND VIBRATIONAL PROPERTIES

The second part of this thesis is concerned with phenomena that, at first glance, do not seem to be related to plasticity. In the first two chapters, we discuss the amorphisation of thin copper layers in metallic glasses, as well as the growth of crystallites in a $Cu_{64}Zr_{36}$ glass. While these effects themselves are of interest, they also serve as an examination of the kind of systems that we will use for deformation testing in Part III of the thesis. The final chapter of Part II deals with the vibrational properties of amorphous metals, i.e., properties which sample mostly the elastic response of the system. As discussed earlier in Sec. 1.8.1, though, this elastic response of the system may be connected to the plastic response of the glass and is therefore of more than theoretical interest.

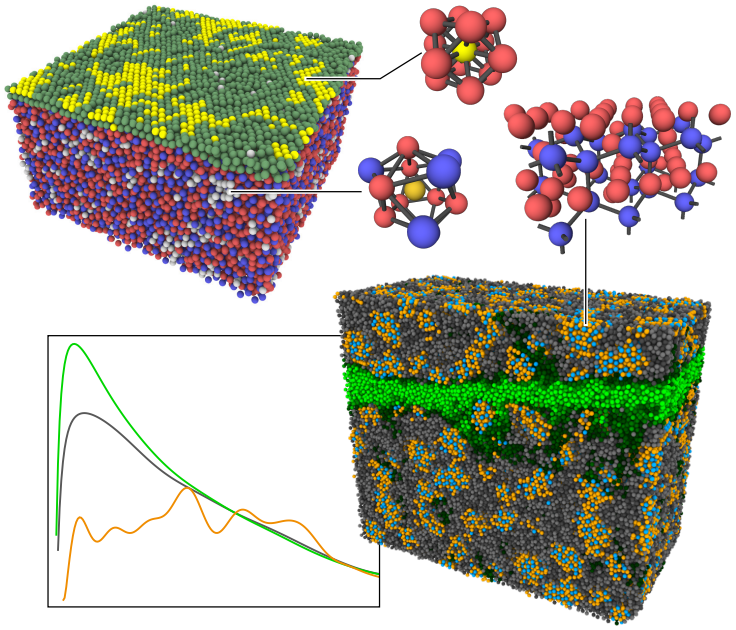

An example of solid-state amorphisation is shown in the top row together with structural motifs that occur in both amorphous phases. These structures also play a role in the elastic and vibrational response of amorphous systems: The bottom row depicts a crystal–glass composite containing a shear band and the corresponding vibrational spectra of different parts of the sample.

4

SOLID-STATE AMORPHISATION OF COPPER EMBEDDED IN A METALLIC GLASS

The results in Sec. 4.1 of this chapter were first published in Ref. 323.

Metals form crystalline phases in equilibrium, whereas amorphous metals are usually metastable and only kinetically trapped in the disordered state. Especially in the case of elemental metals, one would expect the crystalline phase to be stable even if it is part of a metallic-glass-based composite. The thermodynamically stable states of thin metal films are crystalline phases, even in contact with a variety of substrates.[67–71] Energetically-driven amorphisation is observed, but only at high-angle, high-energy grain boundaries[72] and at heterogeneous interfaces.[76–78] In the latter case, the effect is called solid-state amorphisation (SSA). These amorphous phases are stabilised by the very unfavourable lattice mismatch between neighbouring crystallites, which means that such an effect is therefore not expected for metals embedded in a glass matrix. However, Ghafari *et al.* recently demonstrated that iron nanolayers embedded in a $Co_{75}Fe_{12}B_{13}$ glass matrix become amorphous if their thickness is below five monolayers (MLs),[83] while elemental metal layers of comparable thickness are usually crystalline.[69–71] As the nanolayers were sputtered onto the glass, one could argue that the amorphisation is a purely kinetic effect and the layers would eventually re-crystallise. The thermodynamics of this composite system are hard to evaluate experimentally but are readily accessible to atomistic computer simulations. We therefore investigated if metal films in metallic glass matrices can undergo SSA, or if the lack of lattice mismatch makes this case another example of a kinetically driven transformation. After that, we also check if these results can be transferred to spherical precipitates. The size dependencies derived from this are useful to evaluate the feasibility of preparing crystal–glass composite models with nanocrystallites, and to predict their behaviour.

4.1 COPPER NANOLAYERS

Since there is no reliable iron alloy potential which can also be used to model a metallic glass, we opted to stay with the Cu–Zr system instead of directly recreating the experiment by Ghafari and colleagues. In our setup, we used $Cu_{64}Zr_{36}$ glass samples with a size of $10 \times 10 \times 10\,\mathrm{nm}^3$ (63 108 atoms) and inserted crystalline copper nanolayers of various thicknesses. By starting from the crystalline state, we aim to avoid

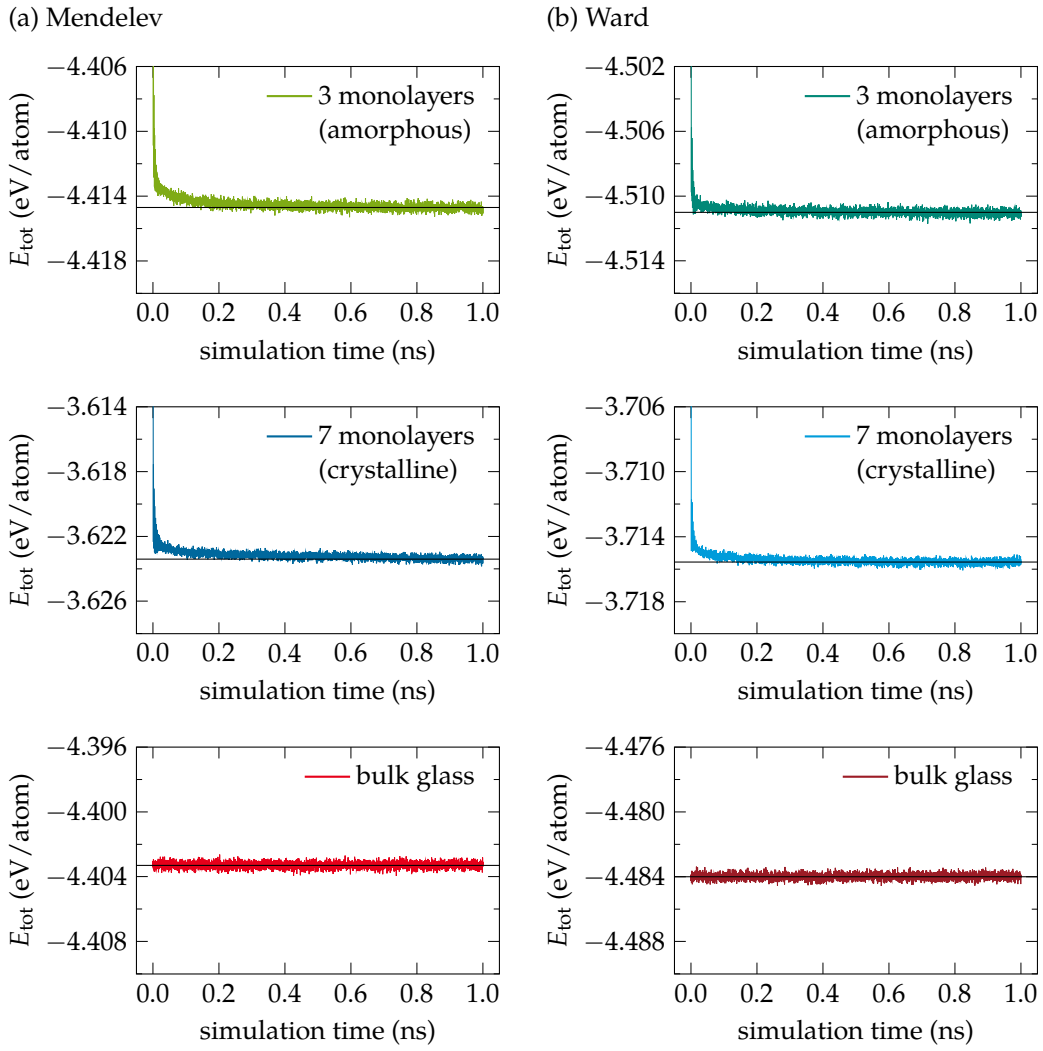

FIGURE 4.1: Equilibration of different multilayer systems. The plots show the total energy over time for systems with amorphous and crystalline nanolayers, as well as for a bulk glass sample. After 1 ns, the samples are equilibrated for both potentials. The bulk glass sample without embedded crystalline phases exhibits a constant energy over the relevant simulation time. Adapted from Ref. 323, © *2015 American Physical Society.*

kinetically trapping the copper in the amorphous state. Instead, any phase transformation should be driven by the thermodynamics of the system.

We performed MD simulations with periodic boundary conditions at 300 K and the copper nanolayers were created with the appropriate equilibrium lattice constants. We used thicknesses between 2 MLs and 15 MLs, as well as (100), (110), and (111) surface orientations. To avoid stresses in the nanolayer, we scaled the x and y dimensions of the glasses to fit exactly to a multiple of the lattice constants of the nanolayers. We re-relaxed the glasses at 300 K with a barostat at ambient pressure

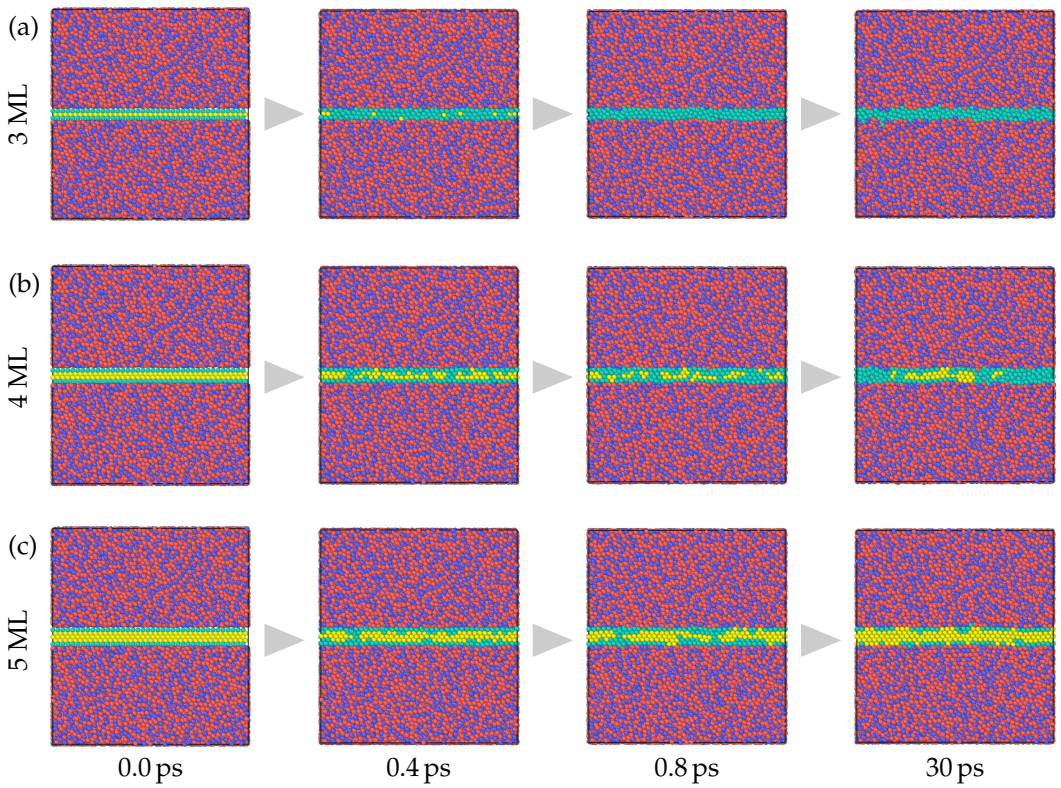

FIGURE 4.2: Evolution of copper nanolayers embedded in a $Cu_{64}Zr_{36}$ glass matrix. This figure depicts samples in which the initial surface orientation of the inserted fcc nanolayer was (100); other orientations exhibit comparable behaviour. The colour scheme indicates the results of the CNA, with copper atoms in the nanolayer coloured in yellow if they are on an fcc lattice and green otherwise. The atoms in the glass matrix are coloured red and blue for copper and zirconium, irrespective of their ordering. (a) A small layer with 3 ML thickness becomes amorphous almost immediately after insertion. (b) At 4 ML thickness, crystalline clusters remain, (c) while the layers stays completely crystalline at 5 ML thickness. Adapted from Ref. 323, © *2015 American Physical Society.*

in z direction for 1 ns. To ensure that the results obtained are independent of the potential, we performed all simulations with both the Mendelev[124] and the Ward[309,310] potential. The composites were then produced by cutting the glass at an arbitrary xy plane and inserting the nanolayer such that the distance between nanolayer and glass atoms was at least 1.5 Å. The composite systems were equilibrated for 1 ns, again with a barostat only in z direction as any lateral relaxation would be dominated by the glass matrix. Figure 4.1 shows that the systems were fully equilibrated at the end of the procedure and that the energy of the bulk glass is unchanged on the timescale of our simulations. The resulting formation of the interface was connected with a heat release due to the high potential energy of atoms with low distance. The possible consequences of this are discussed later in Sec. 4.1.3.

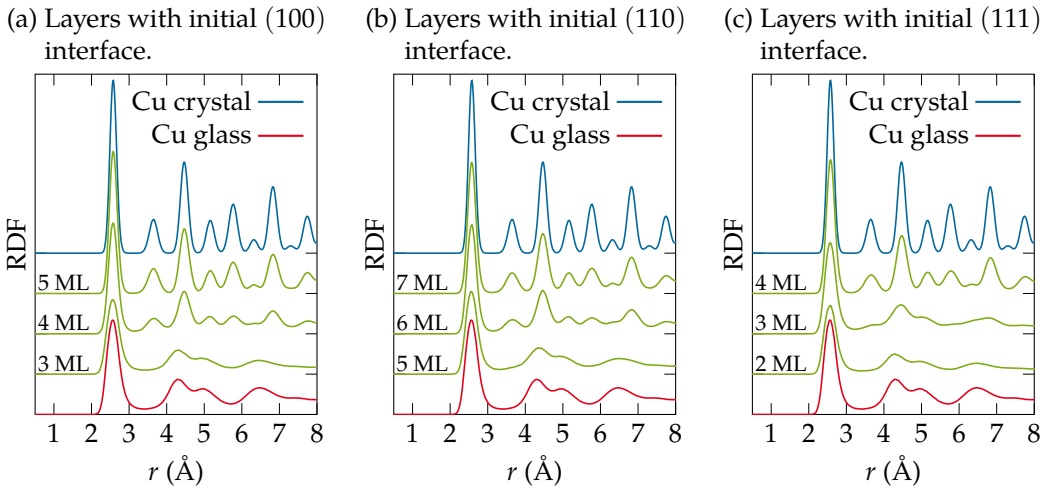

FIGURE 4.3: Radial distribution functions of the copper nanolayers simulated with the Mendelev potential. For every initial surface orientation of the copper layer, three systems around the critical thickness for amorphisation are shown and compared with reference bulk crystalline and glassy copper. Adapted from Ref. 323, © *2015 American Physical Society.*

We also created reference systems of crystalline and amorphous copper. The latter was quenched with very high rates from the melt at 2000 K. We found that the minimum cooling rates needed to avoid crystallisation are about 1 K/ps in case of the Mendelev potential and 25 K/ps in case of the Ward potential. Pure copper in the Ward potential seems to be a worse glass former, which explains the different cooling rates needed for the glass transition to occur. This is probably connected to the lower, but more realistic, cohesive energy of fcc copper in the Ward potential (see Tab. 3.2), which stabilises the crystalline phase.

4.1.1 *Simulation results*

Starting with the results obtained using the Mendelev potential, Fig. 4.2 shows the time evolution of three composite systems with different nanolayer thickness and the results of a common neighbour analysis (CNA). These specific examples had a (100) surface upon insertion. It can be seen that the thinnest layer amorphises after a short time. The nanolayer with a thickness of 4 MLs only partially amorphises, while the 5 ML layer stays crystalline, suggesting that there is indeed a critical thickness below which SSA occurs. The same phenomenon can be observed for the samples with initial (110) and (111) interfaces (not shown here). As an independent confirmation, we also analysed the RDFs of the composite systems, shown in Fig. 4.3 for the systems close to the transition thickness. The RDF is only calculated for the atoms in the nanolayer itself. By comparing the thin layers with the crystalline and amorphous copper reference systems, we can identify the critical thickness by the disappearance

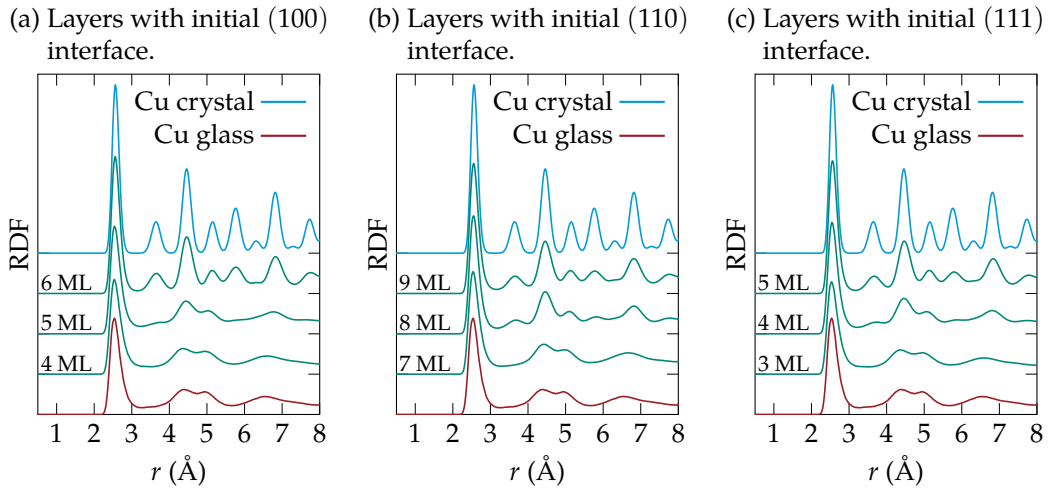

FIGURE 4.4: Radial distribution functions of the copper nanolayers simulated with the Ward potential. For every initial surface orientation of the copper layer, three systems around the critical thickness for amorphisation are shown and compared with reference bulk crystalline and glassy copper. Adapted from Ref. 323, © *2015 American Physical Society.*

of the second crystalline peak and the appearance of the typical double peak between 4 Å and 5 Å of the amorphous system. A mixed state occurs at 4, 6, and 3 ML thickness for initial interface orientations (100), (110), and (111), respectively. This state is characterised by an overlap of crystalline and amorphous features in the RDF. The crystalline nanolayers do not contain all features of the bulk crystal at large r, which is simply an effect of the finite size of the nanolayer.

The simulations with the Ward potential exhibit a qualitatively similar result: SSA occurs below a critical thickness and a mixed crystalline/amorphous state occurs around the critical thickness. RDFs are shown in Fig. 4.4 and agree with the CNA results which are omitted. In contrast to the Mendelev potential, the critical thickness is somewhat higher. The shape of the amorphous RDF is similar, with the first peak at around 2.5 Å in both cases. The second peak in the samples simulated with the Mendelev potential is more defined than with the Ward potential. This may indicate a stronger mid-range ordering in the layer.

All simulations agree that small, initially crystalline nanolayers of copper become amorphous when embedded into a $Cu_{64}Zr_{36}$ glass matrix. From this we can already exclude that the amorphous phase results simply from a deposition process that kinetically freezes the copper in a disordered state, as the layers were initially crystalline. Still, heat that is released during the formation of the interface may lead to a fast melt–quench process similar to the formation of a glass from the melt. In that case, the resulting state would be energetically unfavourable but kinetically frozen-in. It is therefore necessary to illuminate the thermodynamics of the system to determine if the amorphous phase is energetically favourable or not.

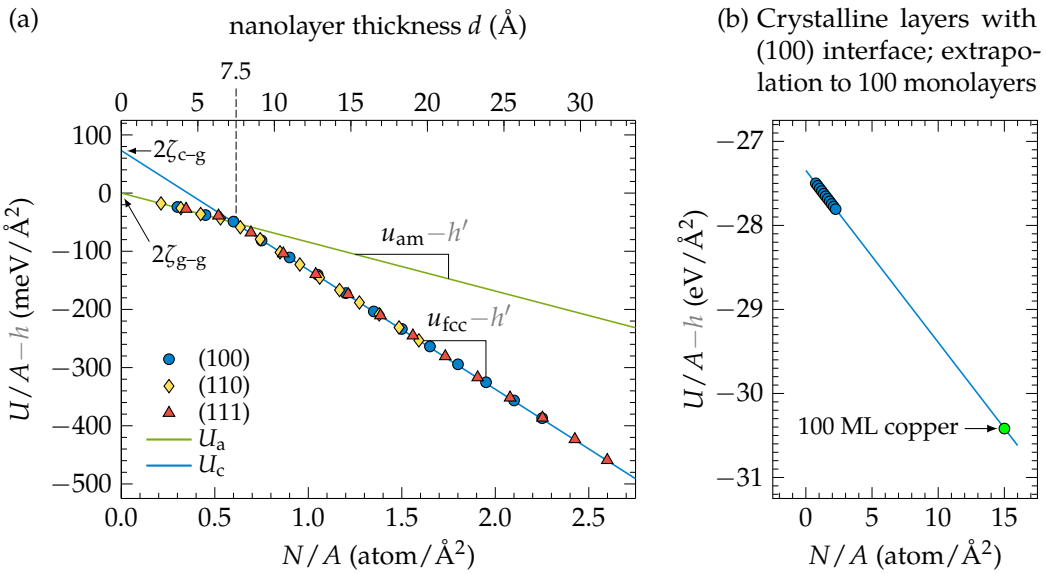

FIGURE 4.5: Dependence of the internal energy on the layer thickness of the composite systems modelled with the Mendelev potential. (a) Data points from simulations and fits of U_c and U_a. The total internal energy minus the energy of the glass matrix U_{MG} is plotted. Interface energies ζ and per-atom energies u can be extracted. (b) The total energy of the systems with crystalline nanolayers. The fit from (a) is extrapolated to a sample with 100 MLs of copper. For visualisation purposes a function $h = h' \cdot N/A$ with $h' = 3\,\text{eV}$ was subtracted in all plots to exaggerate the difference in slopes between U_c and U_a. Adapted from Ref. 323, © *2015 American Physical Society.*

4.1.2 *Thermodynamic model*

We consider, in a first approximation, a stress-free state in which the relevant thermodynamic potential is the Helmholtz free energy

$$F = U - TS. \tag{4.1}$$

The internal energy U is readily accessible from simulation data, while the entropy S cannot be directly derived from the available data. The entropy should consist mainly of a vibrational term, which is comparable in solids of the same composition; a chemical disorder term, which is zero for the single-element copper layer; and a structural term, which should favour the amorphous state. We postulate that the amorphisation in the current system is driven by the internal energy and note that the error made by omitting the TS term is in favour of the amorphisation. We will judge the applicability of this model by a comparison with simulation data.

The internal energy of a composite system, where the embedded nanolayer is crystalline, is then

$$U_c = U_{MG} + N u_{fcc} + 2A\zeta_{c\text{–}g}. \tag{4.2}$$

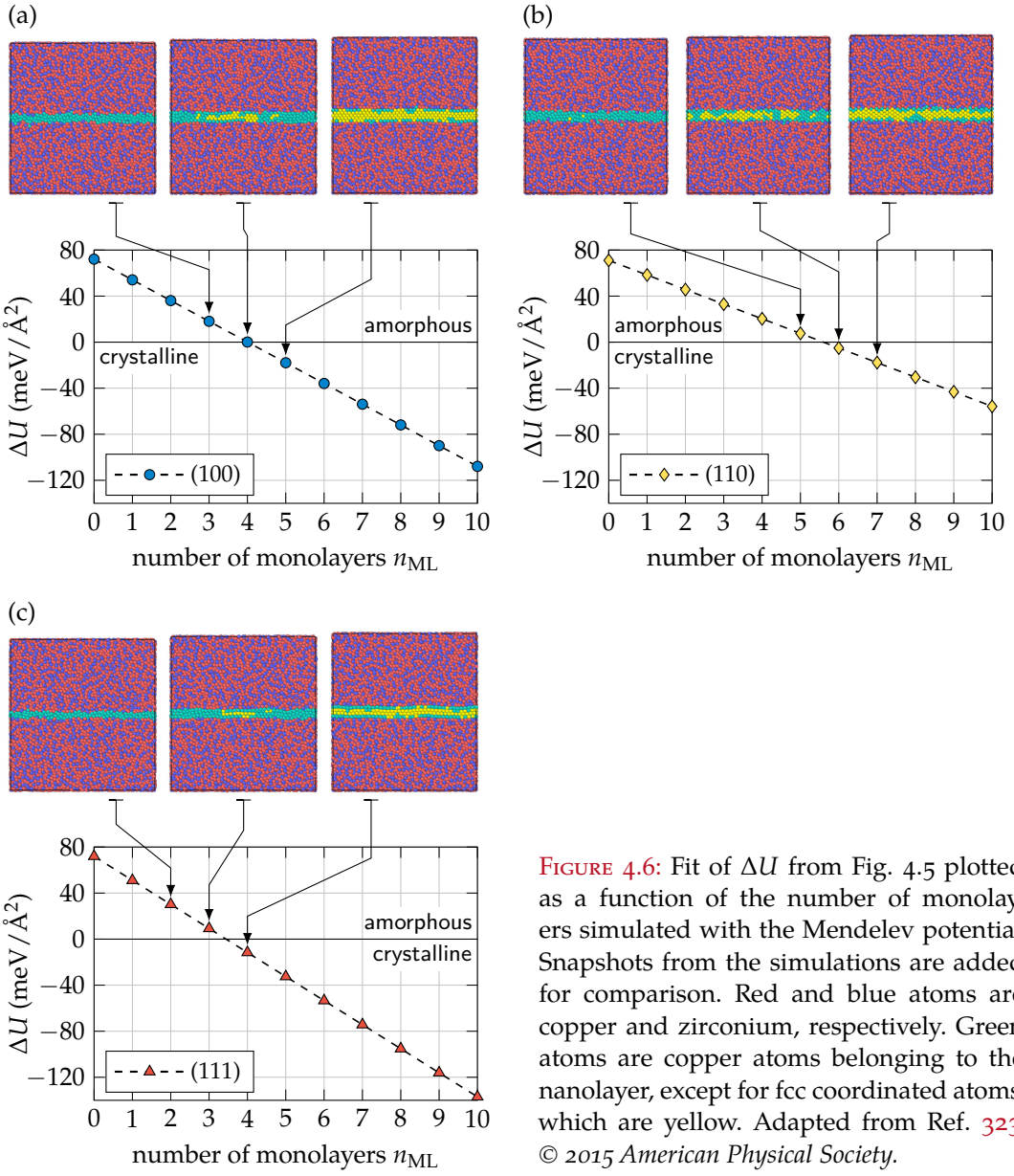

FIGURE 4.6: Fit of ΔU from Fig. 4.5 plotted as a function of the number of monolayers simulated with the Mendelev potential. Snapshots from the simulations are added for comparison. Red and blue atoms are copper and zirconium, respectively. Green atoms are copper atoms belonging to the nanolayer, except for fcc coordinated atoms, which are yellow. Adapted from Ref. 323, © *2015 American Physical Society.*

U_{MG} is the total internal energy of the bulk $Cu_{64}Zr_{36}$ glass phase, N is the number of atoms in the nanolayer, u_{fcc} is the internal energy per atom of the copper fcc crystal. Additionally, there are two interfaces, which contribute an energy of $A\zeta_{c-g}$ each, where A is the interface area. In our setup, the interface area corresponds to the cross-sectional area of the simulation cell.

If the nanolayer is amorphous instead, the internal energy will be

$$U_a = U_{MG} + Nu_{am} + 2A\zeta_{g-g}, \tag{4.3}$$

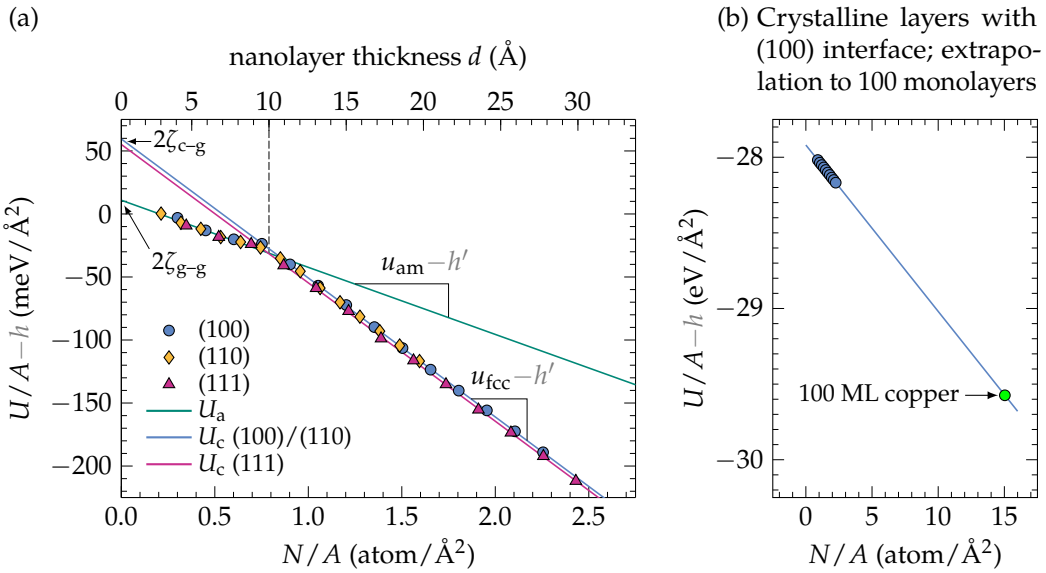

FIGURE 4.7: Dependence of the internal energy on the layer thickness of the composite systems modelled with the Ward potential. (a) Data points from simulations and fits of U_c and U_a. The total internal energy minus the energy of the glass matrix U_{MG} is plotted. Interface energies ζ and per-atom energies u can be extracted. (b) The total energy of the systems with crystalline nanolayers. The fit from (a) is extrapolated to a sample with 100 MLs of copper. For visualisation purposes a function $h = h' \cdot N/A$ with $h' = 3.35\,\text{eV}$ was subtracted in all plots to exaggerate the difference in slopes between U_c and U_a. Adapted from Ref. 323, © *2015 American Physical Society.*

where u_{am} is the per-atom internal energy of the glassy nanolayer and $\zeta_{g\text{–}g}$ is the glass–glass interface energy.

The deciding factor for amorphisation is then the difference between the two energies

$$\begin{aligned}\Delta U &= (U_c - U_a)/A \\ &= \left(\frac{N}{A}u_{fcc} + 2\zeta_{c\text{–}g}\right) - \left(\frac{N}{A}u_{am} + 2\zeta_{g\text{–}g}\right) \\ &= \frac{N}{A}\Delta u_{Cu} + 2\Delta\zeta.\end{aligned} \tag{4.4}$$

We can see that a negative value of ΔU signifies a stable crystalline nanolayer, while a positive value of ΔU signifies a stable amorphous nanolayer:

$\Delta U(N) < 0$	crystalline nanolayer
$\Delta U(N) > 0$	amorphous nanolayer.

It is to be expected that the bulk energy of the crystalline copper is lower than for the amorphous phase, making the thermodynamics dependent on the interface energy:

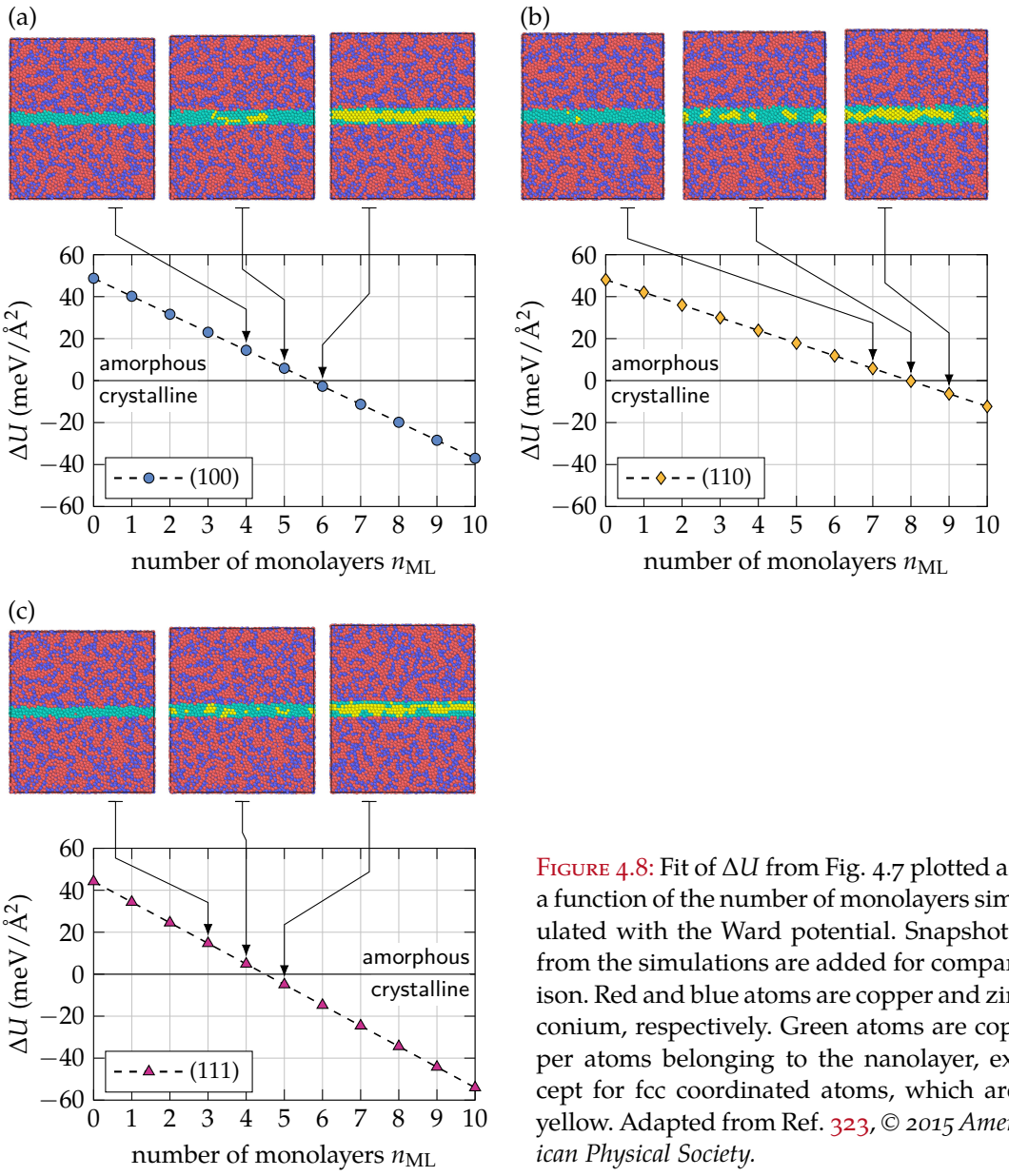

FIGURE 4.8: Fit of ΔU from Fig. 4.7 plotted as a function of the number of monolayers simulated with the Ward potential. Snapshots from the simulations are added for comparison. Red and blue atoms are copper and zirconium, respectively. Green atoms are copper atoms belonging to the nanolayer, except for fcc coordinated atoms, which are yellow. Adapted from Ref. 323, © *2015 American Physical Society.*

Only if $\zeta_{g\text{–}g} < \zeta_{c\text{–}g}$ can the amorphisation be energetically driven. If that is the case, we should find a critical number of atoms N_{crit}, such that $\Delta U(N_{crit}) = 0$ corresponds to the critical thickness observed by CNA and RDF. In practical applications, the number of monolayers or the thickness of the layer are more relevant numbers. They can easily be converted, as these quantities are approximately proportional:

$$\frac{N}{A} \propto n_{ML} \propto d.$$

TABLE 4.1: Values for the interface energies and projected bulk energies of copper nanolayers embedded in the glass matrix. Energies were taken directly from the MD simulations and the critical thicknesses were calculated using Eq. 4.4.

	Initial interface	u_{fcc}	u_{am}	Δu_{Cu}	ζ_{c-g}	ζ_{g-g}	$\Delta\zeta$	N_{crit}/A	d_{crit}
		(eV/atom)			(meV/Å^2)			(atoms/Å^2)	(Å)
Mendelev	(100)	−3.20	−3.08	−0.12	36.5	0.4	36.1	0.601	7.5
	(110)	−3.20	−3.08	−0.12	35.5	0.1	35.4	0.592	7.5
	(111)	−3.20	−3.08	−0.12	36.0	−0.5	36.5	0.606	7.5
Ward	(100)	−3.46	−3.40	−0.06	29.7	5.4	24.4	0.855	10.8
	(110)	−3.46	−3.40	−0.06	29.5	5.5	24.0	0.846	10.7
	(111)	−3.46	−3.40	−0.06	27.6	5.5	22.1	0.781	9.9

We now need to obtain the values of u_{fcc}, u_{am}, ζ_{c-g}, and ζ_{g-g}. Looking back at Eqs. 4.2 and 4.3, we find that

$$u_{fcc} = \frac{dU_c}{dN} \quad \text{and} \quad u_{am} = \frac{dU_a}{dN}, \tag{4.5}$$

which means that the bulk energies can be extracted from the internal energies of systems with different layer thicknesses. Afterwards, the interface energies can be extracted directly from Eqs. 4.2 and 4.3 and correspond to the U-axis intercept of the $U_c(N)$ and $U_a(N)$ curves minus the glass matrix energy. The bulk energy of the glass matrix was simply extracted from the bulk sample. The same could hypothetically be done also for u_{fcc} and u_{am}, but would lead to problems in the case of the bulk amorphous energy: The amorphous phase in the nanolayer is not necessarily the same as in the bulk. The bulk amorphous copper is quenched with very high cooling rates and has therefore more similarity to the melt. The amorphous copper phase in the nanolayer may exhibit different short-range order as it is allowed to relax to a low-energy state. Furthermore, the ratio of interface to volume is very high, which means that the nanolayer structure is highly influenced by interface contributions. Indeed, the structural differences between a copper glass and the amorphous nanolayers are discussed in Sec. 4.1.4. The derivation presented above assumes a constant interface energy, which can be confirmed if the $U(N)$ functions are linear.

The plot of this for data from the Mendelev potential is shown in Fig. 4.5, while the numerical data is listed in Tab. 4.1. The data points correspond to the MD simulations, while the lines are fits to the data. We can see that U_c and U_a are indeed linear and valid even when extrapolated to a system with 100 MLs of copper as plotted in Fig. 4.5 (b). The interface energy for the amorphous layers is lower than for the crystalline layers, compensating the excess bulk energy up to

$$d_{crit} \approx 7.5\,\text{Å}. \tag{4.6}$$

The thickness d_{crit} can only be given approximately because of the different densities of the two phases and the rough interface. Two peculiarities appear in the plot: First, the interface energy of the amorphous layers is approximately zero and second, the interface energies for different crystalline interface orientations are approximately equal. Both effects seem to be properties of the potential as we will see when discussing the results of the simulations with the Ward potential. The non-existent interface energy will be discussed in terms of the structure of the amorphous layer in Sec. 4.1.4. If we re-formulate ΔU in terms of n_{ML}, the number of monolayers, we can compare the predictions of our model with the CNA and RDF results. The former is done in Fig. 4.6. The direct comparison reveals that the calculated energy differences and the solid-state amorphisation observed by the CNA method agree very well. At the critical thickness $\Delta U = 0$ we observe a mixed crystalline/amorphous nanolayer. The figures show that the transition is not as sharp as our model assumes: A partly crystalline layer also exists for ΔU slightly greater than zero. That is a result of omitting a description of the two-phase region in the model; entropy and the additional interfaces play a role here. Nonetheless, the critical thickness is correctly reproduced without these complications. A further comparison with the RDFs in Fig. 4.3 leads to the same conclusions.

Figure 4.7 shows the internal energies as calculated with the Ward potential as a function of the number of atoms. All values are again normalised to the interface area and U_{MG} is already subtracted. The symbols show the internal energies extracted from the MD simulation, while the lines show the linear regression. In the Ward potential the (111) interface has a slightly lower interface energy than the (100) and (110) interfaces, which are approximately the same (see also Table 4.1). As with the Mendelev potential, the glass–glass interface energy is lower than the crystal–glass interface energy, favouring an amorphous nanolayer up to the critical thicknesses

$$d_{\text{crit}}^{(100)} \approx 10.8\,\text{Å}, \tag{4.7}$$

$$d_{\text{crit}}^{(110)} \approx 10.7\,\text{Å}, \text{ and} \tag{4.8}$$

$$d_{\text{crit}}^{(111)} \approx \ \ 9.9\,\text{Å}. \tag{4.9}$$

The difference in critical thickness is a result of different $\zeta_{\text{c–g}}$ for the three surface orientations. The transition thickness is higher than in the Mendelev potential despite a smaller $\Delta\zeta$, since the excess energy of the amorphous phase is lower. By plotting ΔU as a function of the number of monolayers, a direct comparison to CNA and RDF results is possible. Figures 4.8(a)–(c) show $\Delta U(n_{\text{ML}})$ compared with snapshots from the simulation. Again, a good match between the nanolayer phases shown in the snapshots and the predicted critical thickness is visible. For the same reasons as stated earlier, a mixed state occurs.

All in all, the results using both potentials agree qualitatively and support our thermodynamic model. Therefore, a purely kinetic reason for the amorphous nano-

layers can be ruled out and an energetic picture of solid-state amorphisation can be supported.

4.1.3 *Possible problems with model and setup*

One could now argue that the results presented above are trivial and the effect is exactly the same as for a nanoparticle in vacuum: The surface energy of the amorphous state is simply lower and the surrounding glass matrix is irrelevant. We put this to the test by using the composite system with 3 MLs thickness and an initial (111) surface simulated with the Mendelev potential. We start from the state after 30 ps as shown in Fig. 4.2 (b); the nanolayer is partially amorphous and partially crystalline. This means that—if the vacuum case is comparable to the multilayer system—the mixed state should persist in the vacuum. Additionally, if the amorphous phase

(a) An fcc layer of 3 ML thickness with initial (111) interface orientation.

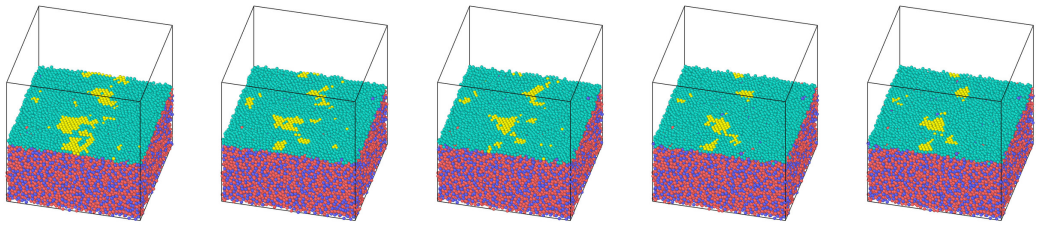

(b) An fcc layer of 3 ML thickness in vacuum with initial (111) surface orientation.

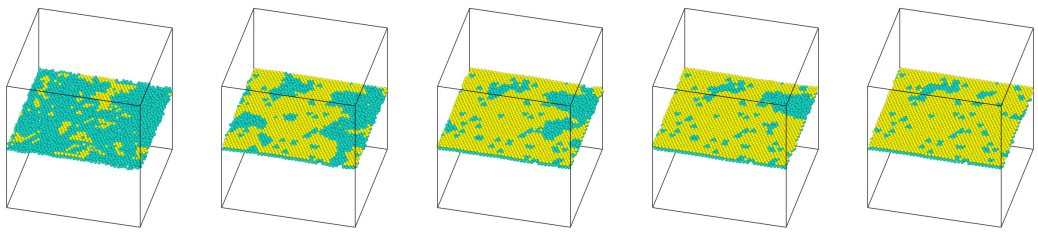

FIGURE 4.9: Long-term stability of a mixed crystalline/amorphous nanolayer in the glass matrix and in vacuum. Simulations performed with the Mendelev potential. (a) Cut through a nanolayer of 3 ML thickness with an initial (111) surface orientation. The crystalline clusters neither grow nor disappear after 100 ns. (b) The same nanolayer removed from the glass matrix crystallises almost immediately. Copper and zirconium atoms in the glass matrix are shown in red and blue; copper atoms belonging to the nanolayer are yellow if they are fcc coordinated and green otherwise. Adapted from Ref. 323, *© 2015 American Physical Society.*

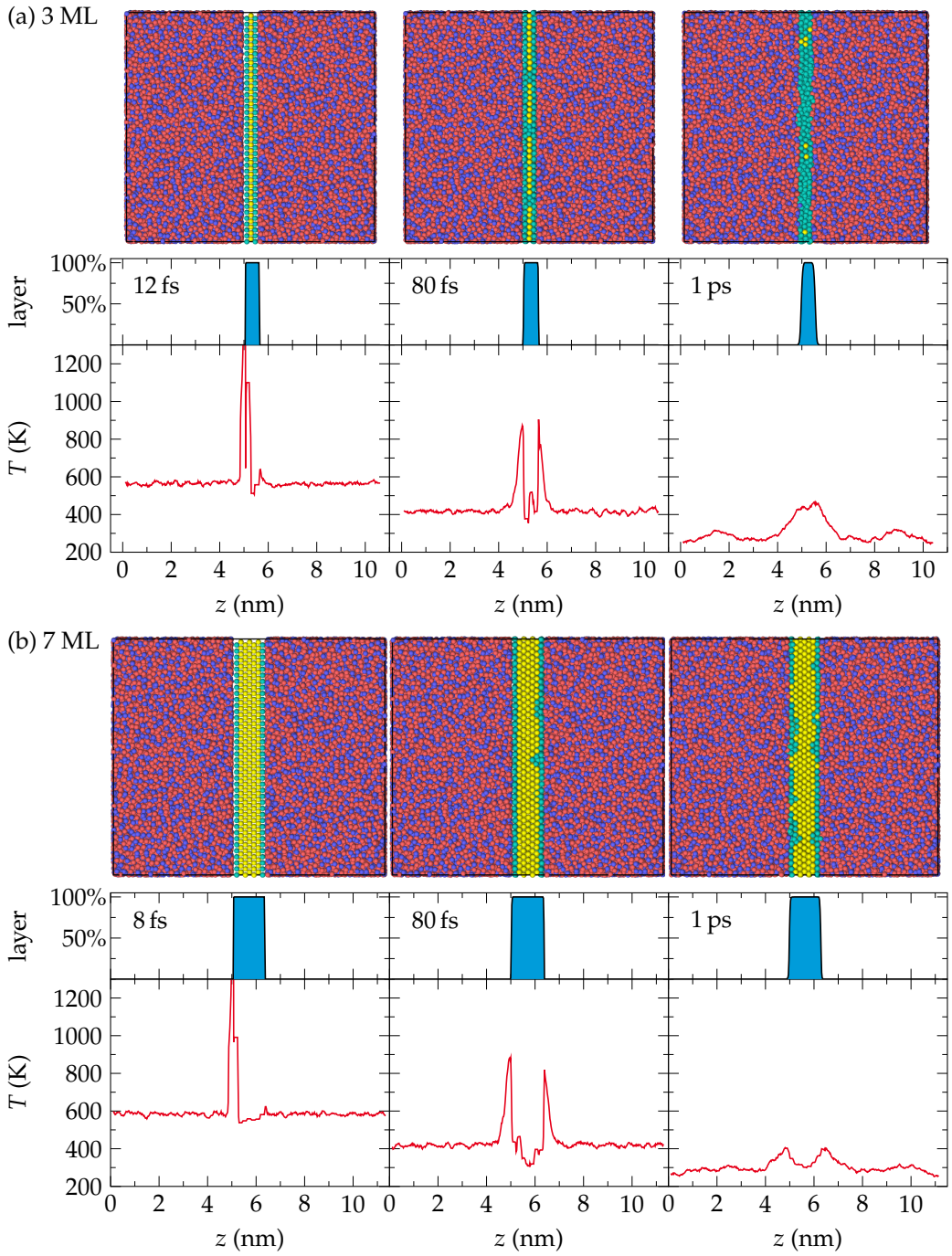

FIGURE 4.10: Temperature profiles over time during interface formation in a composite simulated with the Mendelev potential. (a) Simulation with a 3 ML thick copper layer with initial surface orientation (100). A heat spike occurs at the interface and penetrates the layer upon amorphisation. (b) Simulation with a 7 ML thick copper layer with initial surface orientation (100). Again, a heat spike occurs at the interface but stays largely localised in the glass matrix near the interface. Adapted from Ref. 323, © *2015 American Physical Society.*

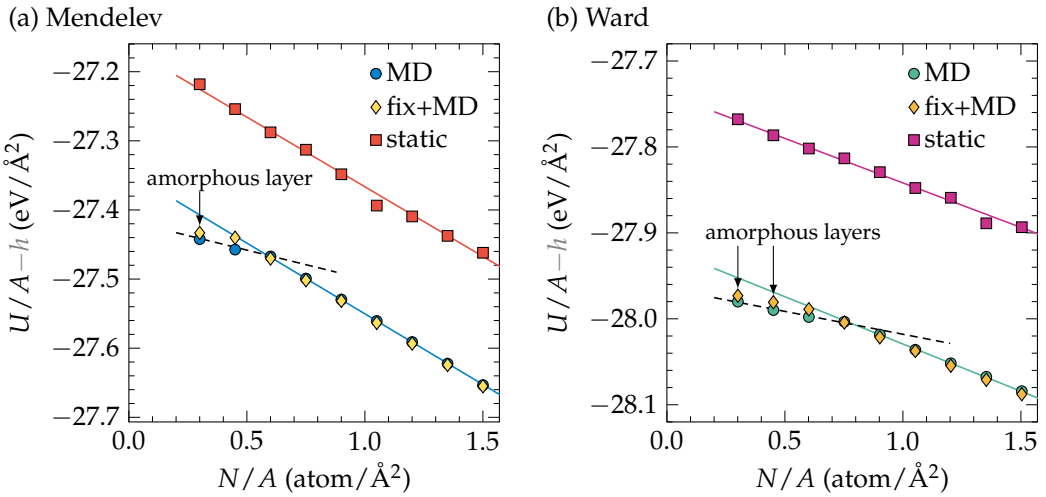

FIGURE 4.11: Simulations which avoid a penetration of heat into the nanolayers. (a) and (b) show results for simulations with the Mendelev and the Ward potential, respectively. Circles are data as presented previously, diamonds represent simulations in which the nanolayer was kept fixed during interfaces creation and only released afterwards, and squares represent molecular statics simulations. Only systems with initial (100) surface are considered. A function h as in Figs. 4.5 and 4.7 was subtracted again for visualisation purposes. In the simulations with initially fixed nanolayers and in the molecular statics simulations, all layers except the marked ones stayed crystalline. For the molecular statics calculation, a $2 \times 3/2 N k_B T$ term was added, to compensate for the missing temperature contribution to the internal energy. Adapted from Ref. 323, © *2015 American Physical Society.*

was only produced by, e.g., stresses in the initial system after insertion of the nanolayer, the crystalline phase should start growing again over the longer time frame. Figure 4.9 (a), though, shows that the mixed state is stable over a long time scale in the presence of the glass matrix. On the other hand, extracting the mixed-state nanolayer from the matrix leads to immediate crystallisation as presented in Fig. 4.9 (b). This means that the interface energy due to the contact with a glass matrix changes the thermodynamics in the nanolayer completely.

As mentioned in the beginning of the section, the formation of the interface may release heat because of the low interatomic distances in our setup. This is indeed the case, as can be seen in Fig. 4.10. Local heating penetrates the layer simultaneously with the amorphisation. Does this mean that the transition is not energetically driven after all? We tested our results by avoiding a melting of the layer and re-evaluating the internal energy as a function of layer thickness. First, we held the layer atoms fixed and equilibrated for 1 ns, only releasing them afterwards and equilibrating for another 1 ns ("fix+MD" in Fig. 4.11). Second, we performed molecular statics simulations, in which the temperature is always 0 K ("static" in Fig. 4.11). In the second case, the amorphisation is completely suppressed, but the energy of the resulting systems is much higher. In the fix+MD case, amorphisation occurs but at a lower critical thick-

ness. Looking at the energies, though, reveals that the amorphous samples obtained using our original protocol are always energetically favourable to the crystalline layers at the same thickness. This leaves only the conclusion that the initial heat release provides the activation energy needed to reach a lower energy state. Given that we are interested in the energetically-driven behaviour of the system and not in any kinetics, these results do not contradict our model but support its conclusions.

4.1.4 *Structure and Energy*

We now consider the short-range order and structure of the amorphous copper nanolayers and how this order influences the interface energy.

Mendelev potential

As a first step, we calculated energy–volume curves of bulk fcc and bulk amorphous copper. The bulk amorphous copper refers to the glass reference sample. A pure comparison of these reference curves, plotted in Fig. 4.12, already shows that the potential energy of the crystalline bulk sample is always preferable, even under tension or compression. This means that, in agreement with our earlier postulate, the driving force for amorphisation must be a reduction of the interface energy. Plotting the energies and volumes of the different nanolayers, we can see two peculiarities: First,

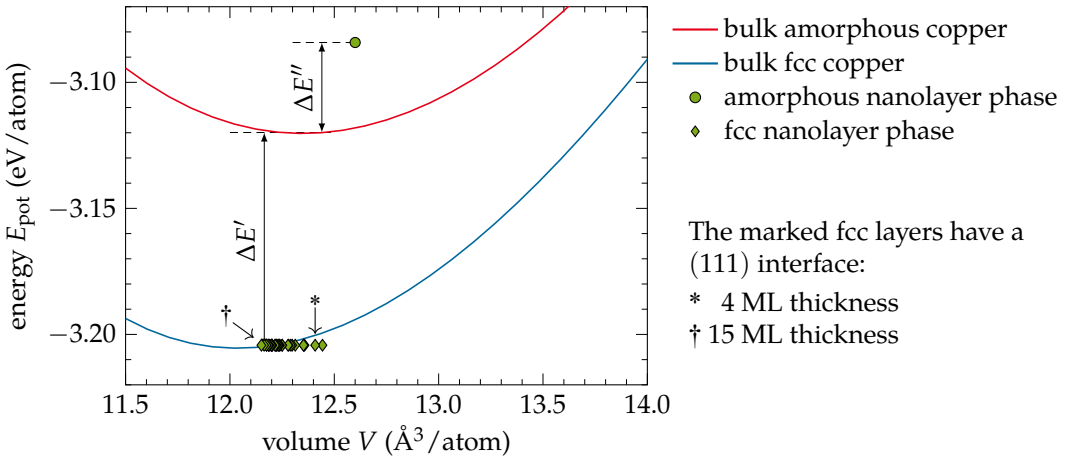

FIGURE 4.12: Energy–volume curves for amorphous and crystalline copper and data points for amorphous and crystalline nanolayers. The amorphous nanolayers show an excess energy $\Delta E''$ compared to the bulk amorphous copper reference. The sum $\Delta E' + \Delta E''$ corresponds approximately to Δu_{Cu}. Thinner crystalline layers are less dense than the reference bulk crystal and reach the bulk density at around 15 ML thickness. The atomic volumes of the nanolayers were obtained by averaging the Voronoi volumes of the layer atoms. Adapted from Ref. 323, *© 2015 American Physical Society.*

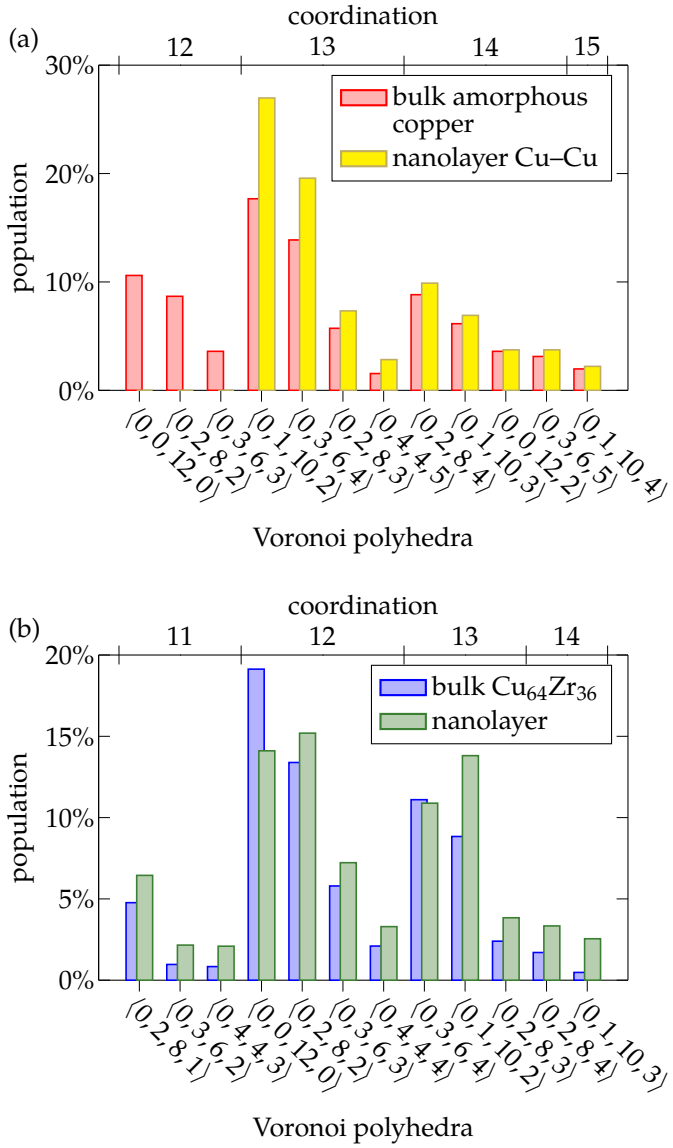

FIGURE 4.13: Voronoi analysis of the amorphous nanolayers in the composites simulated using the Mendelev potential. The twelve most common polyhedra are shown. (a) Comparison of data from the bulk amorphous copper reference phase with those copper atoms in the nanolayer that are only surrounded by other copper atoms. Twelve-fold coordinated atoms are missing from the nanolayer. (b) Voronoi statistics of all nanolayer atoms compared with the bulk $Cu_{64}Zr_{36}$ glass reference. The statistics exhibit a large similarity. Adapted from Ref. 323, *© 2015 American Physical Society.*

the thin crystalline layers are dilated, and second, the amorphous nanolayers have an excess energy of $\Delta E''$ over the reference amorphous sample. The former points to the fact that a tensile interface stress pulls on the small layers and expands them. This effect disappears with increasing layer thickness. The increased energy of the amorphous phase in the layer, as well as the zero glass–glass interface energy can be explained when looking at the structure of the layer. Figure 4.13 (a) shows the Voronoi statistics of those nanolayer atoms that have only copper neighbours. This allows a comparison to the bulk amorphous copper. In contrast to the bulk, the layer has no twelve-fold coordinated atoms. This change in structure necessarily also leads to a change in energy. The reason why the nanolayer does this becomes clear when ex-

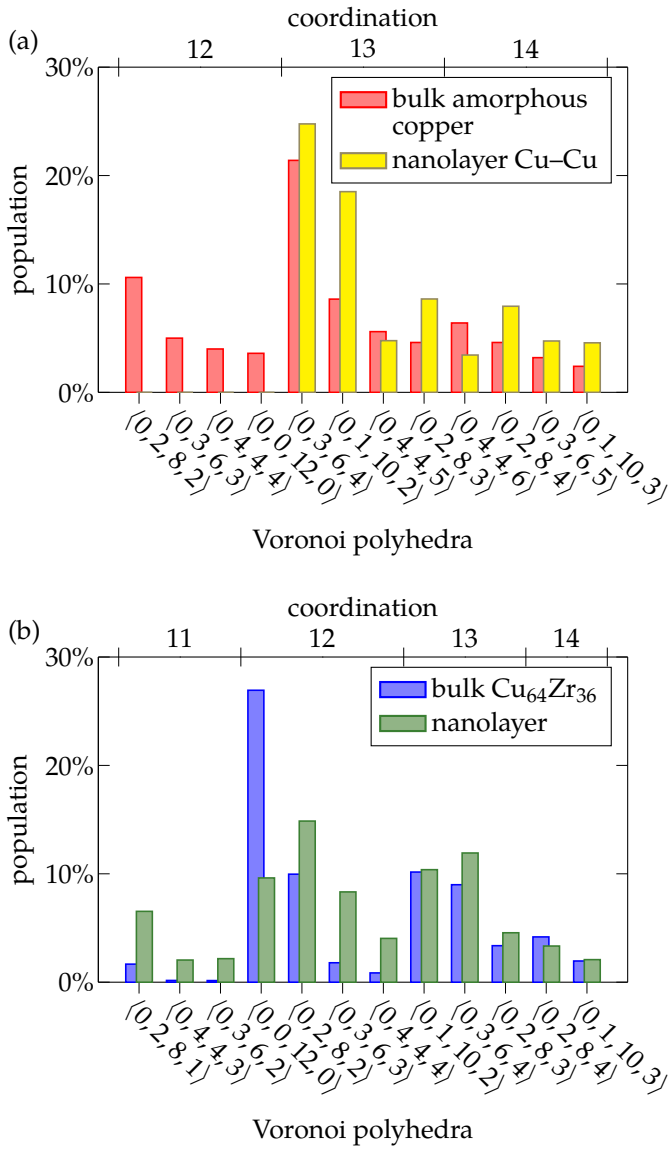

FIGURE 4.14: Voronoi analysis of the amorphous nanolayers in the composites simulated using the Ward potential. The twelve most common polyhedra are shown. (a) Comparison of data from the bulk amorphous copper reference phase with those copper atoms in the nanolayer that are only surrounded by other copper atoms. Twelve-fold coordinated atoms are missing from the nanolayer. (b) Voronoi statistics of all nanolayer atoms compared with the bulk $Cu_{64}Zr_{36}$ glass reference. The statistics differ especially for twelve-fold coordinated atoms. Adapted from Ref. 323, © *2015 American Physical Society.*

amining the Voronoi statistics of the complete nanolayer—including copper atoms with zirconium neighbours—in comparison with the glass matrix [Fig. 4.13 (b)]: The copper atoms in the layer assume configurations that resemble those in the glass matrix. By doing that, they can reduce the interface energy to zero.

Ward potential

The Ward potential behaves differently. The energies of the bulk amorphous reference and the amorphous nanolayer are also different, but the amorphous nanolayer is slightly more favourable (−3.39 eV/atom for the bulk system, −3.40 eV/atom for

the nanolayer). The Voronoi statistics in Fig. 4.14 (a) also exhibit a lack of twelve-fold coordinated copper atoms, although this seems to reduce the amorphous energy in this potential. Regarding a formation of a glass–glass interface, the nanolayer cannot accommodate structural changes to completely adapt to the surrounding matrix: Figure 4.14 (b) shows that the features of the glass are not reproduced, especially the energetically favourable $\langle 0, 0, 12, 0\rangle$ polyhedra are underrepresented, while there is an abundance of $\langle 0, 2, 8, 2\rangle$ and $\langle 0, 3, 6, 3\rangle$ polyhedra. Still, several features of the bulk glass are replicated. This leads to a small but non-zero glass–glass interface energy.

4.2 SPHERICAL COPPER PRECIPITATES

Apart from multilayer systems, the results may also be applicable to spherical precipitates. The only difference to the planar interface is that the curvature may introduce additional interface stresses. We tested this for the results obtained with the Mendelev potential by assuming that the results can be transferred without modification. For this, we rewrite Eq. 4.4 for spherical precipitates. The new critical value, $\Delta U_{\odot}$, is not normalised according to the interface area. We write

$$\Delta U_{\odot} = \left(N \cdot u_{\mathrm{fcc}} + A \cdot \zeta_{\mathrm{c\text{–}g}}\right) - \left(N \cdot u_{\mathrm{am}} + A \cdot \zeta_{\mathrm{g\text{–}g}}\right). \tag{4.10}$$

It is $A = 4\pi r^2$ and $N = \rho_n V = \rho_n 4\pi r^3/3$. We simplify by assuming that the densities of the crystalline and the amorphous phase are approximately equal and obtain

$$\Delta U_{\odot} = 4\pi r^2 \left[\left(\rho_n \frac{r}{3} u_{\mathrm{fcc}} + \zeta_{\mathrm{c\text{–}g}}\right) - \left(\rho_n \frac{r}{3} u_{\mathrm{am}} + \zeta_{\mathrm{g\text{–}g}}\right)\right]. \tag{4.11}$$

In the cubic fcc unit cell, there are four atoms. We obtain a lattice constant of $a = 3.651$ Å for a bulk fcc copper system after equilibration at 300 K. This gives a density

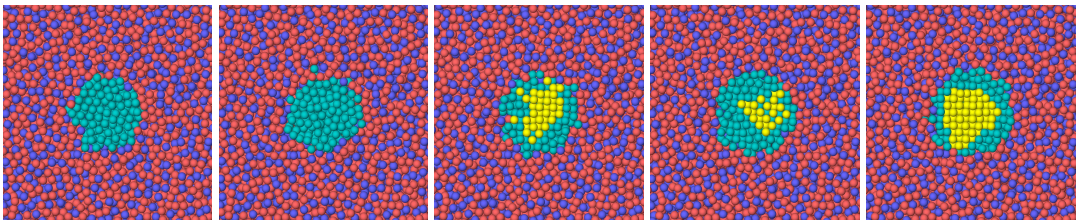

FIGURE 4.15: Critical diameter for solid-state amorphisation of spherical copper particles. Simulations were performed with the Mendelev potential and the samples were equilibrated at 300 K for 1 ns. Colour coding is the same as in Fig. 4.2.

$\rho_n = 82.19\,\mathrm{nm}^{-3}$. By solving for $\Delta U_\odot = 0$, we get a critical diameter d_{crit} for spherical inclusions of

$$\rho_n \frac{r_{\mathrm{crit}}}{3} u_{\mathrm{fcc}} + \zeta_{\mathrm{c\text{–}g}} = \rho_n \frac{r_{\mathrm{crit}}}{3} u_{\mathrm{am}} + \zeta_{\mathrm{g\text{–}g}} \tag{4.12}$$

$$r_{\mathrm{crit}} = \frac{\zeta_{\mathrm{g\text{–}g}} - \zeta_{\mathrm{c\text{–}g}}}{\frac{\rho_n}{3}(u_{\mathrm{fcc}} - u_{\mathrm{am}})} \tag{4.13}$$

$$\approx 10.95\,\text{Å} \tag{4.14}$$

$$d_{\mathrm{crit}} \approx 2.2\,\mathrm{nm}. \tag{4.15}$$

We tested this prediction using a comparable setup to the one in Sec. 4.1: Spherical copper particles with diameters from 2.0 nm to 2.4 nm were inserted into a $Cu_{64}Zr_{36}$ glass matrix. Figure 4.15 shows the results after 1 ns equilibration at 300 K. Indeed, the inclusion with $d < 2.2\,\mathrm{nm}$ becomes amorphous, while bigger crystallites stay crystalline.

4.3 CONCLUSIONS

By analysing crystalline copper nanolayers inserted into a $Cu_{64}Zr_{36}$ metallic-glass matrix, we could show that SSA of thin elemental metal layers is possible even in the absence of strong lattice mismatch. A replication of structural motifs in the glass by the nanolayer atoms can reduce the glass–glass interface energy so much that an amorphous state can be stabilised. This suggests that these amorphisation processes are enabled by the similarity of structure and interatomic bonds and are therefore not observed for, e.g., metals in contact with amorphous carbon.[67] We derived a thermodynamic model based on a competition between bulk and interface energy, which is transferable to spherical crystallites. The amorphous phase in the layer is energetically preferable but cannot be called thermodynamically stable as the surrounding glass matrix is metastable.

Our results are in line with earlier experimental work on iron embedded in amorphous $Co_{75}Fe_{12}B_{13}$, which reports amorphisation below five monolayers of iron,[83] while we find a critical thickness of copper between three and eight monolayers, depending on interface orientation and interatomic potential. Technological applications for these glass–glass composite systems have already been proposed in the realm of magnetic tunnel junctions,[83,324] in which the tunnelling magnetoresistance is increased upon amorphisation.[324]

5 CRYSTALLISATION OF LAVES PHASES IN CU–ZR GLASSES

In order to investigate the influence of crystalline secondary phases embedded in a glass matrix on the properties of the composite, two simulation approaches are available: The most common method is the insertion of artificially created crystallites into holes which are cut into an existing glass matrix. The advantages of this approach are the efficiency—very little computing time is needed to insert the crystallites—and the exact control over crystal phase, crystallite size and crystallite position in the matrix. The disadvantage is that the crystal–glass interface is artificial and it is unclear if it is realistic. This can be avoided by growing the crystallites by an annealing procedure, which on the other hand cedes control over the properties of the precipitates to random processes in the material. In this thesis, we employ both approaches. As a first step, we will treat the growth of crystallites in $Cu_{64}Zr_{36}$ modelled with the Mendelev potential in this chapter.

Tang and Harrowell calculated the phase diagram for the Mendelev potential.[122] They found that the most stable compound down to 0 K is the CuZr phase. This is followed by the Cu_2Zr Laves phase. Experimentally, the metastable CuZr phase easily forms upon annealing of Cu–Zr-based metallic glasses[117–120] and the Cu_2Zr phase is either not included in phase diagrams at all[114] or predicted to be stable only above 1160 K.[112,115] Nevertheless, the crystallisation of Laves phases in Cu–Zr-based glasses has captured research interest. While the phase may not appear at equilibrium conditions below the glass transition temperature, it appears in some Cu–Zr–Ti glasses[126] and Vitreloy 1[127] and may at least serve as a model for a annealing-grown crystal–glass composite in $Cu_{64}Zr_{36}$. Zemp and colleagues first performed simulations in which Laves crystallites were obtained.[110,123,325] They report an annealing procedure in which a $Cu_{64}Zr_{36}$ glass is held at 800 K for several hundred nanoseconds. An increase of copper-centred icosahedra (Voronoi index $\langle 0,0,12,0\rangle$) as well as zirconium-centred $\langle 0,0,12,4\rangle$ polyhedra is observed. These $\langle 0,0,12,4\rangle$ polyhedra are in fact the structural units observed in the C14 and C15 Laves phases (see Fig. 5.1) and are usually designated as Frank–Kasper Z16 polyhedra. The copper atoms in the Laves phases also appear as $\langle 0,0,12,0\rangle$ icosahedra. The difference between the C14 and C15 polymorphs is that in the former case, the zirconium atoms form a hexagonal diamond super-lattice, while in the latter case they form a cubic diamond super-lattice. Earlier simulations probably already found the first traces of this crystallisation by observing an increase of the copper-icosahedra fraction by annealing near T_g[125] and later on by additionally registering an increase of Z16 zirconium motifs.[93] The fact that the copper icosahedra, which are naturally abundant in Cu–Zr glasses, also occur in the Laves phases explains the ease of obtaining these structures and probably

(a) C14 crystal structure

(b) C15 crystal structure

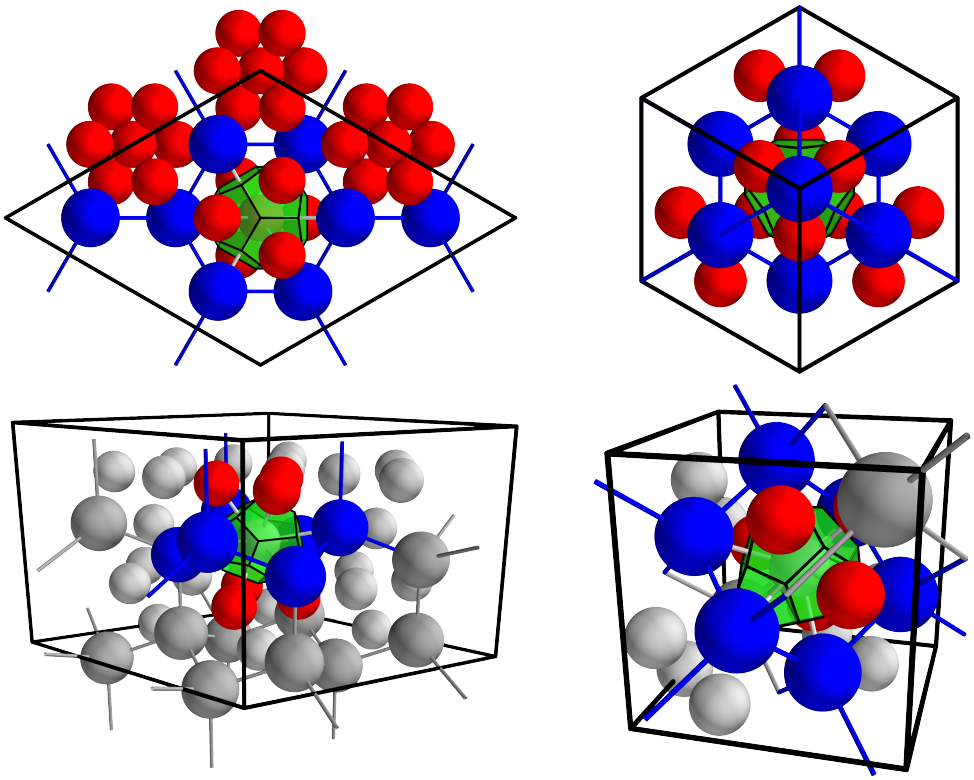

FIGURE 5.1: The C14 and C15 Laves phases. Red atoms are copper, blue ones zirconium. The Laves phases are made up of a diamond super-structure of zirconium atoms—hexagonal diamond in C14 (a), cubic diamond in C15 (b). The copper atoms are always $\langle 0, 0, 12, 0 \rangle$ icosahedra surrounded by six copper and six zirconium atoms. For each structure, one Voronoi polyhedron around copper is shown exemplarily in green. The zirconium atoms are always $\langle 0, 0, 12, 4 \rangle$ Frank–Kasper polyhedra.

leads to a decreased crystal–glass interface energy. First simulational studies report an increase of stiffness and yield strength of the composite, as well as an increased strain localisation.[123,325]

5.1 PROPERTIES OF THE LAVES PHASES

Building on these findings, we started by investigating the properties of the C14 and C15 Laves phases as modelled by the Mendelev potential. The 0 K properties compared with a bulk glass are listed in Tab. 5.1. As expected, the density and stiffness of the crystalline phases are higher, while the cohesive energy is lower.

	C14	C15	glass	
E_{coh}	−4.496	−4.497	−4.483	eV/atom
ρ_n	65.28	65.31	63.17	nm^{-3}
ρ	7.969	7.972	7.710	g/cm^3
c_{11}	235	224	167	GPa
c_{33}	231			GPa
c_{12}	134	141	113	GPa
c_{13}	121			GPa
c_{44}	42	60	27	GPa
c_{66}	50			GPa
$\mathcal{G}_{\text{VRH}}$	48	52	27	GPa
$\mathcal{K}_{\text{VRH}}$	161	169	131	GPa
$\mathcal{E}_{\text{VRH}}$	131	141	76	GPa
$\nu^{\text{VRH}}_{\text{Poisson}}$	0.37	0.36	0.40	

TABLE 5.1: Cohesive energy, density, and elastic constants of the Laves phases C14 and C15 at 0 K. For comparison, the values of the homogeneous glass from Sec. 3.4.1 are also listed. Only the unique elastic constants are listed: C14 has a hexagonal symmetry, C15 is cubic, and the glass is of course isotropic.

5.2 ANNEALING PROCEDURE

In order to produce samples with varying crystalline volume fraction f, we started by heating a $Cu_{64}Zr_{36}$ glass sample with 63 108 atoms (roughly $10 \times 10 \times 10\,\text{nm}^3$ in size) to 800 K with a heating rate of 0.1 K/ps and held it there. We used a barostat at 0 Pa to control the box shape, allowing volume change and shape change including tilt of the box. During the annealing, we monitored the amount of zirconium atoms by applying the diamond structure identification implemented in OVITO[279,295] only on the zirconium atoms. The annealing procedure and the fraction f_1 of zirconium atoms on a diamond super-lattice are shown in Fig. 5.2. As depicted, we selected samples at 12 points during the annealing procedure and cooled them down to 50 K with 0.01 K/ps, the results of which are shown in Fig. 5.3. After 2100 ns, we increased the annealing temperature to facilitate faster crystal growth. No glass transition was observed, so we increased the temperature in steps up to 900 K. As can be seen in Fig. 5.2 (b), the final sample does no longer exhibit significant increase of the crystalline volume fraction and we therefore stopped the procedure.

It is interesting to note that the crystallisation started with the assembly of existing Z16 polyhedra [cf. Figs. 5.3 (b)–(c)]. This explains the rather fast crystallisation kinetics and is probably an indication of a low crystal–glass interface energy.

5.3 PROPERTIES OF THE ANNEALED SAMPLES

In the next step, we characterised the resulting samples I–XIII. As no algorithm for the identification of Laves phases is readily available we used an approximate method. All zirconium atoms identified as belonging to a diamond super-lattice were marked as part of the crystalline phase. Then a Voronoi tessellation was performed and the neighbours of the marked zirconium atoms were identified. Of those neighbours, all

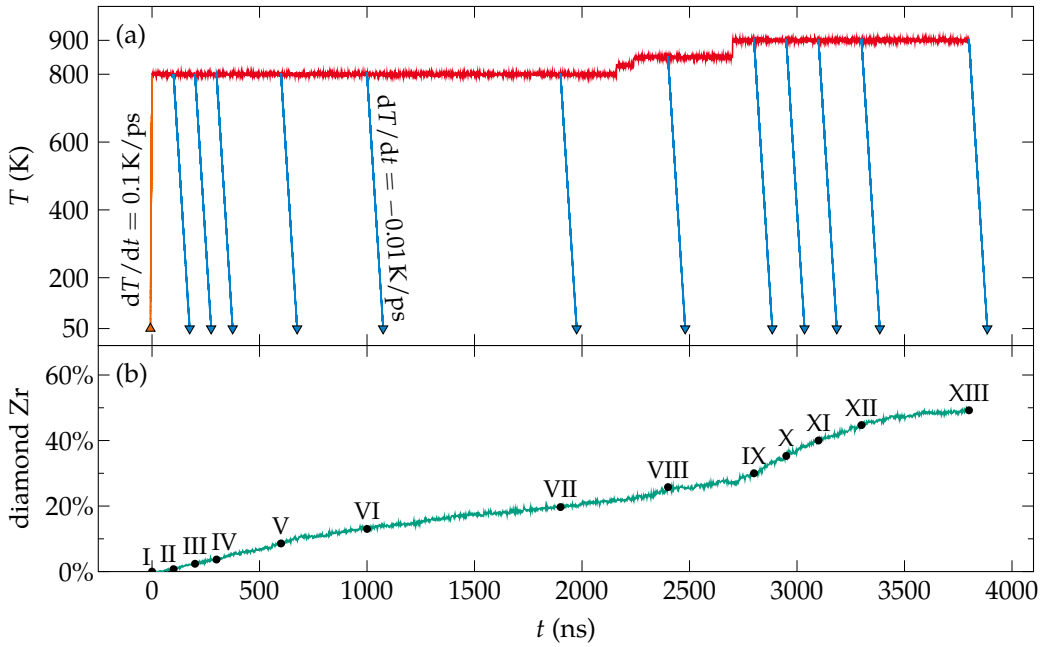

FIGURE 5.2: Annealing procedure. (a) The applied temperature program. The cooling was performed independently to obtain twelve samples annealed for different times. (b) The fraction of zirconium atoms in a diamond super-lattice identified at the annealing temperature. The occurrence of this super-lattice indicates the presence of a Laves phase.

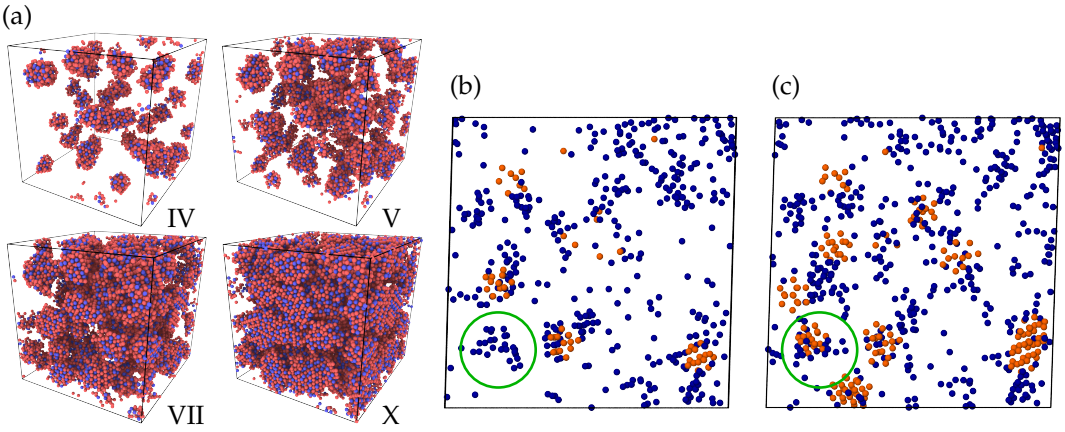

FIGURE 5.3: Snapshots of crystal growth during annealing. (a) Only atoms identified as belonging to Laves phases are shown. Analysis conducted at 0 K. (b)–(c) Slice through samples III and IV, only showing Z16 zirconium atoms. Orange atoms belong to a Laves phase, blue ones do not. Clusters of Z16 atoms act as precursors to crystallisation (indicated by the green circle) and appear frequently around existing crystallites.

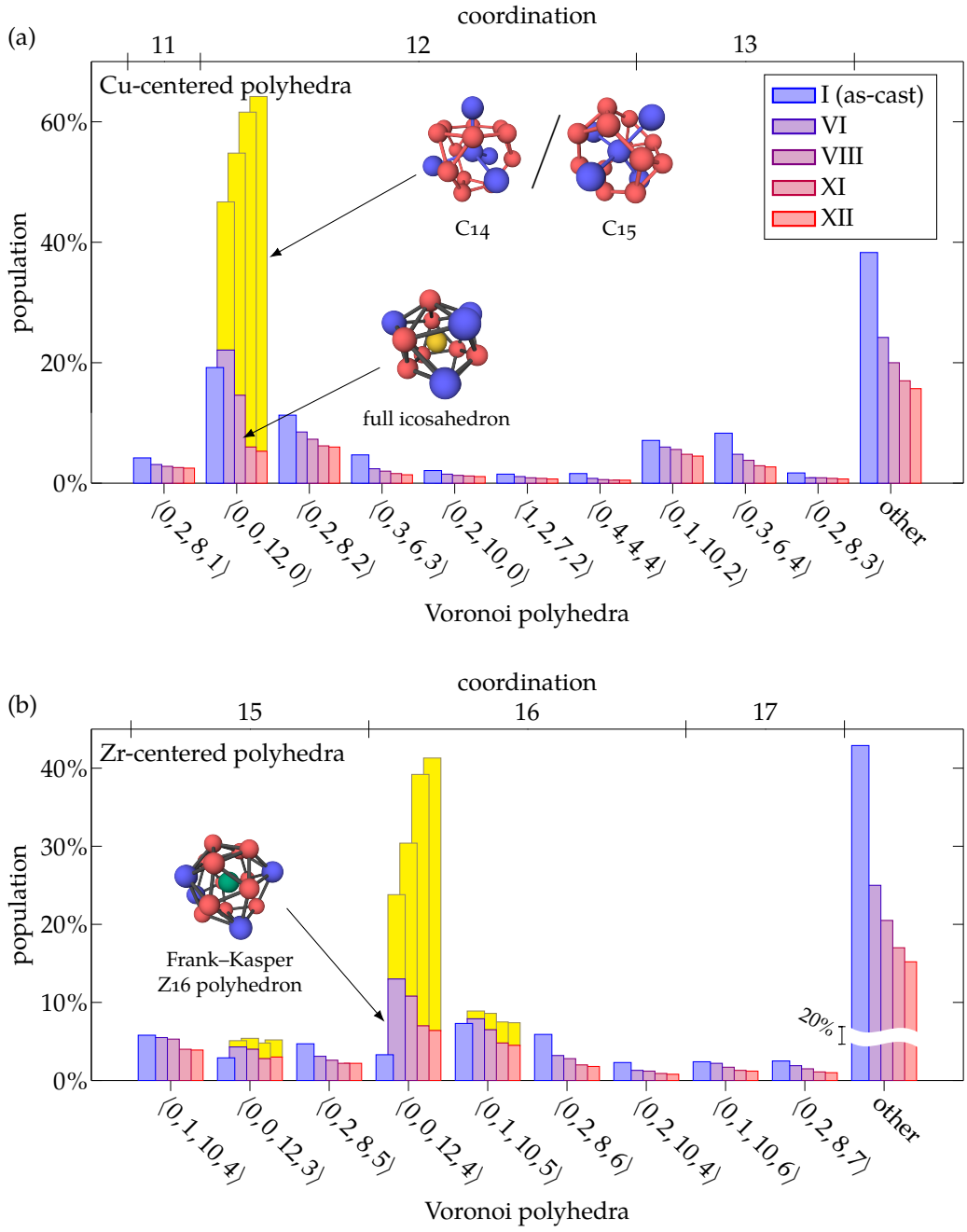

FIGURE 5.4: Voronoi statistics of five annealed samples over time. The yellow bars indicate which fraction of the given polyhedra belonged to C14 or C15 crystallites.

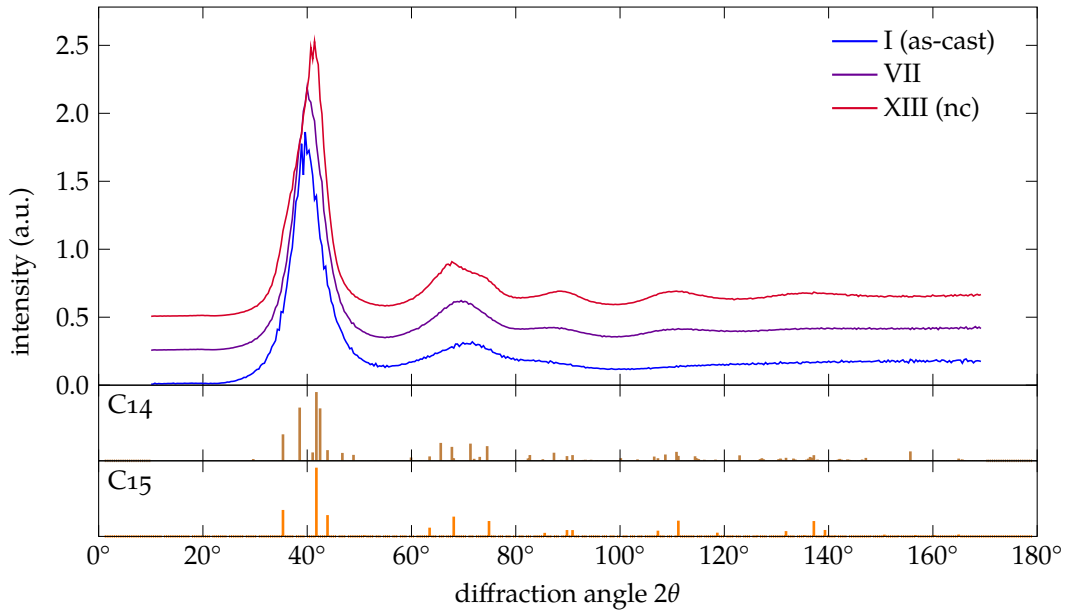

FIGURE 5.5: Simulated x-ray powder diffractograms of samples I, VII, and XIII. The reflexes of the C14 and C15 phases are plotted at the bottom.

copper atoms which are the centre of $\langle 0, 0, 12, 0\rangle$ polyhedra were also marked as belonging to the crystalline phase. The volume fraction of atoms identified with this algorithm is designated f_2. This method slightly overestimates the number of copper atoms in the crystallites, as neighbouring icosahedra belonging to the glass are also caught. The resulting Voronoi statistics of five samples are listed in Fig. 5.4. An increase of the $\langle 0, 0, 12, 0\rangle$ and $\langle 0, 0, 12, 4\rangle$ polyhedra can be observed, while the other polyhedra have an approximately constant relative occurrence. Laves phases cannot be detected in the as-cast sample but appear quickly during the annealing process. One should note that the Z16 polyhedra play only a very minor role in the glass, while distortions like $\langle 0, 1, 10, 5\rangle$ are more numerous. Only upon crystallisation do the Z16 polyhedra occur in significant fractions. In contrast to earlier assumptions,[93] they only seem to occur as precursors to crystallisation and not as a product of glass relaxation [see Figs. 5.3 (b)–(c)].

In addition to the Voronoi analysis, we calculated powder diffraction patterns of samples I, VII, and XIII with the algorithm implemented in LAMMPS.[326] We used virtual x-ray diffraction at 300 K using the wavelength of copper K_α radiation ($\lambda = 1.541\,838$ Å). We repeated the calculation for single-crystalline C14 and C15 and show the combined results in Fig. 5.5. We can see that even the broad peaks in the as-cast glass look like smeared-out peaks of the Laves phases. This underlines the similarity of short-range structural order in both and is reminiscent of the idea that an ideal glass may resemble a Frank–Kasper phase (see Sec. 1.2). The change in the diffracto-

TABLE 5.2: Properties of annealed samples at 0 K. f_1 is the ratio of diamond Zr atoms over total number of Zr. f_2 is the fraction of both Cu and Zr atoms identified as part of a Laves phase. d is the average diameter of the crystallites, assuming a spherical shape.

sample	f_1 (%)	f_2 (%)	d (nm)	ρ_n (nm^{-3})	E_{pot} (eV/atom)	c_{11}	c_{12}	c_{44} (GPa)	$\mathcal{E}_{\text{VRH}}$
I	0.0	0.0		63.15	−4.483	164	110	27	75
II	1.3	2.1	1.4	63.21	−4.488	167	111	27	77
III	2.9	4.4	1.4	63.24	−4.492	169	112	28	79
IV	4.6	6.9	1.5	63.27	−4.495	169	112	28	80
V	9.8	14.4	1.5	63.33	−4.500	172	112	29	82
VI	15.1	21.2	1.7	63.37	−4.505	174	113	31	85
VII	21.7	29.0	1.8	63.42	−4.509	176	114	31	87
VIII	28.3	35.9	1.9	63.43	−4.510	178	114	32	88
IX	33.6	41.5	2.1	63.44	−4.512	178	114	32	90
X	39.5	47.2	2.3	63.47	−4.515	179	114	33	90
XI	44.2	51.5	2.7	63.48	−4.517	181	114	33	92
XII	48.0	55.0	2.8	63.50	−4.519	182	115	34	94
XIII	52.4	59.1	3.1	63.53	−4.522	184	115	34	95

grams from sample I to XIII are subtle, but the shift of the first and second peaks should be detectable even in noisy data obtained from experiment.

Another property of interest is the size of the grown crystallites. This can be approximated from the fraction of Laves atoms f_2, the total number of atoms in the box N, the average atomic volume in the Laves phase Ω, and the number of crystallites n by assuming spherical precipitates and calculating their diameter

$$d = \sqrt[3]{\frac{6 f_2 N \Omega}{\pi n}}. \tag{5.1}$$

All values are already available, except for the number of precipitates. This is slightly trickier than could be assumed, as the crystallites are sometimes very close together. A cluster analysis—in which a network of neighbouring atoms, determined by a cutoff, is built—fails here. In this special case, a trick is available: The diamond structure identification implemented in OVITO identifies atoms on a diamond lattice by considering the first and second nearest neighbours.[295] The output is therefore divided into atoms with full diamond symmetry, atoms where at least one of the second neighbours is not on a diamond lattice, and atoms where at least one first neighbour is not on a diamond lattice. The latter make up the outermost atoms of the crystallite. By removing them and all non-zirconium, non-diamond atoms from the analysis, the remaining atom clusters are separated far enough for the cluster analysis approach to work. In that way we can extract the number of crystallites by counting the number of clusters. The resulting 0 K properties of the samples are listed in Tab. 5.2. One peculiarity is that the potential energy starting from sample V is lower than the refer-

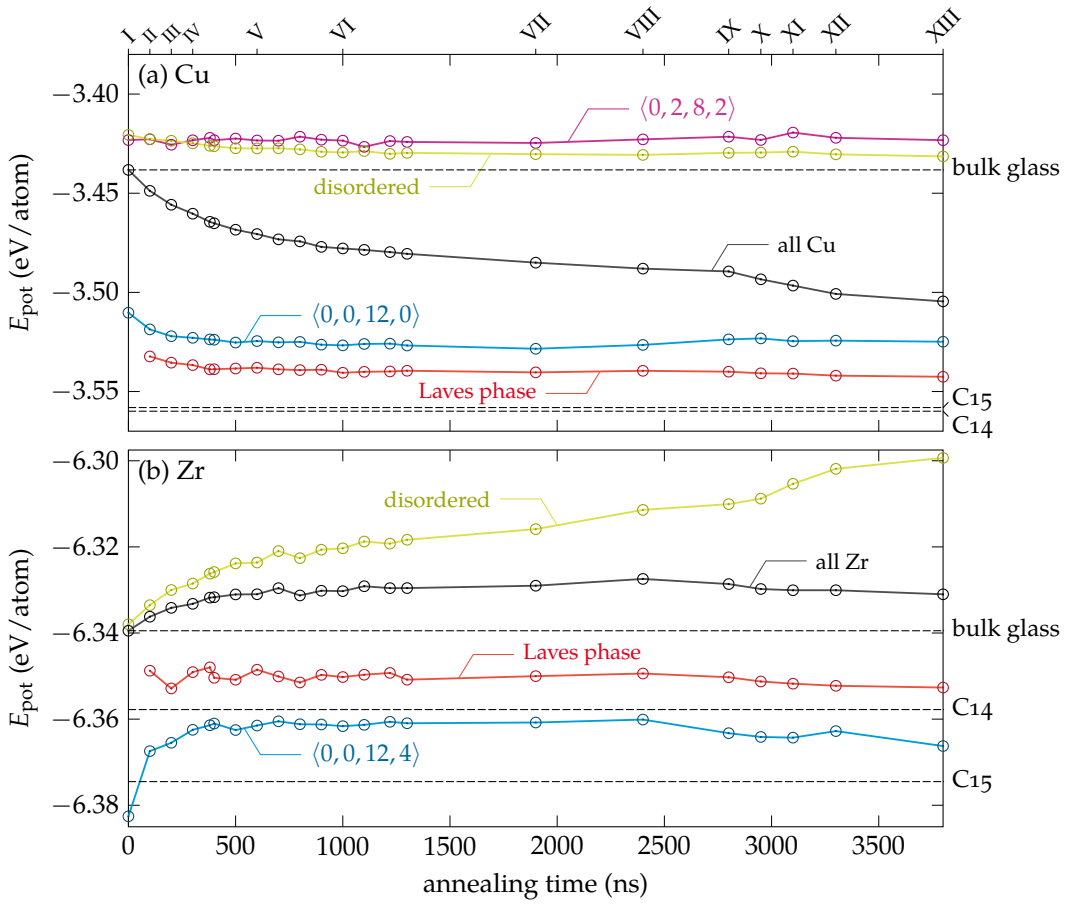

FIGURE 5.6: Energy of different polyhedra for differently annealed samples. The black curves indicate the overall averages for copper and zirconium, indicating that the potential energy of the zirconium atoms slightly increases to enable the reduction of potential energy for the copper atoms.

ence Laves phase. Given the high amount of defects in form of interfaces, this seems wrong. Therefore, a look into the evolution of the per-atom energies is in order. Figure 5.6 lists those. The energies of the different copper polyhedra stay relatively constant over the annealing time. The increasing abundance of icosahedrally coordinated copper reduces the overall energy. The energy of the Laves clusters is higher than in the reference samples because of the large surface area. For the zirconium atoms we find that the $\langle 0, 0, 12, 4\rangle$ atoms have relatively constant energies, but that the overall potential energy of zirconium atoms increases. This can only be explained because the reduction of the average energy of the copper atoms compensates that increase. The lower energy of the annealed samples compared to the reference Laves phase also becomes clear: The zirconium atoms have a lower potential energy than the copper atoms. $Cu_{64}Zr_{36}$ contains around 2.6% more zirconium than the Cu_2Zr

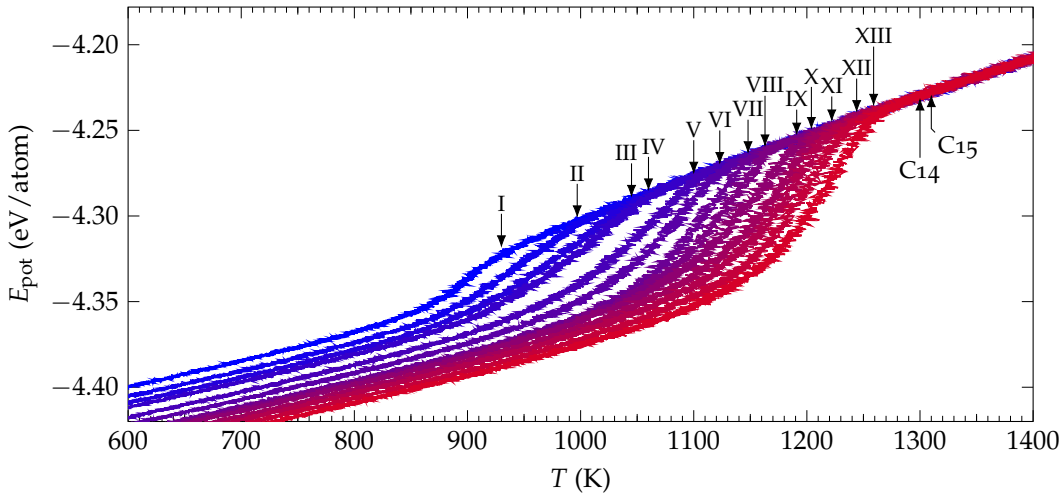

FIGURE 5.7: Change of glass transition temperature with annealing time. The arrows mark the deviation from the liquid curve and the labels indicate the sample. The melting points of C14 and C15 Cu_2Zr are also indicated.

Laves phase, which is the reason for the energetic discrepancy. No previously unknown low-energy phase could be found in the annealed samples.

5.4 CHANGE OF GLASS TRANSITION TEMPERATURE

Finally, we investigated the change of glass transition temperature T_g of the samples by heating them from 50 K to 1500 K with 0.1 K/ps. The results are shown in Fig. 5.7. We can detect the usual glass transition behaviour and a rise of the glass transition temperature with increasing crystalline volume fraction. Interestingly, no signal for the melting of the crystallites could be detected. We estimated the melting points for the C14 and C15 phases as described in Sec. 2.7 to $T_m(\mathrm{C14}) = (1300 \pm 20)\,\mathrm{K}$ and $T_m(\mathrm{C15}) = (1310 \pm 20)\,\mathrm{K}$. This is relatively close to the glass transition of the composites. It stands to reason that the melting of glass and crystal occur simultaneously, increasing the transition temperature of the composite. The high interface to volume ratio should also decrease the melting point of the crystallites.

5.5 CONCLUSIONS

The results presented here serve mostly to describe the procedure of obtaining structures with varying crystalline volume fraction by annealing and to characterise the resulting samples. These results will be built-upon in Chaps. 6 and 9. An interesting question of relevance for the glass state is if there is an upper limit to the number of favoured structural motifs in a glass.[31] The current results imply—especially concern-

ing the zirconium-centred Z16 polyhedra—that this is indeed the case. The growth of copper icosahedra is usually slow below T_g[125] and even experimental data suggests that the icosahedra fractions in typical simulations may not be much lower than in real glasses.[99,102,103] This indicates that the glasses obtained with cooling rates achievable in simulation may contain close to the maximum amount of ordered motifs. This is supported by the fact that the relative change of polyhedra statistics of motifs that do not partake in crystallisation is very small. A significant change of SRO is only due to the appearance of the crystallites, and zirconium-centred Z16 polyhedra seem to be mostly connected to this crystallisation as they play a minor role in the as-cast glass.

6 DISORDER AND THE BOSON PEAK

The results in Secs. 6.1 and 6.3 were first published in Refs. 327 and 328.

Amorphous materials show an excess contribution in the terahertz region of the vibrational density of states (VDOS) as compared to the corresponding crystal or the Debye model. This manifests as a peak when plotting $g(\nu)/\nu^2$ over ν and is called the boson peak. The boson peak is known for decades[221] and its origin has been controversially discussed ever since (see Sec. 1.8). Until recently, the consensus was that "defective" regions in the glass are responsible.[95,227–236,242–245] The nature of these defects is also not conclusively solved, but the idea that the resulting disorder leads to fluctuating force constants—which in turn are responsible for the boson peak—has gained some traction.[220,238–241] The idea of defective regions in the glass has also attracted attracted attention for explaining the mechanical properties of metallic glasses: So-called "soft spots" were not only connected to the boson peak but were also identified as regions susceptible to STZ activation.[95,234]

In 2011, a completely different theory was proposed, in which the boson peak was attributed to a shifted van Hove singularity that is also present in crystalline materials.[248–252] Declaring that the boson peak is not an anomaly, the authors proposed that this shift is simply due to the lower density of amorphous materials and that the boson peak is not an independent phenomenon.

As the possible connection of the boson peak to soft spots in glasses suggests a broader relevance of the boson peak phenomenon, a clearer picture of its origins may also be useful to better understand the mechanical behaviour of metallic glasses. If, on the other hand, the boson peak is simply a shifted van Hove singularity, a connection to the mechanics of glasses seems tenuous. The goal of this chapter is therefore to shed more light on the origin of the boson peak.

6.1 THE BOSON PEAK IN DEFORMED METALLIC GLASSES

The virtual sample of a sheared metallic glass was provided by Leonie Koch from Technische Universität Darmstadt.

While the phenomenon of the boson peak is well known for decades, it was mostly investigated in homogeneous amorphous solids. Given that many models favour a defect-based picture for the boson peak origin, it stands to reason that "defective" regions in the glass—such as shear bands—should have an influence on this anomaly.

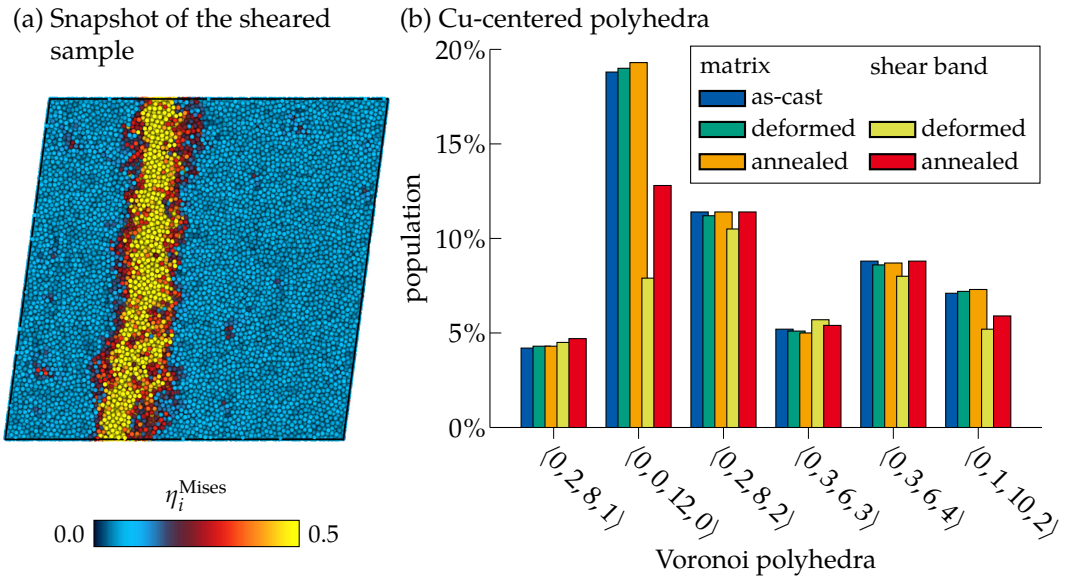

FIGURE 6.1: Structure of the as-cast, deformed, and annealed sample. (a) Snapshot of the sheared sample coloured according to atomic shear strain. (b) Voronoi analysis of the matrix and shear band for the six most common copper-centred polyhedra. Data from the as-cast and deformed glasses, as well as the sample after 40 ns annealing.

Shear bands are characterised by a defective short-range order and often also by a reduced density. While the boson peak's origin is still controversially discussed, at least one of these shear band properties were connected with the boson peak in all currently favoured models.

As such, we investigated the evolution of the boson peak signal for deformed glasses and also for subsequently annealed samples to trace the relaxation processes in the shear band. We performed MD simulations with the Mendelev potential[124] to produce the glass and measure the VDOS. The glass sample was quenched from the melt to 50 K with a cooling rate of 10^{10} K/s and replicated $2 \times 2 \times 2$ times to a final simulation box with 364 500 atoms. Shear band formation was induced by a volume conserving shear deformation with a shear rate of $10^8\,\text{s}^{-1}$ up to a total shear strain of 20%. The system was subsequently unloaded and annealed at 500 K for 40 ns. We extracted snapshots after 20 ns and 40 ns annealing time and cooled them independently to 30 K. In total, we investigated four states: The as-cast sample, the deformed and subsequently unloaded sample, the sample after 20 ns annealing, and the sample after 40 ns annealing.

We differentiated between shear band and matrix with the help of the atomic shear strain, using $\eta_i^{\text{Mises}} > 0.2$ as a criterion for the shear band. Atoms with a lower η_i^{Mises} were marked as belonging to the matrix. We then calculated the partial VDOS for shear band and matrix using the velocity auto-correlation function as described in Sec. 2.8.2. Additionally, to facilitate comparison to the experiment, we used the

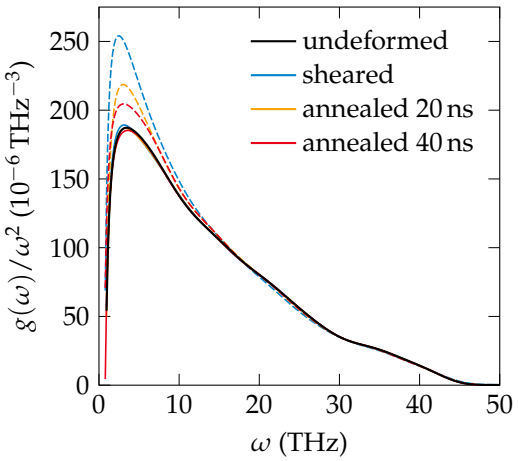

FIGURE 6.2: Vibrational density of states of an as-cast, deformed, and annealed $Cu_{64}Zr_{36}$ metallic glass. Dashed lines represent the VDOS in the shear band, solid lines in the rest of the sample. During processing only the shear band contribution changes, the matrix stays unperturbed. Adapted from Ref. 327, © *2014 American Physical Society.*

harmonic approximation to calculate the heat capacities (cf. Sec. 2.8.3) of the glass samples and a CuZr crystal in the B2 structure.

The deformed sample with a clearly defined shear band is depicted in Fig. 6.1 (a). We performed a Voronoi analysis of the as-cast state, the deformed sample, and after 40 ns annealing. The statistics, shown in Fig. 6.1 (b), reveal that the deformation is accompanied by a reduction of copper-centred icosahedral units. This points to a reduction of short-range order under deformation, as reported in the literature.[125] Additionally, we can see that the matrix stays unperturbed by the localised deformation and exhibits a very slight increase of icosahedral units with time. As already discussed in the previous chapter, the as-cast glass is not fully relaxed and always strives to increase the number of $\langle 0, 0, 12, 0\rangle$ copper polyhedra when it has enough activation energy. Consistent with earlier simulation studies,[125] the density of the shear band is reduced by roughly 1% compared with the matrix and stays like this even during annealing. Because of the constant volume during the simulation, the matrix is slightly compressed by the expanding shear band by less than 0.2%.

After analysing the structure of our system throughout the deformation and annealing procedure, we measured the partial VDOS for matrix and shear band. Figure 6.2 shows the resulting VDOS data. The trend is the same as for the structure: The matrix stays unchanged over all steps, while the shear band region exhibits an increased boson peak signal for the deformed sample. With annealing, this signal is reduced again, while the structural order in the shear band is recovered. It should be noted that the peak position does not shift very much on the frequency axis. Because of plotting $g(\omega)/\omega^2$, shifting a peak to lower frequencies means an increase of the peak height. Models ascribing the boson peak to a shifted van Hove singularity posit that the reduced density of the glass shifts the singularity to lower frequencies thereby increasing its peak height in the chosen reduced plot. If that was the case, the decreased density in the shear band should lead to a boson peak at even lower frequencies. The peak height in our results, though, increases without accompanying

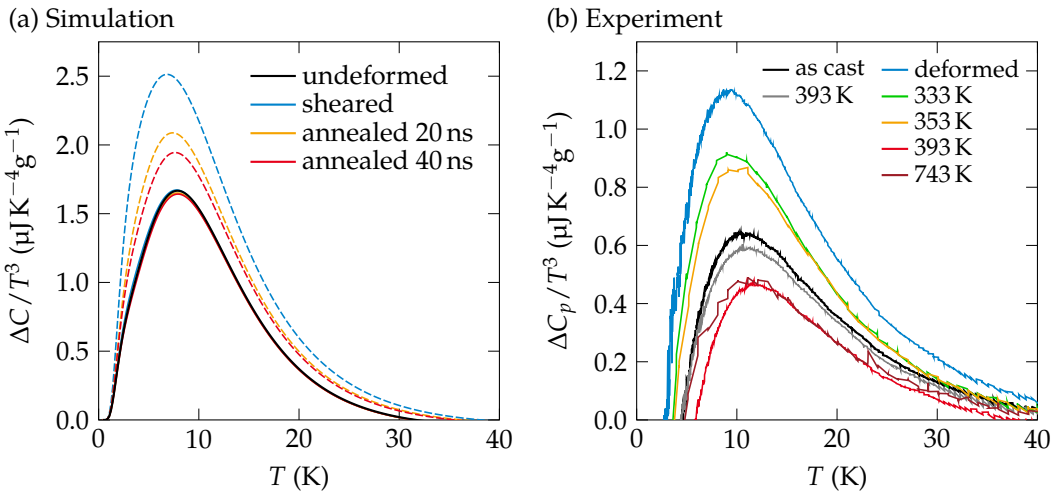

FIGURE 6.3: Boson peak in the heat capacity from simulation and experiment. The plots show $\Delta C/T^3$, where ΔC is the difference in heat capacity between the glass and a reference crystal. (a) Simulation data; dashed lines are data from shear bands, solid lines from the rest of the sample. The reference crystal was a B2 CuZr single crystal. (b) Experimental data from a $Zr_{50}Cu_{40}Al_{10}$ BMG. Annealing below 393 K was done for one week, annealing at 743 K for 10 s. The reference crystal was a glass heated and equilibrated above the crystallisation temperature. Experiments were performed by colleagues from WWU Münster, Germany and National Institute of Materials Science, Japan as part of a collaboration (see Ref. 327 for details). Adapted from Ref. 327, © *2014 American Physical Society.*

frequency shift. This would be an indication that the enhancement is not due to the density change.

The work presented here was part of a collaboration including experimental measurements of the heat capacity.[327] As discussed in Sec. 2.8.3, the boson peak also appears in the heat capacity when plotting C/T^3, so that an excess over Debye's T^3 law for the heat capacity is revealed. This allows for a comparison to the experiment. We first converted the phonon calculations to heat capacities as described in Sec. 2.8.3. This was repeated for a B2 CuZr crystal. Fig. 6.3 (a) contains a plot of $\Delta C/T^3$ with $\Delta C = C_{\text{glass}} - C_{\text{B2}}$ to show the excess heat capacity over the crystal. A boson peak signal is visible and the trend is the same as in Fig. 6.2. The experimental data was obtained by subjecting a $Zr_{50}Cu_{40}Al_{10}$ BMG to severe torsional deformation under a high applied hydrostatic pressure.[327,329] This leads to a plastic deformation of almost the whole sample, which can now be considered a "macroscopic shear band", maximising the signal due to structural changes. Figure 6.3 (b) contains the resulting $\Delta C/T^3$ measurements. In this case the crystalline reference was a $Zr_{50}Cu_{40}Al_{10}$ sample heated above the crystallisation temperature. The findings agree qualitatively with our results. A quantitative comparison is not appropriate, as the glass composition is different and because the volume fraction of the shear band region is unknown in the experiment. Annealing an undeformed sample (which corresponds to

the matrix in our samples) leads to very small relaxation-related changes in heat capacity. The deformed sample instead exhibits a significant increase of heat capacity which is reduced by subsequent annealing. The reduction of the boson peak below the value of the as-cast sample is of note. It indicates that a structural relaxation is made possible in the shear band region that is not accessible to the as-cast sample which was subjected to the same heat treatment. The nature of this relaxation is still unclear—crystallisation could not be detected with x-ray diffraction.

For $Cu_{64}Zr_{36}$, earlier simulations demonstrate that the shear band relaxes back to a glass-like state.[125] This is in contrast to the current experimental data but may be explained by the different composition of the glasses. It is clear that diffusion in shear bands is enhanced,[125,193] which could promote structural relaxation and short to medium range ordering that drives the system to another meta-basin in the energy landscape. The reduction of the boson peak signal hints to an increasingly crystal-like structure which may not be resolvable in x-ray diffraction. The phenomenon seems to be applicable more generally, as it was also found in Pd–Ni–P glasses.[330]

Still, the simulations prove that an increased boson peak signal originates from the defective shear band region and give a first hint that the boson peak may be connected to the increasing disorder and not the decreased density, as a shift of the peak on the frequency axis was observed neither in experiment nor in simulation.

6.2 THE BOSON PEAK IN RELAXED METALLIC GLASSES AND CRYSTAL–GLASS COMPOSITES

If the boson peak signal is sensitive to increasingly defective regions in the glass, the opposite must also be true. Glasses that are thermally relaxed or have started crystallising, such as the samples discussed in Chap. 5, should exhibit a lowered boson peak signal. We therefore measured the VDOS of our annealed systems I–XIII. The results are presented in Fig. 6.4 (a), together with the calculations from the previous section. In general, the trend is that the boson peak signal is the highest in the unrelaxed shear band, followed by the as-cast glass, and reduces further with increasing annealing time of the as-cast glass. In addition to the decrease of the boson peak at $\nu \approx 1\,\mathrm{THz}$, a small peak at 2 THz appears.

As a simple measure for the "strength" of the boson peak signal, we consider the height of the peak. We considered the correlation of this peak height with two quantities in Fig. 6.4 (b). First we used the fraction of "ordered" Voronoi polyhedra f_{ordered}, defined as copper-centred $\langle 0, 0, 12, 0\rangle$ icosahedra and their distortion $\langle 0, 2, 8, 2\rangle$, as well as zirconium-centred $\langle 0, 0, 12, 4\rangle$ polyhedra. Second, we used the number density ρ_n. Both correlations work well for the undeformed and annealed samples, but not for the shear band data. Indeed, the shear band keeps its density approximately constant during annealing while the fraction of ordered polyhedra increases in step with a decrease of the boson peak height.

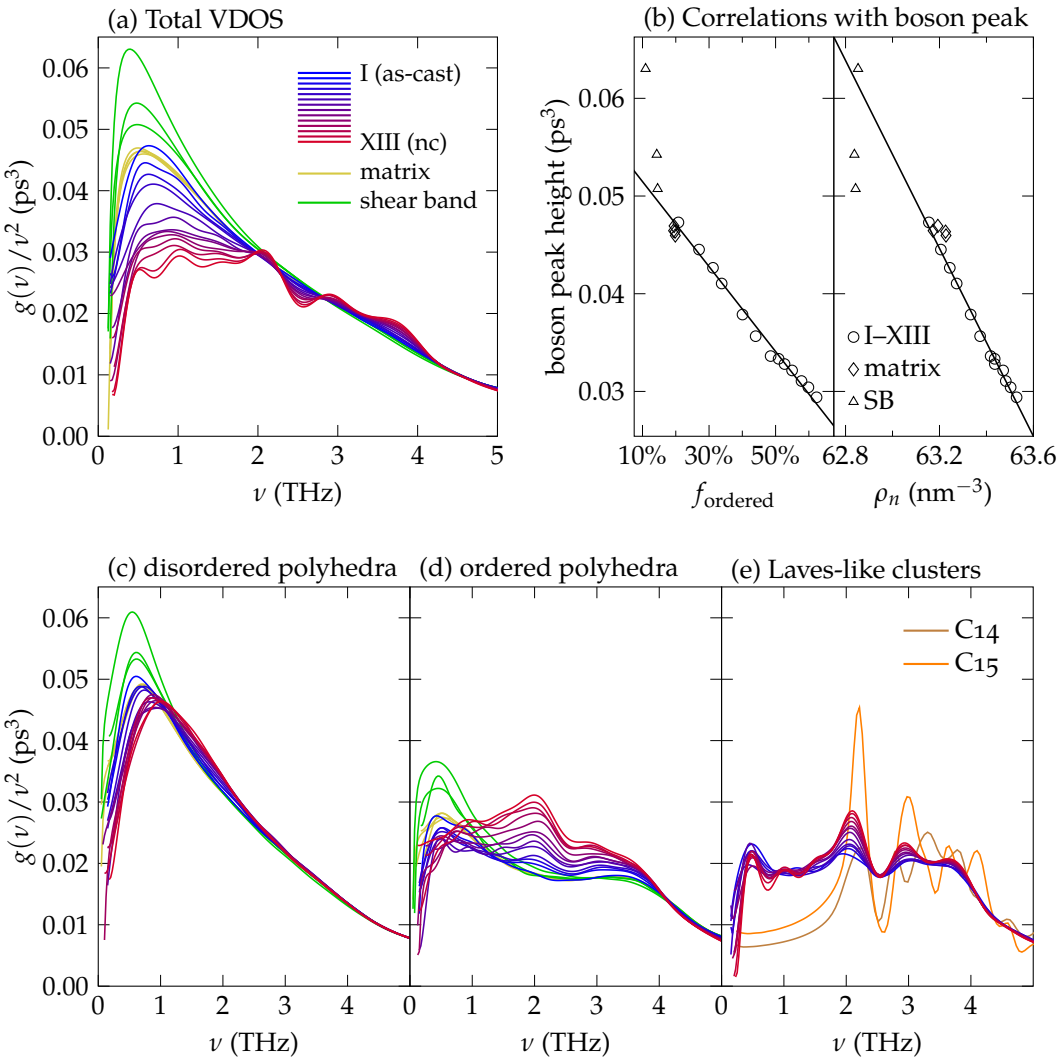

FIGURE 6.4: The boson peak of as-cast, deformed, annealed, and partially crystallised $Cu_{64}Zr_{36}$ glasses. (a) The total VDOS of samples I–XIII from Chap. 5 and the deformed sample from Sec. 6.1. In the latter case the contributions of the shear band and the matrix are plotted separately. (b) Correlations between the boson peak height and f_{ordered}, as well as the density ρ_n. The fraction f_{ordered} is defined is the fraction of atoms at the centre of copper-centred $\langle 0,0,12,0\rangle$, copper-centred $\langle 0,2,8,2\rangle$, or zirconium-centred $\langle 0,0,12,4\rangle$ polyhedra. (c)–(e) Partial VDOS of ordered polyhedra (d), atoms that are part of a C14 or C15 crystal lattice (e), and other atoms (c). The VDOS of single-crystalline Cu_2Zr was added to (e).

An explanation of this can be found by looking at the partial VDOS for disordered polyhedra, ordered polyhedra, and Laves-like clusters in the glass. Figures 6.4 (c)–(e) show that the partial VDOS stays relatively constant for these categories, except for the case of the shear band, which shows an increased boson peak signal in all cases. That indicates that the separation into "ordered" and "disordered" atoms or regions

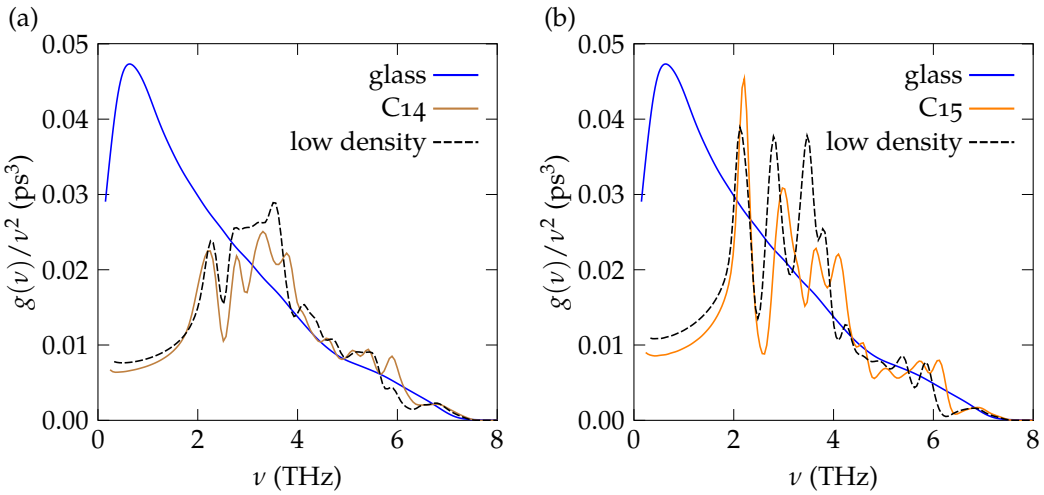

FIGURE 6.5: VDOS for Laves phases elastically expanded to the density of $Cu_{64}Zr_{36}$ glass. In the low-frequency range, no significant changes occur. A comparison with data from a glass shows that the boson peak differs in shape and frequency from the first van Hove singularity of the Laves crystal, even with modified density.

is an incomplete explanation. The appearance of the 2 THz peak can be explained, though: It is a feature of the crystalline VDOS of the C14 and C15 Laves phases. This peak also appears in Figs. 6.4 (c)–(d) because the phonons of the crystalline phase are delocalised and intrude into the neighbouring regions.

We also excluded that a density-induced frequency shift of VDOS features of the C14/C15 phase is identical with the boson peak. Figure 6.5 shows the VDOS of the as-cast glass and the C14/C15 phases compared with "low-density" versions of those crystalline phases. The low-density samples were produced by scaling the crystal to the same number density as the glass. In the low-frequency range, there is only a very small change of the VDOS. Still, the Laves phases have a slightly different composition than the $Cu_{64}Zr_{36}$ glass and may therefore be an unsuitable reference. What is needed to answer the question of the origin of the boson peak is a simpler, more adaptable model.

6.3 THE ORIGIN OF THE BOSON PEAK IN ALLOYS – CHEMICAL DISORDER, STRUCTURAL DISORDER, OR DENSITY?

This work is part of a collaboration with Leonie Koch from Technische Universität Darmstadt, who provided the high-entropy alloy samples. All analyses presented here were performed by the author.

While the above already indicates that the boson peak is disorder related, one could still argue that the disorder is always accompanied by a lower density. Given the

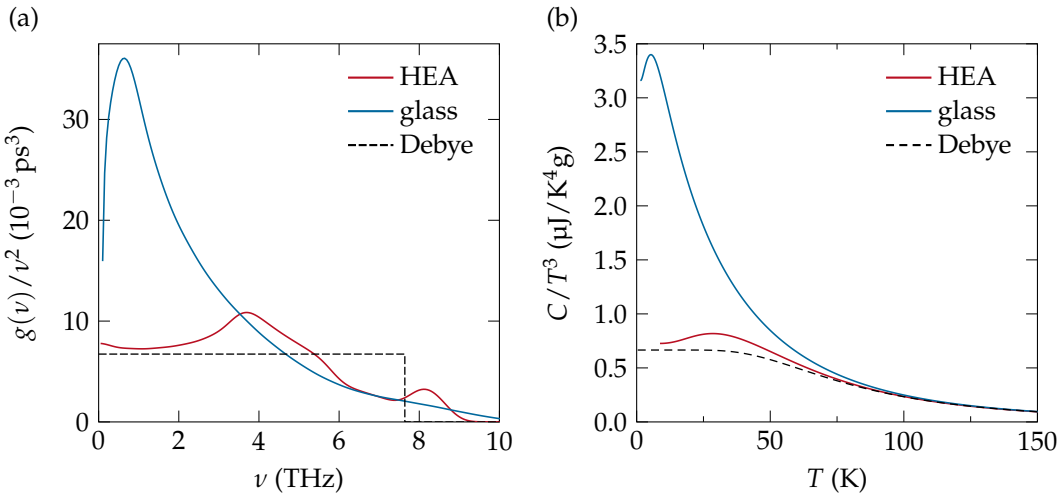

FIGURE 6.6: Vibrational density of states and heat capacity of a CuNiCoFe high-entropy alloy and a glass with the same composition. In addition, the data from the Debye model with a Debye frequency fitted to the HEA data is plotted. Adapted from Ref. 328, © *2016 American Physical Society.*

wide variety of theories for the origin of the boson peak, we opted to test them on a model high-entropy alloy (HEA). HEAs are metallic alloys consisting of at least four elements with equal or near-equal molar fractions.[331–333] Some of these HEAs are considered to be thermodynamically stable, single-phase materials, stabilised by the high configurational entropy.[331–333] If we look at these materials from a lattice dynamics viewpoint, we can consider them to be simple crystal lattices with fluctuating force constants due to the random distribution of elements on the lattice. Because of their chemical disorder, HEAs can be considered to be related to metallic glasses; their highly alloyed state also makes them limited glass formers, allowing us to prepare a glass and a crystal of the same composition. With these ingredients, we obtain a highly tunable model system that contains disorder on a lattice and consequently also fluctuating force constants. We can independently scale the density of the lattice, gradually introduce disorder by introducing defects, and compare the results to a glass of the same composition.

We used MD simulations with an EAM potential by Zhou *et al.*[309] on CuNiCoFe samples consisting of 102 816 atoms (approximately $10 \times 10 \times 10\,\mathrm{nm}^3$). The synthesis of the samples is described in Ref. 328. The HEA consists of equal amounts of all four elements distributed on an fcc lattice. In addition to the HEA, we prepared a glass of the same composition by quenching from the melt with $10^{13}\,\mathrm{K/s}$, which corresponds roughly to the minimum cooling rate needed to avoid crystallisation. VDOS calculations were performed at 30 K as described in Sec. 2.8.2.

A comparison of the VDOS of HEA and glass is plotted in Fig. 6.6 (a). The HEA was a defect-free single crystal. While an excess over the Debye model occurs for

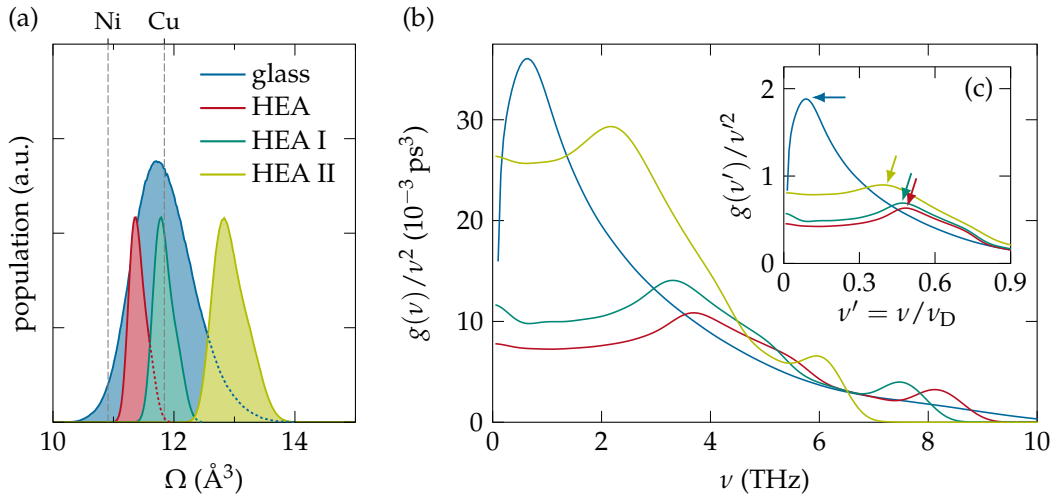

FIGURE 6.7: Change of the VDOS with density in the HEA. (a) Atomic volume (Ω) histogram of a CuNiCoFe glass (blue) and HEA (red) at 30 K. The atomic volumes in the HEA lie between those of fcc Ni and Cu, a small and a large constituent element of the alloy. We scaled the HEA, once so that it has the same average atomic volume as the glass (HEA I), and once so that it covers the range of highest atomic volumes found in the glass (HEA II). (b) The resulting VDOS of the scaled samples show a shift and enhancement of the first peak from around 4 THz to 2 THz, but they do not fall on top of the boson peak of the glass. (c) When plotting the same as a function of the reduced frequency $\nu' = \nu/\nu_D$, the peaks of HEA, HEA I, and HEA II fall more or less on top of each other, but stay different from the boson peak in the glass. Adapted from Ref. 328, © *2016 American Physical Society.*

both materials, the boson peak in the glass is situated—as usual—at around 1 THz, while the HEA has a peak at around 4 THz. An excess contribution is also present in the heat capacity, presented in Fig. 6.6 (b), which is again more pronounced for the glass. So while excess modes exist in the HEA, they are not a boson peak. Recently, though, it was proposed that the boson peak is no glass-specific phenomenon at all and is simply a crystalline van Hove singularity shifted by the difference of density between glass and crystal.[248] Looking at a histogram of atomic volumes in the HEA and the glass in Fig. 6.7 (a), we can see that the glass is expectedly less dense. The volume of atoms in the HEA varies between the equilibrium values of fcc nickel and fcc copper, a small and a large constituent species of the alloy. In a first step we therefore elastically expanded the lattice, so that the average density is equal to that of the glass (HEA I). For Cu–Zr-based glasses, it was reported that only those 10% of atoms contribute to the boson peak which exhibit the highest mean square displacements.[233] It stands to reason that if the boson peak is a density-related shift, these atoms "rattle in their cage" because they are situated in less-dense regions. We therefore prepared another setup, HEA II, in which the lattice was scaled so that the atomic volumes match the highest atomic volumes in the glass. Figure 6.7 (b) shows the resulting VDOS together with data from the glass. While a shift of the HEA peak

to lower frequencies is observed as expected, it only shifts to about 2 THz and does not reach the same height as the boson peak. This excludes that the glassy VDOS is simply a shifted and smeared-out version of the crystalline VDOS. Even if we assume that the total signal is the sum of contributions from regions of different density, the low-density lattice contribution is too weak and is located at frequencies that are too high. In fact, when plotting the data as a function of $\nu' = \nu/\nu_D$ as in Fig. 6.7 (c), the values for the scaled HEAs fall more or less on top of each other, while the boson peak in the glass remains at much lower ν'. With this, we can state that the fluctuation of force constants on a lattice due to chemical disorder is not sufficient to induce a boson peak and neither is the boson peak simply a shifted feature from an equivalent lattice. The latter is in accord with the previous sections.

Given that we previously established some link between the level of disorder in a $Cu_{64}Zr_{36}$ glass and the strength of the boson peak, it stands to reason to introduce defects into the system to investigate their influence on the VDOS. In the literature, a wide range of defects have been proposed for glasses. The boson peak was related to the lattice dynamics of defects[229] or loosely packed atoms[227,231,233] and subatomic voids.[234] We chose to follow interstitialcy theory which proposes that melting can be understood as the generation of increasing numbers of interstitials which finally lead to the collapse of the crystal lattice.[334] These features persist in the melt and therefore also in glasses.[334] To model this process, we introduced varying amounts of interstitials into our HEA and equilibrated the system at 30 K and ambient pressure. CNA reveals the resulting state of disorder in the system. We obtained samples with 0.5% and 1% of interstitials; one sample in which the lattice partially collapsed and which contains a mix of interstitials, stacking faults and dislocations; one sample in which 72% of the atoms are amorphous; and one sample in which only clusters of a few atoms remain on an fcc lattice and the rest is disordered. The VDOS of these systems is plotted together with reference data from the defect-free HEA and the quenched glass in Fig. 6.8. A boson peak occurs already at low defect concentrations and rises with increasing disorder in the system. Looking at the partial VDOS of only the defective atoms, we can see that a boson peak almost comparable to the as-quenched glass already appears for 0.5% of interstitials in the system. The system which also contains dislocations and stacking faults has a weaker boson peak, which indicates that the stacking faults and dislocations do not contribute, thereby reducing the integrated value. The atoms on intact fcc lattice sites only start showing a low-frequency peak when the amount of defects in the system becomes very high, and therefore a lot of fcc-ordered atoms are neighbours of defective structures. In that case the boson peak can partially intrude into the lattice. Still, it seems that the modes of the boson peak are mostly localised at the defects. A look at the non-reduced vibrational spectra in the insets reveals that the general features of the crystalline VDOS persist in the defective samples, although smeared out, and that the boson peak modes are indeed an additional feature. Two additional peculiarities are noticeable. First, the fully amorphous sample has a boson peak at slightly lower frequencies than the quenched

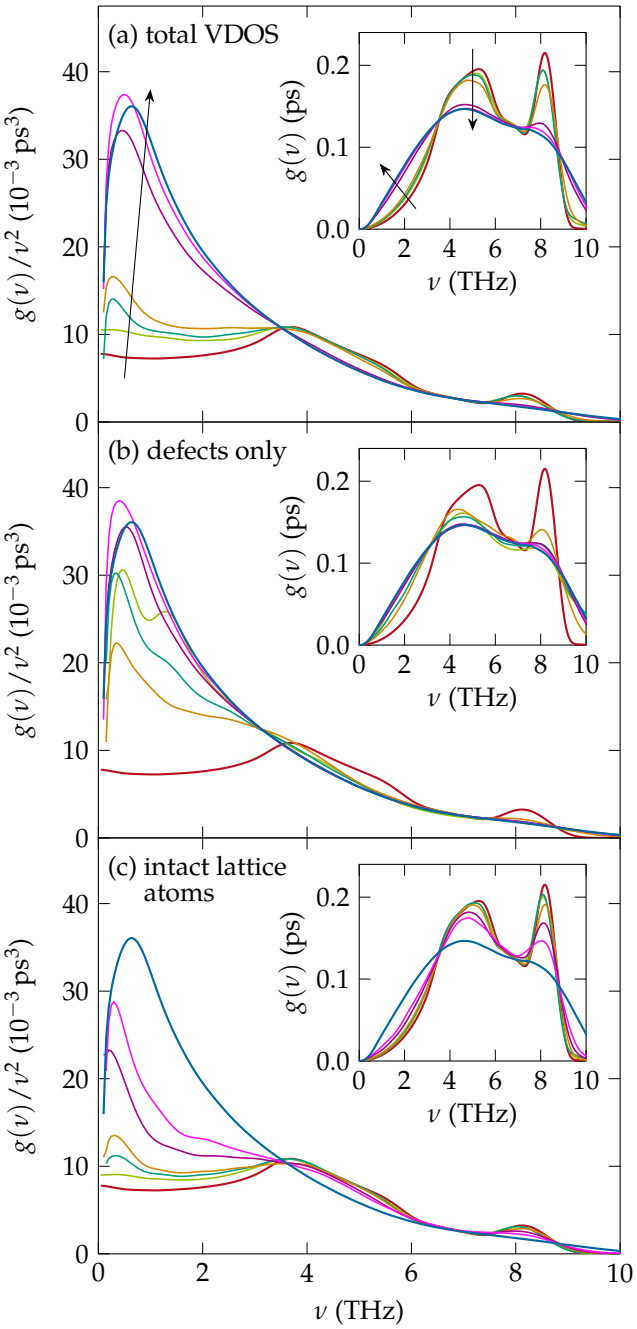

FIGURE 6.8: The VDOS of HEA samples with increasing amount of interstitial defects. The insets show the non-reduced VDOS. (a) The total VDOS increases with the defect concentration. (b) Partial VDOS of the atoms identified as non-fcc by CNA. An almost full boson peak is exhibited by those atoms. Data for the defect-free HEA and the glass are shown for comparison. (c) Partial VDOS for atoms on fcc lattice sites. The boson peak modes intrude only at very high defect concentrations. Adapted from Ref. 328, *© 2016 American Physical Society.*

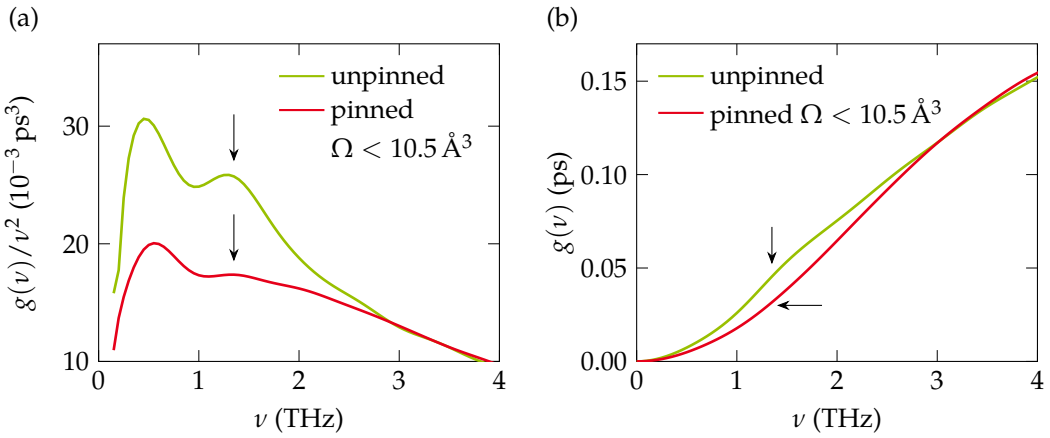

FIGURE 6.9: Origin of the split boson peak for a HEA with 0.5% interstitials. When pinning the atoms with low atomic volume ($\Omega < 10.5\,\text{Å}^3$), the peak above 1 THz disappears. This suggests that the splitting results from a density-related shift of the boson peak. Adapted from Ref. 328, © *2016 American Physical Society.*

glass. The reason is that the collapsed sample did not have time to relax and is therefore less dense. This slightly shifts the VDOS to lower frequencies. Second, the boson peak for the interstitials seems to be split into two separate peaks. This is especially so for the sample with 0.5% interstitials. While a chemically ordered system would only exhibit compressed atoms around interstitials, the HEA will locally re-arrange when inserting interstitials and the resulting system contains both atoms with lowered and atoms with increased atomic volume. Figure 6.9 shows what happens if we pin the atoms with a low volume so that they do not contribute to the vibrations in the system anymore. The boson peak is reduced, but the second peak at around 1.5 THz is suppressed almost completely. This demonstrates that the split observed in the data results from these compressed atoms. As we will see later, the system gets rid of these unfavourable atoms with increasing disorder, as the disturbed lattice can more easily accommodate the excessive atoms.

This data shows that defects in the form of interstitials can induce a boson peak, which is localised at the defects. To understand why, it pays to have a closer look at the fluctuations of force constants again. Derlet *et al.* connected regions exhibiting a softening of the lowest of the five Kelvin shear moduli $\mathcal{G}_1$ (see Sec. 2.5.3) with the boson peak.[243] Atoms which have a positive but reduced $\mathcal{G}_1$ compared to the sample average were found to participate in the low-frequency modes of the boson peak.[243] We calculated a per-atom value of $\mathcal{G}_1$ as described in Sec. 2.5. Histograms of atomic volumes and shear moduli are shown in Fig. 6.10. As expected, fluctuations in both atomic volume and shear modulus are present in a defect-free HEA. The fluctuations in both values are much higher when defects are introduced. Especially noteworthy is that atoms with shear moduli somewhere between 0 GPa and 25 GPa appear as soon as interstitials are introduced. These atoms are mostly defective, as evidenced

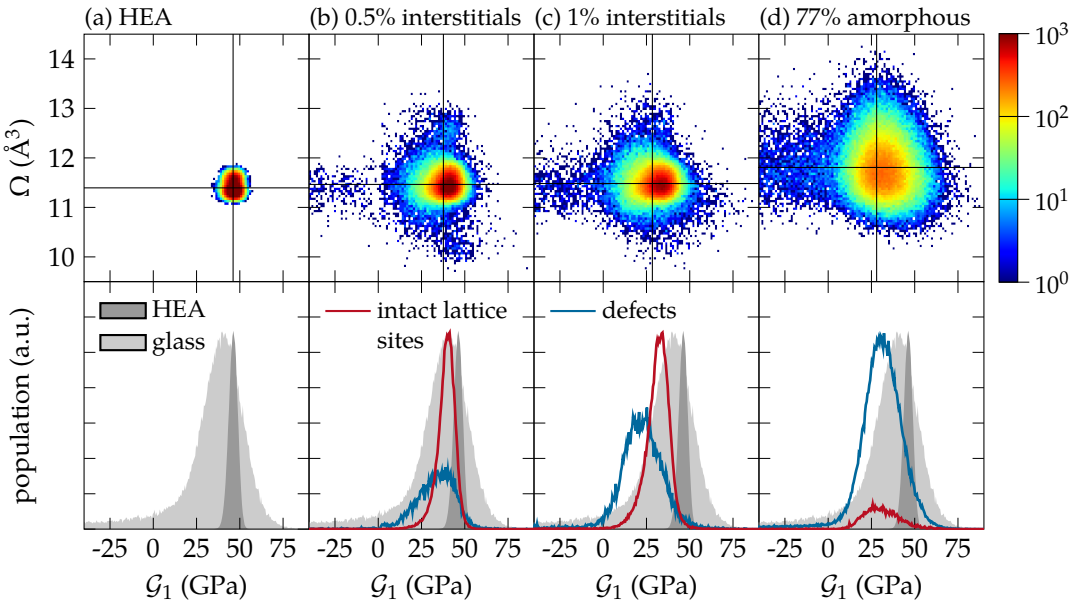

FIGURE 6.10: Histograms of the per-atom shear moduli and the atomic volume. The upper row shows 2D histograms of both the shear moduli $\mathcal{G}_1$, as well as the atomic volumes Ω with a logarithmic colour scale, while the lower row contains only the histograms of the shear moduli divided into defective atoms and atoms on intact lattice sites. The grey areas in the lower row serve as a reference and represent the distributions of shear moduli in the glass (light grey) and in the defect-free HEA (dark grey). For the sample in (b), compressed atoms as well as expanded atoms appear because of relaxation of the complex HEA lattice. In (c) the disorder in the system is high enough to accommodate the compressed atoms and the low atomic volumes disappear. Adapted from Ref. 328, © *2016 American Physical Society.*

by the lower row of Fig. 6.10. Thus, with increasing defect content in the system, the amount of regions with low shear moduli rises together with the boson peak. Additionally, an overall softening of the system with 1% interstitials is observable and hints towards an increasing instability due to the high defect concentration. The mostly amorphous system in Fig. 6.10 (d) is softer than the as-quenched glass which can again be explained by the fact that the latter had more time to relax. None of the atomic volumes in the defective samples exceed the values in HEA II.

As to the boson peak, small fluctuations of the force constants on a lattice are not the origin but rather significant softening is needed which is not present in the defect-free lattice. In the literature, defects which are held responsible for the boson peak are described as interstitialcies,[235,236] "liquid-like" regions,[95,234] "rattling" atoms,[232,233] or simply fluctuating force constants.[220,238–241] This poses the question if these observations are as different as they sound at first. We therefore calculated the mean square displacement of the atoms in our defective samples at 30 K over a period of 100 ps. The results are shown next to maps of the shear moduli and the results of the CNA in Fig. 6.11. There is a clear spatial correlation between low shear moduli,

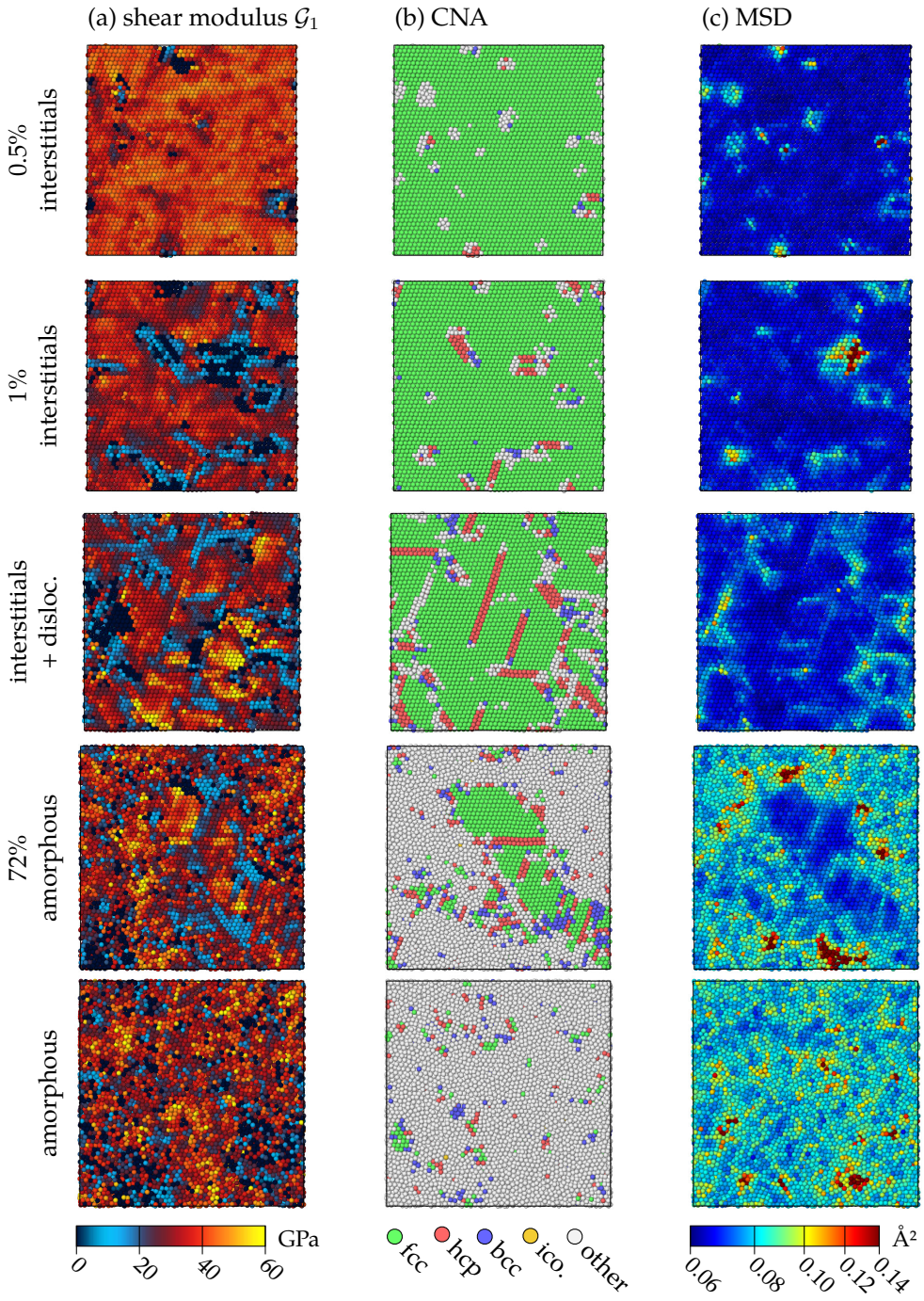

FIGURE 6.11: Snapshots of HEAs with defects, colour coded according to shear modulus, CNA, and mean square displacement (MSD). A correlation between low shear modulus (a), defects as identified by CNA (b), and high mean square displacement (c) is apparent. The colour scale in (c) is logarithmic to enhance the visibility of small displacement values. Adapted from Ref. 328, © *2016 American Physical Society.*

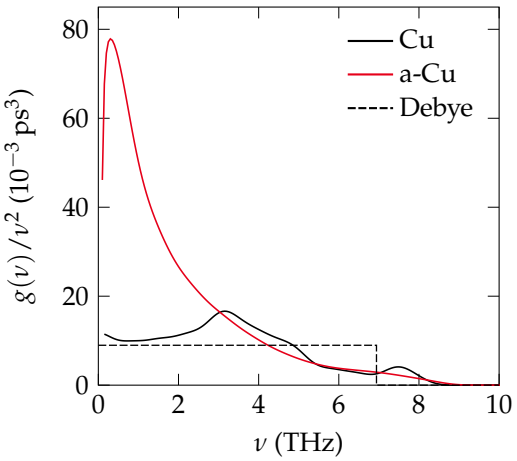

FIGURE 6.12: Vibrational density of states of fcc and amorphous copper. The shape of the crystalline VDOS resembles that of the HEA with a van Hove singularity at $\nu \approx 3.5$ THz. Again, a boson peak occurs only in the glass but does not require chemical disorder. Adapted from Ref. 328, © *2016 American Physical Society.*

structural defects, and high mean square displacement. This connection is not surprising: Defects are known to soften the material[334] and low moduli are indicators of shallow potential wells which lead to increased atomic "rattling", visible as high mean square displacement. These properties of defective regions resemble the picture of "soft spots" proposed for metallic glasses.[95,234] It appears that previous suggestions for the origin of the boson peak are simply different viewpoints on the same phenomenon. These soft spots are almost impossible to introduce into a defect-free lattice, which explains why the HEA does not exhibit a boson peak.

As a final step, we tested if the chemical disorder is relevant at all and removed it by considering a pure copper system. Figure 6.12 contains the VDOS of an fcc copper crystal and an amorphous copper sample (a-Cu) quenched from the melt with 10^{14} K/s. Even without chemical disorder, the structural disorder in the amorphous system is sufficient to induce a boson peak. The fcc copper exhibits an excess over the Debye model at around 3.5 THz, which is a van Hove singularity due to critical points in the Brillouin zone.[335] The shape of the VDOS resembles that of the HEA, indicating that the excess modes in the HEA are a van Hove singularity and that the excessive heat capacity is also due to this singularity. Contrary to recent theories,[248–252] this van Hove singularity is not the same as a boson peak. As demonstrated above, a van Hove singularity which is shifted by modifying the density of the lattice does not necessarily coincide with the boson peak, and does not do so in the presently investigated alloy. Furthermore, the features of the crystalline VDOS also appear in the glass, although heavily smeared out. This points out that there is no general, large shift of frequencies.

All in all, the current work supports the conclusion that the boson peak in alloys results from (quasi-)localised additional modes. The vibrational spectra in defect-free and defective HEAs as well as in a quenched glass of the same composition share the same general features, although more defective structures smear out the VDOS. The modes associated with the boson peak arise as excess modes and are more or

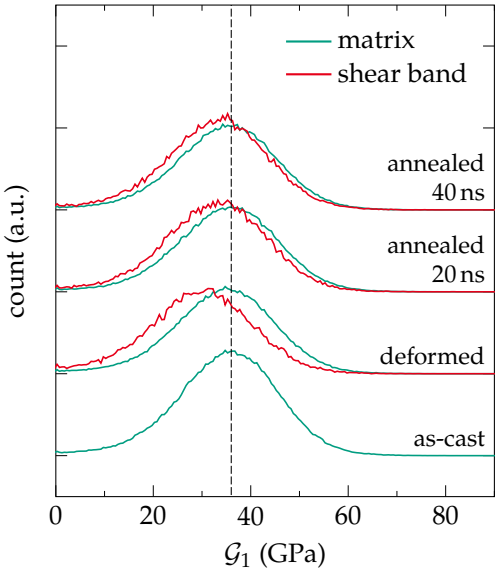

FIGURE 6.13: Change of shear modulus in matrix and shear band by annealing a deformed $Cu_{64}Zr_{36}$ glass. Like the VDOS in Fig. 6.2, the distribution of per-atom shear moduli in the matrix stays constant, while the shear band is softened in comparison. After annealing, the shear band recovers somewhat but is still softer. The counts for the matrix were divided by 5, so that the height of the peak is comparable to the shear band value, as the shear band occupies roughly 1/6 of the volume. The dashed line corresponds to the maximum of the shear modulus distribution in the matrix.

less localised to defective regions. Defect-based pictures of the boson peak origin can be united by considering "rattling" of atoms, low local density, and the softening of moduli to be symptoms of the breakdown of local order. This is equivalent to the picture of soft spots which were also connected to the boson peak in literature.[95,234,242,243] The soft spots were not only connected to the rather specialised topic of the boson peak but also to mechanical properties of glasses, as these soft spots are more susceptible to the activation of STZs,[95,234] suggesting a connection between elastic and plastic mechanical response in glasses.

6.4 SOFTENING IN COPPER-ZIRCONIUM GLASSES

These results point to the importance of softening in the material for explaining the boson peak. We applied this to our Cu–Zr-based samples and calculated the per-atom shear moduli, too. As to be expected, the shear band is softened compared to the matrix, while the matrix does not change its distribution of elastic constants. Figure 6.13 shows the distribution of shear moduli in matrix and shear band. The shear moduli of the matrix atoms stayed more or less constant during the processing, while the shear band in the deformed sample is the softest. Subsequent annealing hardens the shear band again. The amount of atoms softened to values below $\mathcal{G}_1 =$ 25 GPa to 30 GPa seems to be a likely figure of merit for the boson peak.

Conversely, the annealed samples show increased stiffness, exhibited in Fig. 6.14, which shows the spatial distribution of elastic constants. The spots with low shear moduli (black and blue colour) shrink. The crystallites obviously appear as stiff regions. The shear band region in the deformed sample contains an abundance of soft regions but is very heterogeneous, as depicted in Fig. 6.15. A clearer picture emerges

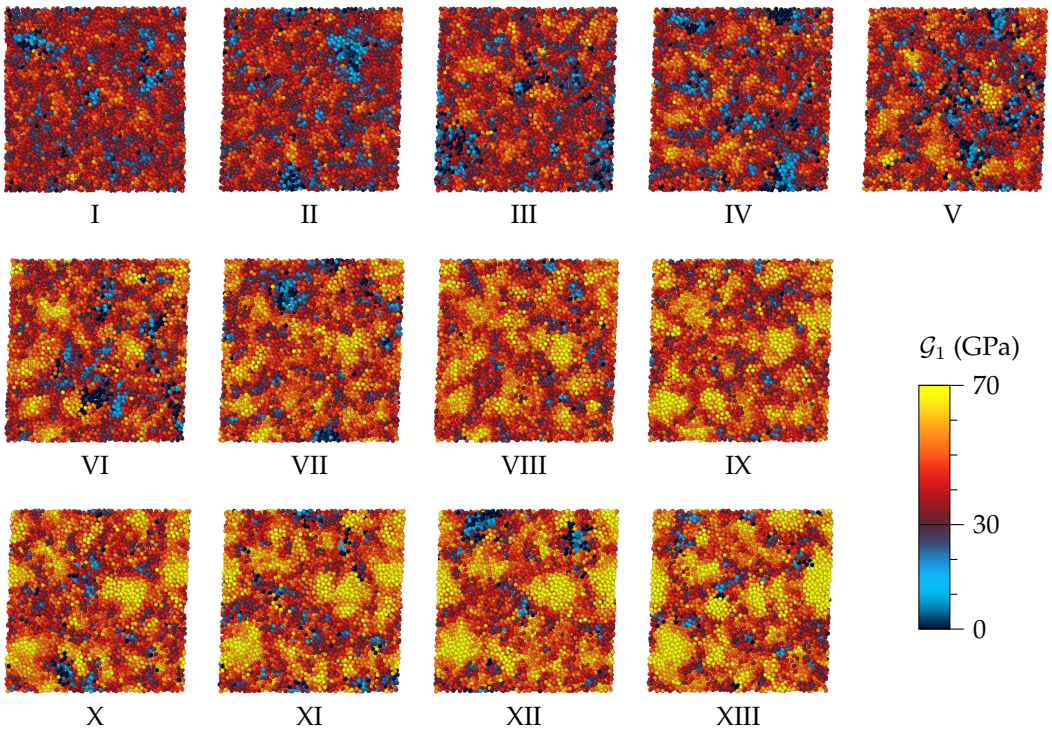

FIGURE 6.14: Spatial distribution of the per-atom shear modulus in annealed and partially crystallised $Cu_{64}Zr_{36}$ glass samples. Samples I–XIII are the same as in Chap. 5. With annealing time the boson peak is reduced (see Fig. 6.4) and the "soft spots" with low $\mathcal{G}_1$ simultaneously reduce in number. The crystallites are clearly visible because of their high stiffness.

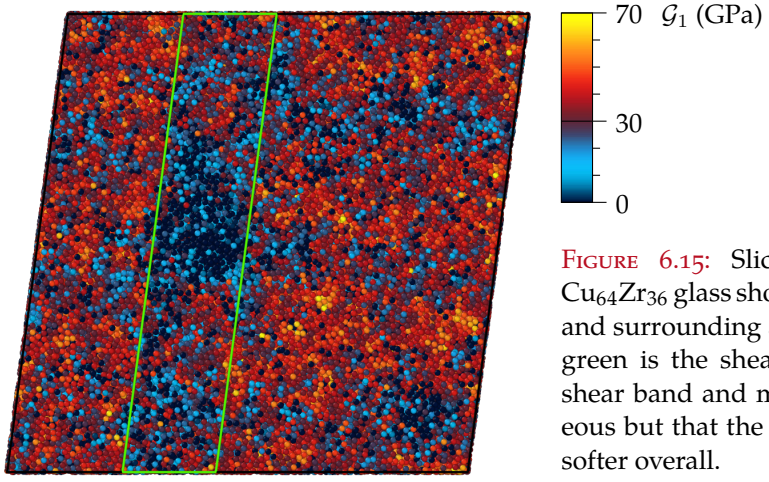

FIGURE 6.15: Slice through a deformed $Cu_{64}Zr_{36}$ glass showing $\mathcal{G}_1$ in the shear band and surrounding areas. The area marked in green is the shear band. We can see that shear band and matrix are very heterogeneous but that the shear band appears to be softer overall.

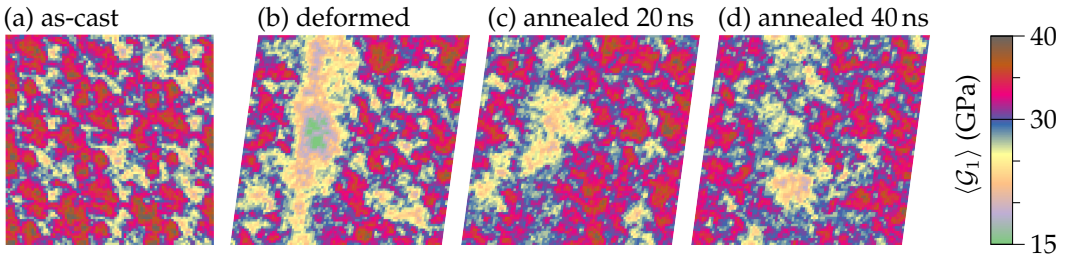

FIGURE 6.16: Map of the shear modulus averaged over the full sample depth of as-cast, deformed, and annealed glasses. The shear band area stays clearly softened even after annealing. The map shows the xz plane with a bin size of $2 \times 2\,\text{Å}^2$.

on a two-dimensional map of averaged shear moduli, such as Fig. 6.16, which contains data averaged over the y direction. A clear softening of the shear band region but also its heterogeneity can be seen. "Soft spots" appear over the whole sample. Interestingly, the soft spots in the as-cast sample also correspond to the position of the shear band. The exact distribution of shear moduli fluctuates during the annealing process, but at least the hard regions in the matrix seem to be mostly preserved.

If, instead of plotting the boson peak height over the fraction of "ordered" atoms, we use the fraction of "soft" atoms, we can attempt an improved correlation over Fig. 6.4 (b). Defining f_{soft} as the amount of atoms with $0\,\text{GPa} \leq \mathcal{G}_1 \leq 28\,\text{GPa}$ gives a very good correlation to the boson peak height, as demonstrated in Fig. 6.17. While there is a connection between "ordered" polyhedra and soft spots, it is not as clear cut as looking directly at the elastic constants. This could be explained by the medium-range order in the glass. It is clear that icosahedra in $Cu_{64}Zr_{36}$ glasses build intertwining networks that are stiff.[93] The destruction of these networks in the shear band also softens the now isolated icosahedra. During the annealing process, the icosahedral backbone is not destroyed but assimilated into crystallites.

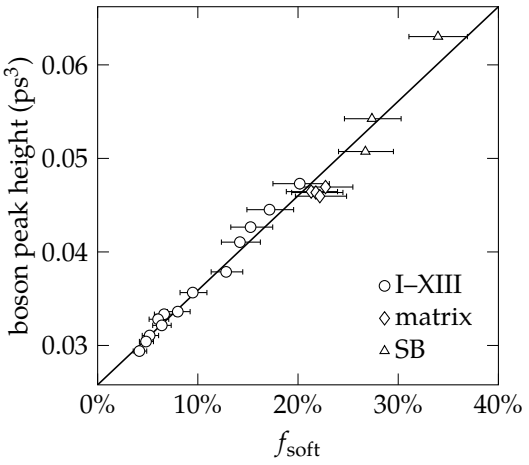

FIGURE 6.17: Correlation of boson peak height with softening in $Cu_{64}Zr_{36}$ glasses. Softening is defined using the fraction f_{soft} of atoms with a Kelvin shear modulus $\mathcal{G}_1$ between 0 GPa and 28 GPa. The error bars indicate the change of f_{soft} when changing the cutoff by ± 1 GPa.

6.5 conclusions

The boson peak in $Cu_{64}Zr_{36}$ metallic glasses can be influenced by modifying the structure of the system: Disturbed short-range order, such as in a shear band, leads to an increase of the boson peak. Increasingly ordered glasses, obtained by an annealing procedure, exhibit increasingly smaller boson peak signals. Both processes are connected with a change of density, but not with a large shift of the boson peak on the frequency axis. This seems to indicate that the boson peak is not a frequency-shifted van Hove singularity as was recently proposed,[248] since the position of the boson peak on the frequency axis would have to be sensitive to changes of density. Still, one could argue that the glass is heterogeneous and that the boson peak results from regions of reduced density in the glass. The above modifications would only serve to increase or decrease the size and number of these regions. Therefore, the hypothesis of a shifted van Hove singularity is not convincingly disproved, it just has to be modified to account for the heterogeneity of metallic glasses.

Thus, we performed a systematic investigation of this issue: We used a HEA sample to obtain an intact lattice, a lattice with reduced density, a lattice with defects, and a glass. All of these samples have the same composition, CuNiCoFe, and we found that only structural defects in the lattice participate in the boson peak. In fact, we could show that the boson peak is correlated with regions of high mean square displacement, low shear modulus, and defective structural order, but not with changes of density. This strongly supports theories which connect the origin of the boson peak with defects, not with density, at least in the case of metallic alloys. By applying the analysis of elastic moduli to the $Cu_{64}Zr_{36}$ glasses, we could show that a local softening is a reliable indicator for the boson peak. Indeed, shear bands are softened and regain their stiffness by annealing, a process that also occurs in an annealed as-cast glass. The boson peak signal mirrors these processes.

Part III

HETEROGENEOUS PLASTICITY

In this part of the thesis, we treat the plastic regime in metallic glasses. We start this research with heterogeneous shear bands in homogeneous glasses, a phenomenon that has been found recently in experiments. Structural and compositional variations along a single shear band were observed and related to small path changes. Afterwards, we turn towards metallic glasses with crystalline secondary phases. These crystalline phases can significantly influence the mechanical properties of the materials, and we cover systems which range from low crystalline volume fractions up to a regime that is comparable to nanocrystalline matter. These simulations are used to develop a mechanism map and to discuss the breakdown of these mechanisms when transitioning towards the nanocrystalline state.

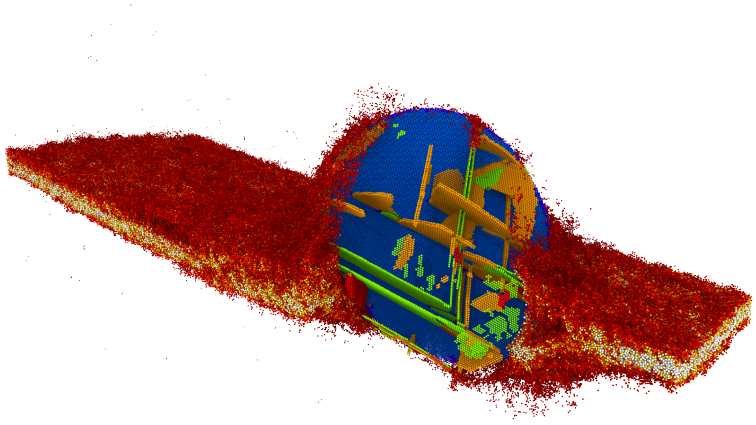

Depicted above is a ductile precipitate being hit by a shear band. The slice through the particle reveals the stacking faults due to partial dislocations, which were induced by slip transfer into the particle. The precipitate is sheared apart by the shear band.

7

HETEROGENEOUS SHEAR BANDS IN HOMOGENEOUS GLASSES

We start our investigations of heterogeneous plasticity of glasses with a treatment of heterogeneities in the shear bands themselves. In as-cast glasses, a heterogeneous structure of shear bands has been observed.[151,159] This heterogeneous structure was connected with small deviations of the shear band path (less than 5°) on length scales between 100 nm and 400 nm.[151,159] On the same length scales, heterogeneous strain response on different segments of the shear band was observed.[160] The reason for this heterogeneity of shear bands is still unclear, although several scenarios are conceivable (see Fig. 7.1). Heterogeneities of the glass itself at the same length scales are a possibility, as well as the stick–slip motion of shear bands. The latter is subject to a number of recent studies (see end of Sec. 1.5) and serrations in the stress–strain curve were connected either to the nucleation of new shear bands[144] or to the arrest of mature, fully-propagated shear bands.[149] Experimentally, only *ex situ* investigations can be performed with the necessary resolution and give little indication as to *why* the shear bands are heterogeneous. MD simulations can help to shed light on these ob-

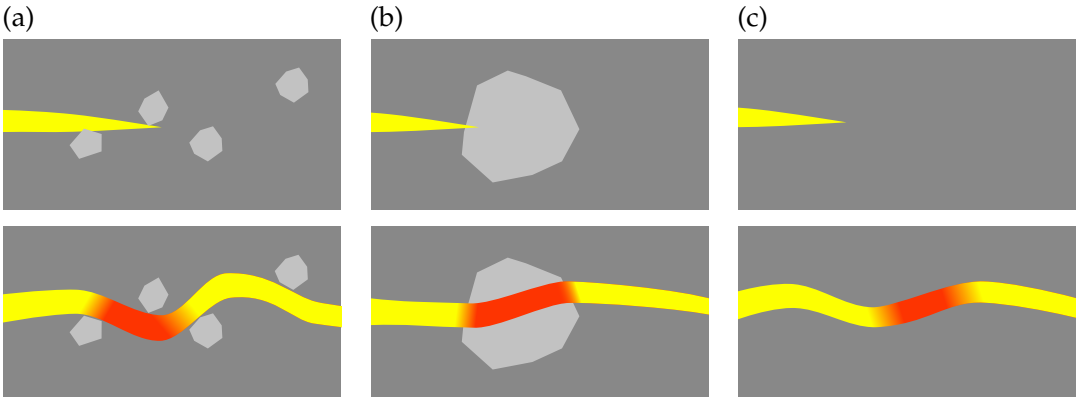

FIGURE 7.1: Models for the wavy propagation of shear bands and the compositional changes connected thereto. The models (a) and (b) assume that the glass itself is heterogeneous on length scales of around 100 nm. (a) The heterogeneities in the glass force the shear band to take a different path, leading to stick–slip and subsequently a change of composition in certain shear band segments. (b) The chemical fluctuations are inherent to the glass and the shear band simple passes through them. A small deflection occurs at the "interface". (c) Without any intrinsic fluctuations in the glass, the only remaining explanation is that a stick–slip-like motion of the shear band leads to a wavy pattern and to compositional changes in segments of the shear band.

servations by offering an *in situ* view on shear band propagation and allowing exact control of the glass structure, but reaching the necessary length scales is challenging.

Although it is conceivable that the aforementioned effects are due to heterogeneities in the structure of the glass, we investigate only glasses that are homogeneous on length scales above around 20 nm. With this setup, we can test whether long-range heterogeneities in the glass are at all necessary for small deviations in the shear band propagation path.

7.1 SIMULATION SETUP

The experimentally observed shear bands are heterogeneous on length scales on the order of several hundred nanometres and we therefore decided on a sample in which a length of 800 nm in shear band propagation direction is reached. Geometrically, a shear test is easiest since the shear band should propagate parallel to the shearing direction, allowing us to use a thin sample. We used a box of dimension $800 \times 20 \times 40\,\mathrm{nm}^3$ in which the shear band should propagate in x direction as sketched in Fig. 7.2 (a). The z direction was chosen to be around four times the shear band width of 10 nm and the y direction was kept as small as possible. The resulting simulation contains 40 389 120 atoms. We therefore opted to use the Cheng potential, which uses less computing resources because of its lower cutoff radius (see Sec. 3.3). We used a $Cu_{64}Zr_{36}$ sample of initial size $20 \times 20 \times 20\,\mathrm{nm}^3$ and replicated it to reach the desired dimensions. A consequence of this is that the glass is homogeneous on the length scales associated with the path changes of the shear band. In order to control the initial propagation direction of the shear band we included an artificial shear band nucleus. For this, we heated a region of size $16 \times 20 \times 4\,\mathrm{nm}^3$ inside one of the $20 \times 20 \times 20\,\mathrm{nm}^3$ glass blocks to 2000 K for 100 ps, while holding all other atoms fixed. After instantaneously quenching the defective region to 50 K and equilibrating for another 100 ps, we assembled the final simulation box: One defective glass block was used alongside the 79 intact ones to build the sample as indicated in Fig. 7.2 (b). We

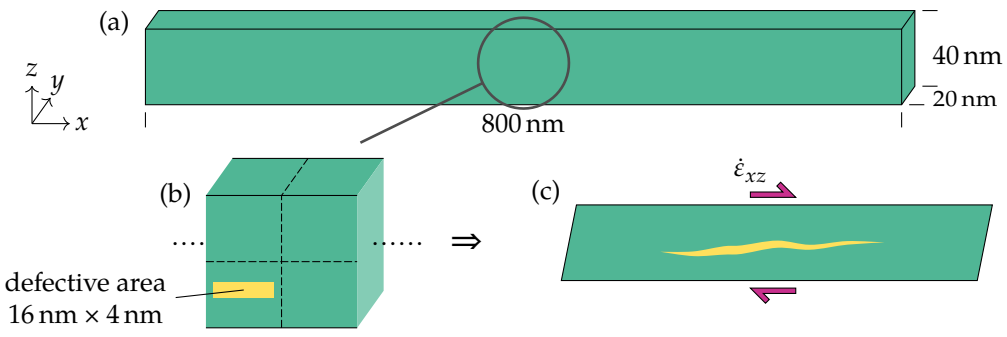

FIGURE 7.2: Simulation setup for a shear band on the micrometre scale. The sample is assembled from smaller glass boxes and an artificial shear band nucleus (yellow) is inserted.

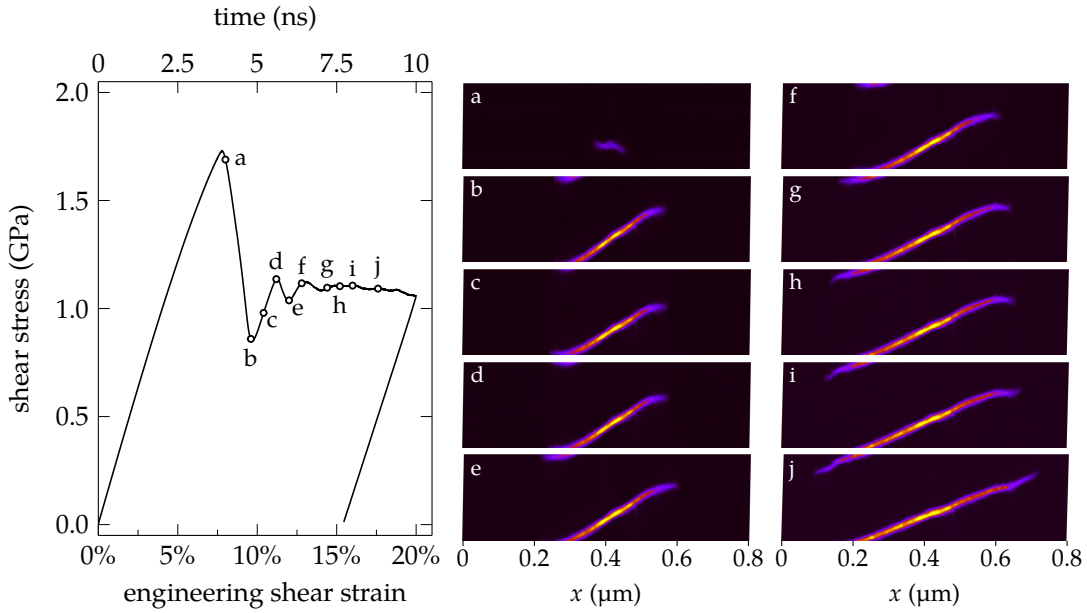

FIGURE 7.3: Stress–strain curves for a shear test performed at 50 K. Maps of the atomic shear strain are shown for selected points on the curve.

used periodic boundaries in all directions. The combined system was equilibrated at the target temperature of 50 K for 100 ps. After that, a shear test in xz direction was performed with a shear rate of $4 \cdot 10^7\,\mathrm{s}^{-1}$. Unloading was performed with a shear rate of $-4 \cdot 10^8\,\mathrm{s}^{-1}$ until a macroscopic shear stress of zero was reached.

7.2 SHEAR TESTS

The shear test was performed up to a shear strain of 20%. The resulting stress–strain curve and selected maps of the atomic shear strain are shown in Fig. 7.3. It should be noted that the yield stress is completely artificial as we inserted an artificial shear band nucleus. By analysis of the macroscopic stress–strain response and the microscopic strain distribution, several observations can be made. First of all, the end of the initial stress drop does not coincide with the shear band propagation reaching the end of the sample. Instead, the overshoot is in all cases followed by an "undershoot" that leads to temporary shear band arrest. The reason for the arrest is most likely that the stress in the system drops below the steady-state stress needed to advance the shear band front. It is interesting to note that the end of the stress drop in MD simulations usually coincides with the point where the shear band front fully propagated through the sample.[145] As evidenced by the simulations at hand, this is simply an effect of the small sample size, which allows the shear band to propagate through the whole sample faster than the stress drop.

The stress drop and subsequent "undershoot" are followed by a ramping of the stress until propagation continues. Smaller serrations follow the initial one, resembling damped vibrations and indicating an initial shock wave going through the system when the elastic energy is released upon yielding. Arrests are accompanied by small changes of propagation direction. During stress drops, the shear band does not propagate horizontally, as would be expected because of the applied stress state, but with a slight inclination. During ramping or constant stress, the propagation is slower, but horizontal. The reason for the inclined propagation is unclear but may be connected to sudden stress releases at stress drops.

As indicated by the time axis in Fig. 7.3, it is impossible to separate the timescales of the shock and the shearing because of the high shear rate. The shape of the stress–strain curve is therefore not comparable to experimental data. Still, the propagation velocity of the shear band front is most likely not rate dependent and the time and length scales of the path changes are likely realistic. Since the shear band is not straight, it is easy to imagine a more complex distribution of barriers that the shear band must overcome to propagate. This may lead to further "micro-serrations" when the shear band grows longer, which would in turn lead to more path changes. It is doubtful if these serrations can be resolved experimentally since they take place in a small fraction of the sample volume, thereby decreasing the amplitude of the stress drop to a very small value.

7.3 ANALYSIS

In order to check for structural and/or chemical changes in the shear band, we unloaded the sample after 20% shear strain. We performed a Voronoi tessellation on the unloaded samples to obtain values for the atomic volumes and calculated the per-atom stress tensor with LAMMPS. Since the atomic volume is ill-defined, it is impossible to obtain useful information on stresses with atomic resolution. We therefore present local stresses and volumes as averages over finite regions, using binned maps.†

Figure 7.4 shows an analysis of residual stresses and Voronoi volume in the system. We can see that large residual stresses remain in the unloaded system. The volumetric stress, plotted in Fig. 7.4 (a), is mostly compressive except at the shear band front. This compressive stress fluctuates along the shear band path and is correlated with the deviation from the plane of highest resolved shear stress: Under pure xz shear, the planes of highest resolved shear stress are the planes with normal vectors in x and z direction. The shear band does not propagate exactly horizontally here, but deviates by roughly 1° to 5° from that plane. Segments with low deviation also exhibit low compressive stresses and vice versa. As plotted in Fig. 7.4 (b), the von Mises

† In fact, LAMMPS outputs a tensor $\sigma_i^{kl}\Omega_i$ for atom i. Thus, we first average this value for a given volume of the sample and then divide this average by the average Voronoi volume of the corresponding atoms.

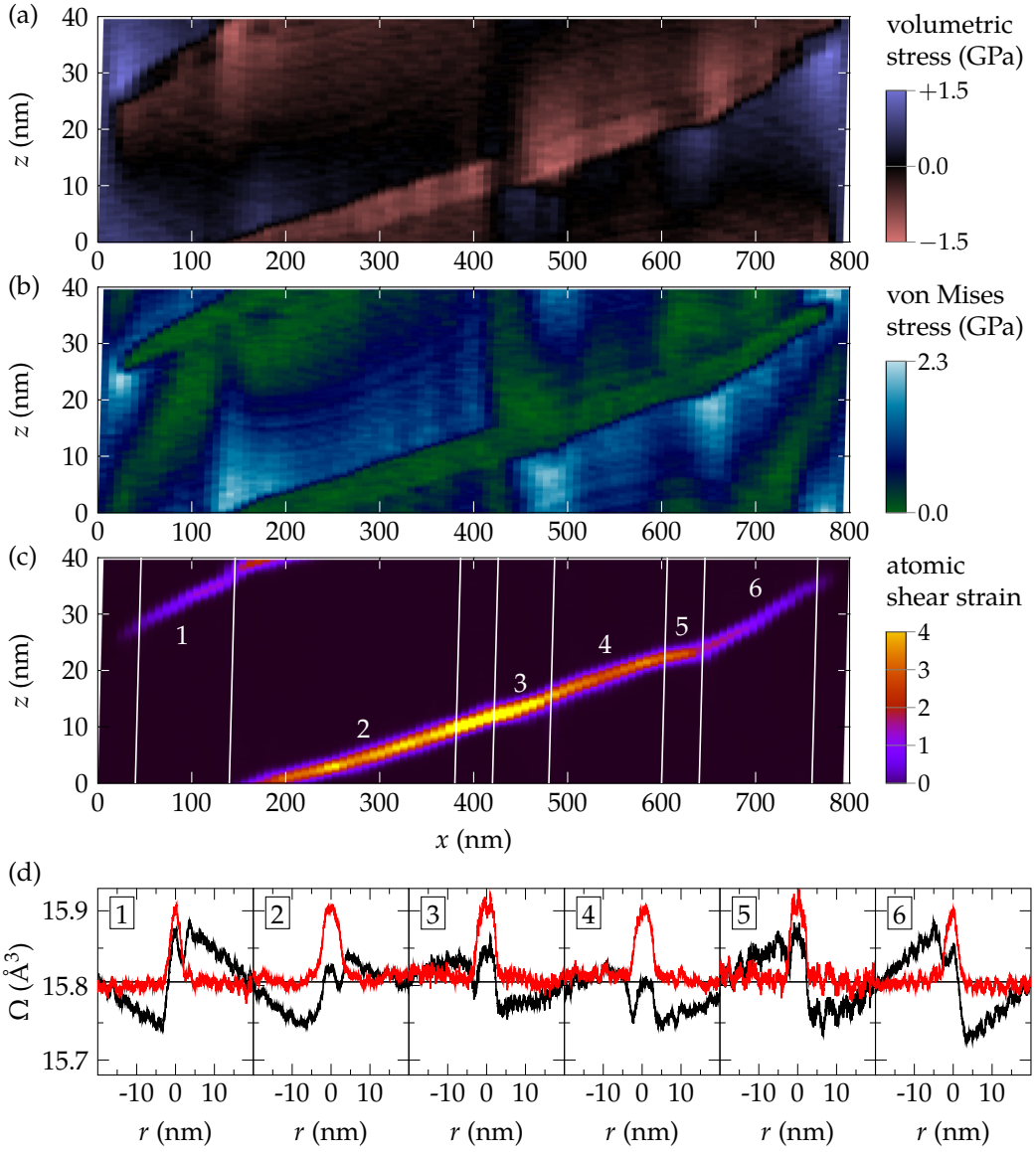

FIGURE 7.4: Analysis of the Voronoi volumes in an unloaded sample deformed at 50 K to 20% shear strain. Maps of local volumetric stress (a), von Mises stress (b), and atomic shear strain (c) are shown. (d) For the marked shear band segments, a scan of Voronoi volumes was performed perpendicular to the shear band. The Voronoi volumes Ω are plotted as a function of distance r from the shear band centre. Black lines show raw Voronoi volumes, red lines are corrected for elastic deformation due to residual stress.

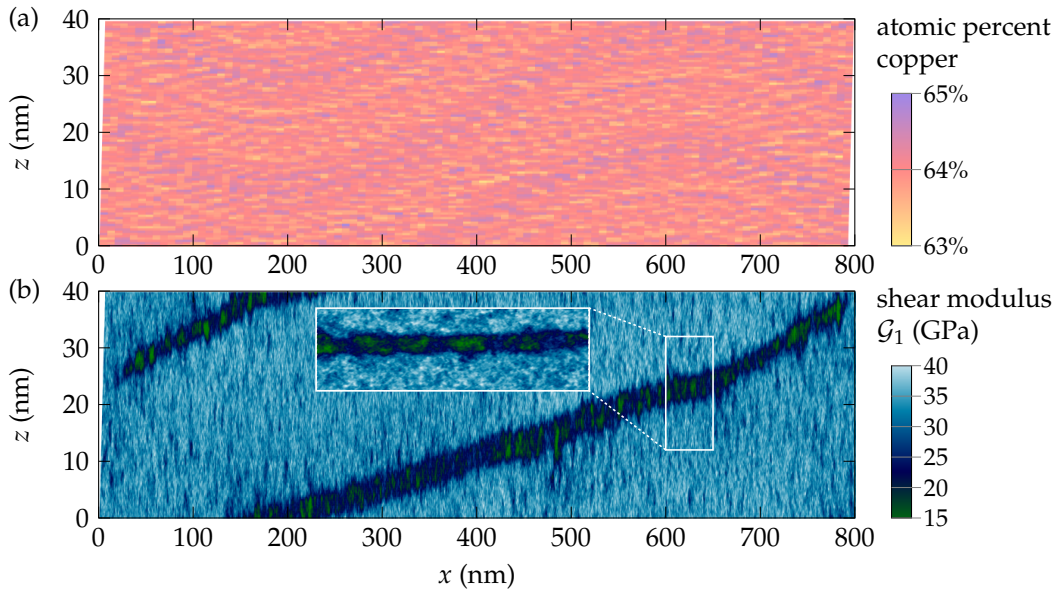

FIGURE 7.5: Chemical and mechanical analysis of an unloaded sample deformed at 50 K to 20% shear strain. (a) No gradient in composition was found. (b) Local shear moduli fluctuate along the shear band direction as observed already in Fig. 6.16.

stress map reveals that shear components play a role at bends and at the front but not inside the shear band. The latter is a rather trivial observation since the shear band has yielded exactly in order to relieve the applied shear stress. Continuing on, we marked six segments of the shear band [Fig. 7.4 (c)], separated where small changes of the propagation direction are observed. For each segment, we plotted the Voronoi volume Ω as a line scan perpendicular to the shear band in Fig. 7.4 (d), with r indicating the distance from the shear band centre. The black lines are plots of the Voronoi volume. A correlation with the compressive stress in the system is visible: Segment 5, for example, is close to horizontal, has a low residual stress, and has rather low density. Segment 4, on the other hand, has volumes below the sample average while being a region of large deviation from the horizontal plane and a large compressive stress. If we assume that these regions are subject to linear elastic deformation, we can correct for the residual internal stresses by using Hooke's law:

$$\Omega_{\text{corrected}} = \Omega \left(1 - \frac{\sigma_{\text{vol}}}{\mathcal{K}}\right), \tag{7.1}$$

where σ_{vol} is the local volumetric stress, i.e., the trace of the local stress tensor. We assume a bulk modulus $\mathcal{K}$ of 121 GPa (cf. Sec. 3.4.1). The corrected volumes are plotted as red lines in Fig. 7.4 (d) and agree with earlier results from simulations on $Cu_{64}Zr_{36}$ glasses.[94] No contrast in density or shear strain along the shear band seems to appear.

In addition to the volume, we also checked other intrinsic properties of the glass, such as the local composition of the material, as well as the per-atom Kelvin shear

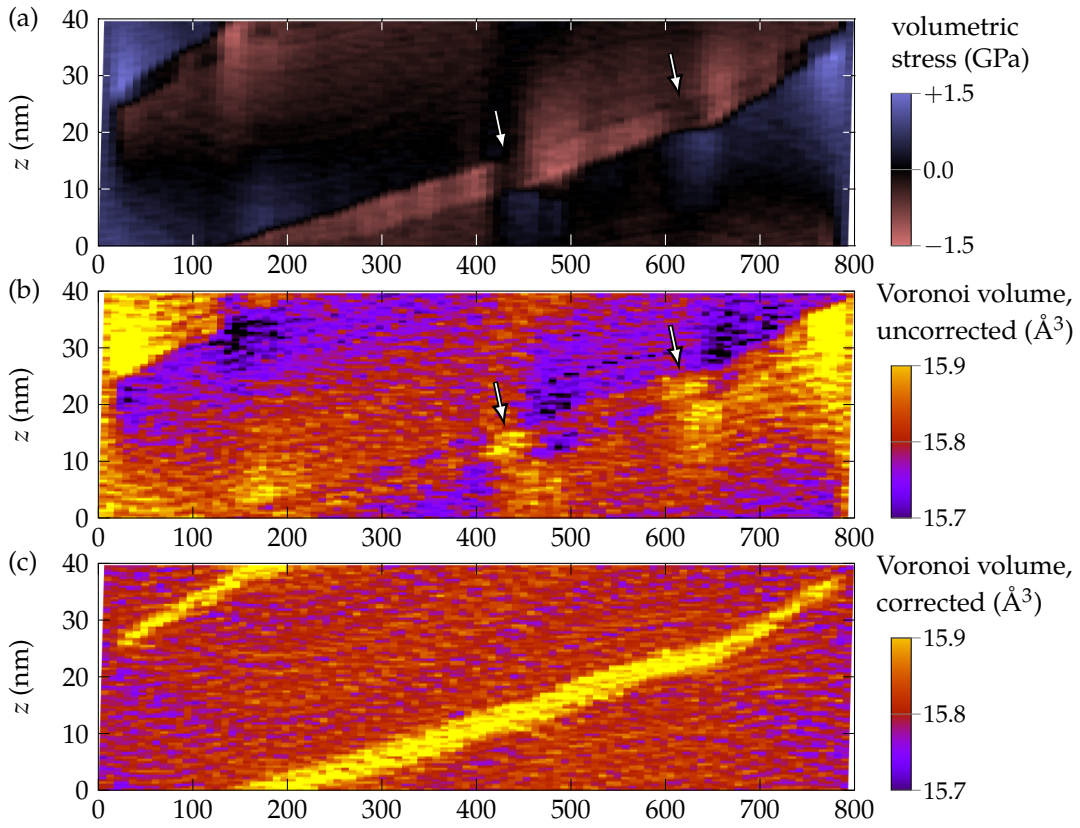

FIGURE 7.6: Analysis of the Voronoi volumes and the residual volumetric stress in the unloaded sample. (a)–(b) Regions of low residual stress in the shear band are marked by arrows. Those regions correspond to horizontal propagation and high Voronoi volume, i.e., low density. The spacing of these regions is on the order of 200 nm, consistent with experimental data[151,159]. (c) The corrected Voronoi volumes in the shear band are above the value in the matrix (15.89 Å^3) but are homogeneous along the shear band.

modulus $\mathcal{G}_1$ (see Sec. 2.5). Those are plotted in Fig. 7.5. The local composition exhibits no fluctuations due to localised deformation. The only heterogeneities appear in the local shear moduli. Soft spots appear inside the shear band but their position bears no relation to the shear band path. Instead, these fluctuations are similar to the ones already observed in Fig. 6.16 and follow a spacing of around 10 nm. This means that only density changes due to *elastic* deformation could be observed.

Taking a closer look at these elastic density changes, Fig. 7.6 shows maps of the volumetric stress and the Voronoi volume, both uncorrected and corrected for elastic deformation. A look at the corrected Voronoi volumes simply paints the same picture as before: The volume change is homogeneous along the shear band. A comparison of uncorrected Voronoi volumes and volumetric stress, though, reveals certain patterns; points of interest are marked by arrows in Figs. 7.6 (b) and (c). Segments of

low compressive stress correlate to high uncorrected Voronoi volume. The spaing of these segments is on the order of 200 nm, which is consistent with thelength scales of experimentally observed density changes.[151,159] The large bright yellow areas in Fig. 7.6 (b) are due to tensile stresses around the shear band front and should be ignored since the shear band front usually propagates to the sample surface, thereby eliminating these tensile regions in a real sample.

7.4 CONCLUSIONS

In summary, we could observe on MD timescales

i) that even a single shear band at athermal conditions shows serrations and small path changes,

ii) that deviations of the shear band from the plane of highest resolved shear stress lead to the build-up of residual compressive stresses,

iii) that all of the intrinsic properties of the shear band—such as composition or shear modulus—were constant along the shear band, and

iv) that the change of Voronoi volumes in the shear band is purely elastic.

So, at first, the simulations seem unable to reproduce the compositional changes along the shear band that were observed experimentally.[159] Still, we could find density changes due to residual stresses. Experimentally, evidence for residual strain was previously observed in a plastically deformed BMG, although it is not clear if this strain is elastic or plastic.[336] Nano-indentation experiments provide evidence for large, inhomogeneous stress fields around shear bands.[161] As such, our results do not seem to be too far away from the experimental reality. An explanation for the absence of chemical heterogeneity along the shear band can—once again—be found in the difference of observable timescale between simulation and experiment: Changes of the composition are due to diffusive processes and our simulations simply cannot cover the timescale required to observe this. Nevertheless, we can identify the driving force of such a diffusion. We know from experiment[192,193] and simulation[125] that the diffusivity in shear bands is higher than in the matrix, which therefore confines any compositional changes to the shear band itself. It further stands to reason that the system strives to reduce the residual stress. Since this stress is compressive, a reduction of density is needed. The system can realise this by locally changing the composition and reordering. Indeed, it was discovered recently that quenching a metallic glass under pressure results in a state with higher density and short-range order but also higher potential energy.[337] In contrast to the present case, a change of composition was impossible, preventing the system from reducing its potential energy by a change of composition. In shear bands, on the other hand, this scenario seems likely.

As such, stress-driven, diffusive reordering in segments of the shear band on length scales of around 100 nm without any intrinsic heterogeneities in the glass seem to provide a probable explanation for the experimental findings. In fact, the complex shear band motion is an intrinsic property of shear bands. The behaviour observed here seems to appear in addition to the usual stick–slip, which is connected to either the nucleation of new shear bands or the arrest and reactivation of fully formed, mature shear bands, i.e., shear bands whose front has reached the other end of the sample.

8

INFLUENCING SHEAR BAND PROPAGATION BY CRYSTALLINE PRECIPITATES

The results in this chapter were first published in Ref. 338.

Metallic glasses deformed significantly below the glass transition temperature exhibit macroscopically brittle behaviour.[9,12] While the high yield strength, large elastic strain limit, and corrosion resistance[9] of the material are already advantageous for a range of applications—such as cases for the next generation of mobile phones (see e.g. Ref. 18)—improved ductility is still sought after. Limited ductility could already be achieved by introducing crystalline secondary phases in the form of precipitates into the glass matrix. Compressive ductility was reported for Cu–Zr-based,[168–172,182] Cu–Ti-based,[173] and Zr–Ti-based metallic glasses,[32,33,174] while a small tensile ductility of 1% to 2% strain was observed in Cu–Zr composites with nanocrystals.[175–177] Significant ductility in tension and compression could be achieved in Zr–Ti-based,[174,178] Ti-based,[179] and Cu–Zr-based metallic glasses[180,181] with large crystalline volume fractions.

Despite advances in engineering solutions and a large body of experimental investigations, the influence of precipitates on the deformation mechanisms in metallic glasses is not yet completely understood. For large amounts of crystalline phase, the mechanisms are relatively clear. The plasticity is carried by both phases, interfaces have been identified as sources and sinks for dislocations, STZs are activated by interactions with dislocations,[187–189] and the macroscopic plasticity can be described by simple composite models. For nanoprecipitates the situation is less clear. Precipitates have been connected with an increased number of shear bands[169,170] and computer simulations have shown that crystal–glass interfaces serve as nucleation sites for shear bands.[145,185,186,199] The participation of the crystalline phase in the plastic deformation has been a subject of a wide range of studies:[175,177,181,190,195] In Cu–Zr-based glasses, twinning in B2 crystallites, as well as a martensitic transformation to the B19′ phase have been observed.[175] The volume change during this deformation was proposed as the origin of toughening,[175] although that interpretation is not generally accepted, with some authors preferring an explanation based on multiplication of shear bands instead.[197] A size dependence of plastic deformation of nanoprecipitates was reported: Only particles exceeding a critical size of 10 nm to 20 nm—depending on the composition—show twinning, while smaller particles appear undeformed.[177,339,340] Quasi-2D computer simulations by Lund and Schuh show that crystallites that are small relative to the shear band either accommodate deformation

in the interface or dissolve, while bigger precipitates are deformed either by heterogeneous or homogeneous dislocation nucleation.[198]

So while a nucleation of shear bands at interfaces seems to be well established by simulation,[145,185,186,199] the interaction of an approaching, pre-existing shear band with precipitates in the glass matrix is unclear. Effects of the precipitate size were observed but not satisfactorily explained.[177] The goal of the current chapter is therefore the investigation of the interaction between an artificially induced shear band and precipitates of systematically varied geometry. We use both brittle CuZr precipitates (B2 phase) as well as pure copper precipitates as a model for ductile precipitates, and finally derive a mechanism map.

8.1 SIMULATION SETUP

As a computer model, we used a $Cu_{64}Zr_{36}$ matrix into which we inserted spherical precipitates by first cutting a hole into the glass and then inserting a perfect crystal with the desired geometry while avoiding overlapping atoms. We found that the resulting interface is mostly stress-free. Precipitate sizes should match the sizes in experimental investigations, so we chose to go from diameters of 3 nm to 45 nm. To contain these, the simulation box was sized 120 nm $\times$ l $\times$ 60 nm, where l was changed to vary the distance between precipitate images. Changing l allowed us to simulate the effect of different crystalline volume fractions at constant precipitate size. The mapping between the two quantities will be derived in the discussion. In a first step, we employed the Mendelev potential[124] and used the experimentally observed B2 structure for the precipitates.[118,119,341,342] In a second step, we used fcc copper and simulated interatomic forces using the Ward potential to obtain a more realistic dislocation nucleation stress (see Sec. 3.4.2 for a comparison of potentials). We did not perform all simulations with this potential since it cannot be used to obtain a stable B2 phase (see Sec. 3.4.3). In the x direction of the simulation box open boundaries were used while all other directions were periodic. On one of the resulting surfaces, we inserted a notch to control the origin of the shear band, which would otherwise start from the interface between glass matrix and precipitate or from a random spot

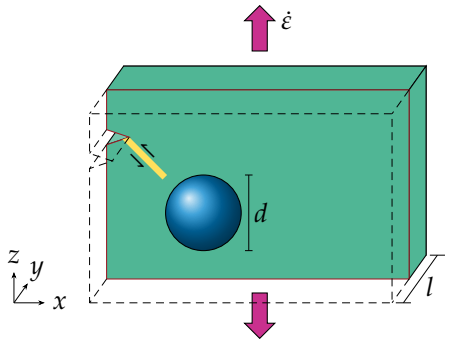

FIGURE 8.1: Simulation setup for metallic glass composites with crystalline nanoprecipitates. A cut through the glass matrix (green) in the xz plane at $y = l/2$ is shown. A spherical precipitate (blue) is inserted at $l/2$ into the matrix. The box has open boundaries in x direction and is periodic otherwise. A stress concentrator in form of a notch serves as the origin of a shear band (yellow) and is positioned such that the shear band hits the precipitate centrally. This figure was first published in Ref. 338.

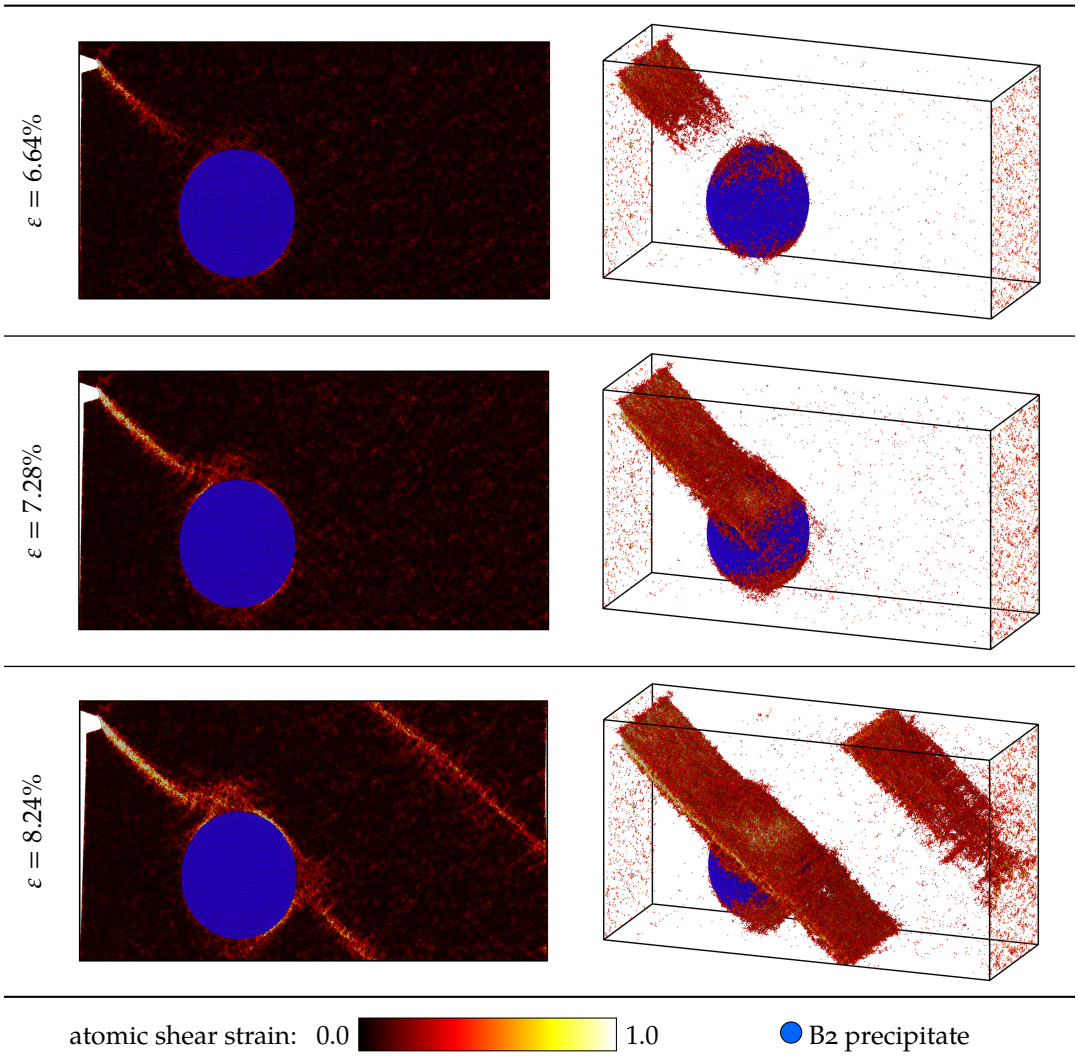

FIGURE 8.2: Snapshots of the wrapping mechanism in a simulation with a 30-nm CuZr precipitate. The shear band propagation is temporarily changed to avoid the precipitate but continues unhindered afterwards. The glass matrix is coloured according to atomic shear strain, while the precipitate atoms are shown in blue if they are on a B2 lattice. No defects in the crystalline phase were detected. The left column depicts a cut through the simulation box at $y = l/2$, in the right column all atoms with $\eta_i^{\text{Mises}} < 0.3$ were deleted. This figure was first published in Ref. 338, which also contains a video of the simulation.

on the surface. The notch was chosen such that the resulting shear band hits the precipitate centrally. On this setup, shown in Fig. 8.1, tensile tests with an engineering strain rate of $4 \cdot 10^7\,\text{s}^{-1}$ were performed. All simulations steps were conducted at 50 K, a regime in which shear banding is observed despite the high strain rates that have to be used in atomistic simulations.

Snapshots of the simulations were recorded and analysed with OVITO.[279] The shear band was identified using the atomic shear strain (see Ref. 280 and Sec. 2.4) and defects in the crystal phase were identified using atomic structure identification with pattern matching (see Ref. 296 and Sec. 2.6.3).

8.2 WRAPPING AND BLOCKING

The first mechanism we observed, shown in Fig. 8.2, is a *wrapping* of the shear band around the precipitate. The simulation used a spherical B2 precipitate with a diameter of 30 nm. We observe that the shear band continues almost unhindered on its propagation path, while the part hitting the precipitate temporarily switches directions to wrap around the obstacle, comparable to a carpet being pulled over a small bump. The crystalline phase only deforms elastically. This athermal mechanism would be completely atypical for a dislocation in crystalline materials. In a crystal lattice, a dislocation is limited to a slip plane, a change of which is only possible for its screw components.[343] This change of slip planes is usually only observed in stage-III work hardening.[344] While dislocation climb is observed in crystals, it is thermally activated. In contrast to this, the wrapping in the glass does not need thermal activation as there is no defined slip plane. If we compare the effect of precipitates in crystals and glasses, see Fig. 8.3, the effect on the carriers of plasticity is different. In the crystal, the dislocations pile up before the precipitate, and if they pass it, it is by the Orowan mechanism. Here, dislocation rings appear around the obstacle which also leads to a pile-up and hardening.[204] In the amorphous case we have an isotropic material—at least on a certain minimal length scale. This means that all slip directions are equivalent and symmetry is only broken under applied load. Thus, the shear band can simply change its course temporarily and wrap around the precipitate.

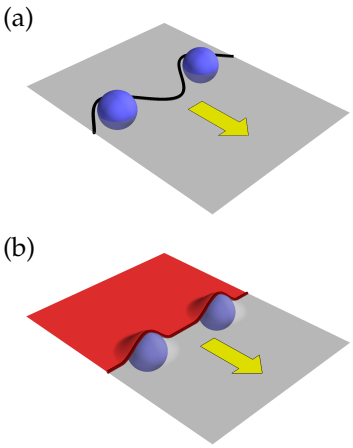

FIGURE 8.3: Precipitation hardening in crystalline materials compared with the interaction between precipitates and shear bands in an amorphous matrix. (a) In crystalline materials precipitation hardening is dominated by the Orowan mechanism. The dislocation (black) moves on a fixed slip plane (grey) and is pinned at precipitates with incoherent interfaces. With increasing stress, dislocation rings pile up around the particles, hardening the composite. (b) In an amorphous matrix, the shear band (red) will slip on a plane of highest resolved shear stress but, due to the lack of a lattice, can temporarily change propagation direction and wrap around an obstacle. This figure was first published in Ref. 338.

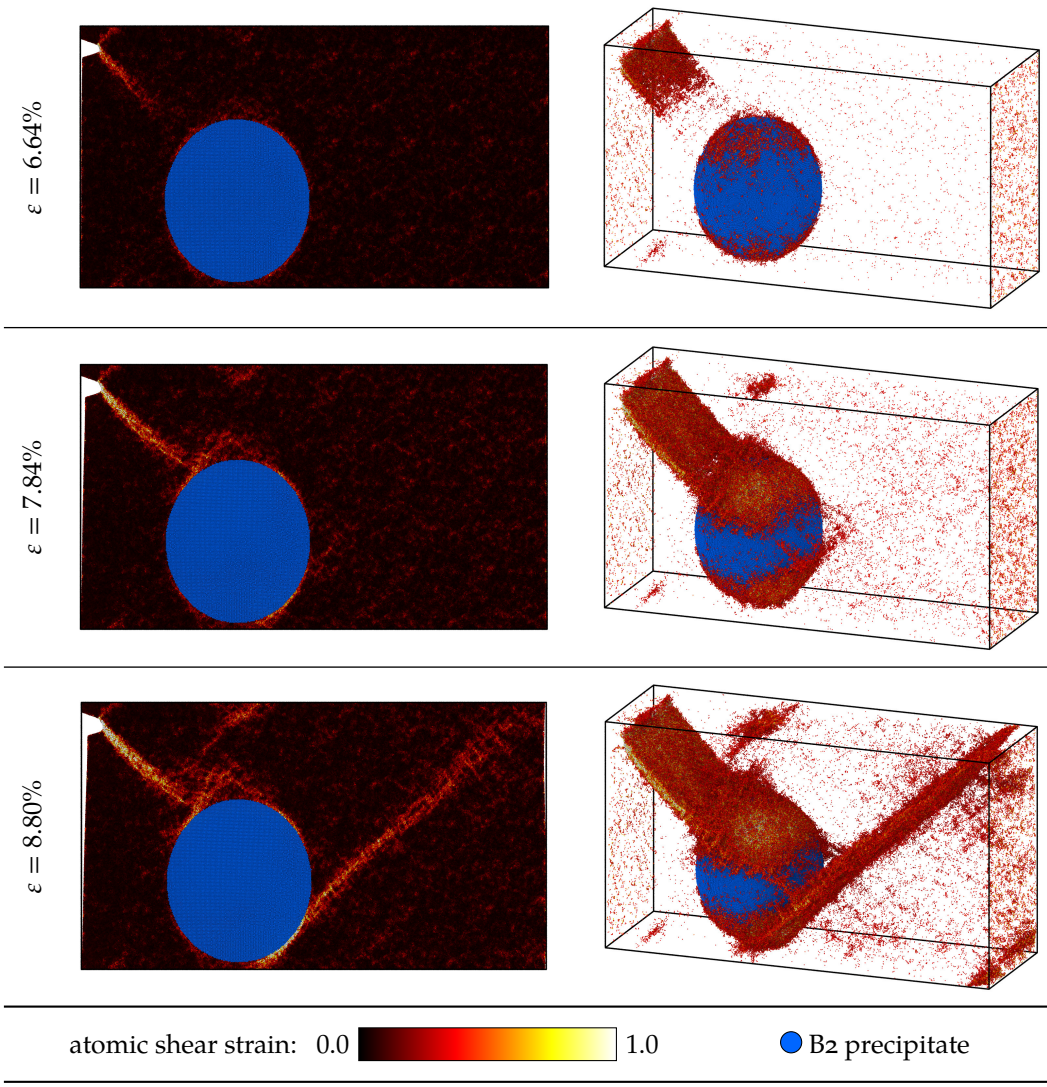

FIGURE 8.4: Snapshots of the blocking mechanism in a simulation with a 37.5-nm CuZr precipitate. The shear band can neither wrap around the particle due to its size, nor can slip transfer into the particle take place as its yield strength is too high. Instead, a second shear band nucleates at the crystal–glass interface. The glass matrix is coloured according to atomic shear strain, while the precipitate atoms are shown in blue if they are on a B2 lattice. No defects in the crystalline phase were detected. The left column depicts a cut through the simulation box at $y = l/2$, in the right column all atoms with $\eta_i^{\text{Mises}} < 0.3$ were deleted. This figure was first published in Ref. 338, which also contains a video of the simulation.

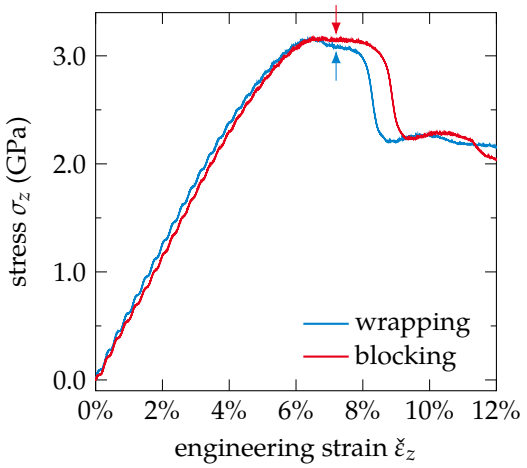

FIGURE 8.5: Stress–strain curves of crystal–glass composites with CuZr precipitates. The data from the simulations depicted in Figs. 8.2 and 8.4 are shown. In the first case, the shear band wrapped around the precipitate while it was blocked in the second simulation. The arrows indicate the strain value at which shear band hits the precipitate. This figure was first published in Ref. 338.

It stands to reason that this wrapping cannot continue for arbitrarily large precipitates since the driving force for continued propagation diminishes for increasing deviation of the shear band from the plane of highest resolved shear stress. Figure 8.4 shows what happens in this case: The shear band is *blocked* by the precipitate. The precipitate has a diameter of 37.5 nm and the same distance l between the centre of the particle and the centre of its images as before. Because of the increased susceptibility to shear band formation at the interface, a second shear band emerges perpendicular to the first one on the opposite side of the precipitate. A complete arrest of the shear band is impossible, as the nucleation stress for heterogeneous shear band nucleation at the interface is available.

The question is now, how these two mechanisms affect the macroscopical mechanical properties. Figure 8.5 contains the corresponding stress–strain curves for Figs. 8.2 and 8.4. No strain hardening can be observed in either case which is consistent with the occurrence of a single critical shear band in all cases. The only source of hardening that may occur in a real sample is due to the constraints on the shear band path. If the shear band is no longer free to traverse the sample on a single plane, but has to follow a "wavy" path, the propagation can be hindered. This is conceivable for a large density of crystallites of sufficient size to block the shear band.

8.3 A CRITICAL VALUE FOR THE TRANSITION

In order to understand how the heterogeneous two-phase microstructure influences the macroscopic deformation, we need a figure of merit for a transition from the wrapping to the blocking mechanism. For this, we systematically varied not only the precipitate diameter, but also the distance between precipitate images by changing the box width l. Because of the setup, the box width l corresponds to the inter-precipitate distance. We additionally investigated the case of $l = 0$, which are an infinite number of overlapping spheres, i.e., an infinite cylinder. This investigation

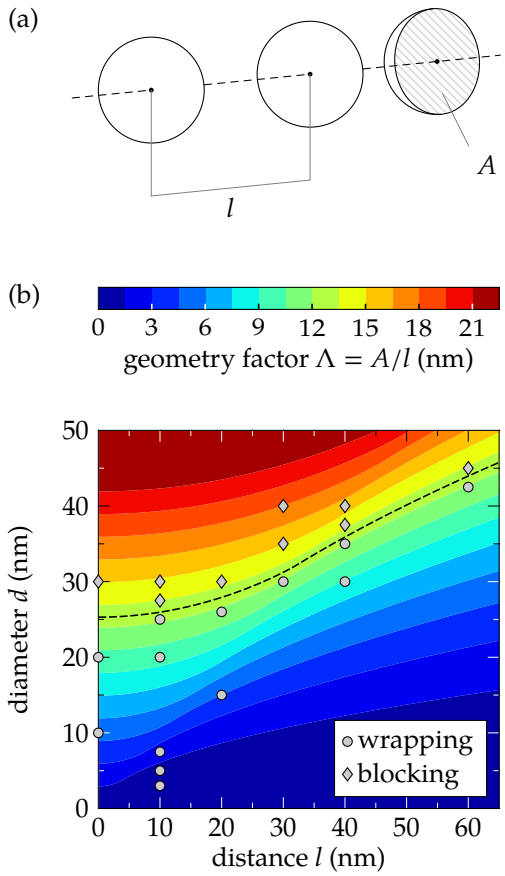

FIGURE 8.6: Precipitate geometry controls the transition from shear band wrapping to shear band blocking. (a) A geometry factor $\Lambda = A/l$ is derived from the distance l of precipitate centres and the area A of a cut through the precipitate perpendicular to the shear band propagation direction. (b) Contour plot of Λ and results of MD simulations as data points. The wrapping to blocking transition occurs at a critical Λ indicated by the dashed line. The data points at $l = 0\,\text{nm}$ are infinite cylinders along the y axis, representing the case of overlapping spheres with infinitesimally small distances between their centres. This figure was first published in Ref. 338.

reveals a clear correlation between geometry and mechanism, which is valid in the seemingly very different case of cylindrical precipitates, too. To quantify this more, we first start from an idea similar to Orowan's stress formula:[204] We connect the crystalline volume fraction $f = V_{\text{precipitates}}/V$ to the average crystallite distance l by

$$l = \frac{d/2}{\sqrt{f}} \qquad \Leftrightarrow \qquad f = \frac{d^2}{4l^2}. \tag{8.1}$$

We now define an empirical geometry factor Λ, given by the ratio of the cross-sectional area A of the precipitate divided by the distance of precipitate centres l [cf. Fig. 8.6 (a)]. This factor can be expressed—with the help of Eq. 8.1—only in terms of the volume fraction and precipitate geometry:

$$\Lambda = \frac{A}{l} = \frac{A\sqrt{f}}{d/2}. \tag{8.2}$$

For non-overlapping precipitates ($d < l$), the area can be expressed in terms of the diameter by $A = \pi d^2/4$, yielding

$$\Lambda = \pi \frac{d}{2}\sqrt{f}. \tag{8.3}$$

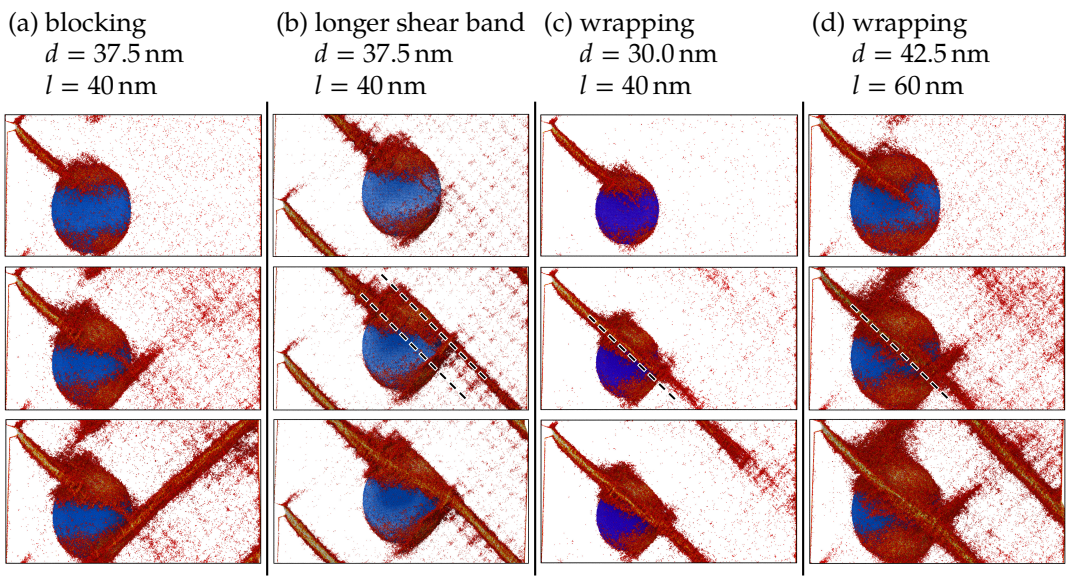

FIGURE 8.7: Influence of shear band length on the interaction with precipitates. (a) is the setup from Fig. 8.4, while (b) is the same except for a longer shear band path before hitting the precipitate. Seemingly, an elongated shear band favours the wrapping mechanism. (c) A comparison with the case of wrapping a smaller precipitate from Fig. 8.2 reveals that this is not the case. In (b), the shear band does not continue on, but a new shear band is nucleated. In contrast to (a), this nucleation appears in the same direction as the approaching shear band, as indicated by the dashed lines. In the case of wrapping, (c), the shear band continues on as indicated by the dashed line. (d) The same can be observed for a larger precipitate.

The Orowan stress, on the other hand, is proportional to $\sqrt{f}/d$. The difference between the two is no surprise, as the mechanism is different: The size of the precipitate plays a role in our case, while for the Orowan mechanism only the inter-particle distance is important. Because of the high computational demand, we had to restrict the box size, so that some simulations were performed with $d > l$, i.e., overlapping precipitates. In this case, the precipitates were constructed such that no stacking faults were introduced. Our parameter Λ was calculated in these cases by subtracting the overlapping circle segments from the area. Figure 8.6(b) shows a contour plot of this geometry parameter. The data points are MD simulations, the symbol of which indicates whether wrapping or blocking occurred. A clear dividing value of Λ can be identified as

$$\Lambda_{\mathrm{crit}} \approx 12.65\,\mathrm{nm}. \tag{8.4}$$

Below this value, the shear band wraps around the precipitate.

We tested the universality of this parameter first by changing the distance of the precipitate from the notch, thereby lengthening the shear band. The results are shown in Fig. 8.7. At first it appears that the longer shear band wraps around the precipitate where a shorter one would be blocked. A closer inspection reveals that this is not the

case: The shear band is blocked in both cases, the only difference is at which side the new shear band nucleates. In case of the longer shear band the newly nucleated shear band lies in the direction of the old shear band. Given that the distance for the "short" shear band is on the same order as l (around 40 nm), we can exclude the long shear band case completely in practice: Because of the three-dimensional placement of the precipitates in space, the free shear-band length will also be of the order of l. But even if it is not, the parameter Λ_{crit} is still correct.

8.4 PLASTIC DEFORMATION OF THE CRYSTALLINE PHASE

Apart from the two mechanisms discussed in the previous section, a third one has been omitted until now: A slip transfer into the crystalline phase, i.e., a precipitate that deforms together with the matrix. The literature already reports dissolution of precipitates smaller than the shear band width,[145,198] which we could also reproduce with small copper precipitates (Fig. 8.8). Interesting for the improvement of mechanical properties, though, are bigger precipitates.

The B2 precipitates used until now have a high antiphase-boundary energy. Therefore, super-dislocations or a martensitic transformation by twinning would be needed to deform the particles. The stress at the shear band tip in our systems is not sufficient

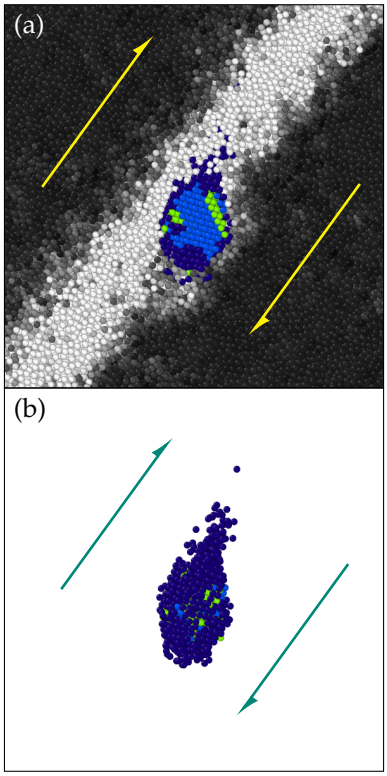

FIGURE 8.8: Mechanical dissolution of a 3-nm copper particle in a shear band. (a) The grey-scale colour coding indicates the atomic shear strain in the glass matrix (scale from 0.0 to 1.0) while the precipitate is coloured according to the structure. Light blue are atoms on an fcc lattice, dark blue atoms are amorphous, and green atoms are part of a stacking fault. (b) Only the atoms initially belonging to the precipitate are shown. The dissolution under shear is clearly visible. This figure was first published in Ref. 338.

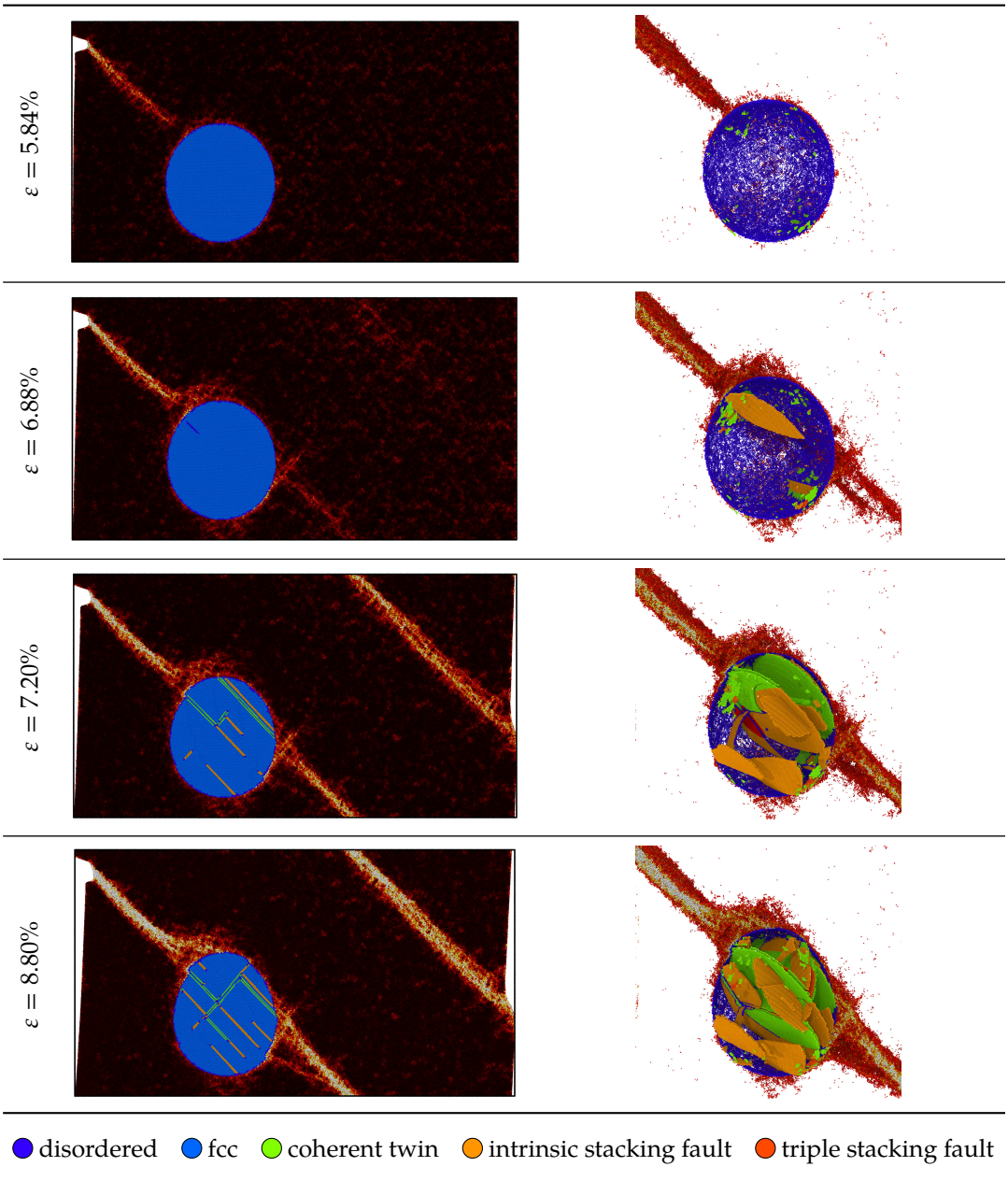

FIGURE 8.9: Slip transfer from from the shear band in the glass matrix into a 30-nm Cu precipitate. This simulation uses the Ward potential, in which the critical stress for dislocation nucleation is realistic. The precipitate is sufficiently "soft" so that it can be deformed plastically. The shear band no longer wraps around the obstacle but cuts through it. The glass matrix is coloured according to atomic shear strain with the same scale as used in Figs. 8.2 and 8.4, while defects in the fcc crystal structure are coloured according to the legend. The left column depicts a cut through the simulation box at $y = l/2$, in the right column all atoms with $\eta_i^{\mathrm{Mises}} < 0.3$, all fcc-coordinated atoms, and one half of the interface atoms were deleted. This figure was first published in Ref. 338, which also contains a video of the simulation.

for this. As a model for a phase that can deform with the matrix, we replaced the precipitates with pure copper. As discussed in Sec. 3.4.2, we used the Ward potential since it provides a sufficiently soft copper phase—in contrast to the Mendelev potential. The result of such a simulation with plastically deformable particles is shown in Fig. 8.9. Slip transfer into the particle takes place and dislocations are nucleated. The particle is sheared off and the shear band continues straight on behind it. A clear spatial correlation between kinks in the precipitate and shear bands can be observed.

8.5 A MODEL FOR THE INTERACTION BETWEEN SHEAR BAND AND PRECIPITATE

To make the results more generally useful, we derived a simple model to explain Λ_{crit}, as well as incorporate an idea of how slip transfer fits into this picture. Empirically, we could already separate the wrapping from the blocking mechanism with the parameter

$$\Lambda = \frac{A}{l} \propto A\frac{\sqrt{f}}{d}, \tag{8.5}$$

where the wrapping mechanism is favoured for $\Lambda < \Lambda_{\text{crit}}$. We can explain this with a simple model using an equilibrium of forces at the point where the shear band hits the precipitate.

First of all, the externally applied tensile stress σ_{ext} results in a shear stress in the shear band which amounts to

$$\tau_{\text{SB}} = \frac{1}{2}\sigma_{\text{ext}}, \tag{8.6}$$

assuming that the shear band moves on the plane of highest resolved shear stress. As the shear band itself is softened, and can reduce stress by plastic deformation, the stress acts mainly on the shear band front which allows us to convert it into a force due to the externally applied stress

$$|\mathbf{F}_{\text{ext}}| \approx \tau_{\text{SB}} \cdot l \cdot h_{\text{SB}} = \frac{\sigma_{\text{ext}}}{2}\, l\, h_{\text{SB}}, \tag{8.7}$$

where h_{SB} is the width of the shear band and l is again the box length and therefore also the length of the shear band front. Figure 8.10 shows the situation when the shear band hits the precipitate. Momentarily, following the principle of *actio est reactio*, a reaction force

$$\mathbf{F}_{\text{back}} = -\mathbf{F}_{\text{ext}} \tag{8.8}$$

from the precipitate occurs. Using the projected area A, this can be converted into a normal stress

$$\sigma_A^n = \frac{|\mathbf{F}_{\text{back}}|}{A/2}. \tag{8.9}$$

We assume that the force mainly acts on one half of the precipitate, given that this is what the bulk of the moving glass pushes against (compare the deformation pattern

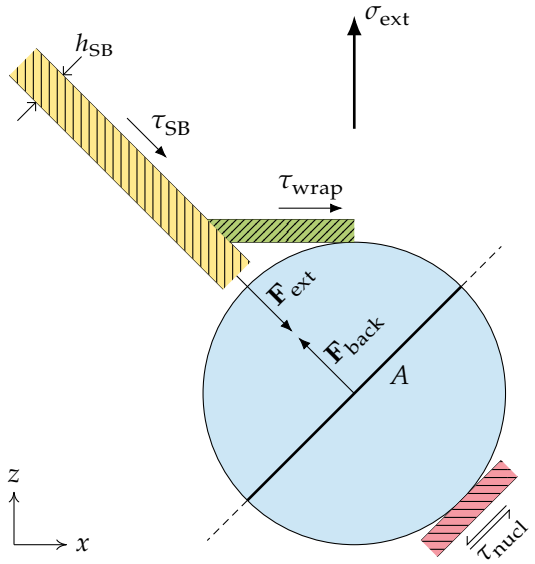

FIGURE 8.10: The forces and stresses around a precipitate hit by a shear band. Hatched areas represent shear bands, where the yellow shear band is the arriving shear band, green represents the path it takes to wrap the precipitate, and red shows a newly nucleated shear band. This figure was first published in Ref. 338.

in Fig. 8.9). This back stress additionally leads to a shear stress in a plane oriented 45° towards $\mathbf{F}_{\text{back}}$. This shear stress

$$\tau_{\text{wrap}} \approx \frac{1}{2}\sigma_A^n \tag{8.10}$$

is illustrated in green in Fig. 8.10. Using Eqs. 8.8 and 8.7, we can write

$$\sigma_A^n = \frac{|\mathbf{F}_{\text{back}}|}{A/2} = \frac{|\mathbf{F}_{\text{ext}}|}{A/2} = \frac{\sigma_{\text{ext}}\, l\, h_{\text{SB}}}{A} = 2\tau_{\text{wrap}}. \tag{8.11}$$

We make the assumption that for the wrapping mechanisms to occur, a critical value

$$\tau_{\text{wrap}} > \tilde{\tau}_{\text{wrap}} \tag{8.12}$$

must be surpassed. The competing mechanism—blocking the shear band—is connected to a shear stress

$$\tau_{\text{nucl}} = \frac{1}{2}\sigma_{\text{ext}} \qquad \text{with a critical value} \qquad \tau_{\text{nucl}} > \tilde{\tau}_{\text{nucl}}. \tag{8.13}$$

Given that $\tau_{\text{nucl}} = \tau_{\text{SB}}$ and that the externally applied stress was sufficient to nucleate a shear band, it stands to reason that the nucleation of the red shear band in Fig. 8.10 should always be possible. The critical value for the wrapping mechanism, though, is geometry dependent. Using Eq. 8.11 we can find a critical value for the externally applied stress of

$$\tilde{\sigma}_{\text{ext}} = \frac{2A\tilde{\tau}_{\text{wrap}}}{l\, h_{\text{SB}}}. \tag{8.14}$$

Below $\tilde{\sigma}_{\text{ext}}$, wrapping is impossible. With this relation, we can find the condition for the wrapping-to-blocking transition:

$$2\tilde{\tau}_{\text{nucl}} = \tilde{\sigma}_{\text{ext}} = \frac{2A\tilde{\tau}_{\text{wrap}}}{l\, h_{\text{SB}}}, \quad \text{giving} \tag{8.15}$$

$$\frac{A}{l} = \Lambda_{\text{crit}} = \frac{\tilde{\tau}_{\text{nucl}}}{\tilde{\tau}_{\text{wrap}}} h_{\text{SB}}. \tag{8.16}$$

It should be noted that this derivation is also applicable to externally applied shear stress by replacing σ_{ext} with $2\tau_{\text{ext}}$ in the above equations. The end result is the same.

If we assume that both $\tilde{\tau}_{\text{nucl}}$ and $\tilde{\tau}_{\text{wrap}}$ are critical stresses for shear band nucleation at interfaces, we can conclude that they are approximately equal in magnitude. This means that

$$\Lambda_{\text{crit}} \approx h_{\text{SB}}, \tag{8.17}$$

i.e., that the critical value is the shear band width. Shear bands in different glass alloys were observed to have widths of around 10 nm[94,125,151,152] which is consistent with our results of $\Lambda_{\text{crit}} \approx 12.65\,\text{nm}$.

In this derivation, we ignore the fact that shear banding is a nucleation process and only introduce athermal terms. We argue that this is reasonable because i) the simulation is performed at very low temperatures and ii) the stresses around the precipitates are close to the yield stress anyway.

The effect of slip transfer into the particle is now also easy to incorporate. For slip transfer into the particle to occur, it must be susceptible to plastic deformation. That means the critical stress for heterogeneous dislocation nucleation $\tilde{\tau}_{\text{disl}}$ must be smaller than $\tilde{\tau}_{\text{nucl}}$, otherwise the nucleation of a new shear band is preferred. The stress for dislocation nucleation must be provided through the shear band, i.e.,

$$\tau_{\text{disl}} = \tau_{\text{SB}} = \frac{1}{2}\sigma_{\text{ext}}. \tag{8.18}$$

That means that plastic deformation of the crystalline phase now competes with wrapping and we can simply replace $\tilde{\tau}_{\text{nucl}}$ by $\tilde{\tau}_{\text{disl}}$ in Eq. 8.15, leading to a new geometry parameter

$$\Lambda'_{\text{crit}} = \frac{\tilde{\tau}_{\text{disl}}}{\tilde{\tau}_{\text{wrap}}} h_{\text{SB}} < \Lambda_{\text{crit}}. \tag{8.19}$$

With increasing "softness" of the precipitate, the wrapping mechanism becomes less relevant in favour of simply deforming the precipitate.

If the model sketched above is correct, the area A used in the model must be perpendicular to the shear band. As our precipitates were symmetrical until now, we cannot differentiate between areas parallel and perpendicular to the shear band. This is important, as another possibility to explain the appearance of the area in the formula is that it is related to the excess path of the wrapping shear band. Every piece of

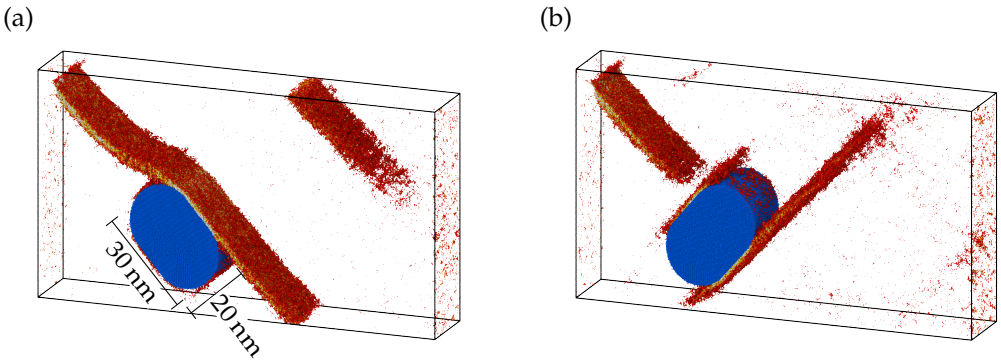

FIGURE 8.11: Orientation of the area A in the geometry factor Λ. Subfigures (a) and (b) contain the same asymmetrical precipitate of infinite length in y direction, simply rotated by 90°. Exposing the thin side to the approaching shear band leads to wrapping, exposing the wide side blocks the shear band.

shear band costs energy, and its lengthening due to the wrapping mechanism could instead be the relevant figure. We excluded this by constructing an asymmetrical B2 precipitate which has a diameter of 20 nm in one direction and 30 nm in the other, and which extends infinitely in y direction. We know that a 20 nm cylinder is wrapped by the shear band, while a 30 nm cylinder blocks the shear band. By exposing once the short side and once the long side of the precipitate to the approaching shear band, we can test whether the cross-sectional area or the surface area is important. Figure 8.11 supports our model: The shear band reacts to the cross-sectional area perpendicular to its propagation. If the precipitate exposes its 20 nm side to the shear band, it is wrapped, while the shear band is blocked by the 30 nm side.

Based on our model we can now also motivate a qualitative mechanism map as shown in Fig. 8.12. Small precipitates will be dissolved in the shear band. It stands to reason that easily deformable precipitates will dissolve even at greater sizes. This mechanism has been discussed in the literature already.[145,198] If the crystallite is too big to be dissolved, the shear band avoids the obstacle by wrapping around it. With further increasing precipitate size this becomes more and more unfavourable. This reason, as detailed in Eq. 8.11, is that the force imposed on the precipitate by the externally applied stress is distributed over a greater area. This in turn reduces the stress available to activate the wrapping process. At a critical precipitate size—which depends on the precipitate distance—the blocking mechanism becomes more favourable since the stress available to initiate it is constant for constant external stress (Eq. 8.13). In case the critical stress for dislocation nucleation in the precipitate is lower than the stress needed to activate a new shear band, the particle will be cut. This slip transfer sets in for smaller crystallite sizes if the dislocation nucleation stress decreases, compare Eq. 8.19.

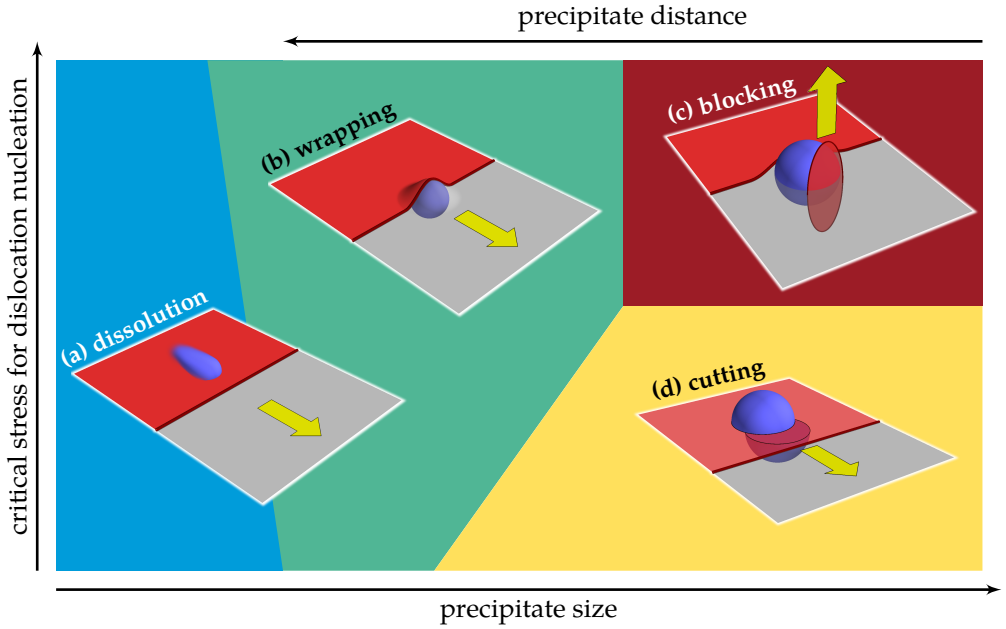

FIGURE 8.12: Mechanism map for the interaction of a pre-existing shear band with a crystalline precipitate. Very small precipitates are dissolved in an approaching shear band. With increasing precipitate size and/or decreasing precipitate distance, the shear band first wraps around the obstacle and is later blocked by it. If the precipitate is sufficiently "soft", i.e. with a sufficiently low critical stress for dislocation nucleation, the shear band cuts through it instead of being blocked. This figure was first published in Ref. 338.

8.6 COMPARISON TO THE LITERATURE AND CONCLUSIONS

The findings presented above also fit to experimental observations from literature. In a joint publication,[338] our colleagues from WWU Münster produced TEM images of deformed Zr–Cu–Ag–Al glass samples, in which the blocking mechanism is also recorded. A comparison between our simulation data and a TEM image of a blocked shear band is provided in Fig. 8.13. In these experiments the number density of precipitates was $n = 10^{20}\,\mathrm{m}^{-3}$ and the average particle diameter was 70 nm. With this we obtain

$$f = \frac{V_{\text{precipitates}}}{V} = n\frac{4}{3}\pi(35\,\text{nm})^3 \approx 1.8\%, \text{ and} \tag{8.20}$$

$$\Lambda = \pi \cdot 35\,\text{nm} \cdot \sqrt{1.8\%} \approx 14.7\,\text{nm} > \Lambda_{\text{crit}}, \tag{8.21}$$

predicting a blocking of the shear band (assuming similar shear band thickness), which is also what was observed. Some particles were found to be passed by the shear band unhindered. This can easily be explained by the fact that i) the particle sizes are Gauss distributed and some fall below the critical size and that ii) particles may not be hit centrally all the time, virtually reducing A.

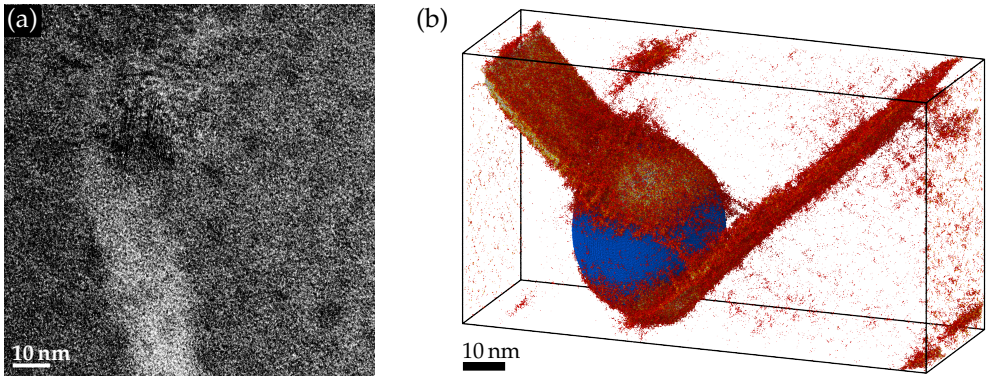

FIGURE 8.13: Comparison of experimentally observed shear band paths in a crystal–glass composite with our simulations. (a) A high-resolution TEM image of a blocked shear band. (b) Simulation snapshot from Fig. 8.4, also showing a blocked shear band. Both images adapted from Ref. 338, DOI: 10.1103/PhysRevApplied.5.054005. © *2016 by the authors, available under the terms and conditions of the Creative Commons Attribution 3.0 License (http://creativecommons.org/licenses/by/3.0/).*

A publication on Zr–Cu–Al glasses with different Al content[177] also fits into our picture. The samples exhibited the following characteristics:

$$\mathrm{Cu_{47.5}Zr_{47.5}Al_5}: \quad f = 0.176 \pm 0.011 \quad d = (20 \pm 5)\,\mathrm{nm} \tag{8.22}$$
$$\mathrm{Cu_{47}Zr_{47}Al_6}: \quad f = 0.154 \pm 0.015 \quad d = (20 \pm 5)\,\mathrm{nm} \tag{8.23}$$
$$\mathrm{Cu_{46}Zr_{46}Al_8}: \quad f = 0.064 \pm 0.010 \quad d = (18 \pm 5)\,\mathrm{nm}. \tag{8.24}$$

All samples show a small plastic strain, which decreases with increasing Al content. Putting the above values into our model, we obtain

$$\mathrm{Cu_{47.5}Zr_{47.5}Al_5}: \quad \Lambda = (13.2 \pm 3.7)\,\mathrm{nm} \tag{8.25}$$
$$\mathrm{Cu_{47}Zr_{47}Al_6}: \quad \Lambda = (12.3 \pm 3.7)\,\mathrm{nm} \tag{8.26}$$
$$\mathrm{Cu_{46}Zr_{46}Al_8}: \quad \Lambda = (7.2 \pm 2.6)\,\mathrm{nm} \tag{8.27}$$

Assuming that the shear band width is on the order of 10 nm again, we can see that with decreasing volume fraction, more and more particles can be wrapped. This is in agreement with the observation that only larger particles were twinned. The twinned particles also exhibited a more elliptical shape, which can be an indication that they were sheared off. If we assume that the participation of the crystalline phase in the plastic deformation influences the mechanical properties, we can understand the results: Only if the particles are not wrapped by shear bands can they enhance the ductility.

For other works such a clear comparison is not possible, either due to volume fractions or precipitate sizes not being provided, or due to crystal growth during de-

formation. In the latter case, an exact geometry at the point of shear band interaction with the precipitate cannot be obtained. Still, the Λ_{crit} from our simulations corresponds to precipitate diameters between 20 nm and 40 nm, depending on the crystalline volume fraction. The order of magnitude is consistent with experimental studies on Cu–Zr–Al-based glasses reporting twinning in precipitates greater than around 20 nm,[177,340] as well as TEM observations in an Al-based glass, where crystallites growing during deformation are sheared off if they reach a size of approximately 10 nm.[339] It was also reported that $Cu_{50}Zr_{45}Ti_5$ metallic glass has a critical size of 9 nm for the twinning of B2 particles.[345] The inter-particle distances in these studies are roughly on the same order of magnitude as our simulations. A transition from wrapping to slip transfer into the particles as outlined by our model is able to explain the above observations.

The current results suggest the possibility of improving the mechanical performance of metallic glasses by the introduction of precipitates. None of the presented mechanisms inhibit the formation of a critical shear band. Still, while smaller precipitates can be wrapped by the shear bands, bigger precipitates either lead to a prolonged shear band path by blocking and re-nucleation or they participate in the plastic deformation. In the latter case, the crystalline phase can be tuned to achieve the desired properties of the composite. The advantage of precipitates as suggested here and in the experimental literature is that they can be grown by an annealing procedure which can be tuned for crystalline volume fraction and crystallite size.

9

MECHANISMS OF PLASTICITY: FROM METALLIC GLASSES TO NANOCRYSTALLINE METALS

In the previous chapter we treated the deformation mechanisms in glass matrices with relatively low volume fractions of crystalline phases. Now, we want to expand this work to higher fractions up to the nanocrystalline regime. The objective is the examination of the transition from the typical mechanisms in metallic glasses to the mechanisms typical of nanocrystalline materials. Such a transition is conceivable, since composites with increasing the volume fraction of the secondary crystalline phase must at some point resemble a nanocrystal with amorphous grain boundaries. As discussed already in Sec. 1.6.1, the Hall–Petch relation, which connects the grain size to the yield stress, becomes invalid for grain sizes on the order of 10 nm or less. The reason is that the mechanism leading to strengthening—dislocation pile-up inside the crystallites—is no longer the only relevant mechanism at these sizes. A mixture of grain rotation, grain sliding, grain growth,[205] and grain boundary migration[206] is added to the dislocation-based mechanisms. This leads to either a plateau or a reduction of the yield stress with decreasing grain size.[201,208] It stands to reason that the plastic deformation of the grain boundary itself starts to play an increasing role. This leads to effects that mirror phenomena we know from glasses: Shear-band-like pile-ups were observed in nanoindentation[201] and $T^{2/3}$ scaling of yield as in Johnson and Samwer's cooperative shear model[150] was found for grain boundary deformation.[203]

Thus, it seems that the transition from glass to nanocrystal is smooth. Our goal in this chapter is the investigation of grain boundary mechanisms while excluding dislocation activity. Using the samples from Chap. 5, we have available a glass which becomes increasingly populated with crystallites until it resembles a nanocrystal with grain sizes of around 3 nm and amorphous grain boundaries. The crystalline phase in this composite is a Laves phase which—similar to the B2 phase in the previous chapter—is highly brittle and resistant against dislocation nucleation. We therefore expect to observe mainly the behaviour of the amorphous phase at the onset of plasticity. To this end, we performed tensile tests on samples with varying crystalline content and grain sizes, as well as at quasi-athermal and thermalised conditions.

9.1 MECHANICAL TESTING

The first set of tensile tests was performed with samples I (the as-cast glass) and IV–XIII (glasses with increasing crystalline volume fraction) from Chap. 5. We rep-

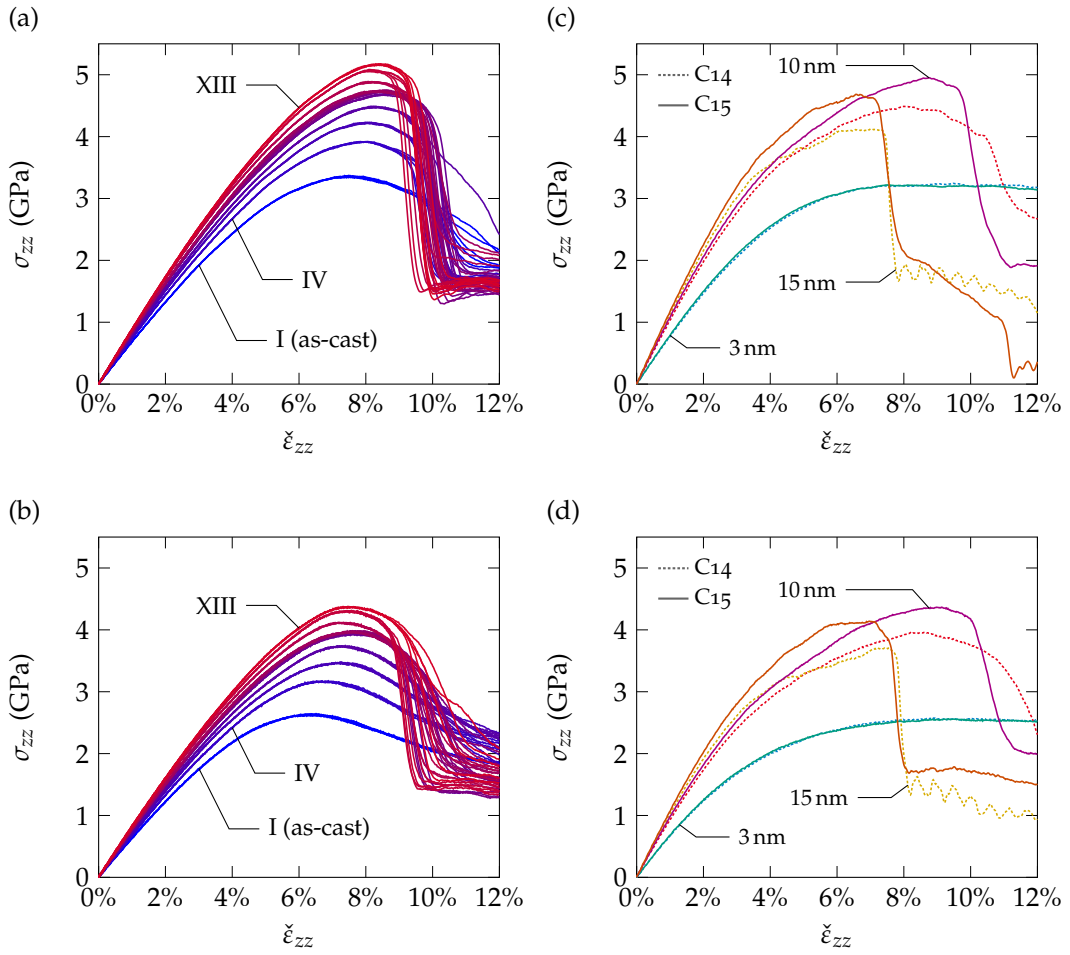

FIGURE 9.1: Stress–strain curves of glasses, composites, and nanocrystals. The plots depict the true stress σ_{zz} in tensile direction as a function of the engineering strain $\check{\varepsilon}_{zz}$. The results for sample I (as-cast glass) and IV–XIII (increasing amount of crystalline phase) at 50 K (a) and 250 K (b) are plotted alongside the Voronoi-constructed samples at 50 K (c) and 250 K (d). All five independent tensile tests are plotted on top of each other for all samples in (a) and (b). The yield stress is very reproducible in independent simulations.

licated these samples $3 \times 1 \times 7$ times to obtain specimens of $30 \times 10 \times 70\,\mathrm{nm}^3$ size. Open boundaries were introduced in x direction to increase the shear localisation as discussed in Ref. 145. The samples were equilibrated at target temperatures of 50 K and 250 K for 1 ns and a constant engineering strain rate of $10^8\,\mathrm{s}^{-1}$ was applied uniaxially in z direction. The tensile test was repeated five times for each sample and temperature to assess the reproducibility of yield stress and strain localisation.

As a comparison, we also prepared artificial nanocrystals using a Voronoi construction. This method works by choosing a number of random points in a simulation cell and constructing Voronoi cells around those points as described in Sec. 2.6.2. Then,

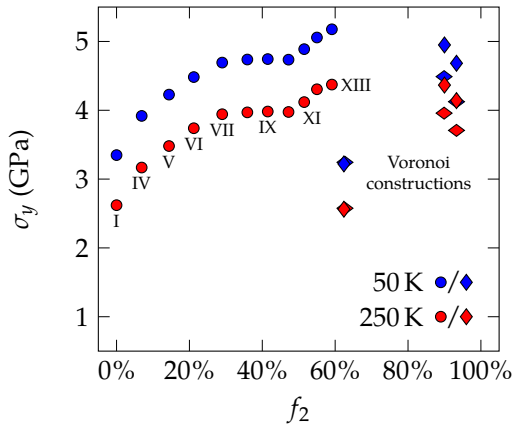

FIGURE 9.2: Yield stress σ_y as a function of the crystalline volume fraction f_2. The circles represent the data for samples with crystallites grown by annealing. The error bars for the yield stress are smaller than the symbols and are therefore omitted. Diamonds represent the artificially created nanocrystals, with ◇ representing C14 polycrystals and ◊ representing C15 polycrystals.

either a C14 or a C15 lattice is oriented randomly and inserted into the Voronoi cell for every point. The number of points and the size of the simulation cell define the grain size. Assuming spherically shaped grains, we can obtain a given grain diameter d in a simulation cell of volume V using

$$n = \left\lfloor \frac{6V}{\pi d^3} \right\rfloor \tag{9.1}$$

points. We selected approximate grain sizes of 3 nm, corresponding to the grain size in sample XIII, as well as 10 nm and 15 nm, which are more typical experimental grain sizes. The samples were prepared with dimensions similar to the grown crystallite composites and also have open boundaries in x direction. Because the algorithm results in a number of atoms that are unrealistically close together, we optimised the structures by molecular statics simulations afterwards in order to avoid high, local forces that could lead to local temperature spikes and numerical problems. Tensile tests were performed with the same parameters as for the previous samples.

The resulting stress–strain curves are shown in Fig. 9.1. We note that the curves are very reproducible up to the yield point and only deviate afterwards, if at all. Ignoring the artificially constructed structures for the moment, we remark that the yield stress increases with increasing crystalline volume fraction. This is quantified in Fig. 9.2 in which the yield stress† is plotted over the crystalline volume fraction f_2 (as defined in Sec. 5.3).

Table 9.1 lists the properties of the annealed samples as determined in Sec. 5.3. If we assume that the failure mechanism in these samples is still glass-like, we can apply the cooperative shear model by Johnson and Samwer.[150] On a basic level, this model states that after an elastic shear limit criterion,

$$\tau_y = \gamma_{\mathrm{STZ}} \cdot \mathcal{G}, \tag{9.2}$$

yield occurs as a fold catastrophe. The factor γ_{STZ} is temperature dependent and can be assumed constant for the current discussion. As we can see in Tab. 9.1, the average

† We define the yield stress simply as the maximum stress in the stress–strain curve.

TABLE 9.1: Properties of annealed and Voronoi-constructed samples at 0 K. The data relating to the annealed samples was taken from Tab. 5.2. Both the ratio of Zr atoms in a diamond superlattice over the total number of Zr atoms, f_1, and the fraction of total atoms identified as part of a Laves phase, f_2, are listed (see Sec. 5.3 for details). The average diameter d of the crystallites was calculated assuming a spherical shape. The number density ρ_n and the potential energy E_{pot} were obtained directly from molecular statics simulations. The elastic constants c_{11}, c_{12}, and c_{44}, as well as the Voigt–Reuss–Hill Young's modulus $\mathcal{E}_{\text{VRH}}$ were calculated for the whole composite.

sample	f_1 (%)	f_2 (%)	d (nm)	ρ_n (nm^{-3})	E_{pot} (eV/atom)	c_{11}	c_{12}	c_{44} (GPa)	$\mathcal{E}_{\text{VRH}}$
I	0.0	0.0		63.15	−4.483	164	110	27	75
II	1.3	2.1	1.4	63.21	−4.488	167	111	27	77
III	2.9	4.4	1.4	63.24	−4.492	169	112	28	79
IV	4.6	6.9	1.5	63.27	−4.495	169	112	28	80
V	9.8	14.4	1.5	63.33	−4.500	172	112	29	82
VI	15.1	21.2	1.7	63.37	−4.505	174	113	31	85
VII	21.7	29.0	1.8	63.42	−4.509	176	114	31	87
VIII	28.3	35.9	1.9	63.43	−4.510	178	114	32	88
IX	33.6	41.5	2.1	63.44	−4.512	178	114	32	90
X	39.5	47.2	2.3	63.47	−4.515	179	114	33	90
XI	44.2	51.5	2.7	63.48	−4.517	181	114	33	92
XII	48.0	55.0	2.8	63.50	−4.519	182	115	34	94
XIII	52.4	59.1	3.1	63.53	−4.522	184	115	34	95
C14	74.0	62.7	2.6	64.53	−4.415	176	115	30	84
	97.1	89.9	9.7	65.02	−4.468	204	123	40	110
	98.4	93.3	14.7	65.12	−4.478	209	125	43	117
C15	73.7	62.4	2.6	64.49	−4.415	178	116	31	86
	97.1	90.0	9.7	65.00	−4.469	211	127	43	117
	98.4	93.3	14.7	65.12	−4.479	219	127	44	123

moduli of the annealed samples increase while Fig. 9.1 shows that the yield strain is relatively constant. This is consistent with Eq. 9.2, but assumes that there is no change in mechanism with increasing crystalline volume fraction. Indeed, taking the Voronoi constructions into account reveals that this average view cannot be correct. The 3 nm sample roughly corresponds in crystallite geometry and crystalline volume fraction to sample XIII, but its yield stress and elastic constants are much lower. Conversely, the 10 nm and 15 nm samples show similar strength to sample XIII, although they have much higher crystalline volume fraction and elastic constants. An argument based solely on the average composite properties seems overly simplistic in this light. It stands to reason that the deformation of the crystalline phase itself does not follow Eq. 9.2 and that the relevant elastic moduli are those of the amorphous phase, not the averaged values for the whole composite. It is furthermore clear that the mechanisms of plasticity of glasses cannot persist as-is in the nanocrystal.

9.2 ATOMIC LEVEL DEFORMATION MECHANISMS

Thus, a look at the microscopic mechanisms of deformation is in order. As a first step, we quantified the shear localisation using the parameter ψ described in Sec. 2.4. Figure 9.3 plots the shear localisation parameter as a function of the crystalline volume fraction. It is clear that the shear localisation increases together with the crystalline volume fraction and decreases with temperature. This can also be observed in the snapshots in Fig. 9.4 (50 K) and in Fig. 9.5 (250 K) which depict the state of the samples at an engineering strain of $\varepsilon = 12\%$. We note that there is considerable scatter in the strain localisation while the yield stress is very reproducible. This scatter is also reflected in the snapshots in Figs. 9.4 and 9.5, especially for the higher temperature. That the yield stress is nonetheless reproducible, suggests that the cooperative shear model works independently of the localisation of the activated STZs; only the critical fraction of activated sites seems to be important. This was also observed in earlier studies, which found that adding an open surface increases localisation but does not significantly change the yield stress.[145]

The changing strain localisation in our samples has its origin in competing mechanisms. The reduction of the amorphous volume fraction leads to a spatial confinement of STZ activation and necessarily increases heterogeneity of the early deformation stages. This is exacerbated by the increasing heterogeneity of the glassy phase itself: Glasses that are deeply relaxed are defined by a greater difference between liquid-like and solid-like regions, making the deformation once again more heterogeneous.[52] On the other hand, dispersions of small crystallites in a glass matrix were observed to increase the density of shear bands.[170] Therefore, the shear localisation stays low for the samples I–VI at 250 K. Here, the increased temperature enables nucleation of multiple shear bands which is supported by the dispersion of crystallites which serve as shear band nucleation sites.[145,185,186] This is confirmed by the snapshots in Fig. 9.5. Starting from sample VII, the percolation threshold of 18.3% for

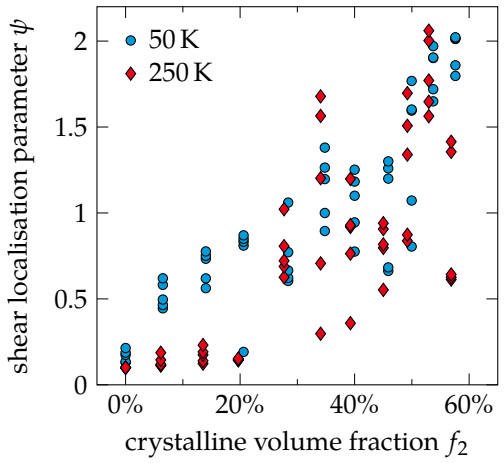

FIGURE 9.3: Shear localisation parameter ψ of the different samples as a function of the crystalline volume fraction f_2. The shear localisation increases together with the amount of crystalline phase, although there is significant scatter.

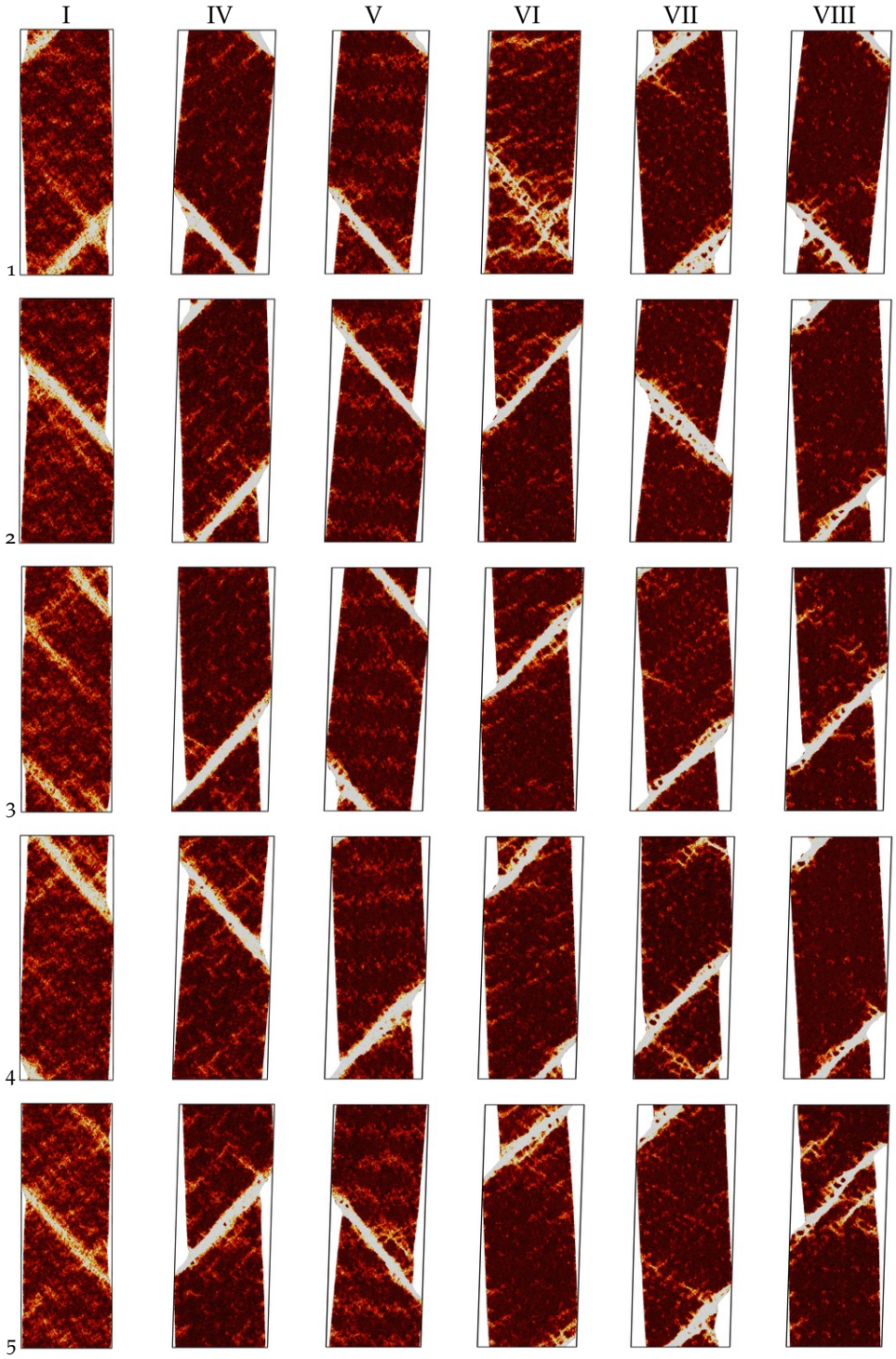

FIGURE 9.4: Snapshots of the samples after deformation at 50 K. Colour coding indicates atomic shear strain and the Arabic numbers on the left and right of each row are used to differentiate tensile test simulations with the same sample. With increasing crystalline volume

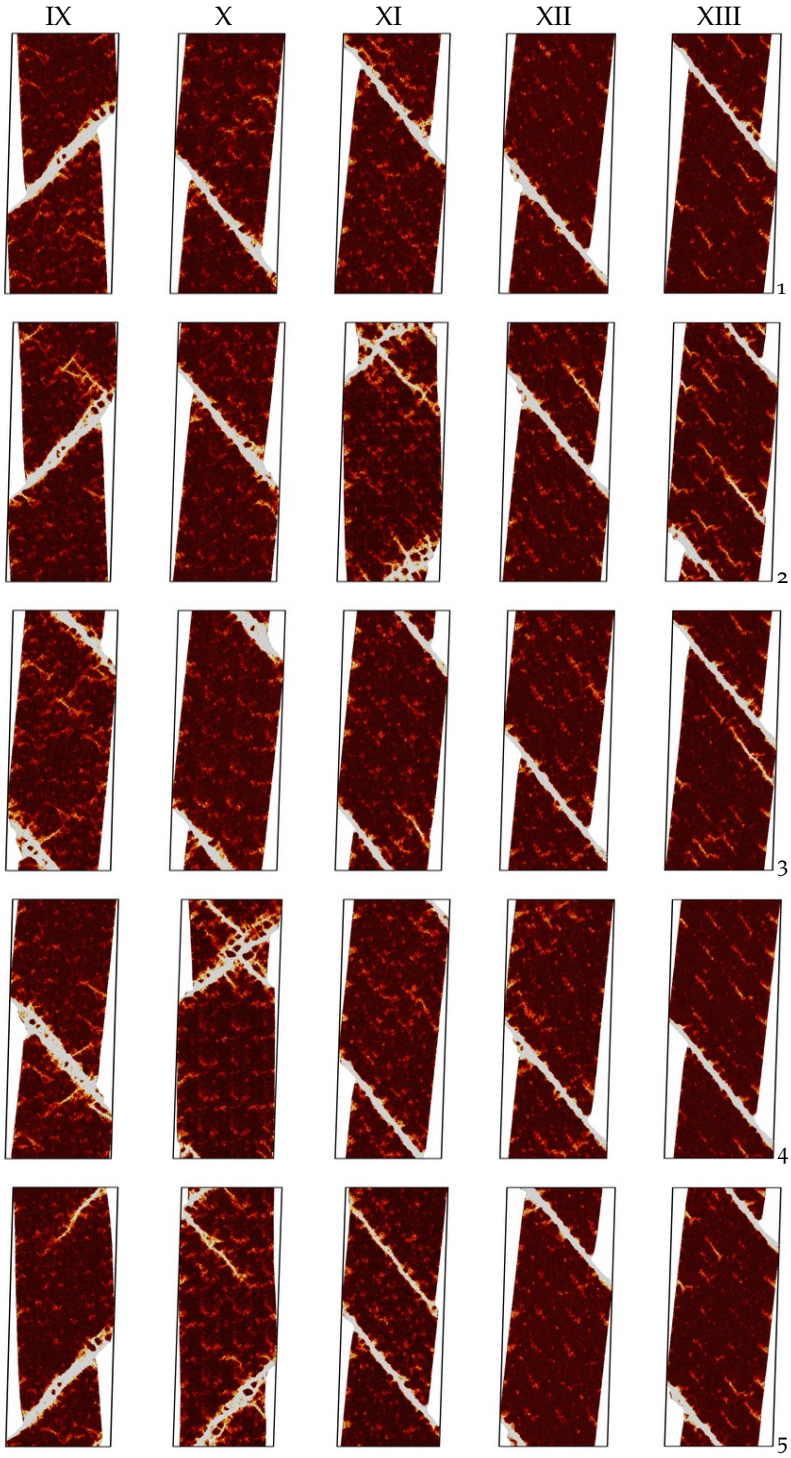

FIGURE 9.4 (cont.): fraction, the shear localisation increases, although different degrees of localisation can be observed for the same sample. Starting from sample V, small, undeformed areas appear inside the shear bands, most likely corresponding to small crystallites.

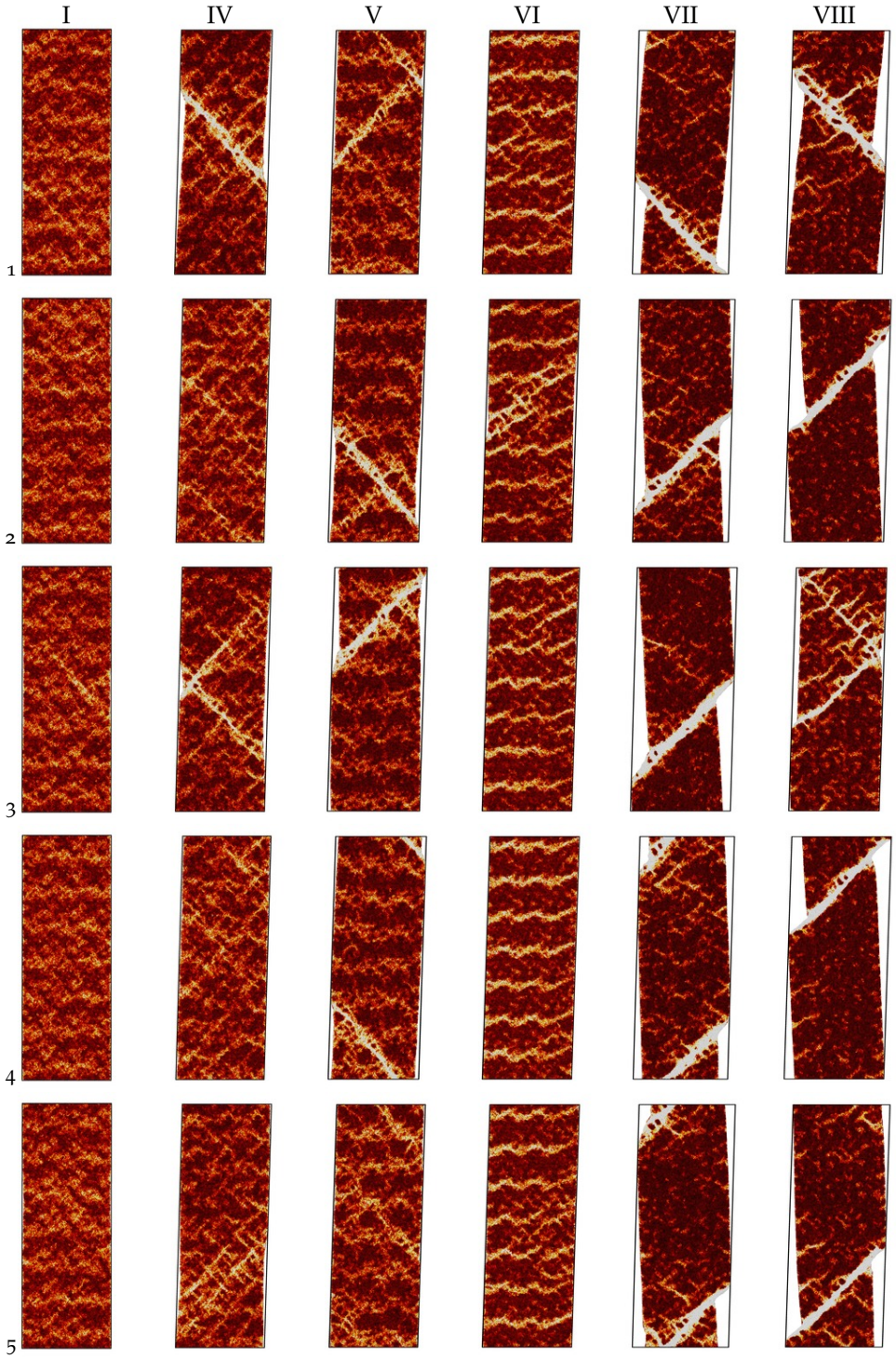

FIGURE 9.5: Snapshots of the samples after deformation at 250 K. Colour coding indicates atomic shear strain and the Arabic numbers on the left and right of each row are used to differentiate tensile test simulations with the same sample. In contrast to the tensile tests at

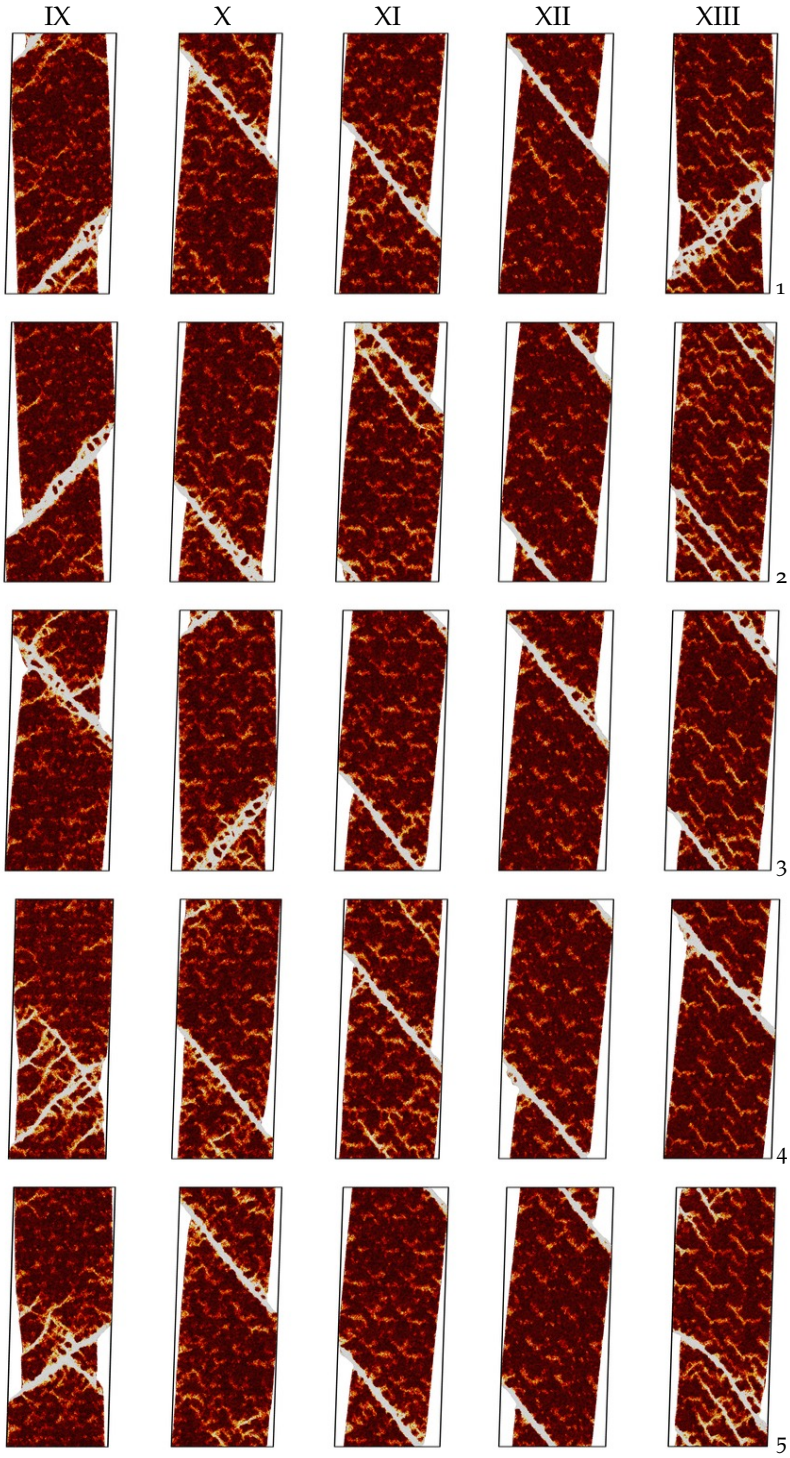

FIGURE 9.5 (cont.): 50 K, samples I–VI do not form shear bands, although certain patterns emerge at higher crystalline volume fractions. These patterns never disappear, but shear banding occurs from sample VII on.

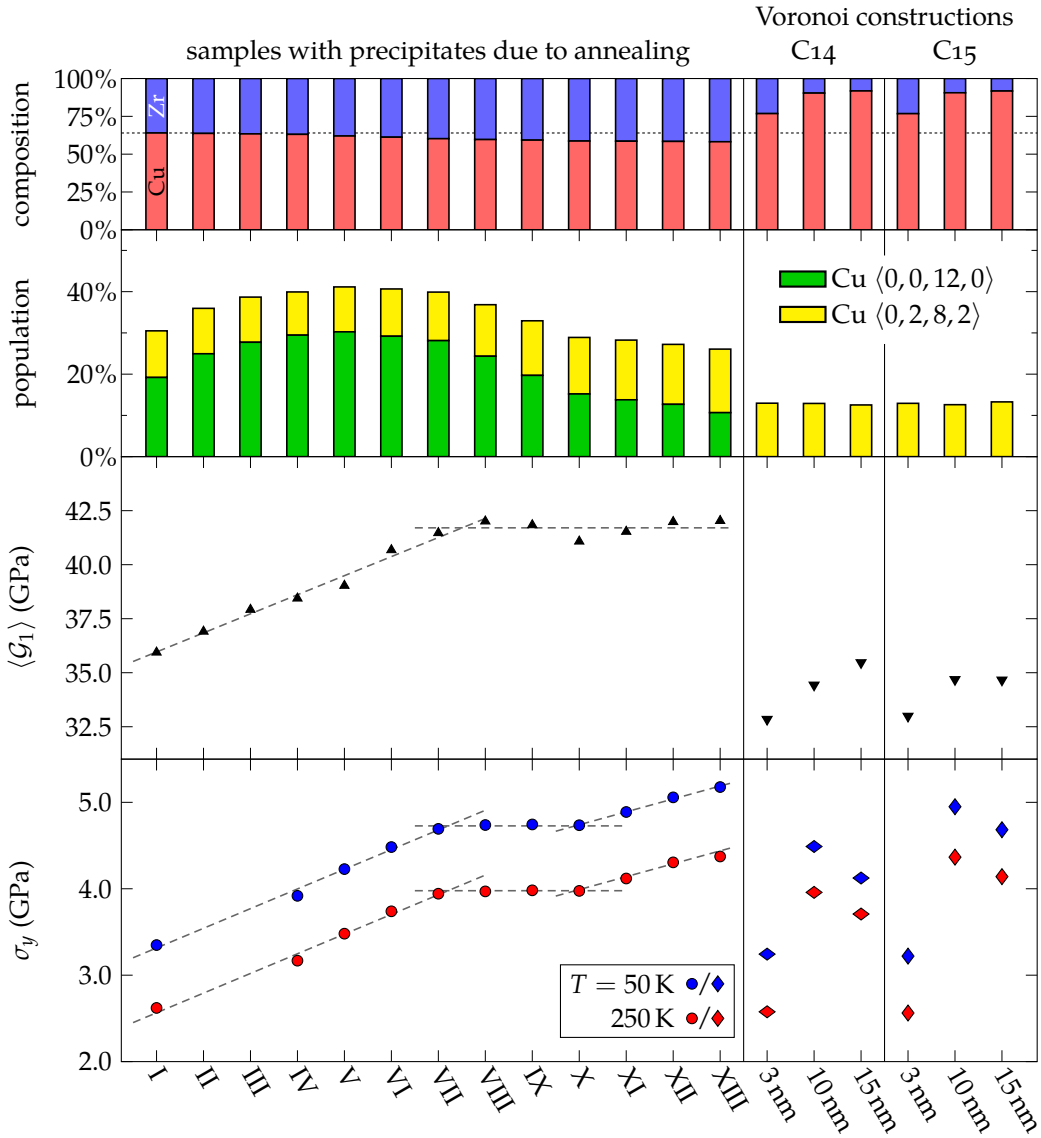

FIGURE 9.6: Properties of the amorphous phases or grain boundaries in the samples. Composition, population of copper-centred icosahedra, and average shear modulus $\mathcal{G}_1$ were calculated for the amorphous atoms only. The value of $\langle \mathcal{G}_1 \rangle$ excludes atoms with negative moduli. The yield stress data is replicated from Fig. 9.2 and applies to the whole sample. The dashed, grey lines indicate trends and serve only to guide the eye.

random, non-overlapping spheres[346] is definitely surpassed and the resulting confinement suppresses the further growth of the nascent shear bands into mature ones. Of course, at least one shear band must traverse the sample at yield and therefore break through its confinement. It can be seen in Fig. 9.5 that patterns of localised deformation persist in samples VIII–XIII at 250 K, indicating that the shear band multi-

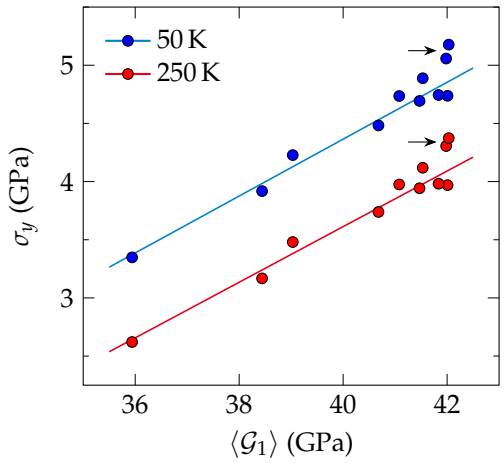

FIGURE 9.7: Yield stress as a function of the shear modulus of the amorphous phase. The lines serve to guide the eye and show that the trend of the yield stress follows the trend of the shear modulus of the amorphous phase, as required by Johnson and Samwer's model. Samples XII and XIII (marked by arrows) lie above this trend as already indicated in Fig. 9.6.

plication still occurs but that the growth of a multitude of shear bands is suppressed. Consequently, strain localisation is increased.

We know from the previous chapter and from literature[145] that the deformation of composites, like the ones presented here, starts in the amorphous phase; we will later see detailed pictures confirming this. Therefore, understanding the onset of plasticity is connected to the understanding of the amorphous phase. We characterised the amorphous phases and grain boundaries according to their composition and their Voronoi statistics. Additionally, we calculated the lowest Kelvin shear modulus $\mathcal{G}_1$ (see Sec. 2.5.3) for the grain boundary atoms and averaged the greater-than-zero moduli. We omitted negative moduli in the average since $\mathcal{G}_1$ is unbounded towards negative infinity and a single unrealistically low value due to numerical errors can skew the whole average. Figure 9.6 presents these values together with the yield stress for all samples we tested. For the annealed samples, the composition slightly changes towards the Zr-rich side as copper atoms are absorbed into the Cu_2Zr phase. The annealing has therefore not only the effect of precipitation, but also of an increase in icosahedral units in the amorphous phase. As discussed earlier, the increasing heterogeneity of the amorphous phase due to the formation of icosahedral networks promotes shear localisation. Since copper icosahedra at the interface are mostly counted towards the crystalline phase because of the detection algorithm, the number becomes less reliable with increasing crystalline volume fraction: An apparent decrease is recorded in the data. A clearer picture for explaining the yield stress is painted by the shear moduli and is also reflected in Fig. 9.7: The moduli increase until they reach a plateau from sample VII on. Concurrently, the yield stress increases, too, until it plateaus at the same time. Starting from sample XI, the yield stress increases again, despite an approximately constant shear modulus. Here we also note that the Voronoi constructions always exhibit low moduli in the grain boundaries, somewhat below the as-cast glass, although their yield stresses vary considerably. This indicates that plasticity in these samples is more complicated and not only a result of the mech-

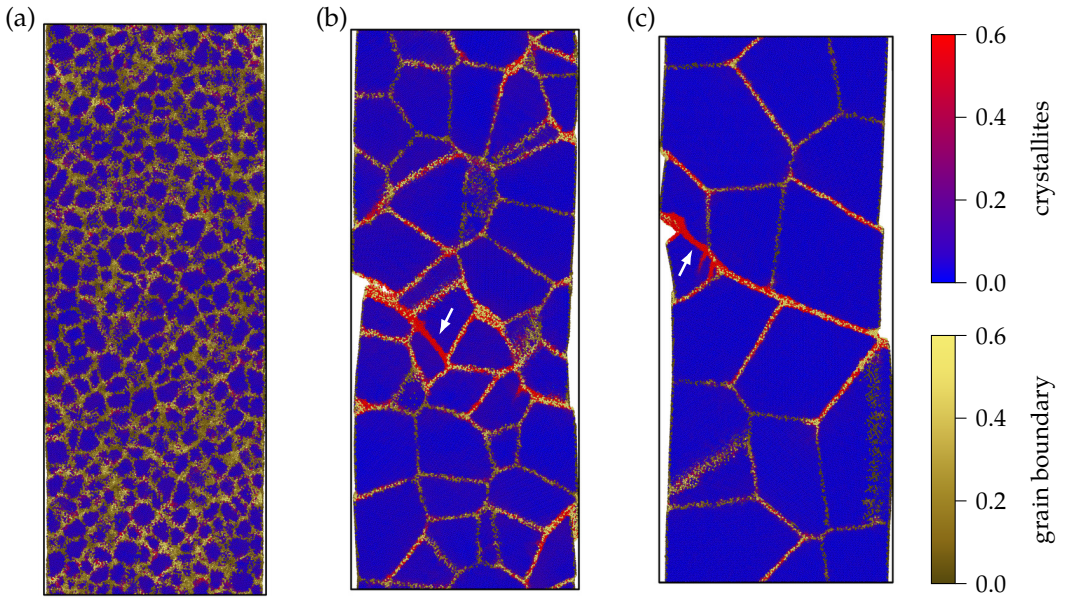

FIGURE 9.8: Plastic deformation of Voronoi-constructed nanocrystals. These snapshots show the C15 samples deformed at 50 K. (a) The sample with 3 nm grain size, depicted after 12% tensile strain, flows homogeneously in the grain boundaries. The samples with grain sizes 10 nm (b) and 15 nm (c) fail along the grain boundaries but have to cut through crystallites because of the compatibility requirement (white arrows). The snapshots were taken at 10% strain (b) and 7.4% strain (c), respectively, which corresponds to the point immediately after yield. The stress drop in Fig. 9.1 (c) therefore directly corresponds to the cutting of a crystallite. The atoms are colour coded according to the atomic shear strain and two colour scales are used: One for the crystallites and one for the amorphous grain boundary phase.

anisms in the amorphous phase. Instead, it is most likely additionally related to the properties of the crystalline phase.

So, let us look at the Voronoi constructions again. The sample with 3 nm grain size deforms homogeneously and only in the grain boundaries [Fig. 9.8 (a)] and its yield stress corresponds to the as-cast glass. The yield stress can be explained by looking at the shear moduli again: The average $\mathcal{G}_1$ in the grain boundary is slightly below the value for the as-cast glass and the yield stresses are similar. This indicates that the grain boundary behaves similarly to the as-cast glass and has a comparable stiffness, leading to a comparable yield stress. There is no difference between the C14 and the C15 polycrystal because the crystalline phase does not partake in the plastic deformation. Compared to the annealed glass, the deformation is more homogeneous. This can be explained by the structure: The Voronoi statistics in Fig. 9.6 reveal that the icosahedral units are missing from the grain boundary, meaning there is no heterogeneous network of GUMs and icosahedra. If the structure is less heterogeneous, the deformation is, too. The confinement due to the large crystalline volume fraction does not play a role since no shear band nucleates.

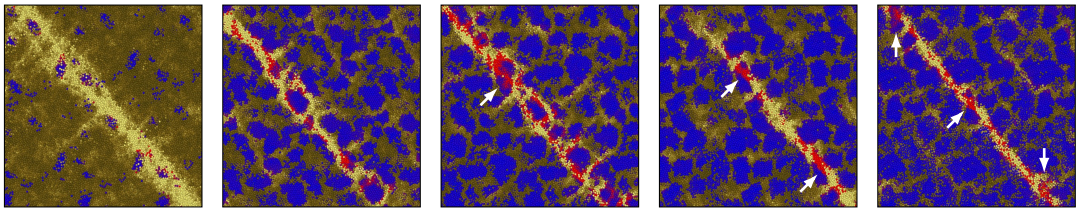

FIGURE 9.9: Snapshots of the shear bands in a selection of samples shortly after yield. The data is from simulations performed at 50 K. Arrows indicate crystallites that were cut by the shear band. Colour coding is the same as Fig. 9.8.

The samples with larger grain sizes exhibit different behaviour despite the fact that their grain boundary is roughly the same in terms of structure and stiffness. The yield stress is comparable to sample XIII and differs between the C14 and the C15 polycrystals. Looking at Figs. 9.8 (b) and (c) explains this. Because of the compatibility requirement crystallites have to deform to obtain macroscopic deformation.[204] Since dislocations are too expensive, this deformation manifests as a shear-band-like slip on crystalline planes which leaves behind an amorphous ribbon. The yield stresses of these samples (and of sample XIII) are therefore equivalent to the theoretical strength of the Laves phases. Therefore the yield stress of C14 and C15 is different—both crystal phases simply differ in strength. Yield strength in this system does not drop significantly with increasing grain size because there are no dislocations: The Hall–Petch relation does not come into play.

As such, we have seen two distinct regimes, depending on crystallite size:

i) glass-like deformation in the weaker amorphous phase or grain boundary that obeys a yielding law according to the cooperative shear model and

ii) polycrystalline deformation in which the total yield strength is defined by the stronger crystalline phase.

Hence, we investigated the increase of yield stress starting from sample X, i.e., at high crystalline volume fractions. Figure 9.9 shows detailed snapshots shortly after yield. The samples with low crystalline volume fraction exhibit behaviour expected from glasses with crystalline precipitates. According to Eqs. 8.17 and 8.19, we predict the shear band to wrap around small obstacles, especially if they have such high yield stresses. And this is in fact what happens. Additionally—and in accord with the literature[145,198]—the small wrapped particles which wind up in the shear band are subsequently dissolved. For higher crystalline volume fraction (starting from sample XI), the particles are suddenly cut despite their small size. This happens more often with increasing f_2, explaining why the yield stress rises again. Figure 9.10 clearly shows how this yield occurs. First, small shear band nuclei appear but are constrained between crystallites. This is connected with some softening of the material. The real

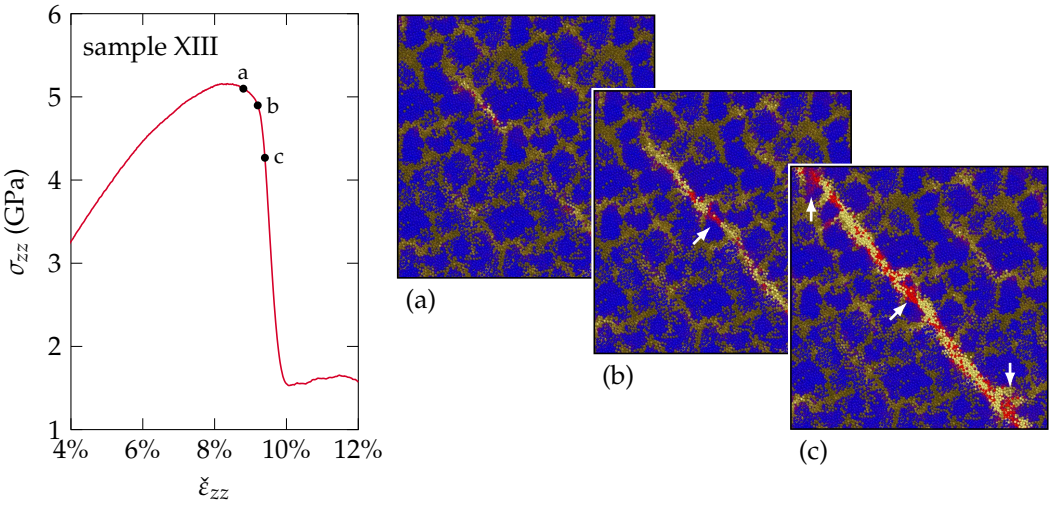

FIGURE 9.10: Detailed depiction of the failure of sample XIII at 50 K. The first softening is connected to the appearance of a nascent shear band (a), while the stress drop requires the cutting of crystallites (b). Further particles are cut during the propagation of the shear band (c). Colour coding is the same as Fig. 9.8.

stress drop, though, only occurs when crystallites are cut. It seems that the transition from a glass-like regime to the nanocrystalline regime is due to confinement of shear bands: Wrapping is suppressed and the crystalline phase starts defining yield. Thus we reached a regime that starts to resemble the nanocrystal, but which is still dominated by shear-band-like strain localisation.

One now needs to ask why the Voronoi-constructed sample with small grains can flow glass-like. This should be connected to the question of shear localisation. If the grain boundary phase is prone to localise the deformation, it will form nascent shear bands which will act as stress concentrators. All further deformation is defined by how these shear band nuclei grow or how slip transfer into the crystalline phase takes place. If the grain boundary phase is very soft and homogeneous, like an unrelaxed glass, it will be prone to homogeneous flow. The crystallites are so small that they can accommodate this flow of the grain boundary phase without jamming.

Looking at Eq. 8.19, we can also see that cutting becomes more favourable if the ratio between the yield stresses of the amorphous and the crystalline phase drops. Taking this into account, it should be possible to modify sample XIII to behave more like the Voronoi construction by softening its amorphous phase, thereby increasing the ratio of yield stresses and discouraging cutting. For this, we performed an additional simulation. We fixed the atoms belonging to the Laves phase and heated the rest to 2000 K and held it there for 400 ps. Afterwards, we equilibrated the whole system at 1000 K for 200 ps to facilitate interface formation and afterwards quenched it instantaneously to 50 K where we equilibrated for another 200 ps. The resulting

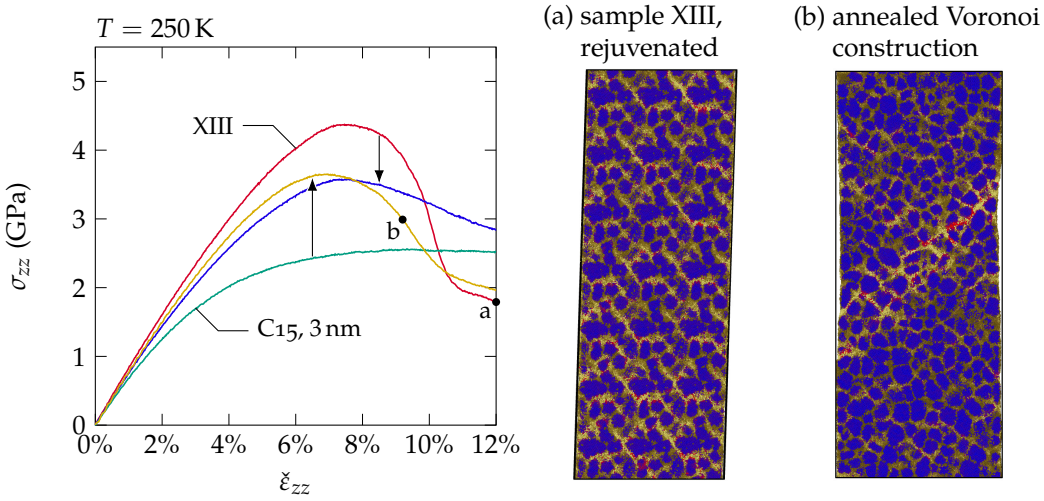

FIGURE 9.11: Tensile tests of the rejuvenated sample XIII and the annealed Voronoi construction at 250 K. The stress–strain curves show that rejuvenation of sample XIII decreases the yield stress from the original value (red) to a lower value in connection with a smoother curve (blue). The corresponding snapshot (a) demonstrates the homogenisation of plastic deformation. The Voronoi construction with 3 nm grain size (green curve) can be hardened by annealing (yellow curve). The deformation changes from the homogeneous flow depicted in Fig. 9.8 to a localised deformation (b). Colour coding is the same as Fig. 9.8.

amorphous phase is rejuvenated, softer, and exhibits a more homogeneous deformation. Figure 9.11 (a) shows a snapshot of the sample after deformation at 250 K. We can see that it is mostly the grain boundary phase which yields. Still, this rejuvenated amorphous phase is stronger and more heterogeneous than in the Voronoi construction and therefore deforms by shear banding at 50 K (not shown).

Vice versa, when annealing the Voronoi construction with grain size 3 nm for 4 ns at 900 K, i.e., below the melting point and around the glass transition temperature, a stronger interface can be produced. Figure 9.11 (b) shows that the deformation becomes much more heterogeneous in this case. Figure 9.11 also contains the corresponding stress–strain curves. These curves reveal that the stress response of sample XIII becomes much smoother upon rejuvenation while the Voronoi construction can be brought closer to the sample XIII by annealing around T_g. This supports the above assertion that the structure of the grain boundary phase dominates the choice of deformation mechanism at the nanoscaled grain sizes treated here. We conjecture that the homogeneous deformation of grain boundaries does not play an important role in experiments, since the strain rates are lower and since the amorphous phase has much more time to relax to a lower-energy structure. Both favour shear localisation in the glass phase (cf. Fig 1.7).

9.3 CONCLUSIONS

The results in this chapter establish that the mechanisms of the plastic deformation of nanocrystalline alloys are governed not only by grain size but also by the grain-boundary properties. In the case of large grains, compatibility requires that the grains themselves deform. Since those are usually the strongest, they define the yield stress. For smaller sizes, i.e., in the sub-10-nm regime, a deformation excluding a participation of the crystallites is possible if the flow of the grain-boundary phase is relatively homogeneous or if the crystalline volume fraction is low enough to allow shear band propagation by wrapping. In the latter case we obtain a glass-like deformation as discussed in the previous chapter. Here, the yield stress of the *weakest* phase defines macroscopic yield.

Even if the crystallites partake in the plastic deformation, a grain boundary phase with volume fractions approaching or surpassing 40% will significantly change the nature of the deformation. Instead of thinking about crystalline plasticity that somehow interacts with grain boundaries, we have to imagine glass-like plasticity, i.e., shear banding, that has to overcome crystalline obstacles. This is in accord with experimental data suggesting shear banding for very small grain sizes.[201] Like in nanocrystals with bigger grain sizes, though, the yield is determined by the *strongest* phase, because shear bands in the amorphous phase alone cannot macroscopically deform the sample. What we know as shear banding in metallic glasses becomes grain-boundary shear and slip. Indeed, grain-boundary shear and slip is experimentally observed already in a nominally elastic regime and indicates the start of micro-plasticity.[209] These effects are constrained by the grains and cannot develop into macro-plasticity without cooperation of the crystalline phase.

Part IV

CONCLUSIONS

SUMMARY

Using molecular dynamics computer simulations, we could provide several new insights into the structure–property relations in heterogeneous copper–zirconium metallic glasses. The primary topics of this thesis are solid-state amorphisation in absence of lattice mismatch, the boson peak in metallic alloys, and the plastic deformation of glasses with and without crystalline secondary phases. The key findings in these areas are summarised below.

STRUCTURE, THERMODYNAMICS, AND VIBRATIONAL PROPERTIES

- **Thin films of copper, an fcc metal with a high propensity for crystallisation, can become amorphous for thermodynamic reasons when embedded into a glass matrix, even in absence of lattice mismatch.** In crystals, solid-state amorphisation is already known, but it is driven by the unfavourable mismatch between neighbouring crystal lattices. In the case of copper layers embedded in a $Cu_{64}Zr_{36}$ glass matrix, though, the reason for amorphisation is a reduction of the glass–glass interface energy due to structural similarities between $Cu_{64}Zr_{36}$ and amorphous copper (Chap. 4). Thus, this novel effect can only occur in composites with structural similarity between the amorphous phases.

- **Plastically deformed metallic glass samples exhibit a stronger boson peak signal.** Previously, the boson peak was measured only for undeformed glasses. In our findings presented in Chap. 6, which agree with experimental measurements performed by our collaborators, a clear increase of the boson peak magnitude appears inside the shear band.

- **The intensity of the boson peak is sensitive to structural changes, while its frequency is not.** The discussion around the origin of the boson peak revolves mostly about the question if it is a van Hove singularity, shifted to lower frequencies by a change of density, or if the boson peak consists of excess modes due to disorder. The fact that the intensity of the boson peak signal changes with the structure of the glass, while the frequency does not, speaks for the latter.

- **Chemical disorder on a regular lattice, such as in high-entropy alloys, does not lead to a boson peak, even when modifying the density.** To get a clearer indication of the boson peak's origin, we investigated a defect-free high-entropy alloy. The shape of the alloy's phonon density of states is the typical one of an fcc structure. Thus, chemical disorder on a regular lattice is not sufficient to

induce a boson peak, and neither is a simple scaling of the density. While a reduction of density to values typical of a metallic glass leads to a shift of the first van Hove singularity of the material, this singularity does not shift down to the frequency range of the boson peak.

- **The introduction of interstitial defects into such a lattice, on the other hand, does induce a boson peak.** The regions around individual interstitial defects already exhibit a boson peak signal of comparable strength to a bulk glass. The total signal in a macroscopic sample is of course much weaker, because the defective regions represent only a low fraction of the total sample volume. A metallic glass can be thought of as consisting of a high number of such defects.

- **The boson peak is connected to defective regions, characterised by reduced stiffness and increased disorder.** A closer investigation of the defective regions in the high-entropy alloy reveals that they are less stiff than the intact lattice. Similarly, Cu–Zr glasses contain regions of reduced stiffness, the so-called soft spots. We could show that the boson peak is an indicator for the amount of these softened regions.

HETEROGENEOUS PLASTICITY

- **In a sufficiently large, homogeneous glass sample, the shear band propagation direction deviates from the plane of highest resolved shear stress.** In Chap. 7, we report on shear tests in which shear band lengths of several hundred nanometres are reached. During stress drops, the shear band propagates in a direction which is slightly inclined away from the plane of highest resolved shear stress, likely connected to the sudden stress release. Otherwise, a slower horizontal propagation takes place.

- **Path deviations lead to a rougher energy landscape for continued shear band movement.** Small serrations in the stress–strain curve therefore occur even in the absence of the nucleation of new shear bands. A stick–slip-like propagation of the shear band front can be observed.

- **Deviations from the plane of highest resolved shear stress are connected with the build-up of compressive stresses. Experimentally observed variations of density and composition along the shear band may be due to diffusive processes driven by stress reduction.** Residual stresses arise because of the propagation path of the shear band: Whenever the shear band leaves the plane of highest resolved shear stress, volumetric stress components arise, which cannot be reduced by the plastic deformation. The diffusivity in the shear band is high and we propose that the residual stresses act as a driving force to reduce

density in the compressed parts of the shear band. This diffusivity is unfortunately too slow to be observed in our MD simulations.

- **In composites with crystalline precipitates, a previously unreported interaction mechanism between shear bands and precipitates occurs: The shear band can wrap around smaller precipitates, which therefore pose no obstacle to shear band propagation.** As there is no defined slip plane for a shear band, a temporary change of propagation direction has no energy barrier. Our computer simulations in Chap. 8 show that smaller precipitates can easily be bypassed. For precipitate diameters larger than 20 nm to 40 nm, nucleation of a new shear band becomes preferable to wrapping.

- **We derived a mechanism map from systematic investigation of the influence of precipitate size and distance.** Based on an equilibrium of forces around the precipitate, we derived a model that can predict the mechanism—wrapping around the precipitate, blocking the shear band, or a plastic deformation of the crystallite—based on the precipitate geometry and yield strength. A comparison with the available experimental data supports our model. The experimental observation that smaller precipitates appear undeformed can be explained by the wrapping mechanism.

- **Thermal annealing of $Cu_{64}Zr_{36}$ samples leads to crystallisation that finally results in nanocrystalline samples with amorphous grain boundaries.** Presented in Chap. 5, samples of varying crystalline volume fraction can be obtained. These samples go through the stages of an as-cast glass, a crystal–glass composite, and finally a nanocrystal.

- **With increasing crystalline volume fraction, the aforementioned wrapping mechanism becomes suppressed because of the compatibility requirement.** In Chap. 9, we use the samples with varying crystalline volume fraction in order to show that at some point the shear band can no longer wrap around all crystallites, even if our model from Chap. 8 still predicts that this mechanism is the most favourable. The reason is that these samples more closely resemble a nanocrystal in which the shear bands are confined by the grains. Thus, the grains must partake in the plastic deformation because of the compatibility requirement of polycrystals. Nevertheless, the plastic deformation at small grain sizes still resembles shear banding and the macroscopic mechanical response of the sample is a mixture of the mechanical response of both the amorphous and the crystalline phase.

- **Similar to a bulk glass, the deformation in the grain boundary phase is highly dependent on the relaxation state of the amorphous phase.** We used differently prepared samples to show that the state of the grain boundary phase defines the plastic response of the whole system. For grain sizes of 3 nm, we

used both relaxed and rejuvenated, i.e., very soft, grain boundary phases. The rejuvenated phase flows homogeneously at the strain rates used in our simulations, similar to a quickly-quenched glass. In this case, the crystallites are only deformed elastically, while the amorphous phase flows around them. The relaxed grain boundary phase, on the other hand, deforms by shear banding and the grains participate in the deformation.

- **With increasing grain sizes, the importance of the grain boundary phase diminishes, and the crystalline phase defines the mechanical properties.** The distinction between different states of the grain boundary phase becomes less important with bigger crystallites. At a grain size of 10 nm, shear banding becomes grain boundary slip and shear. A homogeneous flow around the crystallites is impossible and any deformation needs to include the grain interiors. The yield stress is independent of the grain boundary state.

OUTLOOK

As nearly all scientific research, our work has answered some questions but also raised new ones. We saw in Chap. 6 that the boson peak can serve as an indicator of the relaxation state of the metallic glass. Experimentally, our collaborators found deeper relaxations after annealing in heavily deformed samples compared to as-cast samples, but no crystallisation. Simulations, on the other hand, find that structural relaxations simply drive the state of the shear band back to the same state as the matrix. It is still unclear if this is because of a difference in composition (the experiments were performed on Zr–Cu–Al glass, while most simulations use only the binary Cu–Zr system), a deficiency of the EAM potentials, or a difference between experimental and simulated shear bands. Because of the short timescale, simulations can only observe the earliest stages of shear banding, while new relaxation paths on the potential energy landscape may only open up after heavy damage was incurred on the sample. Since potentials exist for several glass formers—including some ternary alloys—future atomistic computer simulations can easily be expanded to different glasses and compositions. The modified relaxation paths after deformation may also be related to the stress-induced heterogeneities along the shear band path, which we discussed in Chap. 7.

Regarding the mechanical properties of metallic glass composites, our results should open some new avenues of research. First of all, the proposed model from Chap. 8 for the interaction of shear bands with precipitates should be put to the test. Continuum calculations could serve in this context as a means to overcome the size limitations of MD and systematic experimental observations of shear band paths could be used to verify our results. From the standpoint of atomistic modelling, a shift of the focus towards the mechanical properties of the crystalline phase seems promising. Current experimental research reveals that shape-memory alloys may be attractive candidates as secondary phases. As we saw in Chap. 3, the concurrent description of glasses and crystals with a single interatomic potential is still deficient. Hence, potentials that are able to reproduce the properties of both the amorphous and the crystalline phases are needed.

DANKSAGUNG – ACKNOWLEDGEMENTS

An dieser Stelle möchte ich als Erstes Karsten Albe danken, sowohl für das Vertrauen in meine wissenschaftliche Arbeit und die Möglichkeiten, die er mir eröffnet hat, als auch für die guten Rahmenbedingungen in seiner Arbeitsgruppe.

Als Nächstes gilt mein Dank Professor Jürgen Eckert für die Begutachtung dieser Arbeit sowie Professor Karsten Durst und Professor Michael Vogel, die sich als Mitglieder meiner Prüfungskommission zur Verfügung gestellt haben.

Die Zusammenarbeit mit der AG Wilde an der Westfälischen Wilhelms-Universität Münster war eine Bereicherung. Insbesondere möchte ich mich bei Gerhard Wilde, Martin Peterlechner, Harald Rösner und Jonas Bünz für die Kollaboration bei unseren gemeinsamen Veröffentlichungen und für die neuen Forschungsideen bedanken.

I am indebted to Graeme Henkelman at the University of Texas at Austin for hosting me during my extended stay in his group and for the insights into new modelling methods. I also want to thank Kai Nordlund from the University of Helsinki for always welcoming visitors from Darmstadt and for the enlightening discussions with his group.

In unserem Institut in Darmstadt muss der Dank natürlich als Erstes unseren Sekretärinnen Renate Hernichel und Gabi Rühl gelten, die die Organisation unseres Fachgebiets stemmen. Ich danke natürlich auch allen anderen MMs für die große Hilfsbereitschaft in wissenschaftlichen Fragen und selbstverständlich auch für die gute Zeit im Büro und außerhalb. Insbesondere möchte ich Alexander Stukowski erwähnen, der in OVITO-Fragen immer ein offenes Ohr hat. Ich möchte auch auf keinen Fall Constanze Kalcher, Leonie Koch und Omar Adjaoud vergessen, die (zumindest zeitweise) auch mit mir an metallischen Gläsern geforscht haben.

Mein besonderer Dank gilt meinen Eltern, die mich immer bei meinem Werdegang unterstützt haben.

I also want to thank everybody who was not named above, but who enriched my scientific career by private discussions, at conferences, in the publication business, and elsewhere. The community working on atomistic simulation and on the mechanics of metals in general has in many cases been enthusiastic and friendly and has made working as a scientist a pleasure.

Finally, financial support by the Deutsche Forschungsgemeinschaft (DFG) through project grants nos. AL 578/13-1 and AL 578/6-2 is gratefully acknowledged. I benefited from a travel grant to the University of Texas at Austin by DFG SPP 1594 and from the DAAD PPP Finland exchange program. Computing time was granted by the John von Neumann Institute for Computing (NIC) and provided on the supercomputer JUROPA at Jülich Supercomputing Centre (JSC), as well as by the Gauss Centre for Supercomputing (GCS) through the NIC on the GCS share of the supercomputer JUQUEEN at JSC. GCS is the alliance of the three national supercomputing centres HLRS (Universität Stuttgart), JSC (Forschungszentrum Jülich), and LRZ (Bayerische Akademie der Wissenschaften), funded by the German Federal Ministry of Education and Research and the German State Ministries for Research of Baden-Württemberg, Bayern, and Nordrhein-Westfalen. Additional computing time was made available by Technische Universität Darmstadt on the Lichtenberg cluster.

CURRICULUM VITÆ

— RESEARCH EXPERIENCE

Scientific staff member (*Wissenschaftlicher Mitarbeiter*)
and study towards a doctoral degree, 2012–
Materials Modelling group (Prof. Albe)
Technische Universität Darmstadt, Germany

Visiting scientist (three months), 2014
Henkelman group
University of Texas at Austin, USA

Visiting scientist (three weeks in total), between 2012 and 2016
Division of Materials Physics (Prof. Nordlund)
University of Helsinki, Finland

— EDUCATION

Study of materials science (Dipl.-Ing.), 2006–2012
Technische Universität Darmstadt, Germany

Secondary education (*Abitur*), 1996–2005
Werner-Heisenberg-Gymnasium, Neuwied, Germany

— PEER-REVIEWED PUBLICATIONS

Jonas Bünz, **Tobias Brink**, Koichi Tsuchiya, Fanqiang Meng, Gerhard Wilde, and Karsten Albe, *Low temperature heat capacity of a severely deformed metallic glass*, Phys. Rev. Lett. **112**, 135501 (2014), listed as Ref. 327

Tobias Brink, Daniel Şopu, and Karsten Albe, *Solid-state amorphization of Cu nanolayers embedded in a $Cu_{64}Zr_{36}$ glass*, Phys. Rev. B **91**, 184103 (2015), listed as Ref. 323.

Tobias Brink, Martin Peterlechner, Harald Rösner, Karsten Albe, and Gerhard Wilde, *Influence of crystalline nanoprecipitates on shear-band propagation in Cu–Zr-based metallic glasses*, Phys. Rev. Appl. **5**, 054005 (2016), listed as Ref. 338.

Tobias Brink, Leonie Koch, and Karsten Albe, *Structural origins of the boson peak in metals: From high-entropy alloys to metallic glasses*, Phys. Rev. B **94**, 224203 (2016), listed as Ref. 328.

— OTHER PUBLICATIONS

Tobias Brink, Omar Adjaoud, and Karsten Albe, *Nanostructured metallic glasses: Tailoring the mechanical properties of amorphous metals*, NIC Symposium 2016, NIC Series vol. 48, Forschungszentrum Jülich, John von Neumann Institute for Computing, pp. 191–198 (2016).

Tobias Brink, *Atomistic computer simulations of amorphous silicon oxycarbide*, diploma thesis, Technische Universität Darmstadt, November 2012.

— ORAL PRESENTATIONS AT INTERNATIONAL CONFERENCES

Tobias Brink, Daniel Şopu, and Karsten Albe, *Solid state amorphization of thin metal films embedded in bulk metallic glass*, **DPG-Frühjahrstagung 2014**, Dresden, Germany

Jonas Bünz, Tobias Brink, Koichi Tsuchiya, Fanqiang Meng, Gerhard Wilde, and Karsten Albe, *Boson peak in the heat capacity of severely deformed metallic glass*, **DPG-Frühjahrstagung 2014**, Dresden, Germany

Tobias Brink, and Karsten Albe, *Influencing shear band propagation with crystalline precipitates: Atomistic computer simulations on Cu–Zr metallic glass*, **2014 MRS Fall Meeting**, Boston, USA

Tobias Brink, and Karsten Albe, *Potential energy landscape of deformed Cu–Zr based metallic glasses*, **DPG-Frühjahrstagung 2015**, Berlin, Germany

Tobias Brink, and Karsten Albe, *Thermal relaxation of metallic glasses: Influence on structure and mechanical properties*, **DPG-Frühjahrstagung 2016**, Regensburg, Germany

— POSTER PRESENTATIONS AT INTERNATIONAL CONFERENCES

Tobias Brink, Daniel Şopu, and Karsten Albe, *Solid state amorphization of thin metal films embedded in metallic glass*, **Fifth Seeheim Conference on Magnetism 2013**, Frankfurt am Main, Germany

Tobias Brink, Constanze Kalcher, and Karsten Albe, *Potential energy landscape of shear transformation zone activation barriers in Cu-Zr based metallic glasses*, **ISMANAM 2015**, Paris, France

Tobias Brink, Martin Peterlechner, Harald Rösner, Karsten Albe, and Gerhard Wilde, *Influence of nanocrystalline precipitates on shear band propagation in Cu–Zr based metallic glasses*, **ISMANAM 2015**, Paris, France

Tobias Brink, and Karsten Albe, *Mechanisms of plastic deformation of metallic glass composites with crystalline secondary phases*, **MSE Congress 2016**, Darmstadt, Germany.

BIBLIOGRAPHY

[1] A. L. Greer, *Metallic glasses*, Science **267**, 1947–1953 (1995).

[2] R. Zallen, *The physics of amorphous solids*, Wiley VCH, 1983.

[3] W. Klement, R. H. Willens, and P. Duwez, *Non-crystalline structure in solidified gold–silicon alloys*, Nature **187**, 869–870 (1960).

[4] H. S. Chen, *Thermodynamic considerations on the formation and stability of metallic glasses*, Acta Metall. **22**, 1505–1511 (1974).

[5] M. C. Lee, J. M. Kendall, and W. L. Johnson, *Spheres of the metallic glass $Au_{55}Pb_{22.5}Sb_{22.5}$ and their surface characteristics*, Appl. Phys. Lett. **40**, 382–384 (1982).

[6] H. W. Kui, A. L. Greer, and D. Turnbull, *Formation of bulk metallic glass by fluxing*, Appl. Phys. Lett. **45**, 615–616 (1984).

[7] A. Inoue, T. Zhang, and T. Masumoto, *Al–La–Ni amorphous alloys with a wide supercooled liquid region*, Mater. Trans. JIM **30**, 965–972 (1989).

[8] A. Inoue, T. Zhang, and T. Masumoto, *Zr–Al–Ni amorphous alloys with high glass transition temperature and significant supercooled liquid region*, Mater. Trans. JIM **31**, 177–183 (1990).

[9] A. Inoue, *Stabilization of metallic supercooled liquid and bulk amorphous alloys*, Acta Mater. **48**, 279–306 (2000).

[10] W. H. Wang, C. Dong, and C. H. Shek, *Bulk metallic glasses*, Mater. Sci. Eng. R **44**, 45–89 (2004).

[11] M. Telford, *The case for bulk metallic glass*, Mater. Today **7**, 36–43 (2004).

[12] M. F. Ashby and A. L. Greer, *Metallic glasses as structural materials*, Scr. Mater. **54**, 321–326 (2006).

[13] J. Eckert, J. Das, S. Pauly, and C. Duhamel, *Mechanical properties of bulk metallic glasses and composites*, J. Mater. Res. **22**, 285–301 (2007).

[14] C. A. Schuh, T. C. Hufnagel, and U. Ramamurty, *Mechanical behavior of amorphous alloys*, Acta Mater. **55**, 4067–4109 (2007).

[15] J. Schroers, G. Kumar, T. M. Hodges, S. Chan, and T. R. Kyriakides, *Bulk metallic glasses for biomedical applications*, JOM **61**, 21–29 (2009).

[16] M. Carmo, R. C. Sekol, S. Ding, G. Kumar, J. Schroers, and A. D. Taylor, *Bulk metallic glass nanowire architecture for electrochemical applications*, ACS Nano **5**, 2979–2983 (2011).

[17] A. L. Greer, Y. Q. Cheng, and E. Ma, *Shear bands in metallic glasses*, Mat. Sci. Eng. R **74**, 71–132 (2013).

[18] J. A. Yurko, E. E. Vidal, N. W. Hutchinson, J. L. Mattlin, and T. A. Waniuk, *Zirconium (Zr) and hafnium (Hf) based BMG alloys*, Apple Inc., United States Patent Application 20160032435, 2016.

[19] T. C. Hufnagel, C. A. Schuh, and M. L. Falk, *Deformation of metallic glasses: Recent developments in theory, simulations, and experiments*, Acta Mater. **109**, 375–393 (2016).

[20] T. Zhang, A. Inoue, and T. Masumoto, *Amorphous Zr–Al–TM (TM = Co, Ni, Cu) alloys with significant supercooled liquid region of over 100 K*, Mater. Trans. JIM **32**, 1005–1010 (1991).

[21] A. Inoue, W. Zhang, T. Zhang, and K. Kurosaka, *High-strength Cu-based bulk glassy alloys in Cu–Zr–Ti and Cu–Hf–Ti ternary systems*, Acta Mater. **49**, 2645–2652 (2001).

[22] A. Inoue, T. Zhang, K. Kurosaka, and W. Zhang, *High-strength Cu-based bulk glassy alloys in Cu–Zr–Ti–Be system*, Mater. Trans. JIM **42**, 1800–1804 (2001).

[23] Q. Zhang, W. Zhang, and A. Inoue, *New Cu–Zr-based bulk metallic glasses with large diameters of up to 1.5 cm*, Scr. Mater. **55**, 711–713 (2006).

[24] D. Wang, Y. Li, B. B. Sun, M. L. Sui, K. Lu, and E. Ma, *Bulk metallic glass formation in the binary Cu–Zr system*, Appl. Phys. Lett. **84**, 4029–4031 (2004).

[25] D. Xu, B. Lohwongwatana, G. Duan, W. L. Johnson, and C. Garland, *Bulk metallic glass formation in binary Cu-rich alloy series – $Cu_{100-x}Zr_x$ ($x = 34, 36, 38.2, 40$ at.%) and mechanical properties of bulk $Cu_{64}Zr_{36}$ glass*, Acta Mater. **52**, 2621–2624 (2004).

[26] M.-B. Tang, D.-Q. Zhao, M.-X. Pan, and W.-H. Wang, *Binary Cu–Zr bulk metallic glasses*, Chin. Phys. Lett. **21**, 901 (2004).

[27] W. H. Wang, J. J. Lewandowski, and A. L. Greer, *Understanding the glass-forming ability of $Cu_{50}Zr_{50}$ alloys in terms of a metastable eutectic*, J. Mater. Res. **20**, 2307–2313 (2005).

[28] G. Duan, D. Xu, Q. Zhang, G. Zhang, T. Cagin, W. L. Johnson, and W. A. Goddard III, *Molecular dynamics study of the binary $Cu_{46}Zr_{54}$ metallic glass motivated*

by experiments: Glass formation and atomic-level structure, Phys. Rev. B **71**, 224208 (2005), Erratum: Phys. Rev. B **74**, 019901 (2006).

[29] See for example Refs. 52, 59, 60, 91–95, 97, 98, 109, 110, 123, 125, 145, 146, 314, 325 for simulations using $Cu_{64}Zr_{36}$ metallic glasses and Refs. 124, 308, 310, 311 for Cu–Zr potentials.

[30] Y. Q. Cheng and E. Ma, *Atomic-level structure and structure–property relationship in metallic glasses*, Prog. Mater. Sci. **56**, 379–473 (2011).

[31] E. Ma, *Tuning order in disorder*, Nat. Mater. **14**, 547–552 (2015).

[32] C. C. Hays, C. P. Kim, and W. L. Johnson, *Microstructure controlled shear band pattern formation and enhanced plasticity of bulk metallic glasses containing in situ formed ductile phase dendrite dispersions*, Phys. Rev. Lett. **84**, 2901–2904 (2000).

[33] C. C. Hays, C. P. Kim, and W. L. Johnson, *Improved mechanical behavior of bulk metallic glasses containing in situ formed ductile phase dendrite dispersions*, Mater. Sci. Eng. A **304–306**, 650–655 (2001).

[34] M. D. Ediger, C. A. Angell, and S. R. Nagel, *Supercooled liquids and glasses*, J. Phys. Chem. **100**, 13200–13212 (1996).

[35] D. A. Porter and K. E. Easterling, *Phase transformations in metals and alloys*, 2nd ed., CRC Press, 1992.

[36] P. G. Debenedetti and F. H. Stillinger, *Supercooled liquids and the glass transition*, Nature **410**, 259–267 (2001).

[37] C. A. Angell, *Relaxation in liquids, polymers and plastic crystals – strong/fragile patterns and problems*, J. Non-Cryst. Solids **131–133, part 1**, 13–31 (1991).

[38] R. Böhmer, K. L. Ngai, C. A. Angell, and D. J. Plazek, *Nonexponential relaxations in strong and fragile glass formers*, J. Chem. Phys. **99**, 4201–4209 (1993).

[39] D. N. Perera, *Compilation of the fragility parameters for several glass-forming metallic alloys*, J. Phys.: Condens. Matter **11**, 3807 (1999).

[40] H. Tanaka, *Relationship among glass-forming ability, fragility, and short-range bond ordering of liquids*, J. Non-Cryst. Solids **351**, 678–690 (2005).

[41] E. S. Park, J. H. Na, and D. H. Kim, *Correlation between fragility and glass-forming ability/plasticity in metallic glass-forming alloys*, Appl. Phys. Lett. **91**, 031907 (2007).

[42] R. Busch, J. Schroers, and W. H. Wang, *Thermodynamics and kinetics of bulk metallic glass*, MRS Bulletin **32**, 620–623 (2007).

[43] N. Jakse and A. Pasturel, *Local order and dynamic properties of liquid and undercooled Cu_xZr_{1-x} alloys by ab initio molecular dynamics*, Phys. Rev. B **78**, 214204 (2008).

[44] K. Russew, L. Stojanova, S. Yankova, E. Fazakas, and L. K. Varga, *Thermal behavior and melt fragility number of $Cu_{100-x}Zr_x$ glassy alloys in terms of crystallization and viscous flow*, JPCS **144**, 012094 (2009).

[45] W. Kauzmann, *The nature of the glassy state and the behavior of liquids at low temperatures*, Chem. Rev. **43**, 219–256 (1948).

[46] F. H. Stillinger, *Supercooled liquids, glass transitions, and the Kauzmann paradox*, J. Chem. Phys. **88**, 7818–7825 (1988).

[47] J. Jäckle, *Models of the glass transition*, Rep. Prog. Phys. **49**, 171 (1986).

[48] D. R. Uhlmann, *A kinetic treatment of glass formation*, J. Non-Cryst. Solids **7**, 337–348 (1972).

[49] G. Duan, M. L. Lind, M. D. Demetriou, W. L. Johnson, W. A. Goddard III, T. Çaǵin, and K. Samwer, *Strong configurational dependence of elastic properties for a binary model metallic glass*, Appl. Phys. Lett. **89**, 151901 (2006).

[50] Y. Q. Cheng, A. J. Cao, H. W. Sheng, and E. Ma, *Local order influences initiation of plastic flow in metallic glass: Effects of alloy composition and sample cooling history*, Acta Mater. **56**, 5263–5275 (2008).

[51] Y. Q. Cheng and E. Ma, *Indicators of internal structural states for metallic glasses: Local order, free volume, and configurational potential energy*, Appl. Phys. Lett. **93**, 051910 (2008).

[52] Y. Q. Cheng, A. J. Cao, and E. Ma, *Correlation between the elastic modulus and the intrinsic plastic behavior of metallic glasses: The roles of atomic configuration and alloy composition*, Acta Mater. **57**, 3253–3267 (2009).

[53] Y. Ritter, *Molecular dynamics simulations of structure–property relationships in Cu–Zr metallic glasses*, Ph.D. thesis, Technische Universität Darmstadt, 2012.

[54] M. H. Cohen and D. Turnbull, *Molecular transport in liquids and glasses*, J. Chem. Phys. **31**, 1164–1169 (1959).

[55] D. Turnbull and M. H. Cohen, *Free-volume model of the amorphous phase: Glass transition*, J. Chem. Phys. **34**, 120–125 (1961).

[56] D. Turnbull and M. H. Cohen, *On the free-volume model of the liquid–glass transition*, J. Chem. Phys. **52**, 3038–3041 (1970).

[57] T. Egami, *Understanding the properties and structure of metallic glasses at the atomic level*, JOM **62**, 70–75 (2010).

[58] Y. Petrusenko, A. Bakai, V. Borysenko, A. Astakhov, and D. Barankov, *Investigation of bulk metallic glass structure by means of electron irradiation*, Intermetallics **17**, 246–248 (2009).

[59] K. A. Avchaciov, Y. Ritter, F. Djurabekova, K. Nordlund, and K. Albe, *Controlled softening of $Cu_{64}Zr_{36}$ metallic glass by ion irradiation*, Appl. Phys. Lett. **102**, 181910 (2013).

[60] K. A. Avchaciov, Y. Ritter, F. Djurabekova, K. Nordlund, and K. Albe, *Effect of ion irradiation on structural properties of $Cu_{64}Zr_{36}$ metallic glass*, Nucl. Instr. Meth. Phys. Res. B **341**, 22–26 (2014).

[61] M. Goldstein, *Viscous liquids and the glass transition: A potential energy barrier picture*, J. Chem. Phys. **51**, 3728–3739 (1969).

[62] G. P. Johari and M. Goldstein, *Viscous liquids and the glass transition. II. Secondary relaxations in glasses of rigid molecules*, J. Chem. Phys. **53**, 2372–2388 (1970).

[63] F. H. Stillinger, *A topographic view of supercooled liquids and glass formation*, Science **267**, 1935–1939 (1995).

[64] T. Iwashita and T. Egami, *Local energy landscape in a simple liquid*, Phys. Rev. E **90**, 052307 (2014).

[65] R. S. Averback and T. Diaz de la Rubia, *Displacement damage in irradiated metals and semiconductors*, Solid State Physics (H. Ehrenreich and F. Spaepen, eds.), vol. 51, Academic Press, 1997, pp. 281–402.

[66] L. L. Kazmerski (ed.), *Polycrystalline and amorphous thin films and devices*, Academic Press, 1980.

[67] N. Yoshida and F. E. Fujita, *Influence of oxygen on vacuum deposited iron thin film*, J. Phys. F Met. Phys. **2**, 1009 (1972).

[68] H. Bialas and K. Heneka, *Epitaxy of fcc metals on dielectric substrates*, Vacuum **45**, 79–87 (1994).

[69] P. J. Møller and Q. Guo, *Growth of ultrathin films of copper onto α-Al_2O_3(0001): Mechanism and epitaxy*, Thin Solid Films **201**, 267–279 (1991).

[70] G. Dehm, M. Rühle, G. Ding, and R. Raj, *Growth and structure of copper thin films deposited on (0001) sapphire by molecular beam epitaxy*, Philos. Mag. B **71**, 1111–1124 (1995).

[71] C. Koziol, G. Lilienkamp, and E. Bauer, *Intensity oscillations in reflection high-energy electron diffraction during molecular beam epitaxy of Ni on W(110)*, Appl. Phys. Lett. **51**, 901–903 (1987).

[72] P. Keblinski, D. Wolf, S. R. Phillpot, and H. Gleiter, *Structure of grain boundaries in nanocrystalline palladium by molecular dynamics simulation*, Scr. Mater. **41**, 631–636 (1999).

[73] D. Wolf, J. Wang, S. R. Phillpot, and H. Gleiter, *On the thermodynamic relationship between nanocrystalline materials and glasses*, Phys. Lett. A **205**, 274–280 (1995).

[74] G.-P. Zheng and Mo Li, *Crystal instability in nanocrystalline materials*, Acta Mater. **55**, 5464–5472 (2007).

[75] F. Baletto and R. Ferrando, *Structural properties of nanoclusters: Energetic, thermodynamic, and kinetic effects*, Rev. Mod. Phys. **77**, 371–423 (2005).

[76] R. B. Schwarz and W. L. Johnson, *Formation of an amorphous alloy by solid-state reaction of the pure polycrystalline metals*, Phys. Rev. Lett. **51**, 415–418 (1983).

[77] R. Benedictus, A. Böttger, and E. J. Mittemeijer, *Thermodynamic model for solid-state amorphization in binary systems at interfaces and grain boundaries*, Phys. Rev. B **54**, 9109–9125 (1996).

[78] R. Benedictus, K. Han, C. Træholt, A. Böttger, and E. J. Mittemeijer, *Solid state amorphization in Ni–Ti systems: the effect of structure on the kinetics of interface and grain-boundary amorphization*, Acta Mater. **46**, 5491–5508 (1998).

[79] P. R. Cantwell, M. Tang, S. J. Dillon, J. Luo, G. S. Rohrer, and M. P. Harmer, *Grain boundary complexions*, Acta Mater. **62**, 1–48 (2014).

[80] J. Landes, Ch. Sauer, B. Kabius, and W. Zinn, *Critical thickness of the amorphous–nanocrystalline transition in Gd/Fe film structures*, Phys. Rev. B **44**, 8342–8345 (1991).

[81] S. Handschuh, J. Landes, U. Köbler, Ch. Sauer, G. Kisters, A. Fuss, and W. Zinn, *Magnetic properties of amorphous Fe in Fe/Y layered structures*, J. Magn. Magn. Mater. **119**, 254–260 (1993).

[82] U. Herr, *Metastable phases in interface controlled materials*, Contemp. Phys. **41**, 93–104 (2000).

[83] M. Ghafari, H. Hahn, R. A. Brand, R. Mattheis, Y. Yoda, S. Kohara, R. Kruk, and S. Kamali, *Structure of iron nanolayers embedded in amorphous alloys*, Appl. Phys. Lett. **100**, 203108 (2012).

[84] M. De Graef and M. E. McHenry, *Structure of materials: An introduction to crystallography, diffraction, and symmetry*, Cambridge University Press, 2007.

[85] D. Shechtman, I. Blech, D. Gratias, and J. W. Cahn, *Metallic phase with long-range orientational order and no translational symmetry*, Phys. Rev. Lett. **53**, 1951–1953 (1984).

[86] D. Levine and P. J. Steinhardt, *Quasicrystals: A new class of ordered structures*, Phys. Rev. Lett. **53**, 2477–2480 (1984).

[87] D. V. Louzguine-Luzgin and A. Inoue, *Formation and properties of quasicrystals*, Annu. Rev. Mater. Res. **38**, 403–423 (2008).

[88] P. Lamparter, W. Sperl, S. Steeb, and J. Blétry, *Atomic structure of amorphous metallic $Ni_{81}B_{19}$*, Z. Naturforsch. **37a**, 1223–1234 (1982).

[89] D. R. Nelson, *Liquids and glasses in spaces of incommensurate curvature*, Phys. Rev. Lett. **50**, 982–985 (1983).

[90] D. R. Nelson, *Order, frustration, and defects in liquids and glasses*, Phys. Rev. B **28**, 5515–5535 (1983).

[91] J.-C. Lee, K.-W. Park, K.-H. Kim, E. Fleury, B.-J. Lee, M. Wakeda, and Y. Shibutani, *Origin of the plasticity in bulk amorphous alloys*, J. Mater. Res. **22**, 3087–3097 (2007).

[92] Y. Q. Cheng, H. W. Sheng, and E. Ma, *Relationship between structure, dynamics, and mechanical properties in metallic glass-forming alloys*, Phys. Rev. B **78**, 014207 (2008).

[93] J. Ding, Y.-Q. Cheng, and E. Ma, *Full icosahedra dominate local order in $Cu_{64}Zr_{34}$ metallic glass and supercooled liquid*, Acta Mater. **69**, 343–354 (2014).

[94] Y. Ritter and K. Albe, *Chemical and topological order in shear bands of $Cu_{64}Z_{36}$ and $Cu_{36}Zr_{64}$ glasses*, J. Appl. Phys. **111**, 103527 (2012).

[95] J. Ding, S. Patinet, M. L. Falk, Y. Cheng, and E. Ma, *Soft spots and their structural signature in a metallic glass*, Proc. Natl. Acad. Sci. USA **111**, 14052–14056 (2014).

[96] W. Dmowski, T. Iwashita, C.-P. Chuang, J. Almer, and T. Egami, *Elastic heterogeneity in metallic glasses*, Phys. Rev. Lett. **105**, 205502 (2010).

[97] J. Ding, Y. Q. Cheng, and E. Ma, *Correlating local structure with inhomogeneous elastic deformation in a metallic glass*, Appl. Phys. Lett. **101**, 121917 (2012).

[98] J. Ding, Y. Q. Cheng, and E. Ma, *Quantitative measure of local solidity/liquidity in metallic glasses*, Acta Mater. **61**, 4474–4480 (2013).

[99] H. W. Sheng, W. K. Luo, F. M. Alamgir, J. M. Bai, and E. Ma, *Atomic packing and short-to-medium-range order in metallic glasses*, Nature **439**, 419–425 (2006).

[100] Y. Q. Cheng, E. Ma, and H. W. Sheng, *Atomic level structure in multicomponent bulk metallic glass*, Phys. Rev. Lett. **102**, 245501 (2009).

[101] W. K. Luo, H. W. Sheng, F. M. Alamgir, J. M. Bai, J. H. He, and E. Ma, *Icosahedral short-range order in amorphous alloys*, Phys. Rev. Lett. **92**, 145502 (2004).

[102] N. Mattern, P. Jóvári, I. Kaban, S. Gruner, A. Elsner, V. Kokotin, H. Franz, B. Beuneu, and J. Eckert, *Short-range order of Cu–Zr metallic glasses*, J. Alloys Compd. **485**, 163–169 (2009).

[103] M. Li, C. Z. Wang, S. G. Hao, M. J. Kramer, and K. M. Ho, *Structural heterogeneity and medium-range order in Zr_xCu_{100-x} metallic glasses*, Phys. Rev. B **80**, 184201 (2009).

[104] A. Hirata, P. Guan, T. Fujita, Y. Hirotsu, A. Inoue, A. R. Yavari, T. Sakurai, and M. Chen, *Direct observation of local atomic order in a metallic glass*, Nat. Mater. **10**, 28–33 (2011).

[105] A. Hirata, L. J. Kang, T. Fujita, B. Klumov, K. Matsue, M. Kotani, A. R. Yavari, and M. W. Chen, *Geometric frustration of icosahedron in metallic glasses*, Science **341**, 376–379 (2013).

[106] D. B. Miracle, *A structural model for metallic glasses*, Nat. Mater. **3**, 697–702 (2004).

[107] D. B. Miracle, *The efficient cluster packing model – An atomic structural model for metallic glasses*, Acta Mater. **54**, 4317–4336 (2006).

[108] D. B. Miracle, *A physical model for metallic glass structures: An introduction and update*, JOM **64**, 846–855 (2012).

[109] M. Lee, C.-M. Lee, K.-R. Lee, E. Ma, and J.-C. Lee, *Networked interpenetrating connections of icosahedra: Effects on shear transformations in metallic glass*, Acta Mater. **59**, 159–170 (2011).

[110] J. Zemp, M. Celino, B. Schönfeld, and J. F. Löffler, *Icosahedral superclusters in $Cu_{64}Zr_{36}$ metallic glass*, Phys. Rev. B **90**, 144108 (2014).

[111] A. C. Y. Liu, M. J. Neish, G. Stokol, G. A. Buckley, L. A. Smillie, M. D. de Jonge, R. T. Ott, M. J. Kramer, and L. Bourgeois, *Systematic mapping of icosahedral short-range order in a melt-spun $Zr_{36}Cu_{64}$ metallic glass*, Phys. Rev. Lett. **110**, 205505 (2013).

[112] E. Kneller, Y. Khan, and U. Gorres, *The alloy system copper zirconium. 1. Phase-diagram and structural relations*, Z. Metallkd. **77**, 43–48 (1986).

[113] M. H. Braga, L. F. Malheiros, F. Castro, and D. Soares, *Experimental liquidus points and invariant reactions in the Cu-Zr system*, Z. Metallk. **89**, 541–545 (1998).

[114] D. Arias and J. P. Abriata, *Cu–Zr (copper–zirconium)*, Bull. Alloy Phase Diagr. **11**, 452–459 (1990).

[115] N. Wang, C. Li, Z. Du, F. Wang, and W. Zhang, *The thermodynamic re-assessment of the Cu–Zr system*, Calphad **30**, 461–469 (2006).

[116] D. Schryvers, G. S. Firstov, J. W. Seo, J. Van Humbeeck, and Yu. N. Koval, *Unit cell determination in CuZr martensite by electron microscopy and X-ray diffraction*, Scr. Mater. **36**, 1119–1125 (1997).

[117] F. Jiang, Z. B. Zhang, L. He, J. Sun, H. Zhang, and Z. F. Zhang, *The effect of primary crystallizing phases on mechanical properties of $Cu_{46}Zr_{47}Al_7$ bulk metallic glass composites*, J. Mater. Res. **21**, 2638–2645 (2006).

[118] F. Jiang, D. H. Zhang, L. C. Zhang, Z. B. Zhang, L. He, J. Sun, and Z. F. Zhang, *Microstructure evolution and mechanical properties of $Cu_{46}Zr_{47}Al_7$ bulk metallic glass composite containing CuZr crystallizing phases*, Mater. Sci. Eng. A **467**, 139–145 (2007).

[119] S. Pauly, J. Das, C. Duhamel, and J. Eckert, *Martensite formation in a ductile $Cu_{47.5}Zr_{47.5}Al_5$ bulk metallic glass composite*, Adv. Eng. Mater. **9**, 487–491 (2007).

[120] S. Pauly, J. Das, J. Bednarcik, N. Mattern, K. B. Kim, D. H. Kim, and J. Eckert, *Deformation-induced martensitic transformation in Cu–Zr–(Al,Ti) bulk metallic glass composites*, Scr. Mater. **60**, 431–434 (2009).

[121] U. R. Pedersen, T. B. Schrøder, J. C. Dyre, and P. Harrowell, *Geometry of slow structural fluctuations in a supercooled binary alloy*, Phys. Rev. Lett. **104**, 105701 (2010).

[122] C. Tang and P. Harrowell, *Predicting the solid state phase diagram for glass-forming alloys of copper and zirconium*, J. Phys.: Condens. Matter **24**, 245102 (2012).

[123] J. Zemp, M. Celino, B. Schönfeld, and J. F. Löffler, *Crystal-like rearrangements of icosahedra in simulated copper-zirconium metallic glasses and their effect on mechanical properties*, Phys. Rev. Lett. **115**, 165501 (2015).

[124] M. I. Mendelev, M. J. Kramer, R. T. Ott, D. J. Sordelet, D. Yagodin, and P. Popel, *Development of suitable interatomic potentials for simulation of liquid and amorphous Cu–Zr alloys*, Philos. Mag. **89**, 967–987 (2009), the potential file is available at `http://www.ctcms.nist.gov/potentials/Cu-Zr.html`.

[125] Y. Ritter and K. Albe, *Thermal annealing of shear bands in deformed metallic glasses: Recovery mechanisms in $Cu_{64}Zr_{36}$ studied by molecular dynamics simulations*, Acta Mater. **59**, 7082–7094 (2011).

[126] H. Men, S. J. Pang, and T. Zhang, *Glass-forming ability and mechanical properties of $Cu_{50}Zr_{50-x}Ti_x$ alloys*, Mater. Sci. Eng. A **408**, 326–329 (2005).

[127] C. C. Hays, C. P. Kim, and W. L. Johnson, *Large supercooled liquid region and phase separation in the Zr–Ti–Ni–Cu–Be bulk metallic glasses*, Appl. Phys. Lett. **75**, 1089–1091 (1999).

[128] F. Spaepen, *A microscopic mechanism for steady state inhomogeneous flow in metallic glasses*, Acta Metall. **25**, 407–415 (1977).

[129] D. Srolovitz, V. Vitek, and T. Egami, *An atomistic study of deformation of amorphous metals*, Acta Metall. **31**, 335–352 (1983).

[130] M. L. Falk and J. S. Langer, *Dynamics of viscoplastic deformation in amorphous solids*, Phys. Rev. E **57**, 7192–7205 (1998).

[131] S. G. Mayr, *Activation energy of shear transformation zones: A key for understanding rheology of glasses and liquids*, Phys. Rev. Lett. **97**, 195501 (2006).

[132] A. S. Argon, *Plastic deformation in metallic glasses*, Acta Metall. **27**, 47–58 (1979).

[133] A. S. Argon and L. T. Shi, *Development of visco-plastic deformation in metallic glasses*, Acta Metall. **31**, 499–507 (1983).

[134] J. S. Langer and L. Pechenik, *Dynamics of shear-transformation zones in amorphous plasticity: Energetic constraints in a minimal theory*, Phys. Rev. E **68**, 061507 (2003).

[135] M. L. Falk, J. S. Langer, and L. Pechenik, *Thermal effects in the shear-transformation-zone theory of amorphous plasticity: Comparisons to metallic glass data*, Phys. Rev. E **70**, 011507 (2004).

[136] L. Pechenik, *Dynamics of shear-transformation zones in amorphous plasticity: Nonlinear theory at low temperatures*, Phys. Rev. E **72**, 021507 (2005).

[137] E. Bouchbinder, J. S. Langer, and I. Procaccia, *Athermal shear-transformation-zone theory of amorphous plastic deformation. I. Basic principles*, Phys. Rev. E **75**, 036107 (2007).

[138] E. Bouchbinder, J. S. Langer, and I. Procaccia, *Athermal shear-transformation-zone theory of amorphous plastic deformation. II. Analysis of simulated amorphous silicon*, Phys. Rev. E **75**, 036108 (2007).

[139] J. S. Langer, *Shear-transformation-zone theory of plastic deformation near the glass transition*, Phys. Rev. E **77**, 021502 (2008).

[140] M. L. Falk and J. S. Langer, *Deformation and failure of amorphous, solidlike materials*, Annu. Rev. Condens. Matter Phys. **2**, 353–373 (2011).

[141] D. Rodney and C. Schuh, *Distribution of thermally activated plastic events in a flowing glass*, Phys. Rev. Lett. **102**, 235503 (2009).

[142] S. Swayamjyoti, J. F. Löffler, and P. M. Derlet, *Local structural excitations in model glasses*, Phys. Rev. B **89**, 224201 (2014).

[143] S. Swayamjyoti, J. F. Löffler, and P. M. Derlet, *Local structural excitations in model glass systems under applied load*, Phys. Rev. B **93**, 144202 (2016).

[144] C. A. Schuh, A. C. Lund, and T. G. Nieh, *New regime of homogeneous flow in the deformation map of metallic glasses: elevated temperature nanoindentation experiments and mechanistic modeling*, Acta Mater. **52**, 5879–5891 (2004).

[145] K. Albe, Y. Ritter, and D. Şopu, *Enhancing the plasticity of metallic glasses: Shear band formation, nanocomposites and nanoglasses investigated by molecular dynamics simulations*, Mech. Mater. **67**, 94–103 (2013).

[146] Y. Q. Cheng and E. Ma, *Intrinsic shear strength of metallic glass*, Acta Mater. **59**, 1800–1807 (2011).

[147] C. E. Packard and C. A. Schuh, *Initiation of shear bands near a stress concentration in metallic glass*, Acta Mater. **55**, 5348–5358 (2007).

[148] R. Klaumünzer, D.and Maaß and J. F. Löffler, *Stick-slip dynamics and recent insights into shear banding in metallic glasses*, J. Mater. Res. **26**, 1453–1463 (2011).

[149] R. Maaß and J. F. Löffler, *Shear-band dynamics in metallic glasses*, Adv. Funct. Mater. **25**, 2353–2368 (2015).

[150] W. L. Johnson and K. Samwer, *A universal criterion for plastic yielding of metallic glasses with a $(t/T_g)^{2/3}$ temperature dependence*, Phys. Rev. Lett. **95**, 195501 (2005).

[151] H. Rösner, M. Peterlechner, C. Kübel, V. Schmidt, and G. Wilde, *Density changes in shear bands of a metallic glass determined by correlative analytical transmission electron microscopy*, Ultramicroscopy **142**, 1–9 (2014).

[152] Y. Shi and M. L. Falk, *Strain localization and percolation of stable structure in amorphous solids*, Phys. Rev. Lett. **95**, 095502 (2005).

[153] Y. Shi, M. B. Katz, H. Li, and M. L. Falk, *Evaluation of the disorder temperature and free-volume formalisms via simulations of shear banding in amorphous solids*, Phys. Rev. Lett. **98**, 185505 (2007).

[154] R. Maaß, D. Klaumünzer, and J. F. Löffler, *Propagation dynamics of individual shear bands during inhomogeneous flow in a Zr-based bulk metallic glass*, Acta Mater. **59**, 3205–3213 (2011).

[155] F. H. Dalla Torre, D. Klaumünzer, R. Maaß, and J. F. Löffler, *Stick–slip behavior of serrated flow during inhomogeneous deformation of bulk metallic glasses*, Acta Mater. **58**, 3742–3750 (2010).

[156] D. Klaumünzer, A. Lazarev, R. Maaß, F. H. Dalla Torre, A. Vinogradov, and J. F. Löffler, *Probing shear-band initiation in metallic glasses*, Phys. Rev. Lett. **107**, 185502 (2011).

[157] S. X. Song, X.-L. Wang, and T. G. Nieh, *Capturing shear band propagation in a Zr-based metallic glass using a high-speed camera*, Scr. Mater. **62**, 847–850 (2010).

[158] W. J. Wright, R. R. Byer, and X. Gu, *High-speed imaging of a bulk metallic glass during uniaxial compression*, Appl. Phys. Lett. **102**, 241920 (2013).

[159] V. Schmidt, H. Rösner, M. Peterlechner, G. Wilde, and P. M. Voyles, *Quantitative measurement of density in a shear band of metallic glass monitored along its propagation direction*, Phys. Rev. Lett. **115**, 035501 (2015).

[160] I. Binkowski, S. Schlottbom, J. Leuthold, S. Ostendorp, S. V. Divinski, and G. Wilde, *Sub-micron strain analysis of local stick–slip motion of individual shear bands in a bulk metallic glass*, Appl. Phys. Lett. **107**, 221902 (2015).

[161] R. Maaß, K. Samwer, W. Arnold, and C. A. Volkert, *A single shear band in a metallic glass: Local core and wide soft zone*, Appl. Phys. Lett. **105**, 171902 (2014).

[162] J. Jing, A. Krämer, R. Birringer, H. Gleiter, and U. Gonser, *Modified atomic structure in a Pd–Fe–Si nanoglass: A Mössbauer study*, J. Non-Cryst. Solids **113**, 167–170 (1989).

[163] H. Gleiter, *Nanoglasses: a new kind of noncrystalline materials*, Beilstein J. Nanotechnol. **4**, 517–533 (2013).

[164] D. Şopu, K. Albe, Y. Ritter, and H. Gleiter, *From nanoglasses to bulk massive glasses*, Appl. Phys. Lett. **94**, 191911 (2009).

[165] Y. Ritter, D. Şopu, H. Gleiter, and K. Albe, *Structure, stability and mechanical properties of internal interfaces in $Cu_{64}Zr_{36}$ nanoglasses studied by MD simulations*, Acta Mater. **59**, 6588–6593 (2011).

[166] J. X. Fang, U. Vainio, W. Puff, R. Würschum, X. L. Wang, D. Wang, M. Ghafari, F. Jiang, J. Sun, H. Hahn, and H. Gleiter, *Atomic structure and structural stability of $Sc_{75}Fe_{25}$ nanoglasses*, Nano Lett. **12**, 458–463 (2012).

[167] O. Adjaoud and K. Albe, *Interfaces and interphases in nanoglasses: Surface segregation effects and their implications on structural properties*, Acta Mater. **113**, 284–292 (2016).

[168] C. Fan and A. Inoue, *Improvement of mechanical properties by precipitation of nanoscale compound particles in Zr–Cu–Pd–Al amorphous alloys*, Mater. Trans. JIM **38**, 1040–1046 (1997).

[169] S.-W. Lee, M.-Y. Huh, E. Fleury, and J.-C. Lee, *Crystallization-induced plasticity of Cu–Zr containing bulk amorphous alloys*, Acta Mater. **54**, 349–355 (2006).

[170] K. Hajlaoui, A. R. Yavari, A. LeMoulec, W. J. Botta, F. G. Vaughan, J. Das, A. L. Greer, and Å. Kvick, *Plasticity induced by nanoparticle dispersions in bulk metallic glasses*, J. Non-Cryst. Solids **353**, 327–331 (2007).

[171] J. Fornell, E. Rossinyol, S. Suri nach, M. D. Baró, W. H. Li, and J. Sort, *Enhanced mechanical properties in a Zr-based metallic glass caused by deformation-induced nanocrystallization*, Scr. Mater. **62**, 13–16 (2010).

[172] J. B. Li, J. S. C. Jang, S. R. Jian, K. W. Chen, J. F. Lin, and J. C. Huang, *Plasticity improvement of ZrCu-based bulk metallic glass by ex situ dispersed Ta particles*, Mater. Sci. Eng. A **528**, 8244–8248 (2011).

[173] M. Calin, J. Eckert, and L. Schultz, *Improved mechanical behavior of Cu–Ti-based bulk metallic glass by in situ formation of nanoscale precipitates*, Scr. Mater. **48**, 653–658 (2003).

[174] D. C. Hofmann, J.-Y. Suh, A. Wiest, G. Duan, M.-L. Lind, M. D. Demetriou, and W. L. Johnson, *Designing metallic glass matrix composites with high toughness and tensile ductility*, Nature **451**, 1085–1089 (2008).

[175] S. Pauly, S. Gorantla, G. Wang, U. Kühn, and J. Eckert, *Transformation-mediated ductility in CuZr-based bulk metallic glasses*, Nat. Mater. **9**, 473–477 (2010).

[176] N. S. Barekar, S. Pauly, R. B. Kumar, U. Kühn, B. K. Dhindaw, and J. Eckert, *Structure–property relations in bulk metallic Cu–Zr–Al alloys*, Mat. Sci. Eng. A **527**, 5867–5872 (2010).

[177] S. Pauly, G. Liu, S. Gorantla, G. Wang, U. Kühn, D. H. Kim, and J. Eckert, *Criteria for tensile plasticity in Cu–Zr–Al bulk metallic glasses*, Acta Mater. **58**, 4883–4890 (2010).

[178] J. W. Qiao, T. Zhang, F. Q. Yang, P. K. Liaw, S. Pauly, and B. S. Xu, *A tensile deformation model for in-situ dendrite/metallic glass matrix composites*, Sci. Rep. **3**, 2816 (2013).

[179] C. P. Kim, Y. S. Oh, S. Lee, and N. J. Kim, *Realization of high tensile ductility in a bulk metallic glass composite by the utilization of deformation-induced martensitic transformation*, Scr. Mater. **65**, 304–307 (2011).

[180] Z. Liu, R. Li, G. Liu, K. Song, S. Pauly, T. Zhang, and J. Eckert, *Pronounced ductility in CuZrAl ternary bulk metallic glass composites with optimized microstructure through melt adjustment*, AIP Adv. **2**, 032176 (2012).

[181] Fu-Fa Wu, K. C. Chan, S.-T. Li, and G. Wang, *Stabilized shear banding of ZrCu-based metallic glass composites under tensile loading*, J. Mater. Sci. **49**, 2164–2170 (2014).

[182] J. Das, S. Pauly, M. Boström, K. Durst, M. Göken, and J. Eckert, *Designing bulk metallic glass and glass matrix composites in martensitic alloys*, J. Alloys Compd. **483**, 97–101 (2009).

[183] X. L. Fu, Y. Li, and C. A. Schuh, *Mechanical properties of metallic glass matrix composites: Effects of reinforcement character and connectivity*, Scr. Mater. **56**, 617–620 (2007).

[184] K. K. Song, S. Pauly, B. A. Sun, J. Tan, M. Stoica, U. Kühn, and J. Eckert, *Correlation between the microstructures and the deformation mechanisms of CuZr-based bulk metallic glass composites*, AIP Adv. **3**, 012116 (2013).

[185] A. Zaheri, F. Abdeljawad, and M. Haataja, *Simulation study of mechanical properties of bulk metallic glass systems: martensitic inclusions and twinned precipitates*, Model. Simul. Mater. Sci. Eng. **22**, 085008 (2014).

[186] Y. S. Wang, G. J. Hao, Y. Zhang, J. P. Lin, L. Song, and J. W. Qiao, *The role of the interface in a Ti-based metallic glass matrix composite with in situ dendrite reinforcement*, Surf. Interface Anal. **46**, 293–296 (2014).

[187] Y. Wang, Ju Li, A. V. Hamza, and T. W. Barbee, *Ductile crystalline–amorphous nanolaminates*, Proc. Natl. Acad. Sci. USA **104**, 11155–11160 (2007).

[188] B. Arman, C. Brandl, S. N. Luo, T. C. Germann, A. Misra, and T. Çağin, *Plasticity in Cu(111)/$Cu_{46}Zr_{54}$ glass nanolaminates under uniaxial compression*, J. Appl. Phys. **110**, 043539 (2011).

[189] C. Brandl, T. C. Germann, and A. Misra, *Structure and shear deformation of metallic crystalline–amorphous interfaces*, Acta Mater. **61**, 3600–3611 (2013).

[190] Q. P. Cao, J. F. Li, Y. Hu, A. Horsewell, J. Z. Jiang, and Y. H. Zhou, *Deformation-strengthening during rolling $Cu_{60}Zr_{20}Ti_{20}$ bulk metallic glass*, Mater. Sci. Eng. A **457**, 94–99 (2007).

[191] M. Chen, A. Inoue, W. Zhang, and T. Sakurai, *Extraordinary plasticity of ductile bulk metallic glasses*, Phys. Rev. Lett. **96**, 245502 (2006).

[192] G. Wilde and H. Rösner, *Nanocrystallization in a shear band: An in situ investigation*, Appl. Phys. Lett. **98**, 251904 (2011).

[193] J. Bokeloh, S. V. Divinski, G. Reglitz, and G. Wilde, *Tracer measurements of atomic diffusion inside shear bands of a bulk metallic glass*, Phys. Rev. Lett. **107**, 235503 (2011).

[194] Y. Mao, Ju Li, Y.-C. Lo, X. Qian, and E. Ma, *Stress-driven crystallization via shear-diffusion transformations in a metallic glass at very low temperatures*, Phys. Rev. B **91**, 214103 (2015).

[195] Y. Wu, D. Q. Zhou, W. L. Song, H. Wang, Z. Y. Zhang, D. Ma, X. L. Wang, and Z. P. Lu, *Ductilizing bulk metallic glass composite by tailoring stacking fault energy*, Phys. Rev. Lett. **109**, 245506 (2012).

[196] D. Şopu, M. Stoica, and J. Eckert, *Deformation behavior of metallic glass composites reinforced with shape memory nanowires studied via molecular dynamics simulations*, Appl. Phys. Lett. **106**, 211902 (2015).

[197] J. Corteen, M. Rainforth, and I. Todd, *A mathematical approach to transformation toughening in bulk metallic glasses*, Scr. Mater. **65**, 524–527 (2011).

[198] A. C. Lund and C. A. Schuh, *Critical length scales for the deformation of amorphous metals containing nanocrystals*, Philos. Mag. Lett. **87**, 603–611 (2007).

[199] Y. Shi and M. L. Falk, *A computational analysis of the deformation mechanisms of a nanocrystal–metallic glass composite*, Acta Mater. **56**, 995–1000 (2008).

[200] H. Zhou, S. Qu, and W. Yang, *An atomistic investigation of structural evolution in metallic glass matrix composites*, Int. J. Plasticity **44**, 147–160 (2013).

[201] J. R. Trelewicz and C. A. Schuh, *The Hall–Petch breakdown in nanocrystalline metals: A crossover to glass-like deformation*, Acta Mater. **55**, 5948–5958 (2007).

[202] M. Grewer, J. Markmann, R. Karos, W. Arnold, and R. Birringer, *Shear softening of grain boundaries in nanocrystalline Pd*, Acta Mater. **59**, 1523–1529 (2011).

[203] M. Grewer and R. Birringer, *Shear shuffling governs plastic flow in nanocrystalline metals: An analysis of thermal activation parameters*, Phys. Rev. B **89**, 184108 (2014).

[204] G. Gottstein, *Physical foundations of materials science*, Springer, 2004.

[205] Y. B. Wang, B. Q. Li, M. L. Sui, and S. X. Mao, *Deformation-induced grain rotation and growth in nanocrystalline Ni*, Appl. Phys. Lett. **92**, 011903 (2008).

[206] M. Legros, D. S. Gianola, and K. J. Hemker, *In situ TEM observations of fast grain-boundary motion in stressed nanocrystalline aluminum films*, Acta Mater. **56**, 3380–3393 (2008).

[207] C. Brandl, P. M. Derlet, and H. Van Swygenhoven, *Dislocation mediated plasticity in nanocrystalline Al: the strongest size*, Model. Simul. Mater. Sci. Eng. **19**, 074005 (2011).

[208] A. J. Detor and C. A. Schuh, *Tailoring and patterning the grain size of nanocrystalline alloys*, Acta Mater. **55**, 371–379 (2007).

[209] J. Lohmiller, M. Grewer, C. Braun, A. Kobler, C. Kübel, K. Schüler, V. Honkimäki, H. Hahn, O. Kraft, R. Birringer, and P. A. Gruber, *Untangling dislocation and grain boundary mediated plasticity in nanocrystalline nickel*, Acta Mater. **65**, 295–307 (2014).

[210] K. Hajlaoui, T. Benameur, G. Vaughan, and A. R. Yavari, *Thermal expansion and indentation-induced free volume in Zr-based metallic glasses measured by real-time diffraction using synchrotron radiation*, Scr. Mater. **51**, 843–848 (2004).

[211] W. H. Jiang, F. E. Pinkerton, and M. Atzmon, *Mechanical behavior of shear bands and the effect of their relaxation in a rolled amorphous Al-based alloy*, Acta Mater. **53**, 3469–3477 (2005).

[212] K. D. Krishnanand and R. W. Cahn, *Recovery from plastic deformation in a Ni/Nb alloy glass*, Scr. Metall. **9**, 1259–1261 (1975).

[213] S. Xie and E. P. George, *Hardness and shear band evolution in bulk metallic glasses after plastic deformation and annealing*, Acta Mater. **56**, 5202–5213 (2008).

[214] G. Kumar, T. Ohkubo, T. Mukai, and K. Hono, *Plasticity and microstructure of Zr–Cu–Al bulk metallic glasses*, Scr. Mater. **57**, 173–176 (2007).

[215] K. Wang, T. Fujita, Y. Q. Zeng, N. Nishiyama, A. Inoue, and M. W. Chen, *Micromechanisms of serrated flow in a $Ni_{50}Pd_{30}P_{20}$ bulk metallic glass with a large compression plasticity*, Acta Mater. **56**, 2834–2842 (2008).

[216] Y. Xu, H. Hahn, and J. Li, *Effects of room-temperature rolling on microstructure and crystallization behavior of $Zr_{55}Cu_{40}Al_5$ metallic glass*, Intermetallics **18**, 2039–2043 (2010).

[217] R. C. Zeller and R. O. Pohl, *Thermal conductivity and specific heat of noncrystalline solids*, Phys. Rev. B **4**, 2029–2041 (1971).

[218] P. W. Anderson, B. I. Halperin, and C. M. Varma, *Anomalous low-temperature thermal properties of glasses and spin glasses*, Philos. Mag. **25**, 1–9 (1972).

[219] W. A. Phillips, *Tunneling states in amorphous solids*, J. Low Temp. Phys. **7**, 351–360 (1972).

[220] W. Schirmacher, T. Scopigno, and G. Ruocco, *Theory of vibrational anomalies in glasses*, J. Non-Cryst. Solids **407**, 133–140 (2015).

[221] P. Flubacher, A. J. Leadbetter, J. A. Morrison, and B. P. Stoicheff, *The low-temperature heat capacity and the raman and brillouin spectra of vitreous silica*, J. Phys. Chem. Solids **12**, 53–65 (1959).

[222] S. R. Elliott, *A unified model for the low-energy vibrational behaviour of amorphous solids*, EPL **19**, 201 (1992).

[223] V. G. Karpov, M. I. Klinger, and F. N. Ignat'ev, *Theory of the low-temperature anomalies in the thermal properties of amorphous structures*, Zh. Eksp. Teor. Fiz. **84**, 760 (1983).

[224] B. B. Laird and H. R. Schober, *Localized low-frequency vibrational modes in a simple model glass*, Phys. Rev. Lett. **66**, 636–639 (1991).

[225] H. R. Schober and B. B. Laird, *Localized low-frequency vibrational modes in glasses*, Phys. Rev. B **44**, 6746–6754 (1991).

[226] L. Gil, M. A. Ramos, A. Bringer, and U. Buchenau, *Low-temperature specific heat and thermal conductivity of glasses*, Phys. Rev. Lett. **70**, 182–185 (1993).

[227] H. R. Schober and C. Oligschleger, *Low-frequency vibrations in a model glass*, Phys. Rev. B **53**, 11469–11480 (1996).

[228] H. Shintani and H. Tanaka, *Universal link between the boson peak and transverse phonons in glass*, Nat. Mater. **7**, 870–877 (2008).

[229] H. R. Schober, *Quasi-localized vibrations and phonon damping in glasses*, J. Non-Cryst. Solids **357**, 501–505 (2011).

[230] H. R. Schober, U. Buchenau, and V. L. Gurevich, *Pressure dependence of the boson peak in glasses: Correlated and uncorrelated perturbations*, Phys. Rev. B **89**, 014204 (2014).

[231] Y. Li, H. Y. Bai, W. H. Wang, and K. Samwer, *Low-temperature specific-heat anomalies associated with the boson peak in CuZr-based bulk metallic glasses*, Phys. Rev. B **74**, 052201 (2006).

[232] M. Guerdane and H. Teichler, *Short-range-order lifetime and the "boson peak" in a metallic glass model*, Phys. Rev. Lett. **101**, 065506 (2008).

[233] N. Jakse, A. Nassour, and A. Pasturel, *Structural and dynamic origin of the boson peak in a Cu–Zr metallic glass*, Phys. Rev. B **85**, 174201 (2012).

[234] H. W. Sheng, E. Ma, and M. J. Kramer, *Relating dynamic properties to atomic structure in metallic glasses*, JOM **64**, 856–881 (2012).

[235] A. V. Granato, *Interstitial resonance modes as a source of the boson peak in glasses and liquids*, Physica B: Condens. Matter **219–220**, 270–272 (1996).

[236] A. N. Vasiliev, T. N. Voloshok, A. V. Granato, D. M. Joncich, Yu. P. Mitrofanov, and V. A. Khonik, *Relationship between low-temperature boson heat capacity peak and high-temperature shear modulus relaxation in a metallic glass*, Phys. Rev. B **80**, 172102 (2009).

[237] T. S. Grigera, V. Martín-Mayor, G. Parisi, and P. Verrocchio, *Phonon interpretation of the 'boson peak' in supercooled liquids*, Nature **422**, 289–292 (2003).

[238] W. Schirmacher and M. Wagener, *Vibrational anomalies and phonon localization in glasses*, Solid State Commun. **86**, 597–603 (1993).

[239] W. Schirmacher, G. Diezemann, and C. Ganter, *Harmonic vibrational excitations in disordered solids and the "boson peak"*, Phys. Rev. Lett. **81**, 136–139 (1998).

[240] W. Schirmacher, G. Ruocco, and T. Scopigno, *Acoustic attenuation in glasses and its relation with the boson peak*, Phys. Rev. Lett. **98**, 025501 (2007).

[241] A. Marruzzo, W. Schirmacher, A. Fratalocchi, and G. Ruocco, *Heterogeneous shear elasticity of glasses: the origin of the boson peak*, Sci. Rep. **3**, 1407 (2013).

[242] A. Tanguy, B. Mantisi, and M. Tsamados, *Vibrational modes as a predictor for plasticity in a model glass*, EPL **90**, 16004 (2010).

[243] P. M. Derlet, R. Maaß, and J. F. Löffler, *The boson peak of model glass systems and its relation to atomic structure*, EPJ B **85**, 148 (2012).

[244] F. Léonforte, A. Tanguy, J. P. Wittmer, and J.-L. Barrat, *Inhomogeneous elastic response of silica glass*, Phys. Rev. Lett. **97**, 055501 (2006).

[245] C. Fusco, T. Albaret, and A. Tanguy, *Role of local order in the small-scale plasticity of model amorphous materials*, Phys. Rev. E **82**, 066116 (2010).

[246] Y. M. Beltukov, C. Fusco, D. A. Parshin, and A. Tanguy, *Boson peak and Ioffe–Regel criterion in amorphous siliconlike materials: The effect of bond directionality*, Phys. Rev. E **93**, 023006 (2016).

[247] S. N. Taraskin, Y. L. Loh, G. Natarajan, and S. R. Elliott, *Origin of the boson peak in systems with lattice disorder*, Phys. Rev. Lett. **86**, 1255–1258 (2001).

[248] A. I. Chumakov, G. Monaco, A. Monaco, W. A. Crichton, A. Bosak, R. Rüffer, A. Meyer, F. Kargl, L. Comez, D. Fioretto, H. Giefers, S. Roitsch, G. Wortmann, M. H. Manghnani, A. Hushur, Q. Williams, J. Balogh, K. Parliński, P. Jochym, and P. Piekarz, *Equivalence of the boson peak in glasses to the transverse acoustic van Hove singularity in crystals*, Phys. Rev. Lett. **106**, 225501 (2011).

[249] A. I. Chumakov, G. Monaco, A. Fontana, A. Bosak, R. P. Hermann, D. Bessas, B. Wehinger, W. A. Crichton, M. Krisch, R. Rüffer, G. Baldi, G. Carini Jr., G. Carini, G. D'Angelo, E. Gilioli, G. Tripodo, M. Zanatta, B. Winkler, V. Milman, K. Refson, M. T. Dove, N. Dubrovinskaia, L. Dubrovinsky, R. Keding, and Y. Z. Yue, *Role of disorder in the thermodynamics and atomic dynamics of glasses*, Phys. Rev. Lett. **112**, 025502 (2014).

[250] A. I. Chumakov and G. Monaco, *Understanding the atomic dynamics and thermodynamics of glasses: Status and outlook*, J. Non-Cryst. Solids **407**, 126–132 (2015).

[251] A. I. Chumakov, G. Monaco, X. Han, Li Xi, A. Bosak, L. Paolasini, D. Chernyshov, and V. Dyadkin, *Relation between the boson peak in glasses and van Hove singularity in crystals*, Philos. Mag. **96**, 743–753 (2016).

[252] G. Baldi, G. Carini Jr., G. Carini, A. Chumakov, R. Dal Maschio, G. D'Angelo, A. Fontana, E. Gilioli, G. Monaco, L. Orsingher, B. Rossi, and M. Zanatta, *New insights on the specific heat of glasses*, Philos. Mag. **96**, 754–760 (2016).

[253] Y. H. Liu, D. Wang, K. Nakajima, W. Zhang, A. Hirata, T. Nishi, A. Inoue, and M. W. Chen, *Characterization of nanoscale mechanical heterogeneity in a metallic glass by dynamic force microscopy*, Phys. Rev. Lett. **106**, 125504 (2011).

[254] M. Tsamados, A. Tanguy, F. Léonforte, and J. L. Barrat, *On the study of local-stress rearrangements during quasi-static plastic shear of a model glass: Do local-stress components contain enough information?*, EPJ E **26**, 283–293 (2008).

[255] M. L. Manning and A. J. Liu, *Vibrational modes identify soft spots in a sheared disordered packing*, Phys. Rev. Lett. **107**, 108302 (2011).

[256] S. S. Schoenholz, A. J. Liu, R. A. Riggleman, and J. Rottler, *Understanding plastic deformation in thermal glasses from single-soft-spot dynamics*, Phys. Rev. X **4**, 031014 (2014).

[257] E. Ma and J. Ding, *Tailoring structural inhomogeneities in metallic glasses to enable tensile ductility at room temperature*, Mater. Today **19**, 568–579 (2016).

[258] M. Born and R. Oppenheimer, *Zur Quantentheorie der Molekeln*, Annalen der Physik **389**, 457–484 (1927).

[259] M. Herlihy and N. Shavit, *The art of multiprocessor programming*, 1st ed., Morgan Kaufmann, 2012.

[260] S. Plimpton, *Fast parallel algorithms for short-range molecular dynamics*, J. Comp. Phys. **117**, 1–19 (1995), http://lammps.sandia.gov/.

[261] L. Verlet, *Computer "experiments" on classical fluids. I. Thermodynamical properties of Lennard-Jones molecules*, Phys. Rev. **159**, 98–103 (1967).

[262] W. C. Swope, H. C. Andersen, P. H. Berens, and K. R. Wilson, *A computer simulation method for the calculation of equilibrium constants for the formation of physical clusters of molecules: Application to small water clusters*, J. Chem. Phys. **76**, 637–649 (1982).

[263] D. Frenkel and B. Smit, *Understanding molecular simulation: From algorithms to applications*, 2nd ed., Academic Press, 2002.

[264] S. Nosé, *A unified formulation of the constant temperature molecular dynamics methods*, J. Chem. Phys. **81**, 511–519 (1984).

[265] W. G. Hoover, *Canonical dynamics: Equilibrium phase-space distributions*, Phys. Rev. A **31**, 1695–1697 (1985).

[266] M. Parrinello and A. Rahman, *Polymorphic transitions in single crystals: A new molecular dynamics method*, J. Appl. Phys. **52**, 7182–7190 (1981).

[267] W. Shinoda, M. Shiga, and M. Mikami, *Rapid estimation of elastic constants by molecular dynamics simulation under constant stress*, Phys. Rev. B **69**, 134103 (2004).

[268] M. R. Hestenes and E. Stiefel, *Methods of conjugate gradients for solving linear systems*, J. Res. Natl. Stand. **49**, 409–436 (1952).

[269] E. Polak and G. Ribière, *Note sur la convergence de méthodes de directions conjuguées*, ESAIM: Mathematical Modelling and Numerical Analysis - Modélisation Mathématique et Analyse Numérique **3**, 35–43 (1969).

[270] J. Tersoff, *New empirical approach for the structure and energy of covalent systems*, Phys. Rev. B **37**, 6991–7000 (1988).

[271] K. Albe, K. Nordlund, and R. S. Averback, *Modeling the metal-semiconductor interaction: Analytical bond-order potential for platinum-carbon*, Phys. Rev. B **65**, 195124 (2002).

[272] M. I. Baskes, *Modified embedded-atom potentials for cubic materials and impurities*, Phys. Rev. B **46**, 2727–2742 (1992).

[273] M. S. Daw and M. I. Baskes, *Semiempirical, quantum mechanical calculation of hydrogen embrittlement in metals*, Phys. Rev. Lett. **50**, 1285–1288 (1983).

[274] M. J. Stott and E. Zaremba, *Quasiatoms: An approach to atoms in nonuniform electronic systems*, Phys. Rev. B **22**, 1564–1583 (1980).

[275] J. K. Nørskov, *Covalent effects in the effective-medium theory of chemical binding: Hydrogen heats of solution in the 3d metals*, Phys. Rev. B **26**, 2875–2885 (1982), Erratum: Phys. Rev. B **28**, 1138 (1983).

[276] P. Hohenberg and W. Kohn, *Inhomogeneous electron gas*, Phys. Rev. **136**, B864–B871 (1964).

[277] M. S. Daw and M. I. Baskes, *Embedded-atom method: Derivation and application to impurities, surfaces, and other defects in metals*, Phys. Rev. B **29**, 6443–6453 (1984).

[278] M. W. Finnis and J. E. Sinclair, *A simple empirical N-body potential for transition metals*, Philos. Mag. A **50**, 45–55 (1984).

[279] A. Stukowski, *Visualization and analysis of atomistic simulation data with OVITO – the Open Visualization Tool*, Model. Simul. Mater. Sc. **18**, 015012 (2010), `http://ovito.org/`.

[280] F. Shimizu, S. Ogata, and Ju Li, *Theory of shear banding in metallic glasses and molecular dynamics calculations*, Mater. Trans. **48**, 2923–2927 (2007).

[281] J. F. Nye, *Physical properties of crystals: Their representation by tensors and matrices*, Clarendon Press, 1957.

[282] A. Reuss, *Berechnung der Fließgrenze von Mischkristallen auf Grund der Plastizitätsbedingung für Einkristalle*, ZAMM **9**, 49–58 (1929).

[283] W. Voigt, *Lehrbuch der Kristallphysik*, Teubner, 1928.

[284] R. Hill, *The elastic behaviour of a crystalline aggregate*, Proc. Phys. Soc. A **65**, 349 (1952).

[285] W. Thomson, *Elements of a mathematical theory of elasticity*, Philos. Trans. Roy. Soc. London **146**, 481–498 (1856).

[286] C. Kittel, *Introduction to solid state physics*, 8th ed., John Wiley & Sons, 2005.

[287] G. Voronoï, *Nouvelles applications des paramètres continus à la théorie des formes quadratiques. Premier mémoire. Sur quelques propriétés des formes quadratiques positives parfaites*, J. Reine Angew. Math. **133**, 97–102 (1908).

[288] G. Voronoï, *Nouvelles applications des paramètres continus à la théorie des formes quadratiques. Deuxième mémoire. Recherches sur les paralléllοèdres primitifs*, J. Reine Angew. Math. **134**, 198–287 (1908).

[289] G. Voronoï, *Nouvelles applications des paramètres continus à la théorie des formes quadratiques. Deuxième mémoire. Recherches sur les paralléllοèdres primitifs. Seconde partie. Domaines de formes quadratiques correspondant aux différents types de parallélοèdres primitifs*, J. Reine Angew. Math. **136**, 67–182 (1909).

[290] W. Brostow, M. Chybicki, R. Laskowski, and J. Rybicki, *Voronoi polyhedra and Delaunay simplexes in the structural analysis of molecular-dynamics-simulated materials*, Phys. Rev. B **57**, 13448–13458 (1998).

[291] B. Delaunay, *Sur la sphère vide. A la mémoire de Georges Voronoï*, Bulletin de l'Académie des Sciences de l'URSS, Classe des sciences mathématiques et naturelles **6**, 793–800 (1934).

[292] J. D. Honeycutt and H. C. Andersen, *Molecular dynamics study of melting and freezing of small Lennard–Jones clusters*, J. Phys. Chem. **91**, 4950–4963 (1987).

[293] D. Faken and H. Jónsson, *Systematic analysis of local atomic structure combined with 3D computer graphics*, Comput. Mater. Sci. **2**, 279–286 (1994).

[294] A. Stukowski, *Structure identification methods for atomistic simulations of crystalline materials*, Model. Simul. Mater. Sc. **20**, 045021 (2012).

[295] E. Maras, O. Trushin, A. Stukowski, T. Ala-Nissila, and H. Jónsson, *Global transition path search for dislocation formation in Ge on Si(001)*, Comput. Phys. Commun. **205**, 13–21 (2016).

[296] A. Stukowski, *Computational analysis methods in atomistic modeling of crystals*, JOM **66**, 399–407 (2014).

[297] S. Hunklinger, *Festkörperphysik*, Oldenbourg, 2007.

[298] P. Debye, *Zur Theorie der spezifischen Wärmen*, Annalen der Physik **344**, 789–839 (1912).

[299] A.-T. Petit and P.-L. Dulong, *Recherches sur quelques points importants de la théorie de la chaleur*, Annales de Chimie et de Physique **10**, 395–413 (1819).

[300] J. M. Dickey and A. Paskin, *Computer simulation of the lattice dynamics of solids*, Phys. Rev. **188**, 1407–1418 (1969).

[301] K. Kunc and R. M. Martin, *Ab initio force constants of GaAs: A new approach to calculation of phonons and dielectric properties*, Phys. Rev. Lett. **48**, 406–409 (1982).

[302] W. Frank, C. Elsässer, and M. Fähnle, *Ab initio force-constant method for phonon dispersions in alkali metals*, Phys. Rev. Lett. **74**, 1791–1794 (1995).

[303] G. Kresse, J. Furthmüller, and J. Hafner, *Ab initio force constant approach to phonon dispersion relations of diamond and graphite*, EPL **32**, 729 (1995).

[304] K. Parlinski, Z. Q. Li, and Y. Kawazoe, *First-principles determination of the soft mode in cubic ZrO_2*, Phys. Rev. Lett. **78**, 4063–4066 (1997).

[305] A. Togo and I. Tanaka, *First principles phonon calculations in materials science*, Scr. Mater. **108**, 1–5 (2015), http://atztogo.github.io/phonopy/.

[306] R. K. Pathria, *Statistical mechanics*, 2nd ed., Elsevier Butterworth-Heinemann, 1996.

[307] M. T. Dove, *Introduction to lattice dynamics*, Cambridge University Press, 1993.

[308] M. I. Mendelev, D. J. Sordelet, and M. J. Kramer, *Using atomistic computer simulations to analyze x-ray diffraction data from metallic glasses*, J. Appl. Phys. **102**, 043501 (2007), the potential file is available at http://www.ctcms.nist.gov/potentials/Cu-Zr.html.

[309] X. W. Zhou, R. A. Johnson, and H. N. G. Wadley, *Misfit-energy-increasing dislocations in vapor-deposited CoFe/NiFe multilayers*, Phys. Rev. B **69**, 144113 (2004).

[310] L. Ward, A. Agrawal, K. M. Flores, and W. Windl, *Rapid production of accurate embedded-atom method potentials for metal alloys*, arXiv:1209.0619 [cond-mat.mtrl-sci] (2012), the potential file is available at http://atomistics.osu.edu/eam-potential-generator/.

[311] Y. Q. Cheng, E. Ma, and H. W. Sheng, *Atomic level structure in multicomponent bulk metallic glass*, Phys. Rev. Lett. **102**, 245501 (2009), the potential file is the 2011 version from https://sites.google.com/site/eampotentials/Home/CuZr.

[312] H. S. Chen, *Glassy metals*, Rep. Prog. Phys. **43**, 353–432 (1980).

[313] G. Duan, K. De Blauwe, M. L. Lind, J. P. Schramm, and W. L. Johnson, *Compositional dependence of thermal, elastic, and mechanical properties in Cu–Zr–Ag bulk metallic glasses*, Scr. Mater. **58**, 159–162 (2008).

[314] J. Ding, Y.-Q. Cheng, H. Sheng, and E. Ma, *Short-range structural signature of excess specific heat and fragility of metallic-glass-forming supercooled liquids*, Phys. Rev. B **85**, 060201 (2012).

[315] Z. Altounian, Tu Guo-hua, and J. O. Strom-Olsen, *Crystallization characteristics of Cu–Zr metallic glasses from $Cu_{70}Zr_{30}$ to $Cu_{25}Zr_{75}$*, J. Appl. Phys. **53**, 4755–4760 (1982).

[316] S. Ogata, Ju Li, and S. Yip, *Ideal pure shear strength of aluminum and copper*, Science **298**, 807–811 (2002).

[317] K.-W. Park, C.-M. Lee, M. Wakeda, Y. Shibutani, M. L. Falk, and J.-C. Lee, *Elastostatically induced structural disordering in amorphous alloys*, Acta Mater. **56**, 5440–5450 (2008).

[318] N. Mattern, J. Bednarčik, S. Pauly, G. Wang, J. Das, and J. Eckert, *Structural evolution of Cu–Zr metallic glasses under tension*, Acta Mater. **57**, 4133–4139 (2009).

[319] W. C. Overton and J. Gaffney, *Temperature variation of the elastic constants of cubic elements. I. Copper*, Phys. Rev. **98**, 969–977 (1955).

[320] E. M. Carvalho and I. R. Harris, *Constitutional and structural studies of the intermetallic phase, ZrCu*, J. Mater. Sci. **15**, 1224–1230 (1980).

[321] A. Păduraru, A. Kenoufi, N. P. Bailey, and J. Schiøtz, *An interatomic potential for studying CuZr bulk metallic glasses*, Adv. Eng. Mater. **9**, 505–508 (2007).

[322] S. Cui, X. Xiao, H. Hu, Z. Lv, G. Zhang, and Z. Gong, *First-principles study of structural, electronic and elastic properties of single crystal CuZr*, Physica B: Condens. Matter **406**, 3389–3391 (2011).

[323] T. Brink, D. Şopu, and K. Albe, *Solid-state amorphization of Cu nanolayers embedded in a $Cu_{64}Zr_{36}$ glass*, Phys. Rev. B **91**, 184103 (2015).

[324] Li Gao, X. Jiang, S.-H. Yang, P. M. Rice, T. Topuria, and S. S. P. Parkin, *Increased tunneling magnetoresistance using normally bcc CoFe alloy electrodes made amorphous without glass forming additives*, Phys. Rev. Lett. **102**, 247205 (2009).

[325] J. Zemp, *Atomic arrangements in copper-zirconium metallic glasses*, Ph.D. thesis, ETH Zürich, 2015.

[326] S. P. Coleman, D. E. Spearot, and L. Capolungo, *Virtual diffraction analysis of Ni [0 1 0] symmetric tilt grain boundaries*, Model. Simul. Mater. Sci. Eng. **21**, 055020 (2013).

[327] J. Bünz, T. Brink, K. Tsuchiya, F. Meng, G. Wilde, and K. Albe, *Low temperature heat capacity of a severely deformed metallic glass*, Phys. Rev. Lett. **112**, 135501 (2014).

[328] T. Brink, L. Koch, and K. Albe, *Structural origins of the boson peak in metals: From high-entropy alloys to metallic glasses*, Phys. Rev. B **94**, 224203 (2016).

[329] F. Meng, K. Tsuchiya, Seiichiro II, and Y. Yokoyama, *Reversible transition of deformation mode by structural rejuvenation and relaxation in bulk metallic glass*, Appl. Phys. Lett. **101**, 121914 (2012).

[330] Yu. P. Mitrofanov, M. Peterlechner, S. V. Divinski, and G. Wilde, *Impact of plastic deformation and shear band formation on the boson heat capacity peak of a bulk metallic glass*, Phys. Rev. Lett. **112**, 135901 (2014).

[331] J.-W. Yeh, *Alloy design strategies and future trends in high-entropy alloys*, JOM **65**, 1759–1771 (2013).

[332] M.-H. Tsai and J.-W. Yeh, *High-entropy alloys: A critical review*, Mater. Res. Lett. **2**, 107–123 (2014).

[333] D. B. Miracle, J. D. Miller, O. N. Senkov, C. Woodward, M. D. Uchic, and J. Tiley, *Exploration and development of high entropy alloys for structural applications*, Entropy **16**, 494–525 (2014).

[334] V. A. Khonik, *Understanding of the structural relaxation of metallic glasses within the framework of the interstitialcy theory*, Metals **5**, 504–529 (2015).

[335] L. Van Hove, *The occurrence of singularities in the elastic frequency distribution of a crystal*, Phys. Rev. **89**, 1189–1193 (1953).

[336] S. Scudino, H. Shakur Shahabi, M. Stoica, I. Kaban, B. Escher, U. Kühn, G. B. M. Vaughan, and J. Eckert, *Structural features of plastic deformation in bulk metallic glasses*, Appl. Phys. Lett. **106**, 031903 (2015).

[337] N. Miyazaki, Yu-C. Lo, M. Wakeda, and S. Ogata, *Properties of high-density, well-ordered, and high-energy metallic glass phase designed by pressurized quenching*, Appl. Phys. Lett. **109**, 091906 (2016).

[338] T. Brink, M. Peterlechner, H. Rösner, K. Albe, and G. Wilde, *Influence of crystalline nanoprecipitates on shear-band propagation in Cu–Zr-based metallic glasses*, Phys. Rev. Appl. **5**, 054005 (2016).

[339] R. J. Hebert, J. H. Perepezko, H. Rösner, and G. Wilde, *Dislocation formation during deformation-induced synthesis of nanocrystals in amorphous and partially crystalline amorphous $Al_{88}Y_7Fe_5$ alloy*, Scr. Mater. **54**, 25–29 (2006).

[340] C. N. Kuo, J. C. Huang, J. B. Li, J. S. C. Jang, C. H. Lin, and T. G. Nieh, *Effects of B2 precipitate size on transformation-induced plasticity of Cu–Zr–Al glassy alloys*, J. Alloys Compd. **590**, 453–458 (2014).

[341] Y. F. Sun, B. C. Wei, Y. R. Wang, W. H. Li, T. L. Cheung, and C. H. Shek, *Plasticity-improved Zr–Cu–Al bulk metallic glass matrix composites containing martensite phase*, Appl. Phys. Lett. **87**, 051905 (2005).

[342] J. Das, S. Pauly, C. Duhamel, B. C. Wei, and J. Eckert, *Microstructure and mechanical properties of slowly cooled $Cu_{47.5}Zr_{47.5}Al_5$*, J. Mater. Res. **22**, 326–333 (2007).

[343] A. H. Cottrell, *Dislocations and plastic flow in crystals*, Clarendon Press, 1953.

[344] J. P. Hirth and J. Lothe, *Theory of dislocations*, 2nd ed., Krieger Publishing Company, 1982.

[345] G. Wang, S. Pauly, S. Gorantla, N. Mattern, and J. Eckert, *Plastic flow of a $Cu_{50}Zr_{45}Ti_5$ bulk metallic glass composite*, J. Mater. Sci. Technol. **30**, 609–615 (2014).

[346] M. J. Powell, *Site percolation in randomly packed spheres*, Phys. Rev. B **20**, 4194–4198 (1979).